UNIVERSITY OF READING

Department of Meteorology

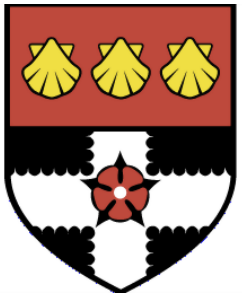

On the Behaviour of Tropical Depressions and their Interaction with the Indian Monsoon Trough Region

Kieran Mark Rainwater Hunt

A thesis submitted for the degree of Doctor of Philosophy

December 2016

DECLARATION

I confirm that this is my own work and the use of all material from other sources has been properly and fully acknowledged.

Kieran Mark Rainwater Hunt

Abstract

This thesis examines the behaviour of Indian monsoon depressions (MDs), synoptic-scale systems that frequent the monsoon trough throughout the boreal summer. The original contribution to knowledge is a substantial advancement of our understanding on the structure, variability, and dynamics of MDs. A feature-tracking algorithm is developed to emulate the subjective methods used by the India Meteorological Department, based on surface wind speed and surface pressure. This is applied to reanalysis data spanning from 1979 to the present day (2016), extracting 106 events. These are used to build a statistical composite, with which we interrogate the structure and variability subject to external forcings. It is found, for example, that MDs significantly intensify during La Niña and active monsoon spells, and have different spatial structure over ocean than land. These events are also examined in satellite data, where we discover and characterise a bimodal, diurnal cycle in surface precipitation; the structure of cloud type with dominating deep convection south of the centre; and present the first composite picture of vertical hydrometeor structure in MDs. A propagation mechanism whereby the MD behaves as a vortex in the presence of a wall (i.e. the Himalayan massif) is presented and shown to perform better than competing theories at predicting the velocity and heading of MDs. It is also shown, using a case study in the Met Office Unified Model (MetUM), that varying antecedent soil moisture conditions can significantly change the length of a MD track but not its direction. The sensitivity of MDs to changes in horizontal resolution in the MetUM are also explored across seven case studies at eight resolutions. It is found that the intensity is typically slightly overpredicted, correlating with too great a latent heat release in the mid-troposphere. Spatial structure is shown to improve with resolution but improvement saturates beyond N512 (40 km) resolution.

ACKNOWLEDGEMENTS

I thank my supervisors, Andy Turner, Pete Inness, David Parker, and Richard Levine for their invaluable guidance and constructive criticism of this work in its entirety. I

would especially like to thank Andy, who often went above and beyond the rôle of supervisor in his friendly and generous encouragement, both academic and pastoral. I

would also like to thank Gill Martin for her support during my involvement with the Met Office, and Steve Woolnough and Emily Black for their rigorous, biannual quality control.

To Jennifer, Mary, Bruce, and Frances

CONTENTS

LIST OF FIGURES

LIST OF TABLES

CHAPTER 1

INTRODUCTION

Opening remarks

This thesis is presented as a collection of five papers completed during the course of the degree, a summary of which is given in Tab. 1.1. Care has been taken to establish a good balance between literary unity of the thesis as a whole and keeping the individual chapters as faithful as possible to the form in which they were published/submitted. The fundamental differences lie in the introduction and conclusion sections of each chapter, which have been altered so as to lead into each other and shortened so as to reduce repetition.

1.1 Background

The South Asian monsoon (from Arabic *mawsim*, meaning *season*) is a major component in the global hydrological cycle, responsible for about 10000 km^3 of rainfall per season, or, approximately 10% of the annual global precipitation over land. This important phenomenon is understood to come about through a reversal of the equatorial winds due to the heat low associated with the Indian peninsula, with blocking from the

Title	Journal	Submission	Acceptance	Citation
On the structure and dynamics of Indian Monsoon Depressions	*Mon. Wea. Rev.*	2014-11-13	2016-01-21	Hunt et al. (2016a)
The movement of Indian Monsoon Depressions by interaction with image vortices near the Himalayan Wall	*QJRMS*	2015-01-20	2016-04-03	Hunt and Parker (2016)
The spatiotemporal structure of precipitation in Indian Monsoon Depressions	*QJRMS*	2016-01-08	2016-08-15	Hunt et al. (2016b)
The effect of soil moisture perturbations on Indian Monsoon Depressions in a numerical weather prediction model	*J. Clim.*	2016-10-10		Hunt and Turner (2016)
The representation of Indian monsoon depressions at different horizontal resolutions in the Met Office Unified Model	*QJRMS*	2016-11-15	2017-03-03	Hunt and Turner (2017)

Table 1.1: A summary of the published/submitted papers that comprise this thesis, ordered by submission date.

steep Himalayan orography, deep tropospheric temperature gradient from the elevated heating of the Tibetan Plateau, and in part, blocking from the Somali highlands. This moisture-laden westerly flow encircles the monsoon trough providing ample water for organised tropical convection over much of peninsular south Asia.

Embedded in the monsoon exist regular cyclonic disturbances that range in intensity from open easterly waves to full-blown tropical cyclones; such disturbances typically originate in the Bay of Bengal, or arrive there having passed over the Indochina peninsula after genesis somewhere in the West Pacific. Either way, the Bay of Bengal provides almost ideal conditions to create or amplify these disturbances (Sikka, 1977): there are warm SSTs (often in excess of 30°C), the steeply curved eastern end of the cyclonic monsoon trough is rich in lower-tropospheric vorticity, and there is the southern extent of the Tibetan anticyclone aloft that enhances divergent outflow. Monsoon distur-

Name	General	Ocean	Land
Low	$\Omega = 1$	$U_* < 17\,\mathrm{kn}$	$\Omega = 1$ within 3°
Depression	$\Omega = 2, 3$	$17\,\mathrm{kn} < U_* < 27\,\mathrm{kn}$	$\Omega = 2$ within 3°
Deep depression	$\Omega = 2, 3$	$28\,\mathrm{kn} < U_* < 33\,\mathrm{kn}$	$\Omega = 3, 4$ within 3°
Cyclonic storm	$\Omega > 4$ and $34\,\mathrm{kn} < U_* < 47\,\mathrm{kn}$		
Severe cyclonic storm	$\Omega > 4$ and $48\,\mathrm{kn} < U_* < 63\,\mathrm{kn}$		
Very severe cyclonic storm	$\Omega > 4$ and $63\,\mathrm{kn} < U_* < 119\,\mathrm{kn}$		
Super cyclonic storm	$\Omega > 4$ and $U_* > 120\,\mathrm{kn}$		

Table 1.2: The most recent official classifications for monsoon disturbances, as outlined by the glossary published by the India Meteorological Department (e.g. IMD, 2015). Ω is the count of closed even isobars (i.e. ..., 998, 1000, 1002, ... hPa) at the surface, U_* is the surface wind speed. All relevant criteria must be met for the classification to be made. 1 knot = 0.51 m s^{-1}.

bances are classified by the India Meteorological Department (IMD, 2015) into distinct categories based on surface wind speed and pressure anomalies, and these are collated in Tab. 1.2. For the sake of the rest of this work, 'deep' depressions will be merged with depressions to form a single category, as has been done by other authors (Cohen and Boos, 2014) and the IMD itself. The definitions given here are the most recent published by the IMD, and offer only slight variation from previous iterations (the general, as opposed to land only, isobar criterion and the 3° constraint are not mentioned in previous literature). It is rare to see a disturbance of cyclonic storm intensity or above during the monsoon season as the prominent westerlies in the lower troposphere and the tropical easterly jet in the upper troposphere result in substantial vertical wind shear that inhibits cyclonic development (Riehl and Shafer, 1944; DeMaria, 1996). To illustrate this, a summary of depressions, cyclonic storms, and severe cyclonic storms, taken from the IMD eAtlas (`http://www.rmcchennaieatlas.tn.nic.in/`), is given in Tab. 1.3. As can be seen from the table, depressions are by far most common during the months of the boreal summer (June - September), whereas the more intense storms peak outside the season in May, October, and November. A quick calculation from the data in Tab. 1.3 suggests a mean frequency of 4.8 MDs per season (June-September),

Month	D(BoB)	CS(BoB)	SCS(BoB)
January	11(11)	6(5)	2(2)
February	4(4)	1(1)	1(1)
March	2(2)	3(3)	2(2)
April	10(7)	14(12)	18(14)
May	38(29)	26(21)	60(41)
June	107(72)	44(33)	20(5)
July	144(104)	37(34)	8(8)
August	188(151)	29(25)	3(3)
September	160(124)	32(25)	20(15)
October	122(100)	66(49)	53(41)
November	65(44)	54(48)	86(70)
December	39(32)	28(25)	27(25)

Table 1.3: Summary, by month of genesis, of cyclonic events in India and surrounding seas (the Bay of Bengal and the Arabian Sea) from 1891-2014. Events are classified by the maximum intensity reached during their lifetime (D = depression or deep depression, CS = cyclonic storm, SCS = severe, very severe, or super cyclonic storm), and the bracketed values are for events whose geneses were in the Bay of Bengal. Data are from the IMD eAtlas.

an average of 3.6 of which spin up over the Bay of Bengal[1], with a further 1.6 events per season with a more intense classification than deep depressions.

With an average of 4-5 synoptic-scale disturbances moving across the peninsula each season, and an average duration of around 5 days (e.g. Yoon and Chen, 2005), we should expect these systems to be responsible for at least a significant minority of rainfall in the monsoon trough, where they are found most frequently Godbole (1977); Hurley and Boos (2015). Yet, there is huge variance on this number across previous studies: Dhar and Bhattacharya (1973) suggested a value around 10% over the Ganges basin; Mooley and Shukla (1989) found a value of 14% for the whole of India, and 27% for the central part; yet (Yoon and Chen, 2005) used a water budget analysis to determine the value was between 45% and 55%. This is surprising given the depth of careful work

[1]Many of the rest can be attributed to one of two sources: firstly, monsoon onset vortices in June over the Arabian Sea (Krishnamurti et al., 1981) which have been known to develop into full-blown tropical cyclones (Willetts et al., 2016); and secondly, MDs can often spin up over land, typically in September, if the surface is wet enough (Hurley and Boos, 2015).

done on constraining precipitation in the context of individual monsoon depressions (e.g. Roy and Roy, 1930; Mull and Rao, 1949; Pisharoty and Asnani, 1957; Mooley, 1973; Rajamani and Rao, 1981; Kripalani and Singh, 1986), much of which draws on careful statistical analysis of rain gauge data. The difficulty in constraining this figure is made all the more troubling by Stowasser et al. (2009) who suggest that depressions will become more intense and precipitating in a warming climate. Despite issues with attribution of MD rainfall to monsoon totals, these studies have left us with a fairly sound picture of precipitation relative to the MD. We have known since Roy and Roy (1930) and Ramanathan and Ramakrishnan (1933) that MD precipitation is maximum southwest of the centre of the system; Pisharoty and Asnani (1957) produced the first significant analysis and suggested that rainfall in that area had an average maximum of 75 mm day^{-1}; Rajamani and Rao (1981) were the first to show that this asymmetry was likely due to quasigeostrophic uplift, a fact forgotten until it was rediscovered independently by Boos et al. (2015). In addition, Mooley (1973) synthesised a number of synoptic hypotheses from previous literature that we will consider in further detail in Chapter 4.

The synoptic description of MDs led any serious dynamical treatment by several decades because upper air soundings were sufficiently rare to permit only intensive observations of single events, compared to the general abundance of rain gauges. Many studies indeed analysed individual depressions (Das, 1952; Ananthakrishnan and Bhatia, 1958; Koteswaram and George, 1958, 1960; Kulshrestha and Gupta, 1964; George and Datta, 1965; Rao and Rajamani, 1972; Daggupatty and Sikka, 1977; Rao et al., 1978) but it was not until the study of Godbole (1977) that the first three-dimensional picture emerged. He followed the examples of Reed and Recker (1971) and Williams and Gray (1973) for tropical wave disturbances in the Pacific and Frank (1977) for tropical cyclones and computed a five-depression composite for the disturbances of 1973, using approximately 100 upper air and 100 surface observations. Though lacking serious rigour and entirely lacking observations over the ocean (a common problem

until the satellite era), his study was the first to explicitly identify a number of features as being common to MDs: westward axial tilt with height, warm core aloft, circulation asymmetry, and dry mid-troposphere. Despite their use, and continued frequency for other types of disturbance, composite studies of MDs remained peculiarly sparse. Soon after, Keshavamurty et al. (1978) considered dynamic fields of a 15-depression composite, going so far as to subtract a climatology in an attempt to study MDs as the transient disturbances that they are. Later, Sarker and Choudhary (1988) looked at wind, moisture, and thermal fields of a 22-depression composite, and Prasad et al. (1990) looked at the wind and cloud structure of a 40-disturbance composite split by number of closed isobars; however neither study considered (and nor did Godbole, 1977, for example), the importance of removing monsoon westerlies to get a true picture, and so all came to the arguably incorrect conclusion that the strongest MD winds are found to the south of its centre.

More detailed background discussions are delegated to the chapters in which they are relevant.

1.2 Motivation

Given the frequency of these disturbances (Mooley and Shukla, 1989) and the quantity of rainfall associated with them (Pisharoty and Asnani, 1957), a sound understanding of their underlying structure and dynamics is crucial so that we can produce quality forecasts for the region (which depends heavily on its agrarian economy; Ramage, 1971; Jha, 2003). Further to this, understanding of MDs is also important for climate model simulations in light of poor representation of rainfall over the monsoon trough in many CMIP5 models and the climate configuration of the MetUM (Levine and Martin, 2016); improvement is crucial both for getting the climatology right and predicting future changes in extreme events. Despite this, attempts to interrogate the three-dimensional structure via a statistical treatment of observational data are approaching forty years

old and have a typically small sample size (Mulky and Banerji, 1960; Godbole, 1977; Sikka, 1977; Keshavamurty et al., 1978); those that are newer and have a larger sample size concern themselves with just a small handful of synoptic variables (Sarker and Choudhary, 1988; Prasad et al., 1990). In the modern era, where we have extensive reanalysis datasets assimilating globally reporting networks of automatic sensors and dozens of satellites, no such study exists[2], and we are left without a complete or reliable database with which we can inform theory or models. What would such a composite structure look like? Would it be statistically robust? Using even an intermediate length reanalysis, such as ERA-Interim (Dee et al., 2011, see §2.2.1 for details) which extends from 1979 to the present would, at a conservative rate of two depressions per year give us a dataset of over eighty to analyse.

This presents an intermediate problem: with no tracking data available[3], we must generate our own if we are to produce any meaningful statistics. What then, is the best method for converting the subjective method used by the IMD for finding the trajectories of these systems into an objective, feature-based algorithm that can be applied to a suitable dataset? If this can be done successfully, we will have a sufficient sample size of MDs to be able to probe second-order questions about structure that will illuminate the relationship between these events and their environment, that is: how do monsoon depressions respond to large-scale forcing? This will open up questions about how ENSO, the Indian Ocean Dipole, and the active and break spells of the monsoon strengthen, weaken, or otherwise alter present MDs. This avenue can be expanded to consider smaller scales too: to what extent are depressions affected by a diurnal cycle? How do they behave over land as opposed to over the ocean? This latter question is of particular importance given the historical sparsity of ocean-based measurements. Now, assuming the sample size is sufficient, we should also be able to probe the structure

[2]This was certainly true at the outset of this work, but has since been partially covered by the global depression climatology of Hurley and Boos (2015).

[3]Except for those of the India Meteorological Department which are not made publicly available and those of Hurley and Boos (2015) which were not available at the commencement of this work (and use different criteria for the definition of *monsoon depression*).

with satellite data. This raises a new issue: given the data from satellite overpasses is not dense (cf. reanalysis), how can we construct a composite picture of MDs that has statistical significance? If we can solve this, we will be able to examine directly the vertical structure of important moist thermodynamical processes at a very fine resolution.

Quantifying the structure and variability of depressions is of clear importance, but it is static. If one wishes for a complete picture of these systems, we must also determine the process(es) governing their propagation. Climatologically, MDs that originate in or around the Bay of Bengal propagate northwestward (Sikka, 1977). This could probably be explained by beta drift if it were not for the fact that this underpredicts the propagation speed and that depressions are embedded in strong lower-tropospheric westerlies. Historically, this anomalous movement has been attributed to quasigeostrophic vortex stretching towards the westsouthwest (Rao and Rajamani, 1970), the convergence maximum being southwest of the centre (Krishnamurti et al., 1975), or to anomalous circulation being supported by latent heat release above the precipitation maximum in the same place (Chen et al., 2005). Both of these hypotheses, however, predict southwestward, rather than northwestward, propagation, and so are wrong by some ninety degrees. To date, no study has addressed this issue[4], and so we retain the question we started with: what is the mechanism responsible for the northwestward propagation of monsoon depressions against monsoon westerlies? If such a singular dominant mechanism (or coupled group thereof) does exist, it seems unlikely that it would not be further modulated by subordinate processes. For example, antecedent soil moisture in north India has been associated with extended MD duration (Chang et al., 2009), and assimilation of soil moisture data into numerical weather prediction models has been associated with improved track forecasts (Chandrasekar et al., 2008). So, how does the land surface state affect a passing depression?

At the start of this section, we part motivated this research into monsoon depres-

[4]Again, this was true at the outset of this work, but some advance has since been made by Boos et al. (2015).

sions by asserting that improved knowledge of their structure and behaviour would inform models and give us more material with which to validate their output. It is important, also, to determine how such systems are currently represented in models, a problem which again lacks detailed analysis in existing literature[5]. This raises the first important question: how well are depressions currently represented in global models? This simple question opens the door to a *salmagundi* of others; of these, we shall concern ourselves with those regarding how the representation can be improved. Firstly, it is no great mystery that models are generally improved by increasing the resolution at which they are run; however, this is typically an expensive process, so, what improvement (if any) do we see in the structure of monsoon depressions as we increase model resolution? And, at least equally as important: are MD track forecasts sensitive to model resolution? Secondarily, seeing as many forecasts over the Indian region are run as global models where convection is not permitted and must thus be parameterised: how sensitive is the structure of a modelled monsoon depression to tuning of the convective parameterisation scheme?

In Chapter 2 we will fully describe the tracking algorithm that forms a core part of much of the work carried out, as well as outline important, reoccurring external datasets that are used. The first work chapter, Chapter 3 (Hunt et al., 2016a), explores a 106-depression composite generated by applying the tracking algorithm to reanalysis data; here we also investigate the causes of variability in MDs, from large-scale atmospheric phenomena down to the diurnal cycle and land-sea contrast. The composite structure and diurnal cycle are then explored in greater detail in Chapter 4 (Hunt et al., 2016b) using satellite swath data from TRMM and CloudSat. We then, motivated by the analysis in Chapter 3, propose a novel propagation mechanism for MDs in Chapter 5 (Hunt and Parker, 2016), hypothesising that the vortex behaves as one of an image pair in the presence of the Himalayas, and showing that this predicts propagation velocity more accurately than other simple models. In Chapter 6 (Hunt and Turner, 2017) we

[5]Or any analysis at all until the recent work of Praveen et al. (2015) and Johnson et al. (2016)

explore the relationship between model resolution and MD propagation, structure, and variability in the Met Office NWP. Then, in the last work chapter, Chapter 7 (Hunt and Turner, 2016), we use the Met Office NWP to explore to what extent MD structure and tracks are affected by antecedent soil moisture, before concluding in Chapter 8.

CHAPTER 2

DATA AND METHODS

Opening remarks

This short chapter is designed to give the reader a broad overview of recurring methodology and external data sources that are used throughout the rest of this thesis. Although we intend to keep the working chapters as close as possible to their published/submitted forms, there is inevitable overlap when describing commonly used tools and datasets. As such, this chapter should serve as a overview and primer for the reader, with those parts unique or important to each chapter being retained therein.

2.1 Tracking algorithm

2.1.1 Motivation

Detailed study of any type of system requires an unbiased dataset of their tracks, without which performing any system-relative analysis is rendered impossible and even basin-relative statistics become tedious to disentangle. Such datasets exist for example, for tropical cyclones (e.g. IBTrACS, Knapp et al., 2010) and diabatic Rossby waves (Boettcher and Wernli, 2011); but at the outset of this work no published dataset on

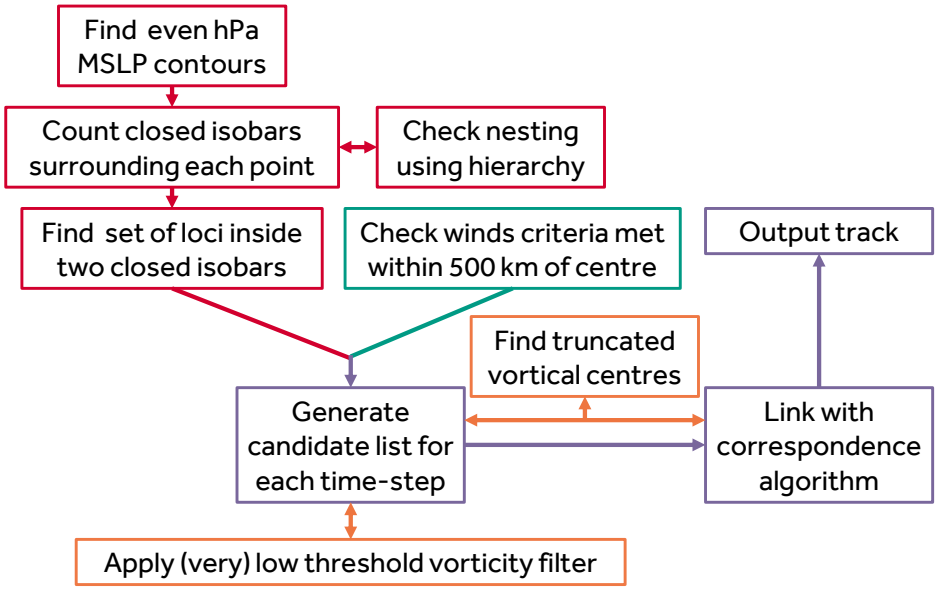

Figure 2.1: Schematic of the tracking algorithm. Descriptions of each term are given in the text. Red, turquoise, orange, and purple boxes are described in §2.1.2, §2.1.3, §2.1.4 and §2.1.5 respectively.

monsoon depression tracks was freely available – only maps from the India Meteorological Department's eAtlas (`http://www.rmcchennaieatlas.tn.nic.in/`) from which the only available data are images of tracks overlaid on maps. It was therefore decided to devise a tracking algorithm that would be run in reanalysis data and could return the times and locations of events that satisfied the monsoon depression criteria established by the IMD (see Tab. 1.2). We note that there now exist several freely available track datasets on monsoon depressions (Hurley and Boos, 2015; Praveen et al., 2015). It was decided that the tracking algorithm (see Fig. 2.1) should attempt to follow as closely as possible the IMD depression criteria in surface pressure anomaly and surface wind speed. There are two important caveats here: firstly, we do not have access to the archive of synoptic weather station data collected by the IMD – they do not make it publicly available – and secondly, their tracks are produced subjectively ('by hand') using the criteria, rather than objectively by some automated process. Both of these factors will inevitably produce some discrepancies between the two sets of tracks, but these ought be minor and insignificant.

2.1.2 Counting contours

One of the two criteria used by the IMD specifies that a monsoon depression (over land, specifically) must have at least two closed isobars (of even hPa) associated with the circulation[1]. Determining this is not trivial, but it is fortunately not computationally intractable either. This is deconstructed into two parts: firstly, the locations of the contours must be computed, and secondly, we must determine the set of loci that are enclosed by – for the case of depressions, at least – two or more closed contours. For the former, we follow a very common method used by many graphical software packages: consider a grid of equal resolution to the input data whose vertex values are defined by said data, and then the vertices of the (polygonal) contour are interpolated accordingly. For example, if one wants to find the location of a contour line of value p, and there are two adjacent gridpoints, $g_{i,j}$ and $g_{i,j+1}$, with values $p - p_m$ and $p + p_n$ respectively, we suppose from simple linear interpolation that there must exist a vertex of that contour set at $(i,\ j + p_m/(p_m + p_n))$. An illustration of this is given in Fig. 2.2, with the graphical addition of representative contour lines computed using a composite Bézier spline. With the set of polygons describing the contours established, we turn to the problem of determining the set of loci that find themselves fully enclosed by at least n of them. This is the standard *point-in-polygon* problem of computer science which is considered an important topic in computational geometry (Preparata and Shamos, 2012). Since then, a number of successful and efficient techniques have been developed; we are not concerned with an intercomparison of these algorithms, it will be sufficient to agree with existing literature that the ray-casting algorithm of Shimrat (1962) is best-suited to our purposes. This is a simple algorithm: take the locus and contour polygon of interest, draw a straight line from the locus to the edge of the domain – if this line intersects the polygon an odd number of times, the locus is in the polygon.

[1]Technically speaking, the IMD glossary (IMD, 2016) requires that these contours be within 3° of the centre. This is fine when tracking MDs subjectively as the centres are determined *a priori*; however, as we use the existence of contours to identify and track the systems in the first place, this criterion can only be evaluated efficiently *post hoc*. It has been left out of the tracking procedure, and no tracked MDs were found to violate it.

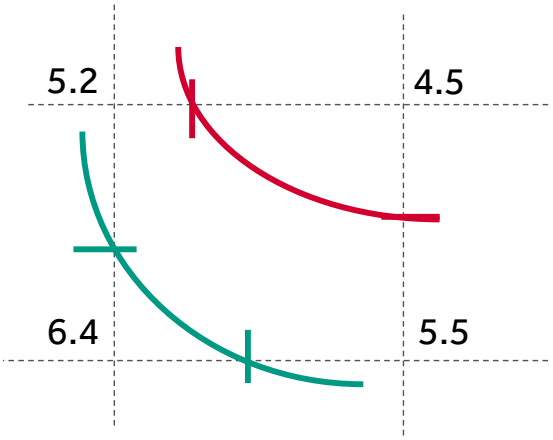

Figure 2.2: Simple example of the interpolating contour-seeking algorithm discussed in the text. The values of the bivariate field are defined at each grid vertex, and the points of intersection of the contour lines are determined by interpolation. Here, the red line represents part of a contour set of value 5, and the cyan line is of value 6.

One then simply iterates through the known (prescribed) contour values for each point and runs a count of how many closed contours surround it. This works fine so long as the environment is climatologically flat (i.e. there is no existing structure in the contour field), but we must remember that depressions inevitably interact with the monsoon trough which in itself typically has at least two such closed contours; this could result in a substantial quantity of false positives as weak one-isobar monsoon lows would pick up a gratuitous isobar and be incorrectly categorised as depressions. There are two options here: we could subtract the climatology and directly extract the pressure anomaly rather than inferring it, or we could somehow use the asymmetric shape of the trough with its deepening towards the northwest to have the algorithm neutralise its effect. The former choice is apt for datasets where we can produce a long-term climatology, but given our intent for this to be applicable even to short-term datasets produced by NWP models, is unsuitable.

Fortunately, the latter option presents an alternative solution. The monsoon trough is roughly elliptical with its major axis orientated northwest-southeast, deepening (usually significantly) towards the former, which almost always provides several closed contours over northwest India and Pakistan. Now, the set of all contour polygons can be

represented as nodes in an unordered tree (or group thereof), i.e. if a contour polygon is completely encircled by another, it shall be considered a child of it, and vice versa for parents. It is a trivial process to create these trees, particularly since we want to construct a directional hierarchy[2] – starting from the contour polygon at the highest pressure, a unique pointer is assigned to each polygon, each of which will form the head node of a distinct tree; we then iterate through each polygon at the next-highest value, running the aforementioned *point-in-polygon* test on each vertex of the polygon across each potential parent until a match is found, if no match is found, this contour polygon is assigned the head node of a new tree. This process is repeated until all contour polygons have been assigned to a parent or as head node of a new tree. These trees can then be used to find and eliminate the effect of the trough – we know that the trough exists as one elongated contour polygon (speaking in terms of even hPa intervals) that extends across northern India with additional contours towards the dry northwest where it deepens. Thus, if a potential MD is not in the trough, it is very likely to exist as a single tree with an equal number of levels and nodes (i.e. each parent node has exactly one child); if, however, it moves to interact with the trough, we expect to see a tree where one node has at least two children nodes (with their respective descendants). Knowing this, we can remove from consideration of the contour counting any contour polygon with two or more children, and its parents; examination of a selection of highly differing case studies indicated that this was by far the most effective method at stripping false positives caused by the presence of the trough.

This leaves us with one final issue to resolve before concluding this discussion. Previously, when we computed the vertices of a given contour polygon set, we simply made the assumption that the polygon was closed; there is essentially only one reason why this might not be the case, when the polygon is intersected by the edge of the domain. There are two simple solutions that we can consider: assigning the edge of the

[2]That is to say, for the purposes of tracking low pressure systems using surface pressure contours in this way, we would consider, for example, a 994 hPa contour inside a 996 hPa contour to be a child but not vice versa.

domain in between the two points of intersection as part of the polygon for the purposes of closing it, or simply removing it from consideration altogether. The former can cause unreliable results when trying to create the hierarchy trees discussed earlier, and so it is suitable to choose a suitably-sized domain and reject any contour polygons that extend beyond it – this process of creating a contour tree is shown in Fig. 2.3. Fig. 2.4 shows the difference in number of encircling contours computed with and without applying the hierarchy and domain filters described here.

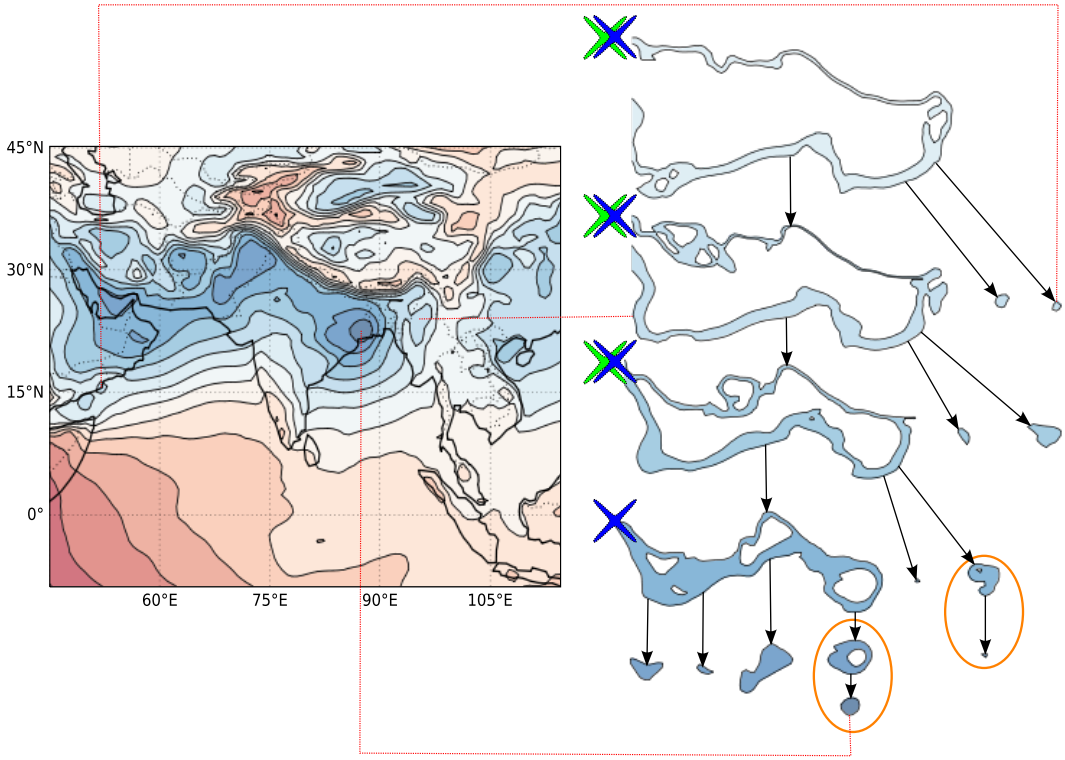

Figure 2.3: Example contour polygon subtree including MD signal; this is for mean sea-level pressure (even hPa intervals) at 2014-08-04 06Z. Dotted red lines indicate the links between selected contour polygons on the map and tree, orange ellipses denote possible MD candidates according to the two closed contour requirement, green crosses indicate that the contour polygon would be rejected for intersecting the domain boundary, and blue crosses indicate that the contour polygon would be rejected for having more than one child.

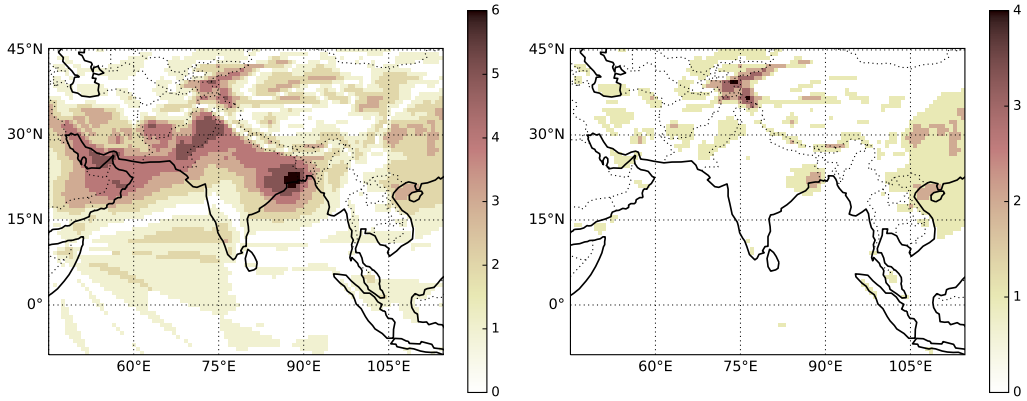

(a) No hierarchy or domain filter

(b) Hierarchy and domain filter

Figure 2.4: The results of the contour counting algorithm for ERA-Interim reanalysis mean sea-level pressure at 2014-08-04 06Z, (a) without applying the additional stability filters discussed in the text, and (b) with them. Colour indicates contour count as described by the respective colour bars.

2.1.3 Wind criteria

Along with sea-level pressure contours, the other important variable to consider in diagnosing the presence of a monsoon depression is surface wind speed. In §1 we saw that the IMD specified surface wind speed (over the ocean) must be between 8.5 and 16.5 m s^{-1}. Determining this is made nontrivial by the fact that cyclones have a wind speed minimum at the centre and that monsoon depressions exist in a region of nonzero climatological wind speed. Fortunately, near the surface this is typically not more than 2-3 m s^{-1}, and while this effect is impossible to disentangle without a suitable climatology, there is no evidence that the IMD perform any such subtraction during their diagnoses. Either way, the tracking algorithm was run on reanalysis data both with and without the subtraction of the climatology – tracks from the former were occasionally extended at the beginning or end by a single timestep (owing to the received boost from arguably unrelated background winds) – owing to this fact and for the sake of consistency, no attempt is made hereafter to remove climatological winds during the tracking procedure.

So, we are at the point of having a set of 'blobs' of loci computed from mean sea-

level pressure over land; we now set upon the task of adding to these by applying the IMD depression wind criterion over the ocean in some appropriate way. The IMD do not make public any information on how they do this, but it seems sensible to determine some radius in which the maximum wind speed is to be found that is not so large that we would likely pick up potentially high wind speeds from other phenomena. From inspection of synoptic charts, and early work on composite MD structure (e.g., Godbole, 1977) it seems that there is typically a wide margin between the radius of maximum winds and the closest radius at which other phenomena typically get when near a depression. Erring on the side of caution, and noting there is little variance in the former, we select the search radius at 500 km. Therefore if the prescribed wind criterion is met anywhere within this radius from any of the previous loci then they are accepted as possible depression candidates. This selection is consistent with later work by other authors (e.g., Hurley and Boos, 2015).

2.1.4 Vorticity filters

Had we applied the techniques described thus far in this section to a dataset in which we were interested in tracking MDs, we would have returned the set of all loci which meet the requirements specified by the IMD. This is a good start, but it still yields an unacceptable number of false positives that are easily rejected by eye, and hence by the subjective method used by the IMD (but not the objective method used here). These unwanted events can come from a number of sources, but the most common are transient systems at the Himalayan foothills, and the high cross-equatorial winds near the East African coast. Here, we must break with the strict criteria of the IMD and seek assistance from the variable commonly used in tracking cyclones – vorticity (e.g., Hoskins and Hodges, 2002; Hurley and Boos, 2015). Lower-tropospheric relative vorticity is a very useful diagnostic: in the tropics, it is really only ever organised on a large-scale by the presence of some synoptic cyclonic circulation or by the horizontal shear of some barrier flow. There is barrier flow against the Himalayan foothills, but

these are typically southeasterlies during the monsoon and thus have an anticyclonic vorticity signal. The general presence of steep, tall orography in northern India can generate very high vorticity values (of both signs) but the spatial scale of these disturbances is very small, and they are simply filtered out using a low-pass filter; for this, we use a Gaussian filter of width 300 km. At this scale, the vorticity signal from a depression is preserved, but the noise from local orography is eradicated. We know from earlier composite work (Godbole, 1977) that relative vorticity in monsoon depressions reaches a maximum of about 14×10^{-5} s^{-1} at around 850 hPa, so we choose to threshold the filtered 850 hPa vorticity at 1×10^{-5} s^{-1}: this is still significantly below the lowest central vorticity values found even in weak monsoon lows (though this was discovered retrospectively by interrogating the dataset of Hurley and Boos, 2015), while remaining far above any typical value generated by orography or chance. We will come to use this useful diagnostic later in the tracking process.

2.1.5 Linking candidates to form a track

We now have a selection of different MD candidates at different times, presumably with some remaining false positives, but also with some missing parts of depressions; these missing candidates are usually either the result of assumptions made during the identification procedures mentioned previously, or because the depression simply weakens for a short period. Fortunately, these gaps are typically not more than one or two consecutive timesteps when applied to six-hourly reanalysis data (or model output with similar temporal resolution). Attaching these candidates to each other in coherent groups and filling in the gaps requires an algorithm that solves the *correspondence problem*. Such algorithms have common applications in computer vision software, ranging from ball tracking in sports to particle velocimetry in experimental fluid mechanics, and this wide range of uses has resulted in the availability of a number of popular algorithms, some of which were evaluated for use in a meteorological context by Hodges (1994). He used the algorithm described by Salari and Sethi (1990), essentially minimising

a trajectory smoothness cost function, using 'phantom' points extrapolated from existing paths in an attempt to cover any missing feature points (or candidates, as we have referred to them thus far). Hodges (1994) notes that minimising this smoothness cost function can be problematic, but that the Salari and Sethi (1990) algorithm is particularly good when there are many simultaneous features to track, and that the smoothness constraint is not a likely issue in meteorological applications provided that the input data have sufficiently high temporal resolution. Nevertheless, in our application, we do not expect more than two depressions to occur simultaneously, let alone the scores that the algorithm is designed to handle; as such, we keep the 'phantom point' method for finding missing candidates, but exchange the smoothness cost-minimisation function for a simple greedy nearest neighbour algorithm. This is where the filtered lower-tropospheric relative vorticity is re-used. We make the justified assumption that each MD snapshot (i.e. the representation of an MD candidate in a single timestep of data) will have a centre associated with a local maximum in the filtered vorticity field. Each candidate is given a unique link to the closest vorticity maximum, and the tracks are built simply by appending the nearest candidate in the next timestep to the end of the trajectory. The maximum trajectory speed is fixed arbitrarily at a generous 20 m s^{-1} (the speed of an MD does not typically exceed one quarter of this value), and if the nearest neighbour is outside this radius, it is assigned to the start of a new track. Missing points are then dealt with thus: for a given existing track, if no point is found using the nearest neighbour search, the track is held in the buffer and the search radius increased accordingly for the next timestep. This results in one of two eventualities: either no suitable point is found and the track is considered terminated at the location of the most recent candidate point; alternatively a suitable candidate point is found, this is added to the track and the missing candidate(s) are found by creation of phantom points. The locations of these phantom points are found by simple cubic

interpolation of the relative coordinates[3], and are then linked to the missing candidates by finding the nearest filtered vorticity local maximum. Fig. 2.5 shows a schematic of a simple example of the algorithm outlined here.

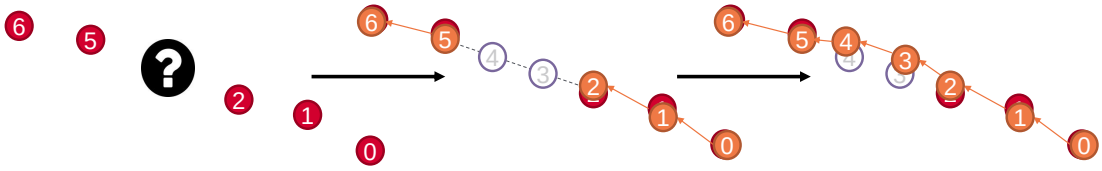

Figure 2.5: Simple application of our correspondence algorithm. Left: red markers indicate identified candidates according to wind speed/surface pressure criteria, with numbers representing some arbitrary timestamp. Centre: existing candidates are attached to the nearest vorticity local maximum (orange markers), and phantom points are interpolated for timestamps with missing candidates (white markers). Right: phantom points are attached to nearest vorticity local maximum and the track is completed.

2.1.6 Recent developments to the tracking algorithm

Since this body of work was completed, the tracking algorithm has been updated to improve efficiency and efficacy. The prescription (see Hunt et al. (2017) for application) is given below.

1. Compute the mean relative vorticity in the 850-800 hPa layer, then truncate the spectral resolution at T63 ($\sim$ 200 km at equator). We shall call this quantity ξ.

2. Locate all local maxima in ξ subject to some radius δ. I.e. a point is considered a local maximum if no points with a distance δ have a greater value of ξ. We shall call this set of points χ_i.

3. For each χ_i, associate local nonzero values of ξ and integrate to find the centroid of ξ for each. We shall call this set of points X_i.

4. To convert the candidate points into tracks: for each X_i at time point j, seek and attach the nearest neighbour, so long as it is within some distance Δ, using

[3]This ought to be done using some absolute measurement such as zonal/meridional distance from a given point, rather than using geoid coordinates like latitude/longitude, as these are not strictly independent axes.

a kd-tree nearest neighbour algorithm (e.g. Yianilos, 1993). The efficacy of this step can be increased by introducing the concept of a background drift, a very salient notion when considering the high-frequency, high-velocity nature of WDs. Here this is simply done by biasing the search radius using the contemporaneous wind field.

5. We also hold the tracks in memory for one time point, looking for a candidate in time point $j + 2$ within 2Δ of X_i. This prevents breaking a track into two unnecessarily in the event of a candidate disappearing for a frame.

6. These resulting tracks are then filtered thrice. Firstly, "stubs" of length shorter than one day are rejected. Secondly, tracks that do not pass through India, here defined as 5-30°N, 65-100°W, are rejected. Finally (and optionally) tracks whose geneses are east of 75°N are rejected (this filters out systems spinning up in the Arabian Sea). Those that remain are brought forward.

7. The methods described earlier in this chapter are used to determine the local wind speed maximum and number of surrounding closed isobars. These can be used to determine the ultimate classification of the system per IMD criteria.

8. The values of δ and Δ are determined empirically by running the algorithm over several case study dates and choosing the combination resulting in the highest fidelity. These were chosen to be 1000 km and 500 km (6 hours)$^{-1}$ respectively for monsoon low pressure systems.

2.2 Data overview

2.2.1 ERA-Interim reanalysis

Reanalyses are attempts at producing long-term meteorological datasets, using as far as possible a consistent method. In a broad sense, they typically take in historical and current observations from a variety of sources, including for example: satellites,

automatic weather stations, buoys, radiosondes, radar, and ships; these observational data are then assimilated into a unchanging forecast model. It should be noted that reanalyses are not generally regarded as suitable climate datasets (e.g. for trend analysis) owing to the methodological changes and different quantities of input data used over such long periods (e.g. Bengtsson et al., 2004). The idea is usually to produce something as close as possible to a historical global analysis where the gaps in data are filled by some numerical weather prediction model over at least several decades. Of course, not all reanalyses are global or span scores of years, e.g. the 2000-2012 Arctic System Reanalysis (Hines and Bromwich, 2008; Bromwich et al., 2009), but a good number do and it is our duty to select one with reasonable length and high skill in the tropical troposphere. Many long-term global reanalyses start in 1979, coinciding with the commencement of the satellite reconnaissance era (and the wealth of data collected for the First GARP Global Experiment; Jastrow and Halem, 1972); any such dataset would be suitable for interrogating monsoon depressions, of which there have been over a hundred since 1979. The European Centre for Medium-Range Weather Forecasting (ECMWF) Re-Analysis Interim (ERA-Interim) dataset was selected for its ease-of-access, its comparatively high skill (and that of its similar predecessor, ERA-40) compared with other reanalyses (Bosilovich et al., 2008; Dee et al., 2011; Schenkel and Hart, 2012; Moalafhi et al., 2016), and large selection of output variables.

The ERA-Interim reanalysis dataset (hereafter used interchangeably with the shorthand *ERA-I*) covers from January 1979 to the present day and continues in near real-time; it has T255 spectral resolution (approx. 78 km grid spacing at the equator) with 37 vertical levels spanning from the surface to 0.1 hPa (Berrisford et al., 2011). 27 of these vertical levels are in the troposphere (below 100 hPa), and the output analyses have a four-daily resolution: 00, 06, 12, and 18Z. The data assimilation is a 4DVAR scheme incremented in 12-hour steps: fundamental 3D variables such as temperature, humidity, and wind are taken from the most recent model forecast and combined with observations to form the analysis for the next forecast. The model also outputs some

variables not assimilated, such as cloud cover and radiative tendencies.

2.2.2 Tropical Rainfall Measuring Mission

The Tropical Rainfall Measuring Mission (TRMM) was launched at the end of 1997 as a joint mission between NASA and the Japan Aerospace Exploration Agency (JAXA); it operated continuously until the instruments were powered down in April 2015 in preparation for deorbit. On board were a number of instruments intended to probe key mechanisms in the tropical hydrological cycle (Simpson et al., 1988, 1996; Kummerow et al., 1998, 2000): the Precipitation Radar (PR), the Microwave Imager (TMI), the visible and infrared scanner (VIRS), Clouds and the Earth's Radiant Energy Sensor (CERES), and the Lightning Imaging Sensor (LIS). We will come to make substantial use of the first two instruments: the 13.8 GHz active-sensor PR had a swath width of 220 km, with resolution at the surface of 4 km[4], and provided a vertical profile of precipitation from near the surface (excepting ground clutter) to an altitude of approximately 20 km at a resolution of 250 m, with a detection threshold of 0.7 mm hr^{-1}; the five-band passive-sensor TMI operated at 10.7, 19.4, 21.3, 37, and 85.5 GHz – each of these (apart from the 21.3 GHz) had dual-polarization – with frequency dependent surface resolution ranging from approximately 7 to 70 km. One of the most useful datasets to arise from this mission was the TRMM Multi-Satellite Precipitation Analysis (TMPA; Huffman et al., 2007); in particular the $0.25° \times 0.25°$ 3-hourly gridded precipitation product, TRMM 3B42. This combines data from a wealth of satellites including the Geostationary Meteorological Satellite (GMS, also known as Himawari), the Geostationary Operational Environmental Satellites (GOES-E and GOES-W), Meteosat-7, Meteosat-5, and NOAA-12; version 7 also included the Global Precipitation Climatology Centre Project (GPCP) surface rain gauge analysis (Adler et al., 2003).

[4]The TRMM orbit was boosted in August 2001, increasing the swath width to 250 km with a footprint of 5 km × 5 km.

2.2.3 CloudSat

CloudSat was launched in April 2006 under the NASA Earth System Science Pathfinder program, its primary instrument is the 94 GHz nadir-only active reflectivity radar (Stephens et al., 2002, 2008). This has 125 m vertical resolution from the surface to 30 km, and a horizontal (along-track) resolution of approximately 1.5 km. Among the important outputs are cloud profile information and ice and liquid water profiles. We present a full description of the CloudSat datasets used in the relevant chapter, in Tab. 4.2

CHAPTER 3

ON THE STRUCTURE AND DYNAMICS OF INDIAN MONSOON DEPRESSIONS

3.1 Introduction

As discussed in Chapter 1, detailed investigation of depression structure in and around the Indian monsoon trough region has been performed previously (e.g., Godbole, 1977; Ding, 1981; Ding et al., 1984; Sarker and Choudhary, 1988; Prasad et al., 1990; Stano et al., 2002). Although the largest composite generated was of forty depressions (split into four categories of intensity) by Prasad et al. (1990), they only considered wind, and included analysis of satellite-imaged cloud cover on a case-study basis. Sarker and Choudhary (1988) analysed a number of variables (temperature, moisture, winds, vorticity) of a 27-depression composite based on events during 1961-74, but their data were interpolated from a relatively sparse array of radiosonde stations, all over land. More recently, Stano et al. (2002) conducted hydrometeor analysis on three depressions from 1999.

With the advent of extensive satellite and reanalysis datasets, a truly thorough analysis of a large depression composite over land and sea has now become a possibility. Hurley and Boos (2015) considered a 117-depression composite for 1979-2013, but they

did not go into specific detail, instead considering the worldwide climatology of monsoon depressions and examining the winds, potential temperature, and potential vorticity of Indian monsoon depressions. Boos et al. (2015) looked at a potential vorticity analysis of the same dataset. Their analysis also contains more depressions because they consider those originating over the Arabian Sea, whereas we do not.

Here, newly developed feature tracking software was applied over to reanalysis data over 36 years (1979-2013), recovering 106 depressions (Fig. 3.1(a)) that generally initiated in the Bay of Bengal and made landfall on the Indian subcontinent. These tracks were corroborated with the Indian Meteorology Department (IMD) Cyclone and Depression eAtlas (`http://www.imdchennai.gov.in/cyclone_eatlas.htm`). Thirty-four of these occurred between 1999 and 2013 and thus fall within the Tropical Rainfall Measuring Mission (TRMM) regime (Kummerow et al., 1998).

We will analyse horizontal and vertical structure of the composite depression, and compare the structure and dynamics of depressions when situated over ocean and land, as well as the influence of large scale forcing from modes of intraseasonal and inter-annual variability on depression strength and structure. An outline of the data and methodology is given in §3.2. We analyse horizontal cross-sections of the composite monsoon depression in §3.3, looking at both satellite-based and reanalysis data. In §3.4 we then look at vertical cross-sections of the composite.

Subsequently we look at local variability within the composite in §3.5, and also look at how intraseasonal and interannual modes of variability affect depressions in §3.6, investigating the effects of ENSO (§3.6.1), the Indian Ocean Dipole (§3.6.2) and the active/break cycle of the monsoon itself (§3.6.3). We finally conclude in §3.7.

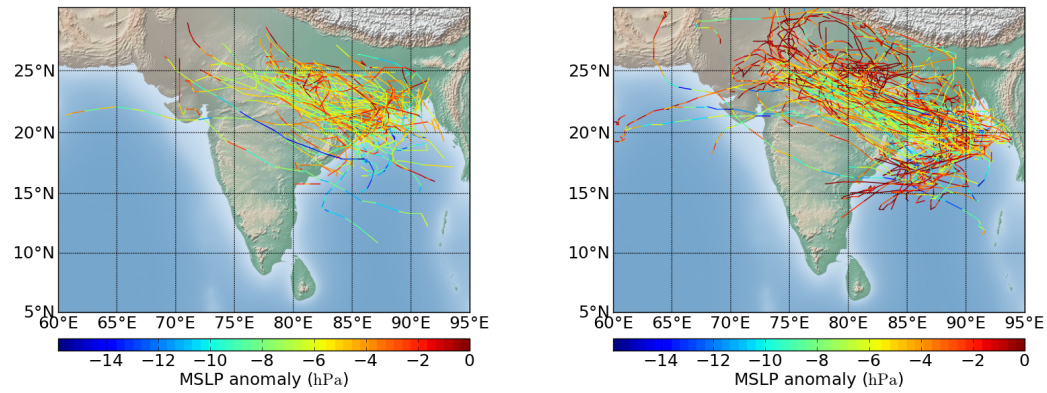

Figure 3.1: Depression tracks from (a) the 106 depressions used in this study, and (b) the 98 depressions from the dataset outlined by Hurley and Boos (2015) that fulfil our location criteria. Note that Hurley and Boos (2015) also defined their tracks under monsoon low conditions. Colour indicates depression intensity using SLP anomaly to a 21-day running mean.

3.2 Methodology

3.2.1 Data

Tropical Rainfall Measuring Mission

We outlined the TRMM dataset and our motivation for using it in §2.2.2. In this chapter, we will not make full use of the suite of products, concerning ourselves only with the 3B42 gridded product (version 7) which derives from the on-board precipitation radar, whose details we shall highlight again. The product consists of 3-hourly gridded $0.25° \times 0.25°$ surface precipitation over the latitude range 50°N - 50°S (Huffman et al., 2007, 2010; Liu et al., 2012b), with a nominal intensity resolution of 0.7 mm hour^{-1} (Kozu et al., 2001). The advantage of the 3B42 algorithm product is its calibration and merging with products from a number of other IR-based precipitation satellites: GMS, GOES-E, GOES-W, Meteosat-7, Meteosat-5, and NOAA-12. When compared to a climatology of surface observations over India, TRMM 3B42 performs well, although it tends to underestimate both low and high rainfall rates, generally slightly overestimating overall (Prakash and Gairola, 2014) and significantly underestimate rainfall over the Western Ghats (Nair et al., 2009).

ERA-Interim Reanalysis

A full description of ERA-I is given in §2.2.1. We will not add to it here, except to note the important caveat that the cloud cover field is purely model-derived – it is calculated by summing the contributions of stratiform and convective cloud covers respectively. Stratiform cover is predicted from local relative humidity (Sunqvist et al., 1989), whereas convective cover is predicted from parametrisation of convection (Slingo, 1987).

3.2.2 Tracking software

A full description of the tracking algorithm used is given in §2.1 and will not be repeated here. The algorithm was applied to 35 years of ERA-I reanalysis data (1979-2013), with the results shown in Fig. 3.1(a). For verification, monsoon depressions from the Hurley and Boos (2015) dataset with the same spatial criteria[1] are shown in Fig. 3.1(b), with whom, for the same period, we share some 90% of events. The tracks from their dataset appear longer because they also include the parts of depression tracks where they were only strong enough to be considered a monsoon low (as demonstrated by the colouring). Prajeesh et al. (2013) considered both the IMD depression archive and the dataset of Sikka (2006) and showed that in each, a statistically significant decline in frequency exists. This was debated, however, by Cohen and Boos (2014), who used several independent datasets (including that of Hurley and Boos, 2015) to show that this might not be case, consequently calling into question the validity of the downward trend in the IMD dataset.

The mean depression heading in the composite was 332°; although this relaxes to the more northwestward 295°when the small minority of eastward-propagating MDs are removed from the sample. The mean propagation speed was 2.75 m s^{-1}, and all depressions that fit our criteria initiated and terminated between 11°N and 27°N, and

[1]These criteria are simply that the genesis is not in the Arabian Sea, and that if it is in the Bay of Bengal it must subsequently transition to land at some point during its lifetime.

62°E and 94°E.

Next, each depression was centralised to 0°N, 0°W and reoriented using output heading data to create a forward (northward) propagating composite. Rotation during compositing allows us to determine system-relative features and mitigates orographic artifacts, e.g. forced ascent by the Eastern Ghats. We use the term *relative* with compass directions to describe sectors of the depression; relative north being the direction of propagation. The resulting array was then sliced horizontally (and later vertically) through different pressure levels to reveal internal structure of the composite depression. Apart from variables that are usually defined at the surface, the chosen pressure levels are usually 850 hPa and 200 hPa. A formal definition of the composite is given in Appendix A

3.2.3 Significance testing

We have sufficient data to perform significance testing on the total composite and an intercomparison within the composite, to ensure the robustness of our results.

1. A Student's t-test is performed to see whether the composite state significantly differs from the mean state (i.e. the summer climatology). Areas where a 95% confidence threshold is not satisfied are coloured grey in these figures.

2. Subsets are tested against their superset composite (e.g. if we propose that a variable, χ, can be meaningfully split into subset fields χ_i, we would test χ_i against χ, rather than the background climatology). This testing is performed by bootstrap resampling the superset (see, e.g., Efron, 1979) and producing 10000 random samples replicating the size of the subset. The subset and random samples are then individually composited and each gridpoint in the subset is placed in the respective gridpoint distribution from the random samples. For 95% confidence that the subset is significantly different from its superset, a percentile either below 2.5% or above 97.5% must be returned.

3. On pairs of subsets we perform an analogous method, except the bootstrapping produces 10000 *pairs* of random samples (again, each with the same sample size) and differences each pair to produce the distribution of differences for comparison with the observed inter-subset differences.

3.2.4 Choosing a suitable climatology

It is important to choose an appropriate climatology (e.g. a summer mean, a daily mean, or a fixed-length running mean) for our analysis on depressions as anomalies to the monsoon background state. When considering the full composite, as in Sections 3.3 and 3.4, we bear in mind that not having a significant trend in depression frequency across the summer entitles us to make an arbitrary choice of climatology. This was confirmed with several sensitivity experiments on the composite. When we discuss time-dependent large-scale forcings, this assertion is no longer valid; thus if we are to use a climatology in that analysis, it must be a running mean one so as to capture the background effect of the forcing.

3.3 Composite horizontal structure

In this section we describe the horizontal composite structure of the depressions, first looking at precipitation and then reanalysis fields.

3.3.1 Precipitation

TRMM precipitation data were composited for 1998–2013, the range of the dataset; Fig. 3.2 shows the average precipitation for all 34 depressions that initiated in the Bay of Bengal during this period. The most intense rainfall rate found during any 3-hourly TRMM timestep was 68.4 mm hr^{-1} (1.6 m day^{-1} equivalent). Comparing this to the highest mean intensity in the composite (38.6 mm day^{-1}) indicates that such intense events can be sparse and highly variable.

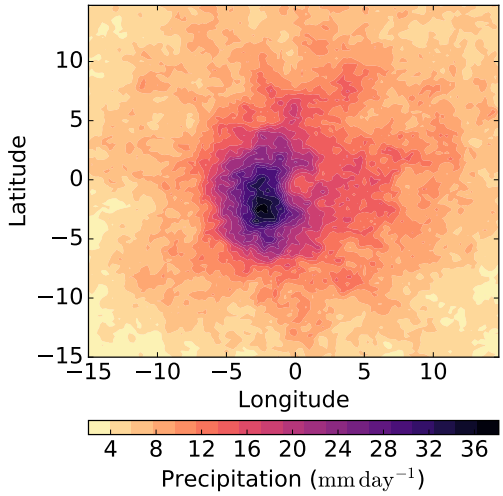

Figure 3.2: Rotated, composited, system-relative precipitation (mm day^{-1}) - the direction of propagation is upwards on the page. Data from TRMM 3B42 for the 34 depressions in the period 1998–2013

The location of the average rainfall maximum to the relative southwest agrees with many previous authors, including Godbole (1977) and Yoon and Chen (2005). That the rainfall is most intense to the left of the central track has been known for some time (Ramanathan and Ramakrishnan, 1933). Mooley (1973) provided a good summary of the literature on why this might be the case, including hypotheses from Roy and Roy (1930); Ramanathan and Ramakrishnan (1933); Mull and Rao (1949); Desai (1950); Petterssen (1956). He came to the conclusion that a combination of factors are responsible: (i) the southwest axial tilt of the depression core with height, (ii) a convergence maximum in the relative west/southwest sector, and (iii) cyclonic mixing of warm, southwesterly air from the Arabian Sea with the generally cooler, easterly monsoon flow; we will come to discuss this phenomenon in some detail in Chapter 4. Inspection of the distribution for "extreme" rainfall events (not shown) indicates that the probability for higher rainfall rates is increased near the composite maximum, although the highest intensities are seen sporadically outside this area, and are probably usually unrelated to the depression itself.

Fig. 3.3(a) shows the total rainfall across India for depression days, and Fig. 3.3(b) shows the anomaly of this relative to the summer mean for the TRMM period. The wettest anomalies are found around coastal areas (particularly the Bay of Bengal), and wet anomalies persist across much of the trough region, displaced from the track

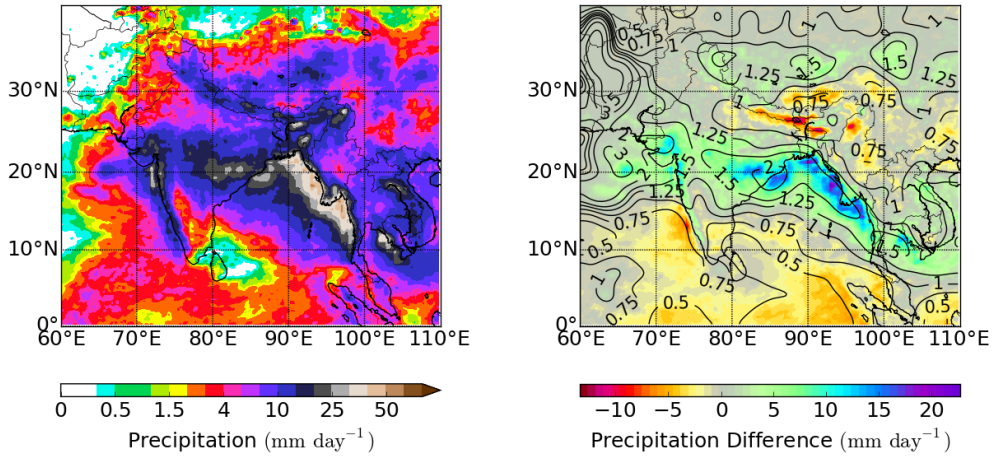

(a) (b)

Figure 3.3: Composite precipitation data from TRMM 3B42 for the 34 depressions in the period 1998–2013. (a) average precipitation (mm day^{-1}) for South Asia on depression days; and (b) the difference between depression days and the boreal summer mean (colours), and their ratio (lines).

density (see Fig. 3.1(a)) several degrees to the southwest, as the precipitation structure (see Fig. 3.2) predicts. There are also dry anomalies over the Himalayan foothills and northern Indian Ocean, creating something of a "wet" channel with dry edges, implying that a passing depression drags in surrounding moist air from a large surrounding area where precipitation is suppressed by atmospheric subsidence.

3.3.2 Reanalysis fields

We will next examine a selection of dynamic and thermodynamic fields from reanalysis to help elucidate the composite MD structure.

Firstly we will examine wind: Fig. 3.4 shows 850 hPa wind speed and direction for the composite depression (Fig. 3.4(a)). We see the maximum wind intensity is in the relative southeast, approximately 3° away from the centre, whereas a local minimum occurs at the centre (along with the streamfunction minimum, not shown), as in the eyes of more intense systems such as tropical cyclones. Removal of the background climatological winds (Fig. 3.4(b)) shows the perturbation the depression makes to the

monsoon: the structure is more circular since the asymmetrical presence of the climatological monsoon winds at 850 hPa is now absent – particularly in the relative south and west sectors, and we see an intensification of the winds in the relative east due to the presence of the Himalayas via the image vortex mechanism that will be described in Chapter 5. The overall wind speed pattern is very similar in shape, although with reduced intensity, to that described in Catto et al. (2010) for extratropical cyclones in that there is a clear central minimum, some asymmetry, and a well-defined radius of maximum wind speed; and is also similar to that of the smaller composites described in Godbole (1977) and Prasad et al. (1990).

Above 200 hPa (not shown), the depression contributes a weak (< 4 m s^{-1}) anticyclone to the much stronger (> 20 m s^{-1}) monsoonal jets at this height. There is an upper level wind speed minimum above the core, as there is above tropical cyclones (DeMaria, 1996). The background flow provides the vertical shear that restricts further development of the depressions into cyclones in mid-summer (e.g. Ramage, 1959; DeMaria, 1996) so that tropical cyclones in the Northern Indian Ocean have a bimodal distribution with maxima in May and November, and minima in February and August (Kikuchi and Wang, 2010).

We can now examine two more of the variables used in tracking/categorising MDs: relative vorticity and pressure (Fig. 3.5). At 850 hPa, (Fig. 3.5(a)) the negative relative vorticity imparted to the depressions by the presence of the Himalayas, through processes related to friction and vortex squashing, is notable in the relative vorticity field towards the left of the figure. Indeed, depressions at latitudes nearing the foothills are shorter lived (Fig. 3.1(a)), and north of a certain latitude, only depressions from the more favourable La Niña years (not shown) tend to persist, since the Bay of Bengal has greater relative vorticity and relative humidity (Felton et al., 2013). The relation between depression variability and ENSO will be discussed further in §3.6.1. At 200 hPa (Fig. 3.5(b)), the pattern is similar to lower levels, but with a weaker signal. Positive vorticity is confined to within 500 km of the centre, becoming negative over

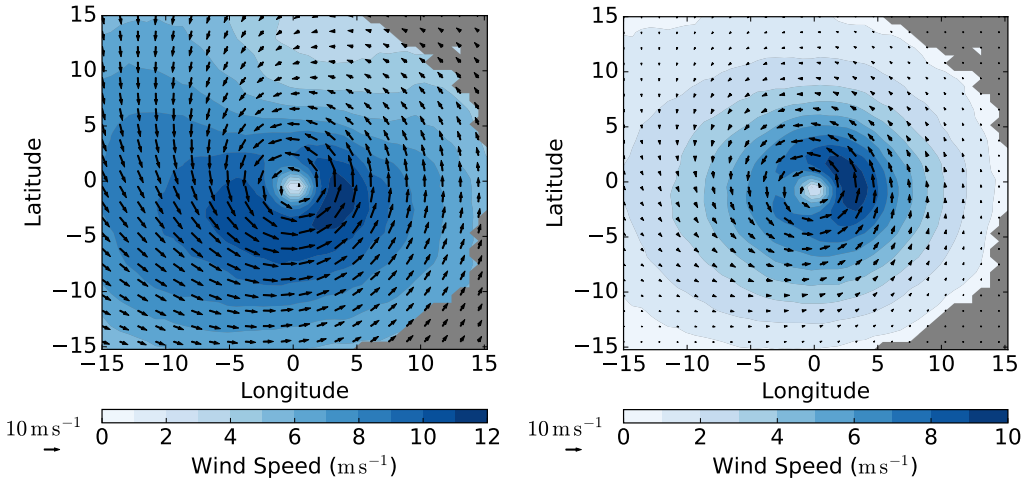

(a) Composite wind structure

(b) Composite wind structure with background flow removed

Figure 3.4: 850 hPa wind speed (m s^{-1}) in coloured contours, with wind vectors overlaid, for the 106-depression composite, using ERA-Interim reanalysis data over 1979–2014, for (a) the full composite, and (b) the composite as an anomaly to the summer mean circulation. Coloured contours are greyed out where the composite does not significantly differ from the climatology at the 95% level.

the relative east due to vortex squashing from the Himalayas and interaction with the Tibetan High, whose signal is also present in the geopotential anomaly.

Two horizontal temperature slices are given in Fig. 3.6. At the surface, the low-level cold core nature of the composite is clear, with a temperature minimum in the relative southwest sector. There is a consistently steep rise in temperature away from the centre until a radius of approximately 7°; eventually becoming a slightly anomalously warm environment. At 350 hPa, the anomaly has opposite sign, becoming warm compared to the climatology, indicating the thermal structure of a MD is warm-over-cold core, unlike tropical cyclones. This warm maximum is located slightly relative southward of the centre, and has similar magnitude and gradient to its surface companion. However, there is greater asymmetry: the anomaly is nearly half a degree colder in the lee of the depression than ahead of it.

We now turn to relative humidity and analysed cloud cover (Fig. 3.7). This *total* cloud cover bears some similarity with that of the extratropical cyclones in the atlas

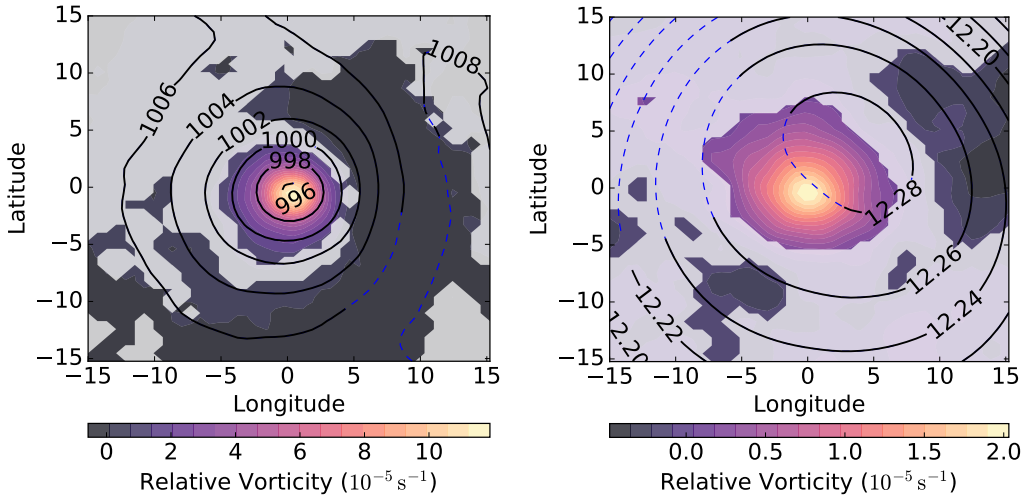

(a) Mean sea-level pressure with relative vorticity (ζ) at 850 hPa

(b) Geopotential height and ζ at 200 hPa

Figure 3.5: Composite relative vorticity (10^{-5} s^{-1}) shown as shading in the (a) lower and (b) upper troposphere along with line contours indicating (a) surface pressure and (b) 200 hPa geopotential height. Positive vorticity indicates cyclonic, counterclockwise rotation. Line contours become blue dashes where the composite does not differ significantly from the climatology at the 95% level; likewise, coloured contours are reduced to 20% intensity.

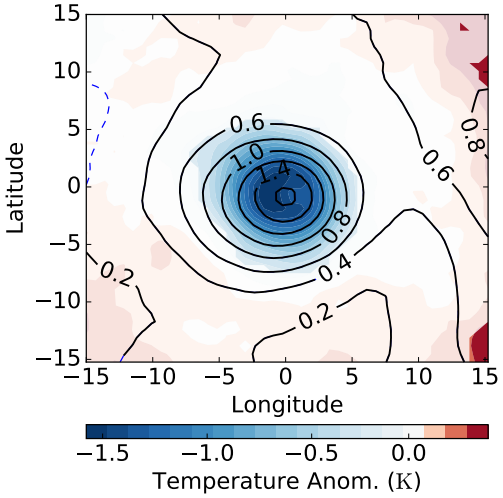

Figure 3.6: 2-m temperature anomalies (K) in coloured contours, 350 hPa temperature anomalies (K) in line contours. Both shown as anomalies to the boreal summer mean.

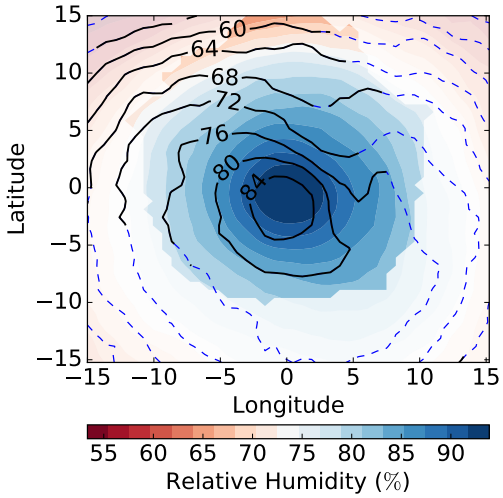

Figure 3.7: Composite relative humidity (%) at 850 hPa in coloured contours with total cloud cover (%) in line contours. Statistical significance is displayed as in Fig. 3.5.

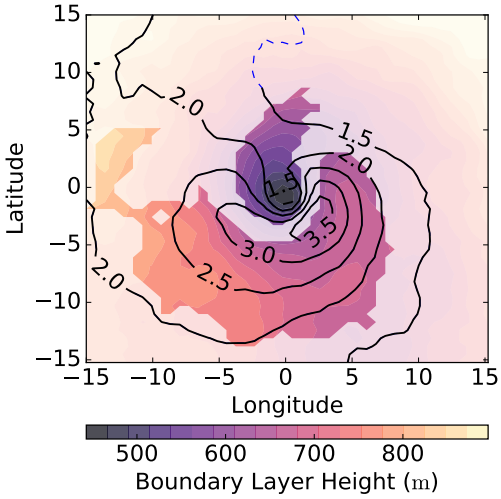

Figure 3.8: Composite boundary layer height (m, coloured contours) and boundary layer dissipation (W m^{-2}, line contours). Statistical significance is displayed as in Fig. 3.5.

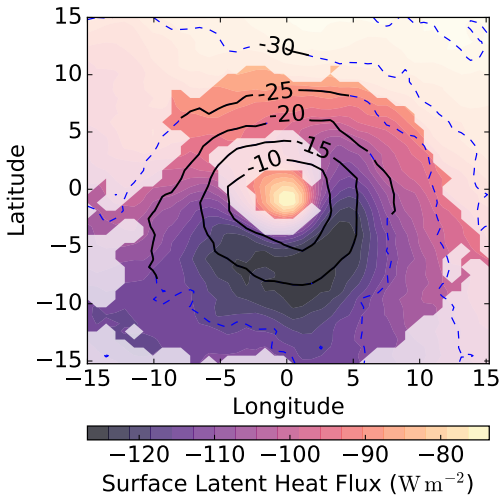

Figure 3.9: Composite surface latent heat flux (W m^{-2}, coloured contours) and surface sensible heat flux (W m^{-2}, line contours). Statistical significance is displayed as in Fig. 3.5.

defined by Dacre et al. (2012). There is a maximum composite cloud cover of 87% in the relative southwest sector, near the precipitation maximum. There is greater cover in the lee of the depression, likely owing to the larger quantity of moisture and stronger surface winds there than in the advance of the depression. The 850 hPa relative humidity field features a maximum in the relative southwest sector, as with rainfall and cloud cover. We see that the humidity falls away more rapidly ahead of the depression than behind it, since the depressions tend to have the Bay of Bengal environment behind them and the drier Indian subcontinent ahead.

We also analysed boundary layer processes (Fig. 3.8) and surface heat exchanges (Fig. 3.9); we caution that these are entirely modelled products within the reanalysis and thus have higher uncertainty than previous composite fields. However, our findings are in line with theoretical results (Potty et al., 2001): we find the boundary layer height drops sharply near the centre to around 500 m, from the climatological value of 800 m. This couples with a reduction in magnitude of both sensible and latent surface heat fluxes: values are reduced from the typical climatologies of ∼30 W m^{-2} and ∼100 W m^{-2} to ∼8 W m^{-2} and ∼75 W m^{-2} over the centre respectively.

3.4 Composite vertical structure

Stano et al. (2002) estimated the vertical extent of a monsoon depression to be in the region of 12-15 km (200-120 hPa) based on radar hydrometeor data from TRMM, so we shall look at vertical cross-sections over the 27 available ERA-Interim pressure levels from 1000 hPa to 100 hPa. We start by considering the overall 106-depression mean composite before looking at the effects of larger-scale monsoon variability. ERA-Interim repeats or extrapolates values for the lowest atmospheric level over orography at all sub-surface levels down to 1000 hPa; those unphysical data are not composited. The vertical composites are drawn above the zero-latitude line in a horizontal composite using the central gridpoint in the north/south direction, with relative west on the left and relative east on the right.

3.4.1 Moisture

Analysis of the vertical distribution and transport of moisture in the composite serves to verify the rainfall structure and provide further insight into the moist mechanisms of the depression.

Relative humidity (Fig. 3.10(a)) slightly resembles the structure of cloud cover; two strong maxima, one just above the surface at the centre, and one much nearer the tropopause. There is again (as with, e.g. divergence) a relative westward axial tilt persisting until the axial minimum at approximately 350 hPa. The 90% isohume near the surface is large, spanning a cross-sectional area of approximately 1500 km^2 (a volume of over 800,000 km^3 assuming azimuthal symmetry), indicating the composite depression has a vast, nearly saturated core within it. It is well known (e.g. LeMone et al., 1998; Cetrone and Houze, 2006) that the tropical atmosphere has a high relative humidity, so we should explore exactly how much moisture the depression adds to the environment. The composite structure of relative humidity as an anomaly to the climatology (Fig. 3.11) again shows westward tilt with height, corroborating the rainfall

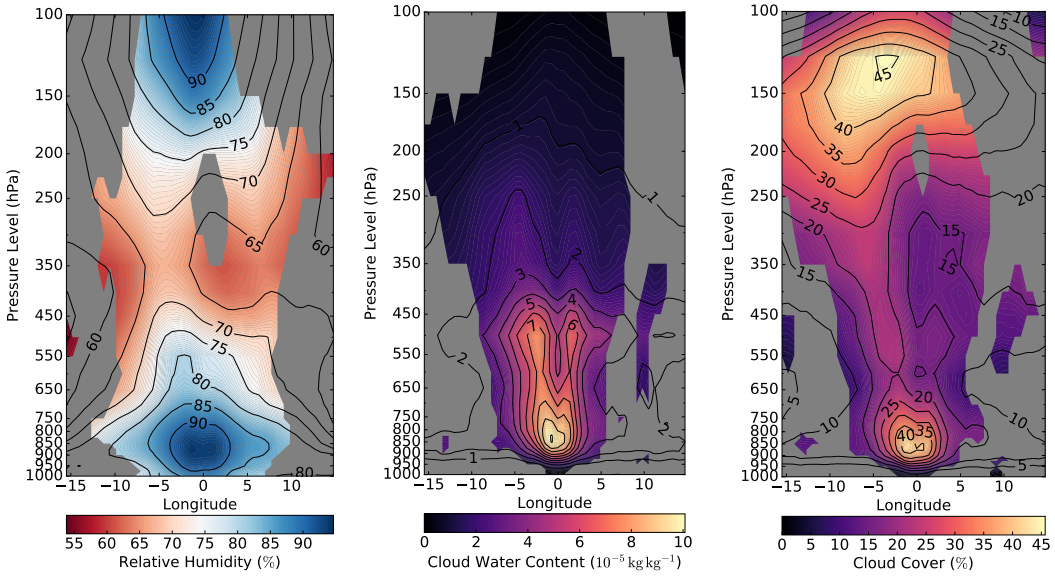

(a) Relative humidity (b) Cloud water content (c) Cloud cover

Figure 3.10: (a) relative humidity (%), (b) cloud water content (10^{-5} kg kg^{-1}; the summation of liquid and ice contributions), and (c) cloud cover (fraction of unity) as functions of pressure levels as viewed on a plane normal to the direction of depression propagation. Direction of propagation into the page. Coloured contours are greyed out where the composite does not significantly differ from the climatology at the 95% level.

asymmetry discussed in §3.3.1. In the middle and lower troposphere, the depression contributes around 10-15%, resulting in a nearly saturated environment.

3.4.2 Cloud features

Fig. 3.10(b) shows the vertical structure of *cloud water content* (CWC) across the depression. Cloud products from ERA-Interim are heavily reliant on the reanalysis model, but since they are constrained by other observations we may have some confidence in their patterns. CWC is a proxy for cloud type (Hess et al., 1998; Rosenfeld and Lensky, 1998), with the threshold for cumulonimbus at 7×10^{-5} kg kg^{-1} and stratocumulus at 3.5×10^{-5} kg kg^{-1}. We can identify a probable cumulonimbus base at about 900 hPa, and at around 550 hPa clouds are clearly more dense away from the depression centre, again lending evidence to axial tilt with height. Above approximately 450 hPa, most cloud mass comprises ice. The vertical structure of cloud cover (Fig. 3.10(c)) reveals

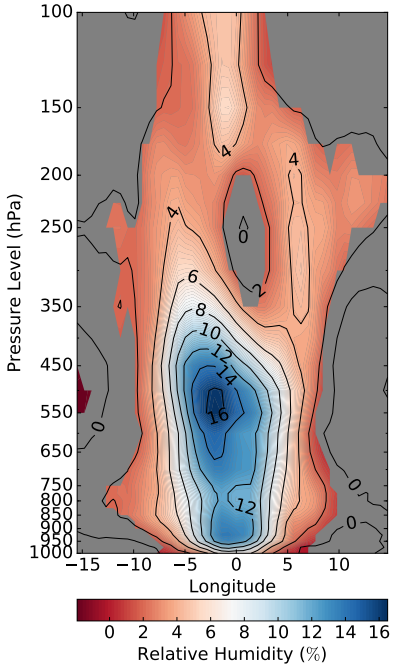

Figure 3.11: Following Fig. 3.10(a). Vertical structure of relative humidity (%) as an anomaly to the summer climatology.

two distinct regions of large cloud cover: a maximum near 850 hPa surrounding the centre, and an upper level maximum, to the relative west of the centre, near 150 hPa. These are the clouds that dominate the visible-light satellite pictures, anticyclonically rotating cirrus and cirrostratus clouds (Houze, 2010). The general shape resembles that of a classic cumulonimbus cross-section (with resolved low-level cloud and an anvil fed by deep convection/ascent), and there are potential rainbands visible in the relative east flank. We will be in a stronger position to make these claims after analysing satellite data in Chapter 4.

3.4.3 Potential vorticity and circulation

The vertical structure of potential vorticity (Fig. 3.12(a)) has a bimodal maximum core of a little over 10^{-6} K m^2 kg^{-1} s^{-1} extending from approximately 750-450 hPa. There is a minimum aloft, at approximately 250-200 hPa before the effect of the high-PV stratosphere becomes apparent.

Tangential wind speed anomaly (Fig. 3.12(b)) follows approximately what we might expect from a classical cyclonic structure, with two lobes of local maximum intensity

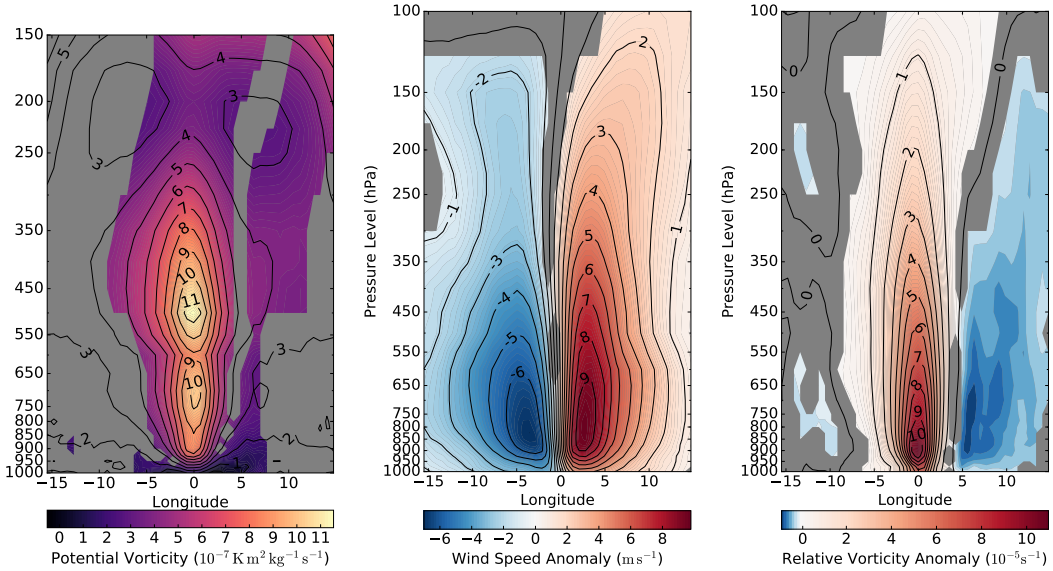

(a) Potential vorticity (b) Tangential wind speed (c) Relative vorticity

Figure 3.12: View and significance as defined in Fig 3.10, (a) potential vorticity (10^{-7} K m^2 kg^{-1} s^{-1}), (b) tangential wind speed (m s^{-1} - positive values going into the page, negative coming out), and (c) relative vorticity (10^{-5} s^{-1}), all viewed as anomalies to the summer climatology. Note the different y-axis for (a).

found slightly above the surface (∼850 hPa) and at a distance of several hundred kilometres from a relatively calm centre. The axial tilt to the relative west is mentioned both above and in Godbole (1977). Approaching the tropopause, the anticyclone is considerably affected by the strong zonal monsoon flow (∼20 m s^{-1}), and the axis starts to tilt instead to the relative northeast (corroborated by the horizontal slice at 200 hPa, see Fig. 3.5(b)). When the climatology is not removed, the tangential wind speed structure strongly resembles that shown in Sikka (1977) based on work by Sikka and Paul (1975) on a composite of July/August depressions in 1966-70, and the composite of Godbole (1977).

The vertical structure of relative vorticity anomaly is given in Fig. 3.12(c). It has a very symmetric form, with a maximum intensity found at approximately 900 hPa. Godbole (1977) reported a similar shape, but with a slightly more elevated maximum, at approximately 800 hPa. Also visible is the very slight relative westward axial tilt also observed by Godbole (1977). The anticyclonic behaviour expected near the tropopause

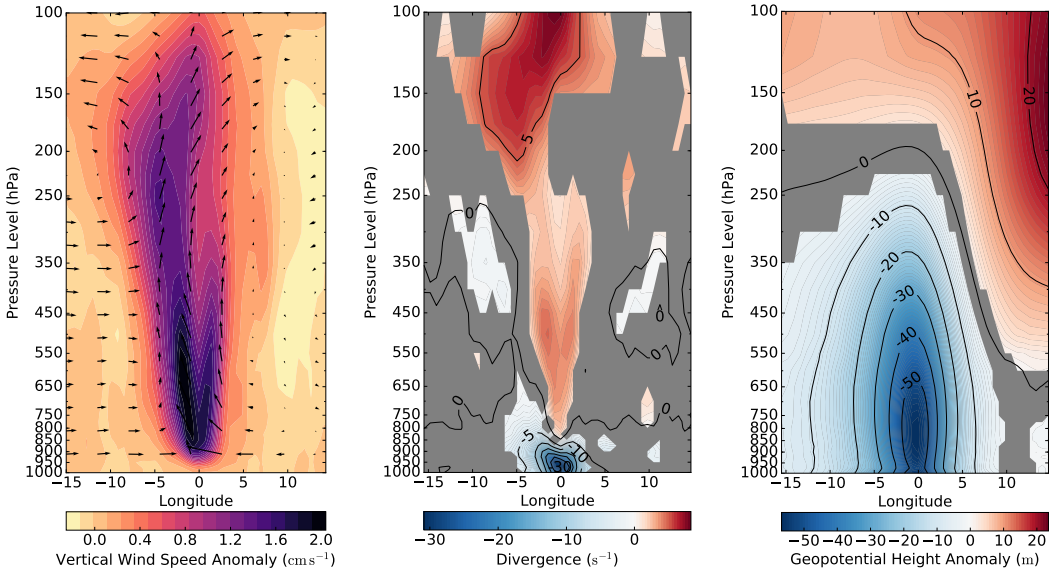

(a) Vertical wind speed (b) Divergence (c) Geopotential height anomaly

Figure 3.13: View and significance as defined in Fig 3.10. (a) vertical wind speed (cm s $^{-1}$) and quivers for vertical/zonal wind at the cross-section boundary, the vertical component is increased by a factor of 100 for the quivers; (b) divergence (10^{-6} s^{-1}); (c) geopotential height (m) as an anomaly to the summer climatology.

is apparent away from the centre (as seen in Fig. 3.5(b)). Again, the imposition of negative vorticity from the Himalayas in the relative east is visible.

Vertical velocity (Fig. 3.13(a)) has an axial tilt and slightly bilobal structure extending into the mid-troposphere. There is weak ascent at the surface, but parcels are rapidly accelerated near the core, reaching a peak of over 0.2 Pa s^{-1} (corresponding to 0.02 m s^{-1}) slightly to the relative west of the centre at approximately 800 hPa. The ascent slowly decelerates thereafter and the bilobal shape becomes asymmetric, favouring the relative west side, coming almost to a stop by the tropopause. Fig. 3.13(a) also shows the zonal circulation through the centre of the composite. Perhaps most apparent is the strong blocking signal at most heights from the Himalayas in the east - a considerable majority of the wind inflow at the centre comes from the west, although outflow aloft is roughly symmetric. These strong easterly inflow near the centre and the surface could be the result of cyclonic flow being suppressed near the Himalayas, and results in slightly easterly flow throughout the axis up to the 350 hPa level (potentially

supporting the westward axial tilt). Divergence (Fig. 3.13(b)) is rather noisy, although there is an area of concentrated, strong convergence at the centre near the surface; near the tropopause, where the outflow is situated, there is an area of weak divergence, approximately five times weaker than the convergence at the surface, slightly to the relative west of the centre. Geopotential height (Fig. 3.13(c)) is taken as an anomaly relative to the seasonal mean, as, like temperature, the vertical gradient is orders of magnitude than the horizontal perturbations created by a passing depression. A strong low pressure core exists, with the -50 m isohypse persisting from the surface to 650 hPa. The anticyclonic outflow aloft is also visible, shifted considerably towards the relative east by the Himalayas. The geopotential height anomaly associated with the low-level cyclone is considerably stronger than that of its upper-level anticyclone counterpart.

3.4.4 Moisture flux

For horizontal moisture transport in the composite, we must consider sources of both water and advection and do so by separating the specific humidity flux vector into contributions from both the mean state and the depression-induced perturbation, i.e.:

$$q\mathbf{v} = \bar{q}\bar{\mathbf{v}} + q'\bar{\mathbf{v}} + \bar{q}\mathbf{v}' + q'\mathbf{v}' \,, \tag{3.1}$$

where q is specific humidity, $\mathbf{v}$ is the wind vector, $\bar{\square}$ represents the mean state of the variable (i.e. the climatology), and $\square'$ represents the depression anomaly to the mean state (i.e. the perturbation). The presence of a depression contributes only a fraction of the total moisture present in the composite (Fig. 3.13(c)), and the base monsoon state contributes little to the depression winds near the centre (Fig. 3.4); therefore, we might expect the most significant contribution on the right hand side of eq. 3.1 to come from the anomalous (i.e. depression induced) advection of climatological moisture ($\bar{q}\mathbf{v}'$). To confirm this, we examine the structure of each perturbation term (shown in Fig. 3.14). We see that the greatest contribution indeed comes from $\bar{q}\mathbf{v}'$, and that although the

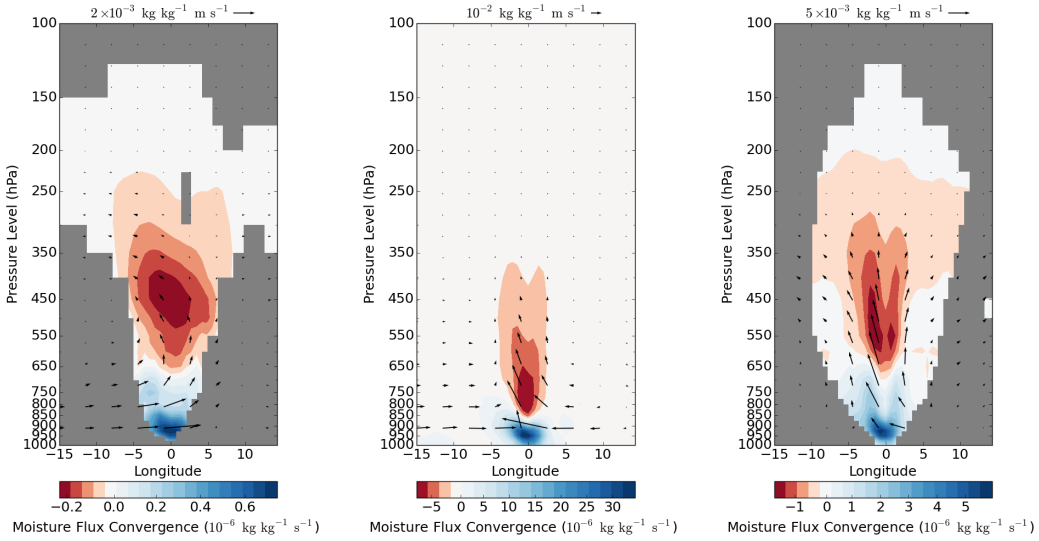

(a) $q'\bar{\mathrm{v}}$ (b) $\bar{q}\mathrm{v}'$ (c) $q'\mathrm{v}'$

Figure 3.14: Vertical structure of the three specific humidity flux perturbation terms from eq. 3.1 (kg kg^{-1} m s^{-1}) and associated convergence (kg kg^{-1} s^{-1}) in coloured contours: (a) the anomalous moisture advected by the climatological wind, (b) the climatological moisture advected by the anomalous wind, and (c) the anomalous moisture advected by the anomalous wind. Colours are greyed where the moisture flux is not significantly different at the 95% confidence level from a bootstrapped zero-centred distribution derived from differencing random pairs of samples from the composite of $q\mathbf{v}$. Note the differing colour scales and unit vectors. Quivers are vertically exaggerated by a factor of 100.

contribution from $q'\mathbf{v}'$ is roughly a fifth as large, it has greater relative vertical and horizontal extent and a more strongly bifurcated structure.

3.4.5 Temperature profile

The vertical structure of temperature is given in Fig. 3.15(a) and is shown (due to the strong temperature gradient with height) as an anomaly relative to the structure of the boreal summer mean temperature profile. The resulting composite is a cold-core event in the lower troposphere, agreeing with Sarker and Choudhary (1988), Douglas (1992a) and Hurley and Boos (2015), amongst others. Sarker and Choudhary (1988) suggest the reasons for the cold anomaly include dynamical uplift, evaporating precipitation, and radiative cooling. We speculate that Fig. 3.10(c) corroborates the last point, indicating that cloud cover reduces insolation (cooling the lower levels) and blocks

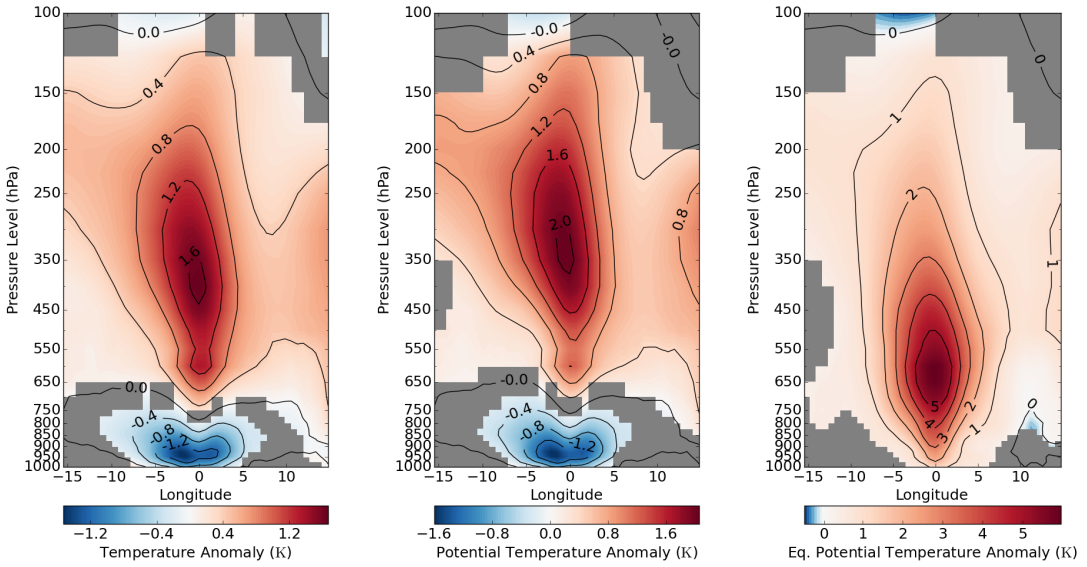

(a) Temperature (b) Potential temperature (c) Equivalent potential temperature

Figure 3.15: Vertical structure of (a) temperature (K), (b) potential temperature anomaly (K), and (c) equivalent potential temperature anomaly (K). Colours are greyed out where the profiles are not significantly different from the climatology at the 95% significance level.

outgoing longwave radiation (heating the upper levels) - a mechanism that would be absent if there were the fully developed eye of a tropical cyclone. The warm core aloft is a result of the high instability at lower levels and resulting rapid ascent, coupled with strong latent heating from the high rates of convective precipitation associated with depressions, although its magnitude ($\sim$ 2 K) is considerably less than that of a tropical cyclone (La Seur and Hawkins, 1963; Hawkins and Rubsam, 1968; Hawkins and Imbembo, 1976; Stern and Nolan, 2012).

For comparison, the potential temperature anomaly is shown in Fig. 3.15(b). Whilst this is directly related to the temperature structure given in (a) via the Exner function, it is presented here for completeness and to allow direct comparison with the composite given in Hurley and Boos (2015) with which it indeed bears a striking resemblance. The equivalent potential temperature (Fig. 3.15(c)) shows the importance of moisture in the depression structure – the maximum has lower altitude (around 650 hPa) and larger positive anomaly ($\sim$ 5.8 K).

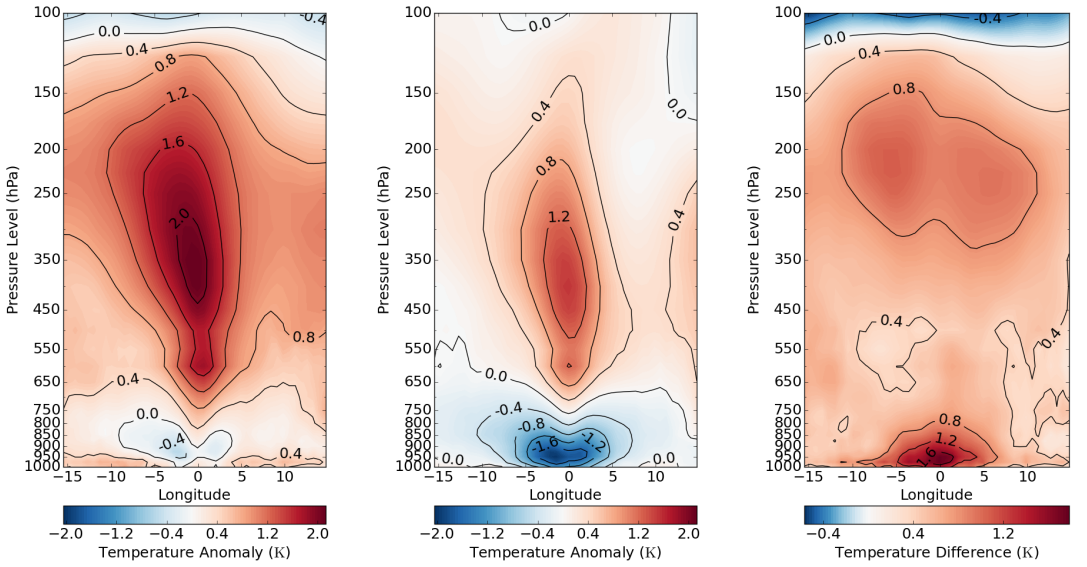

(a) Neutral-core (28 events) (b) Cold-core (76 events) (c) Neutral- minus cold-core

Figure 3.16: Vertical structure of the temperature (K) as an anomaly to the boreal summer mean for a composite depression with both main core categories, and their difference: (a) neutral-core, (b) cold-core, (c) their difference. In (a) and (b), colours are greyed out where the subsets do not significantly differ from the full composite temperature profile at the 95% confidence level, ascertained by the bootstrapping method; in (c), colours are greyed out where the difference does not significantly differ from zero at the 95% confidence level using the bootstrapping difference method on the full composite temperature profile.

We categorise the 106 depressions into warm-core, neural-core, or cold-core by calculating the average 1000 hPa temperature anomaly in a 1.5° box surrounding the centre. Using $T_{\text{warm}} \geq 0.75\,\text{K} > T_{\text{neutral}} \geq -0.75\,\text{K} > T_{\text{cold}}$, we count 2, 28, and 76 events respectively. Whilst SSTs are usually used in the description of tropical cyclones, the significant duration spent by monsoon depressions over land meant that surface air (1000 hPa) temperature provided a more useful measure. The criteria were established by identifying and removing the two warm-core outliers, then fitting a two-Gaussian-sum (giving a better mean square error than one) to the distribution of central temperatures, constraining one to be centered on the origin. The strongest cold-core event registered at -3.6K (with a mean of -1.9K). Neutral-core events exhibit a much steeper temperature anomaly gradient approaching the tropopause and larger anomalous heating aloft (Fig. 3.16). The sample of warm-core depressions is too small

Percentile	Cold core (mm day^{-1})	Neutral core (mm day^{-1})
50	~ 0	~ 0
75	1.75	3.47
90	22.9	29.0
95	50.4	60.2
99	141	165
99.9	305	339

Table 3.1: Some data showing rainfall rates (mm day^{-1}) of selected percentiles for cold- and neutral-core depressions over the domain used in, e.g. Fig. 3.17.

to draw any significant conclusions. The neutral-core-minus-cold-core PV composite (not shown) has lower tropopause height above cold-core depressions, and higher PV in the flanks near the surface; the centres of each type appear very similar. Also not shown graphically is the comparison of surface rainfall rates between cold- and neutral-core events; these are given in Tab. 3.1. The greater rainfall rates, and the slightly larger area of influence of neutral-core events, should be expected upon inspection of the temperature profiles which show that neutral-core events exhibit a warmer core aloft, indicating stronger latent heating.

3.4.6 CAPE and tephigram analysis

Variables relating to convection are important because they provide an insight into how thermal energy is distributed and used within a system.

Fig. 3.17 shows that the maximum CAPE is found approximately 5° ahead of the centre, reaching a peak value of 2050 J kg^{-1}. The minimum CIN is found near the centre, with a value of -1.2 J kg^{-1} but increasing exponentially ahead of the depression. There are two competing effects at the centre: a strong positive moisture anomaly (reducing the CIN, i.e. less negative) and a steeper temperature anomaly gradient (increasing the CIN); however, the moisture anomaly has a much stronger effect and dominates the CIN.

Fig. 3.18 shows soundings through the centre (single gridpoint) in the compos-

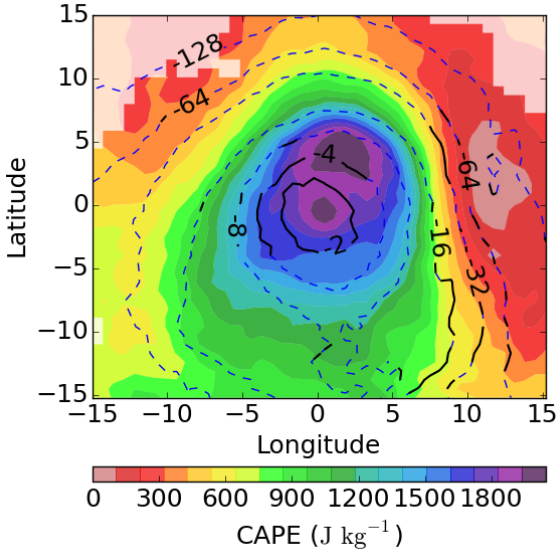

Figure 3.17: Horizontal composite of CAPE (J kg^{-1}) in coloured contours and CIN (J kg^{-1}) in line contours. Significance as in Fig. 3.5

ite depression and two subsets, for whom some thermodynamic variables are given in Tab. 3.2. The full composite (Fig. 3.18(a)) has evidence of strong ascent through the lower and middle troposphere, and we can deduce large CAPE by finding the saturated pseudoadiabat coinciding with Normand's point (approximately 950 hPa). Extrapolation of this adiabat to the upper troposphere suggests a level of neutral buoyancy at approximately 120 hPa. We also split the composite into two pairs of subsets: day/night (Fig. 3.18(b)) and land/ocean (Fig. 3.18(c)). The day/night tephigram indicates that the daytime sounding is slightly warmer and drier throughout its height, though the more substantial temperature and moisture differences in the boundary layer engender high CAPE and very small CIN during nighttime (lower temperature but same dew point raises the relative humidity). The land/ocean contrast shows that, particularly in the mid-troposphere, there is generally a cooler, moister environment over the ocean with lower CAPE and greater CIN.

Calculable products from these tephigrams and several others are given in Tab. 3.2. Important results are larger CAPE and reduced (less negative) CIN in the final day (almost always over land) when compared to the first day (almost always over ocean), and larger CAPE in neutral-core events than cold-core events (because, despite the

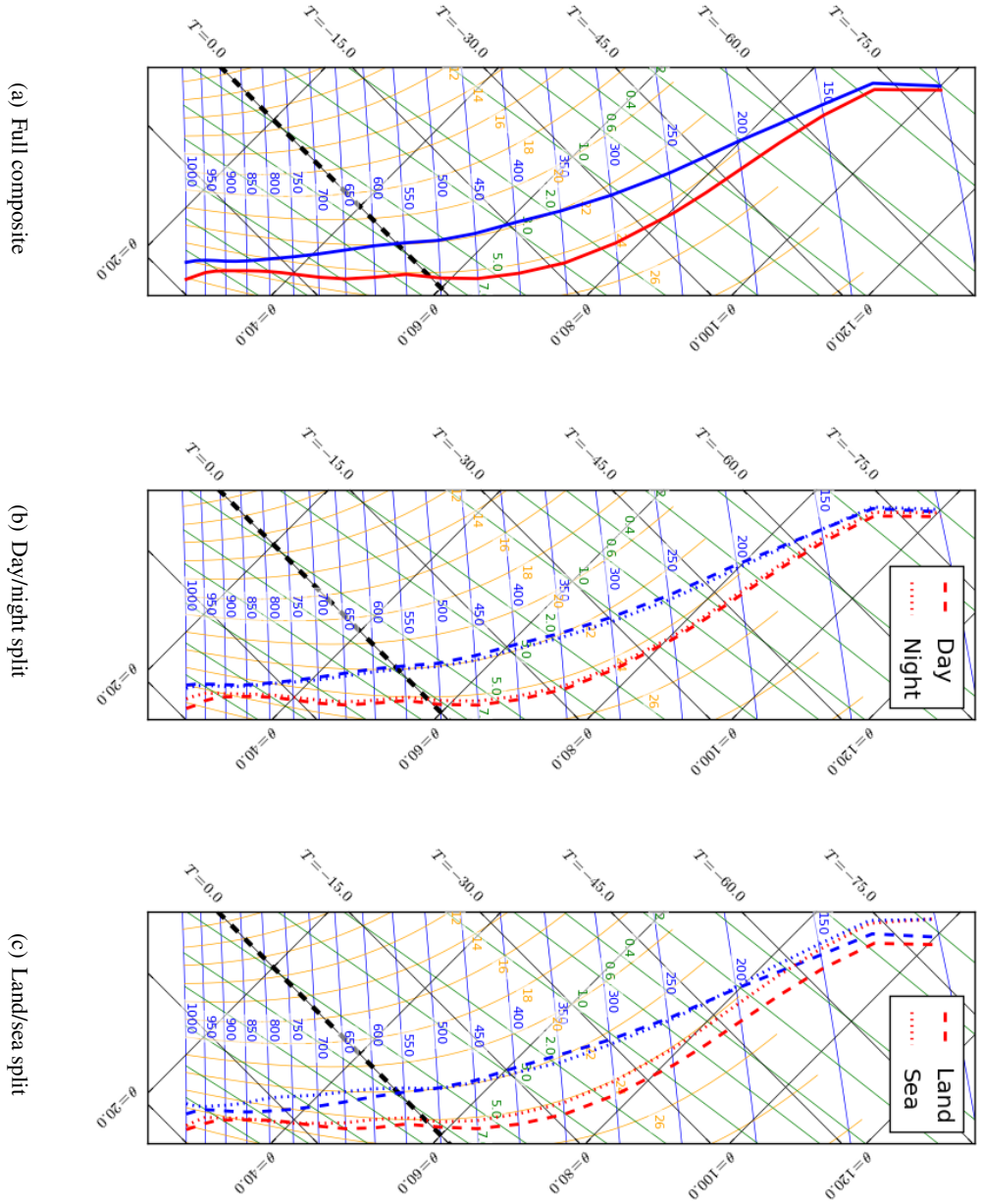

Figure 3.18: Tephigrams of simulated soundings going through the centre of the composite depression and selected subsets. Temperature in red, dew point temperature in blue.

	LCL (hPa)	LFC (hPa)	LNB (hPa)	CAPE (J kg^{-1})	CIN (J kg^{-1})
Full	972.9	938.0	117.8	2007	-1.29
Neutral-core	963.7	913.1	112.8	2174	-3.03
Cold-core	976.9	948.5	119.9	1940	-1.20
First 24 hours	967.8	915.7	123.1	1693	-2.24
Final 24 hours	970.0	931.3	117.4	2139	-1.81
Land	975.0	944.0	113.8	2373	-1.26
Coast	972.2	933.6	121.2	1788	-1.70
Ocean	964.8	892.6	118.6	1798	-2.80
Upper quartile intensity	974.8	943.8	111.9	2161	-1.51
Lower quartile intensity	971.8	929.3	125.2	1792	-1.85
Day	962.7	920.3	119.2	1900	-3.30
Night	983.1	961.3	117.0	2109	-0.43

Table 3.2: Some tephigram data for different composites. Abbreviations: LCL - lifted condensation level, LFC - level of free convection, LNB - level of neutral buoyancy, CAPE - convectively available potential energy, CIN - convective inhibition. These values were calculated directly from the relevant composite.

shorter distance (in pressure units) between the level of free convection and the level of neutral buoyancy, the parcel temperature is comparatively much higher - compare Fig. 3.16(a) and Fig. 3.16(b)). In neutral-core depressions CIN is nearly three times greater than in cold-core depressions due to higher surface temperature and resultant lower relative humidity. This is a significant difference because there is very low variance in CIN at the centre of the composite (not shown).

In general, the level of neutral buoyancy is near the top of the cloud deck (cf. Fig. 3.10(c)), and any difference is likely accountable to entrainment of surrounding cool, dry air. The lifted condensation level is comparable to the bottom of the cloud deck. We examine variations in profiles according to the diurnal cycle or surface type in the next section.

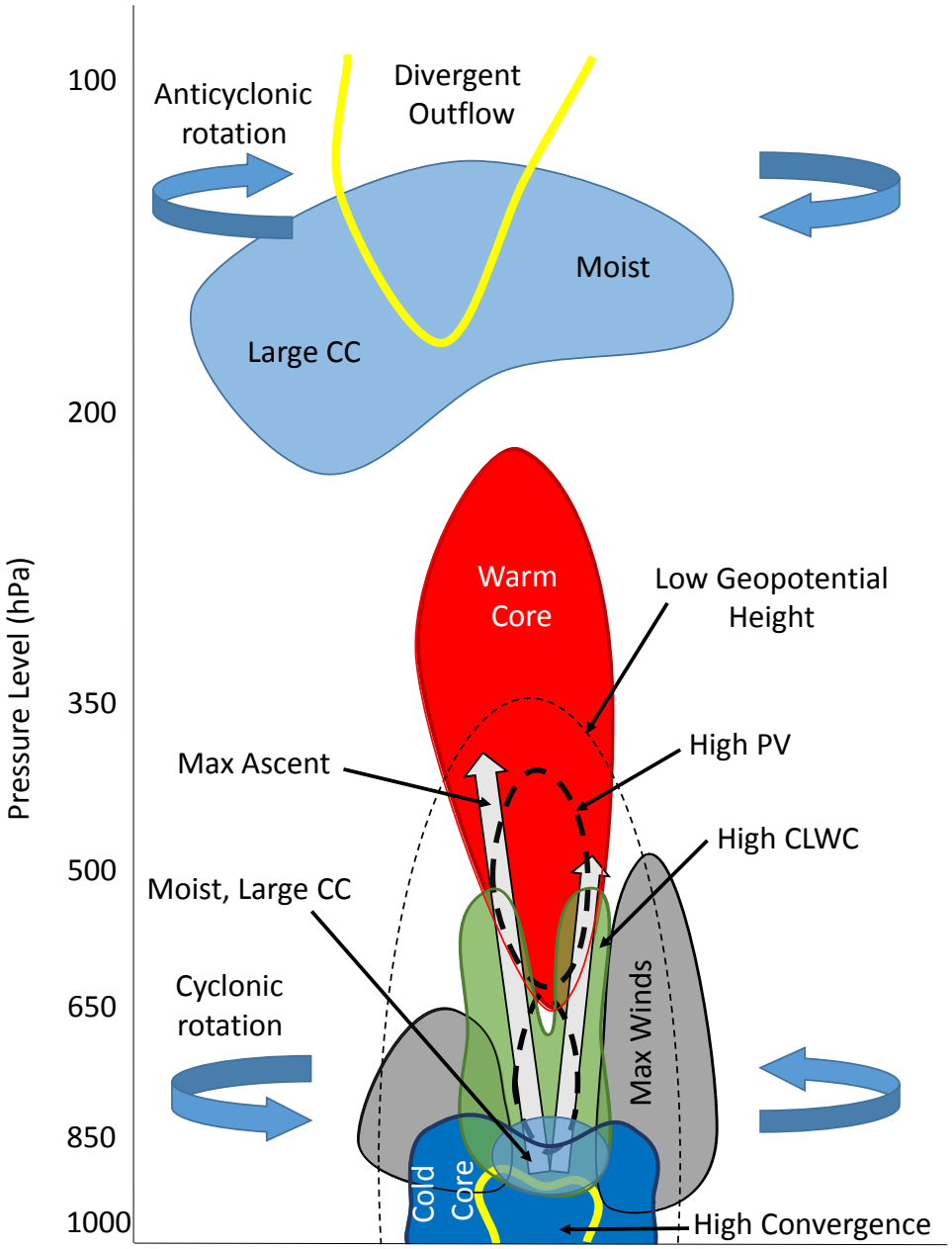

Figure 3.19: Schematic of the composite monsoon depression. CC = cloud cover; CLWC = cloud liquid water content; PV = potential vorticity.

3.4.7 Summary of composite vertical structure

Fig. 3.19 shows some key features of the vertical structure presented throughout this section. In particular, we note the generally asymmetric structure: a westward axial tilt in many fields, and an intensification of the lower-tropospheric winds on the Himalayan side of the vortex.

3.5 Variability within the composite

Although most of our composite diagnostics have been presented with a test of statistical significance, we also discuss the stability of the composite, firstly using standard deviation of the entire composite; and secondly by breaking the composite down and contrasting land, sea, and transitional (coastal) phases. The latter is particularly important as the conditions surrounding a depression spinning up in the Bay of Bengal are very different to those as it decays over north India. We also consider the diurnal contrast within depressions. We note that generally, most fields are highly homoscedastic, with a standard deviation far smaller than the anomaly to the climatology; hence the large areas of significance in the horizontal and vertical cross-sections presented above. Variance invariably reaches a maximum in the deep flanks of the composite, where influence from the major processes within the depression is very low; and the effects of varying environment, composite rotation, and different depression sizes start to become significant.

3.5.1 Variability over the lifetime

If we can understand how the structure of depressions transforms over time, it follows that we would be better able to represent their processes in models and better predict their durations and trajectories. Almost all depressions form over the ocean and eventually die over land, so there is likely to be some correlation between young/old depressions and the land/sea contrast: the latter is discussed in detail in the next

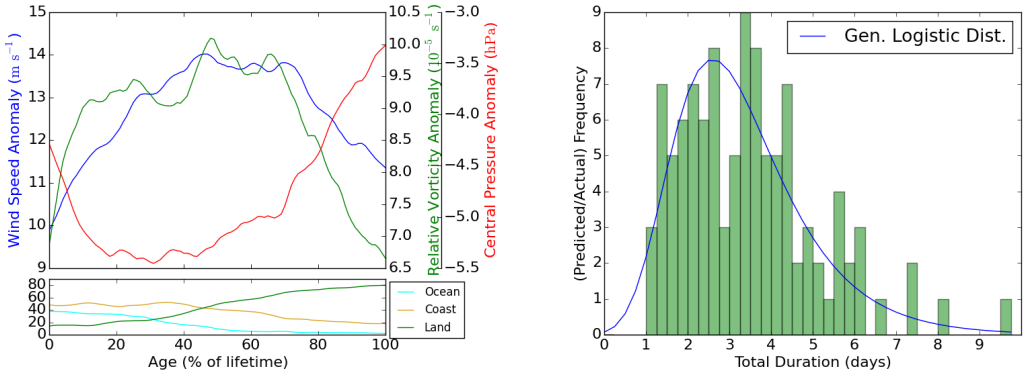

(a) Evolution of some selected variables

(b) Histogram of durations

Figure 3.20: (a) Surface pressure anomaly at centre (hPa), maximum 850 hPa wind speed anomaly (m s^{-1}), and 850 hPa central relative vorticity anomaly (10^{-5} s^{-1}) of the composite depression as a function of percentage of lifetime duration, with respective percentage of systems over land, coast (defined as within 150 km of coastline) and sea shown underneath, anomalies are relative to a 21-day running mean; and (b) histogram of depression durations, with the generalised logistic function fitted. The mean depression duration is 3.3 days, with a standard deviation of 1.6 days.

section.

Fig. 3.20(a) shows how the central pressure, wind, and vorticity extrema vary as a function of depression age. The variables for each depression were interpolated onto a lifetime-percentage array (i.e. normalised by duration), rather than using an absolute timescale because depressions have considerably variable durations (see Fig. 3.20(b)). All variables demonstrate a mid-life extremum: central pressure reaches a minimum before wind speed and relative vorticity, both of which have maxima around 60% before decaying significantly and rapidly during the dissipation phase of the depression. If we compare first-day and final-day PV composites (not shown, but see Fig. 3.12(a)), the most immediate difference is the extent of the upper anticyclone which has larger (more positive) PV in the flanks in the final day when compared to the first one. Differences near the surface extend to approximately 550 hPa and feature generally lower (less positive) PV in the centre and higher PV in the flanks on the final day.

A histogram giving the lifetimes of each individual depression tracked is shown in Fig. 3.20(b). It shows the shortest lived depressions last approximately a day: this is the

threshold for the IMD and our tracking software, but depressions can have lifetimes as long as nearly ten days, with a mode of just over three days. This distribution is the reason information in Fig. 3.20(a) is presented as it is. Several well known probability distributions were fitted to the data in Fig. 3.20(b), with the generalised logistic distribution (shown) having the smallest mean squared error.

We also find that there is no significant relationship between depression frequency and time of year, and that the frequency has little effect on all-India rainfall; Raghavan (1967), Dhar and Rakhecha (1976), and Krishnamurthy and Ajayamohan (2010) showed that this is because low pressure systems result in excess rainfall in some areas but deficient rainfall in others. The correlation coefficient between trough rainfall and the depression frequency for the relevant period (1998–2013) is 0.77.

3.5.2 Coastal transitions and the land-sea contrast

Land-atmosphere and ocean-atmosphere interactions can differ from each other considerably, so we expect monsoon depressions (which as we have seen, are fairly dependent on surface interactions) to differ considerably also. For example, Annamalai et al. (1999) showed that almost exclusively MDs strengthen over the ocean and weaken over land. To explore the effect of surface type (land, coast, ocean) of monsoon depressions, we first define a *coastal transition region*, sufficiently wide to span the typical horizontal scale of the core of a passing depression, but not so large as to prejudice the sample sizes of land or ocean composites. A threshold of $\pm 3^\circ$ either side of the coast was chosen, providing a sample of 680, 687, and 159 six-hourly depression timesteps for land, coastal, and ocean areas respectively, with the advantage that many fields (e.g. potential vorticity, geopotential height anomaly, vertical wind speed) have values of less than half their central extrema at this radius. The location of the *centre* is used to define the entire depression.

For specific humidity (not shown), the difference between the three partial composites is again significantly less than the standard deviation (by at factor of four) across

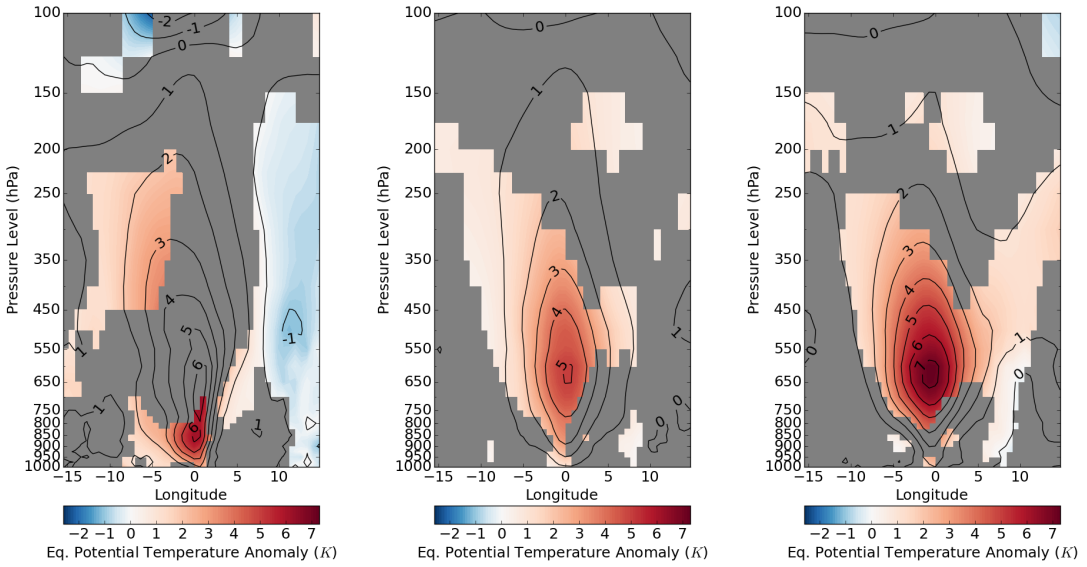

(a) Ocean (b) Coast (c) Land

Figure 3.21: Vertical structure of equivalent potential temperature (K) ocean, coastal, and land composites. Colours are greyed out where the subset is not significantly different from the full composite at the 95% confidence level.

the full composite, even though this variable is so dependent on surface composition. There is, however, a "tightening up" in the lower levels, where the horizontal extent of the central maximum at each height is reduced at each progressive stage. This is a common theme throughout the comparison of ocean/land composites - the magnitude of any central extremum differs insignificantly if at all, but in many fields we observe an increasing confinement to the central axis, resulting in a steeper horizontal gradient. The same analysis with potential vorticity (not shown) reveals little significant variation across the surface types.

There is little difference between the three partial composites for equivalent potential temperature anomaly (Fig. 3.21): the maximum is highest in the land-based composite, but does not differ much from either the ocean- or coast- based composites. All three demonstrate a warm core at approximately 650 hPa.

CAPE around the centre of the land-based composite is much higher than its ocean-based counterpart (Tab. 3.2), but this maximum has a much smaller extent ($\sim 6^\circ$ wide

as opposed to $\sim 20^\circ$ wide, not shown).

We also separately composited points according to their instantaneous location, resulting in "purely oceanic" and "purely land-based" composites. Fig. 3.22 shows the wind structure of such a composite: average sample sizes are 465 timesteps for ocean and 1060 for land in this and subsequent composites. The near-surface winds around the core are weaker over land, partly due to friction, and partly due to the loss of warm water vapour as an energy source. The strong winds also become a lot more constrained to the centre as the depression passes over land and weakens. The difference between the two in Fig. 3.22(c) reflects the weakening and constriction of the winds near the surface. The tropospheric winds round the core strengthen more over land to the relative east than to the relative west, likely owing to orographic channeling by the Himalayas.

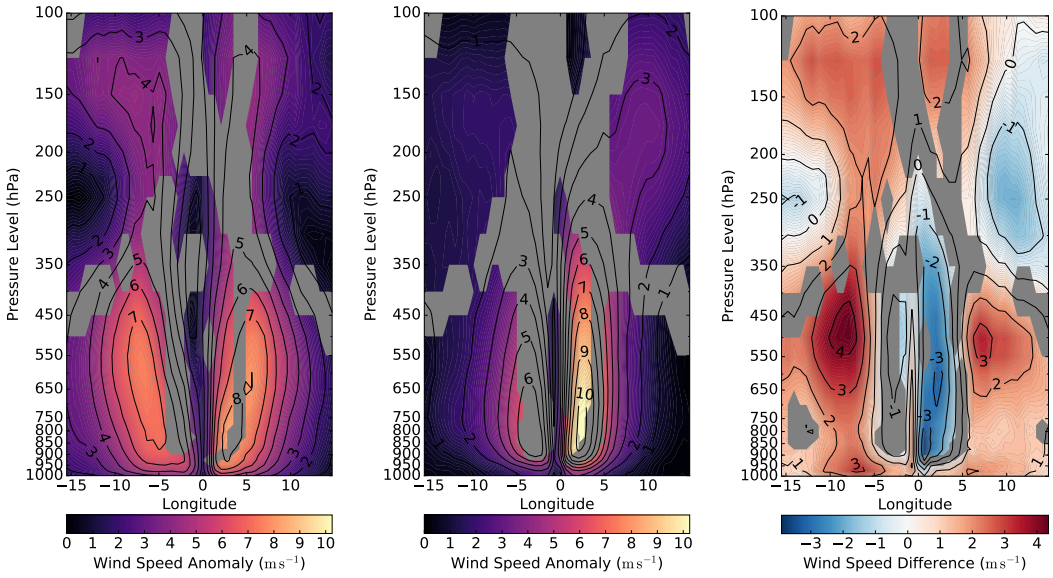

(a) Ocean (b) Land (c) Ocean-minus-land

Figure 3.22: Vertical structure of wind speed anomaly (m s^{-1}) for purely oceanic and land-based composite depressions; (c) shows their difference. Significance as in Fig. 3.16

Further ocean-minus-land vertical composites (as Fig. 3.22(c)) are shown in Fig. 3.23. Specific humidity shows little contrast between the two in the lower levels, with the only significant difference being the drier flanks above the ocean at a radius of $\sim 10^\circ$.

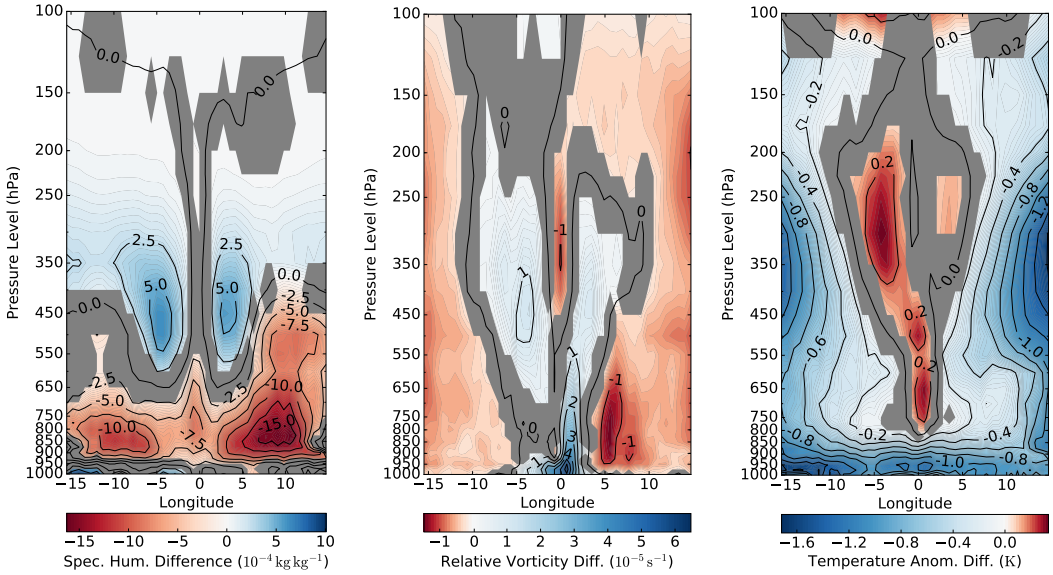

(a) Specific humidity (b) Relative vorticity (c) Temperature anomaly

Figure 3.23: Vertical structure of the ocean-minus-land composite (as in Fig. 3.22(c)) for specific humidity (10^{-4} kg kg^{-1}), relative vorticity (10^{-5} s^{-1}), and temperature anomaly (K). Significance as in Fig. 3.16(c).

In the middle and upper troposphere, however, the ocean composite has considerably more moisture, particularly outside the centre. The difference in relative vorticity (Fig. 3.23(b)) shows that the composite is less constrained to the centre over the ocean, and that the vortical core penetrates nearer to the ocean surface than to the land, a plausible result of orographic friction. So the depression is larger and more intense over water than land, although these differences are fairly small when compared to the mean structure. The tropical summer atmosphere is generally cooler over the ocean than land, so it is important to see how the depression organises this difference, shown in Fig. 3.23(c). As expected, it is cooler throughout, although the deep latent heating from increased precipitation removes and reverses much of the difference at and near the centre; in the flanks, the difference is of order 1-2 K, and explains much of the counter-intuitive structure of the difference in specific humidity.

Surface latent heat flux (not shown) is substantially larger over the ocean (maximum 185 W m^{-2}, average 150 W m^{-2}) than over land (maximum 95 W m^{-2}, average

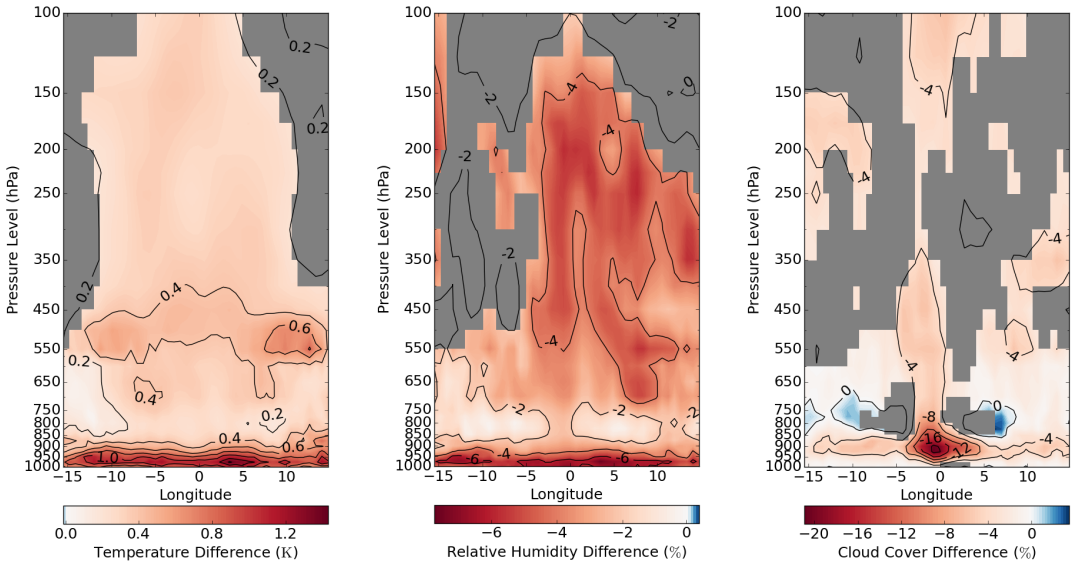

(a) Temperature (b) Relative humidity (c) Cloud cover

Figure 3.24: Diurnal variation as represented by a day-minus-night composite for (a) temperature (K), (b) relative humidity (%), and (c) cloud cover (%). Significance as in Fig. 3.16(c)

65 W m^{-2}): as expected, the maxima are colocated with lower-tropospheric wind speed and they have local minima at the centre. Surface sensible heat flux (not shown) also has central minima over both land and ocean, following the surface temperature structure. As in the full composite, there exists a boundary layer height minimum of equal magnitude ($\sim$ 500 m) over both the land and ocean composite centres, rising to the respective climatological values within several hundred kilometres, agreeing with the case study of Seetaramayya et al. (1993).

3.5.3 Diurnal cycle

We have already noted contrasts between composite depression structure in day/night conditions. As ERA-Interim data are released in six-hourly timesteps starting with 0000UTC, the night composite was constructed from 1800UTC and 0000UTC (2330 and 0530 Indian Standard Time), and the day composite from 0600UTC and 1200UTC. We examined the day-night difference in selected composite variables (Fig. 3.24); only a few of many fields examined showed significant differences away from the centre.

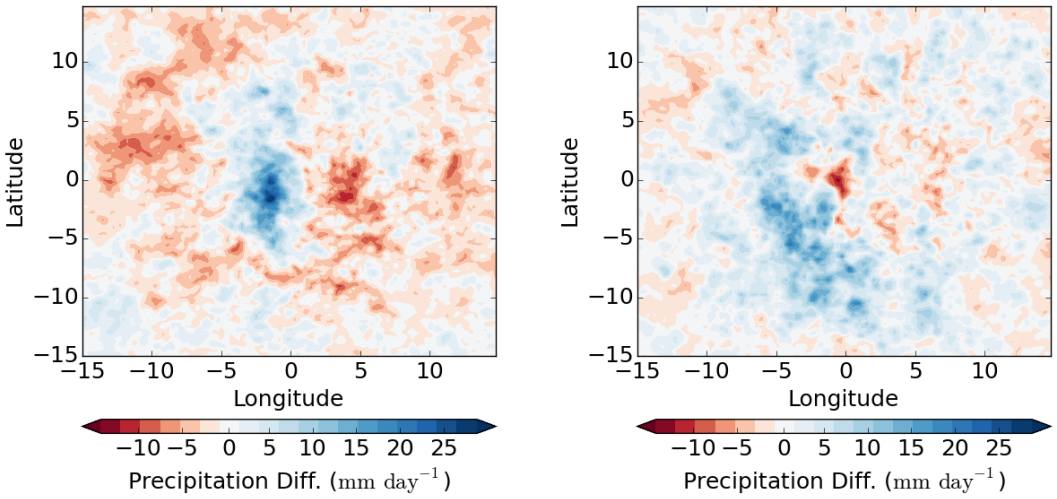

(a) El Niño-minus-La Niña

(b) Active-minus-normal

Figure 3.25: TRMM rainfall difference composites (mm day^{-1}) for (a) El Niño minus La Niña and (b) active-minus-normal.

Fig. 3.24(a) shows that the day composite is almost ubiquitously 0.2 K hotter, with the increase rising to over 1.3 K in the lower troposphere, this maximum being due to strong thermal interaction between the atmospheric boundary layer and the surface (see also §3.4.6). Fig. 3.24(b) shows that (as in Fig. 3.18(b)) the daytime depression is also drier throughout in terms of relative humidity. Fig. 3.24(c) shows that there is a nearly universal reduction in cloud cover by day, particularly in the low-level cloud at the centre.

3.6 The influence of large-scale forcing

We now consider whether organised modes of variability such as intraseasonal and interannual modes connected to the monsoon can influence the structure of monsoon depressions.

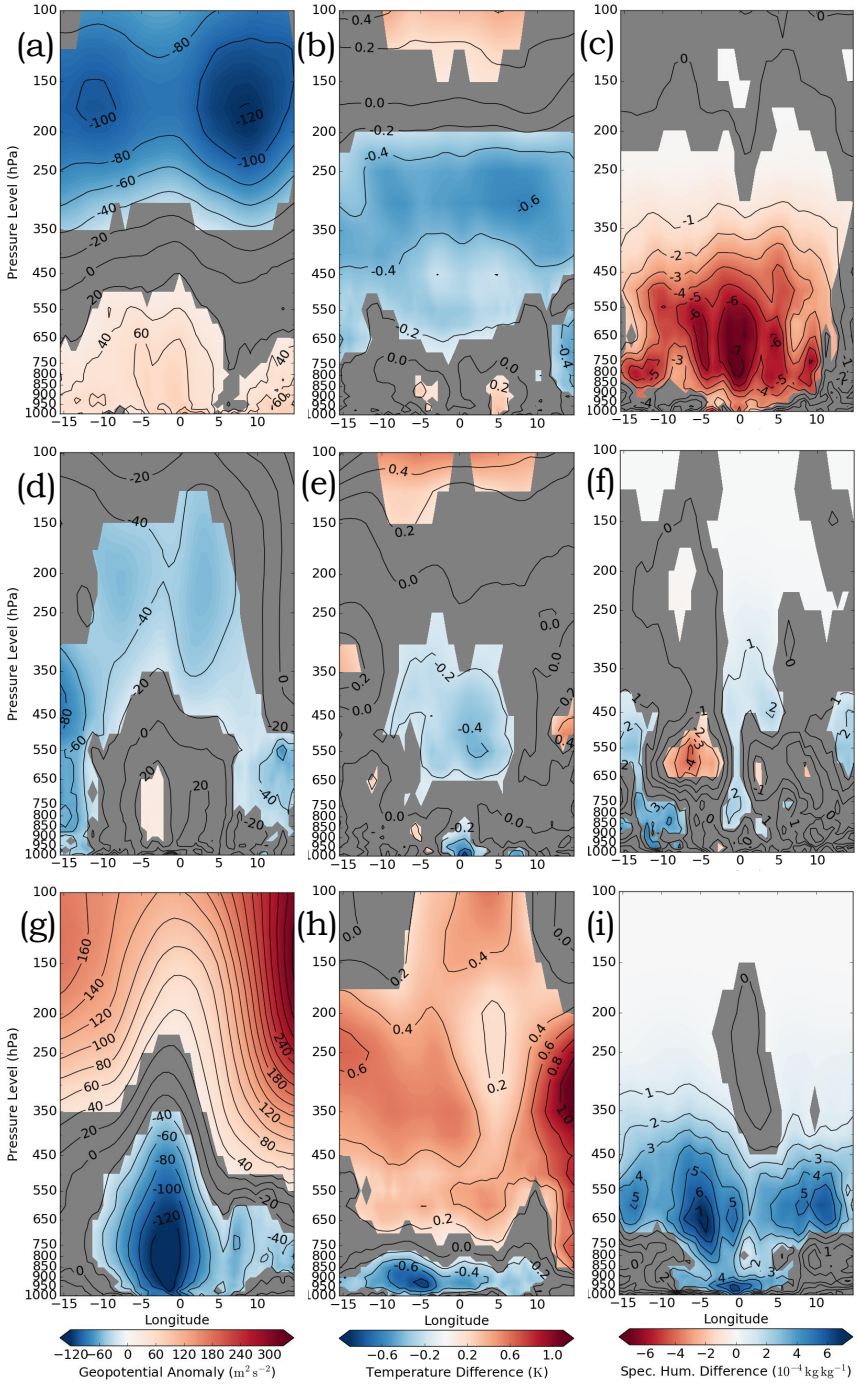

Figure 3.26: Vertical structure of the (a-c) El-Niño-minus-La-Niña, (d-f) IOD positive-minus-negative and (g-i) active-minus-neutral composites for (a,d,g) geopotential height (m), (b,e,h) temperature (K) and (c,f,i) specific humidity (10^{-4} kg kg^{-1}) respectively. The colours are greyed out in areas where the composite difference does not significantly differ from zero.

	Active	Neutral	Break	Jun/Sep/2010-	Total
El Niño	39	42.5	0	48.25	129.75
Neutral	20.25	38.25	1.75	59	119.25
La Niña	27.25	30.25	1.25	73.75	132.5
Total	86.5	111	3	181	381.5

Table 3.3: Distribution of depression days with respect to ENSO and active-break cycles. Active/break data are limited to July and August, and runs until 2010, so those events falling outside this period are tallied in the penultimate column.

3.6.1 El Niño Southern Oscillation

The El Niño Southern Oscillation is responsible for a significant fraction of the inter-annual variability within the monsoon system; affecting precipitation by as much as 20% (Webster et al., 1998). It is therefore plausible that synoptic scale systems (such as depressions) within the monsoon might also be significantly affected by ENSO. We define an ENSO event as a contiguous seven month period with a Niño-3.4 region index of greater than 0.5 K. Such an episode is then linked to the monsoon season that precedes it, as is convention.

Whilst warm-core tropical cyclone activity is enhanced over the Indian Ocean during La Niña and suppressed during El Niño (e.g. Bell et al., 2014), we find that the reverse is true for cold-core depressions, with approximately 16% more activity during El Niño years than La Niña (cf. 12% in the Hurley and Boos, 2015 dataset); note that we are considering the total number of events here, rather than event days as summarised in Tab. 3.3. Krishnamurthy and Ajayamohan (2010) studied monsoon low pressure systems (rather than specifically depressions) and found a slight increase in LPS days during La Niña.

Fig. 3.25(a) shows the El Niño minus La Niña rainfall composite for depressions in La Niña years during the TRMM dataset period. The overall rainfall rate, away from the centre, in La Niña depressions is considerably greater than that of El Niño years; this agrees with the strong correlation between drought/flood years and El Niño/La Niña years respectively (e.g. Rasmusson and Carpenter, 1983; Ropeleski and Halpert,

1987; Webster and Yang, 1992). However, there is evidence of a stronger, more moist core to the El Niño depressions.

ERA-Interim reanalysis data in timesteps of 6 hours show a total of 381.5 depression days spread among the 106 depressions (Table 3.3). For El Niño years, there were 7 and 29 neutral-, and cold-core depressions respectively, whereas for La Niña years, the count was 10 and 23 (with 11 and 22 for neutral years). So, for neutral and La Niña years, cold-core depressions were only a little over twice as likely as neutral-core counterparts; whereas for El Niño years they were over four times as numerous here. This could be in part due to El Niño depressions being drier (Fig. 3.26(c)), allowing greater reduction in temperature via latent heat of evaporation. However, the sample sizes are small, so the results may not be significant.

Fig. 3.26(a-c) show the vertical structure for several variables in the El Niño-minus-La Niña composite. The structure of the geopotential height (see Fig. 3.26(a)) is quite different. We see the surface is almost entirely at a higher geopotential height (i.e. higher pressure) for the El Niño composite compared to the La Niña one. With altitude this falls, with a 0 m isohypse passing over the centre at approximately 420 hPa. Therefore an El Niño depression is typically colder than a La Niña depression from the mid-troposphere upwards (Fig. 3.26(b)), since pressure falls off more rapidly with height. This is probably because weaker mean-state convection in El Niño depressions releases less latent heat aloft. The differences in structure of relative vorticity (not shown), indicate the core is considerably less cyclonic in El Niño depressions, remaining so (with reducing intensity) up to the tropopause. This comparatively less vigorous core is surrounded by zones of higher relative vorticity which also persist and spread out aloft, indicating that these depressions have a less tightly wound centre but stronger rotation in the flanks.

As we might expect from Fig. 3.25(a), the La Niña composite (Fig. 3.26(c)) is generally relatively moister, especially in the mid-troposphere, with some closed -6×10^{-4} kg kg^{-1} isohumes around 600 hPa in El Niño relative to La Niña. There is also a

surface gradient, with the El Niño composite possessing comparatively drier air in the relative west. A more detailed analysis of the ENSO differences is beyond the scope of this study.

3.6.2 The Indian Ocean Dipole

The Indian Ocean Dipole (IOD) was first identified by Saji et al. (1999) and we represent it by their dipole mode index (DMI), defined as the difference in SST anomalies between two boxes in the west (50°E -70°E, 10°S -10°N) and southeast (90°E -110°E, 10°S -0°N) Indian Ocean respectively. Values greater than 0.5 (less than -0.5) are named positive (negative) IOD events. Krishnan et al. (2011) considered the positive IOD event of 2006 and its contemporaneous depressions, showing that there was a positive feedback system that contributed to the longevity of depressions. They subsequently generalised their study to a climatology and found that positive IOD events added approximately 12% to the lifetime of depressions. Here, we briefly explore (see Fig. 3.26(d-f)) the difference in structure between monsoon depressions in positive and negative IOD environments. The state of the IOD has a much lesser impact on depressions than does ENSO.

The difference in geopotential height is shown in Fig. 3.26(d) and indicates that depressions associated with positive IOD events are slightly weaker and larger. This is corroborated by the temperature structure (Fig. 3.26(e)) which shows a weakening of the warm core aloft. This may be connected to the cooling of the ocean at the head of the Bay of Bengal, where most depressions originate (Fig. 3.27(a)) resulting in less moisture being available from evaporation for early intensification processes. However, as Krishnan et al. (2011) showed, positive IOD events result in greater cross-equatorial moisture flux and an increase in the meridional shear of the zonal wind (resulting in greater barotropic instability) which supports the depression in its transit across the trough and stalls the dissipation. The difference in specific humidity between positive and negative IOD events (Fig. 3.26(f)) displays little coherent structure and is not significantly different from zero almost anywhere.

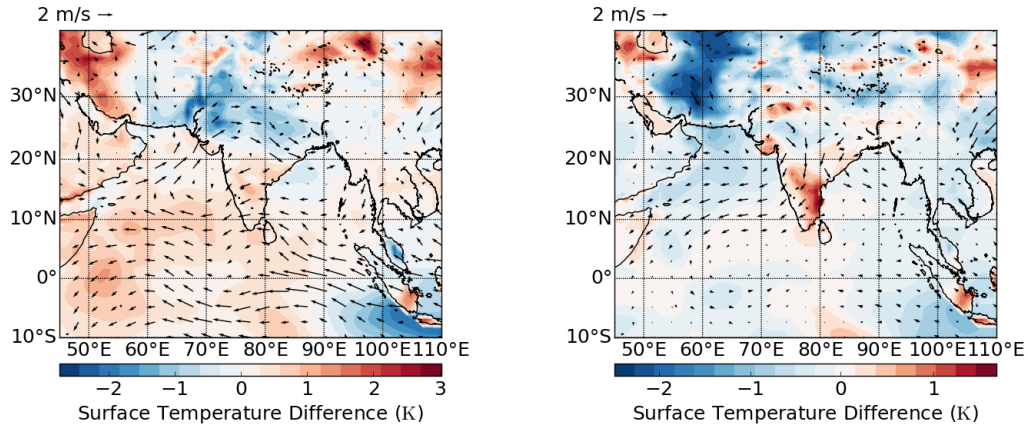

(a) IOD positive-minus-negative depression days

(b) ENSO positive-minus-negative depression days

Figure 3.27: Surface temperature (K, coloured contours) and wind (m s^{-1}) at 850 hPa for (a) IOD positive-minus-negative and (b) El Niño-minus-La Niña depression days. Note the differing colour scales.

The state of the subcontinent in both 850 hPa winds and surface temperature is given for IOD positive-minus-negative and ENSO positive-minus-negative depression days in Figs. 3.27(a) and 3.27(b) respectively. The well-defined IOD structure in SST induces an anomalous north-south land surface temperature gradient and a slight strengthening of the monsoonal winds. In contrast, the ENSO difference pattern shows a slight weakening of the monsoonal winds and a warmer surface due to deficient rainfall. To conclude, El Niño conditions may produce more depressions than La Niña, but they are weaker; whereas the IOD makes no significant difference to the structure of depressions. The influence of the IOD on surface rainfall (not shown) is also slight, but in agreement with the small difference in temperature: the slight drop in temperature throughout the profile of the IOD positive composite is accompanied by a small reduction in precipitation. The maxima in both composites are still found in the relative southwest sector, with an IOD positive maximum of 50 mm hr^{-1}, and an IOD negative maximum of 56 mm hr^{-1}.

3.6.3 Active and break phases

Active (enhanced rainfall) and break (suppressed rainfall) phases of the monsoon significantly affect both spatial rainfall distribution and depression frequency (Krishnamurthy and Shukla, 2007), with a far more depression days during active periods. We can combine ENSO-based prevalence with active-break prevalence (see Tab. 3.3). We used data on active and break spells from Pai et al. (2013), requiring constriction of the dataset to July and August 1979-2010 (leaving 54% of samples). Due to the relative sparsity of depressions coinciding with breaks (Krishnamurthy and Shukla, 2007, also Tab. 3.3), meaningful statistics of break depressions were unrealisable. Therefore, we compare depression composites in active and neutral spells (see Fig. 3.26(g-i)). Active-spell lower-tropospheric geopotential height (Fig. 3.26(g)), is much lower pressure in the centre, with a much steeper vertical gradient, suggesting that depressions intensify under active conditions.

The maximum magnitude of the temperature difference is little greater than 0.5 K (Fig. 3.26(h)), but active depressions clearly exhibit a slightly colder core at the surface and a warmer upper troposphere because of the greater release of latent heat through the stronger convection. This is an amplification of the structure seen in Fig. 3.15(a) and further implies a strengthening of depressions under active monsoon conditions.

The active composite has a much more cyclonic core, flanked on either side by areas of considerable relative anticyclonicity, and with a weaker corresponding anticyclone. The composite active depression is considerably wetter in the mid levels (750-500 hPa) as expected (Fig. 3.26(i)). This difference composite also exhibits a slight relative east-west gradient at the surface (as with El Niño-La Niña): wetter in the west and drier in the east.

The average relative vorticity (again, as an anomaly to the climatology) over South Asia for depression days is illustrated in Fig. 3.28(a). The most immediately apparent feature is the strong anticyclonic vorticity band located across the Himalayan foothills, seen already in Figs. 3.5(a) and 3.10(a). The corresponding region of anomalous pos-

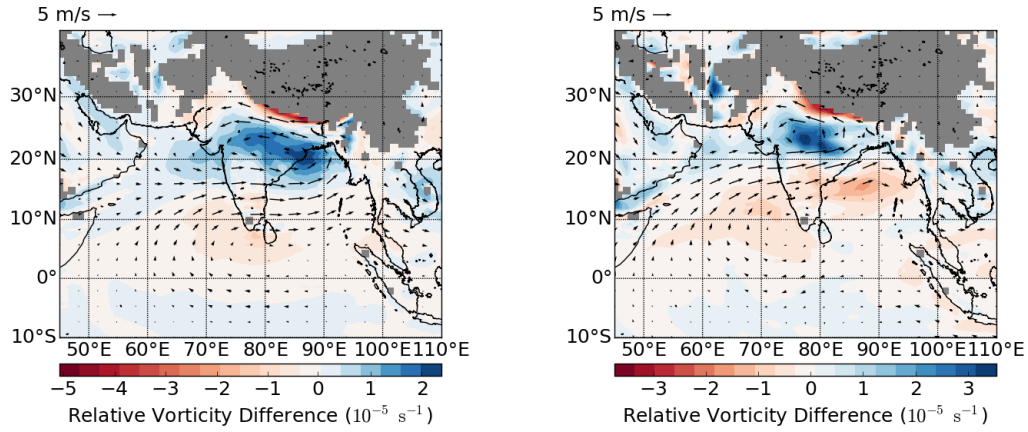

(a) All depression days minus JJAS climatology

(b) Active-minus-neutral depression days

Figure 3.28: Relative vorticity (coloured contours, 10^{-5} s^{-1}) and wind (m s^{-1}) for (a) all depression days as an anomaly to the boreal summer mean and (b) active-minus-neutral depression days. The coloured contours are greyed out where the orography rises above the 850 hPa level.

itive relative vorticity is strongly correlated with the track density of depressions (see Fig. 3.1(a)), with a colocated maximum on the coast of Odisha and West Bengal. There are also several smaller, weaker areas of negative anomalous relative vorticity; notably over Pakistan where many lows eventually dissipate (Krishnamurthy and Ajayamohan, 2010). This pattern is in agreement with Godbole (1977). Fig. 3.28(a) also shows the depression winds (at 850 hPa) less the climatology, revealing a structure very similar to that of an active-minus-break composite (Webster et al., 1998), and bearing some resemblance to the equivalent ENSO pattern (Fig. 3.27(b)); but it seems to bear no relation to the strength of the monsoon itself (Turner et al., 2005); this demonstrates that certain aspects of large scale variability (La Niña and active phase) favour the circulation anomaly in which depression days occur. The sign change in zonal wind that occurs at ∼20°N is greatly assisted by the addition of cyclonic vorticity from the presence of depressions in the north of the Bay of Bengal and over northeast India. The shear imparted on the 850 hPa easterly by the Himalayas is also visible. For comparison, the difference in 850 hPa winds and relative vorticity between active depression days and non-active depression days is shown in Fig. 3.28(b). It demonstrates that the

active state is an amplification of both the monsoon and the depression-day anomaly, and it therefore corroborates what we saw in Fig. 3.26(g-i), that depressions occurring when the monsoon is active are somewhat more intense (lower central pressure, greater vertical temperature gradient, more moisture) than when it is in a normal or break phase.

3.7 Conclusion and discussion

Monsoon depressions are cyclonic tropical lows, averaging 2-5 days in lifetime, that spend much of their time over the Indian subcontinent. They are important as they contribute much rain to the north east of the Indian peninsula, a region known to be particularly dry in coupled GCMs (Sperber et al., 2013). It is therefore important to quantify their structure, movement, and behaviour, so as to evaluate and understand their dynamics. This will in due course enable evaluation and improvement of numerical models, leading to deeper understanding and to more reliable prediction, and thus to improved local community preparedness for flooding and related impacts.

We confirmed the existence of a rainfall maximum in the southwest sector of a rotated northward propagating depression (Ramanathan and Ramakrishnan, 1933; Mooley, 1973; Godbole, 1977). There are several orders of magnitude between the rainfall maximum of the composite (38.6 mm day^{-1}) and the maximum individual event (1.6 metre day^{-1}), indicating the diversity and local detail of such extreme events.

Reanalysis data were used on the 106-depression composite to determine horizontal and vertical structure; showing that many fields have their maximum intensity in the relative southwest sector. The Himalayas were found to have a pronounced anticyclonic effect on the relative east/northeast sector of the depressions, both at the surface and aloft; as confirmed by the relative vorticity field during depression days which exhibited an intense band of anticyclonicity along the foothills. A schematic diagram of the major results is shown in Fig. 3.19. We confirmed the warm-over-cold temperature

core structure is present in almost all depressions, relating the near-surface cold core to reduced insolation from increased cloud cover, and the warm core aloft to strong latent heating from convective precipitation. We also found a bimodal potential vorticity structure at the centre (also recently discovered by Hurley and Boos, 2015), as well as an intensification of the tangential winds on the Himalayan side of the depression.

The slight westward axial tilt observed in e.g., Godbole (1977) and Douglas (1992a) was also confirmed in the lower levels in many fields, though some fields also exhibited an eastward axial tilt near the tropopause.

We have shown that depressions can be separated into three separate core types: warm (rare and tropical cyclone-like), neutral (weak temperature anomalies near the surface, strong warm core aloft, strong temperature anomaly gradient near the tropopause), and cold (much colder at the surface, warm core aloft, most frequent type); we found that cold-core depressions are comparatively more likely to form in El Niño conditions than neutral or La Niña ones, and that neutral-core depressions are responsible for greater and more widespread rainfall.

We compared composites of depressions over land and ocean. Most differences were not large given the scatter between depressions, but depressions over land had weaker near-surface winds owing to friction, and more anticyclonic vorticity to the relative east owing to the Himalayas. There was no significant difference in potential vorticity between the subsets, although equivalent potential temperature had a more extended maximum over land owing to differing moisture structures. We also found that the boundary layer height drops over the centre of the depression. Latent and sensible surface heat fluxes were also considered, both have minima at the centre and strong land/ocean contrasts: latent heat flux being much higher over the ocean.

Depressions during La Niña have moister, more vortical cores than during El Niño. They also have a warmer middle troposphere and slacker vertical geopotential height gradient, and though they yield less intense precipitation at the centre, they are associated with higher rainfall rates in the flanks. The influence of the Indian Ocean Dipole

on monsoon depressions was very slight.

Depressions occurring during active monsoon phases are more intense: greater lower/mid-tropospheric geopotential height anomaly, greater vertical temperature anomaly gradient, and substantially more moisture throughout. The active-period intensification of the background monsoon conditions strongly resembles an amplification of the depression-day anomaly relative to the monsoon climatology.

Monsoon depressions are colder, wetter, and have more cloud throughout during the local nighttime than the daytime.

These diagnostics represent a firm basis for assessing monsoon depression representation and behaviour in NWP and high-resolution climate models.

So, we have gained much from using our tracks to interrogate reanalysis data, but a number of these fields are purely modelled and we have not verified them. To do so, we will need to modify these analysis tools to cope with the sparser data that satellite overpasses offer. Aside from the advantage of verifying existing results from ERA-Interim, successful compositing of satellite fields would provide the potential for a much higher-resolution product[2], with the ability to correctly represent convective processes. These will be among the leading questions as we open discussion in the next chapter.

[2]Satellite swath data has resolution of the order of hundreds of metres to a kilometre, as opposed to the approximately seventy kilometre resolution of ERA-I

CHAPTER 4

THE SPATIOTEMPORAL STRUCTURE OF PRECIPITATION IN INDIAN MONSOON DEPRESSIONS

4.1 Introduction

As we have seen, MDs are capable of providing very heavy precipitation across much of northern India (Godbole, 1977; Stano et al., 2002), which, as a predominantly agrarian society, relies prominently on rainfall. It is therefore crucial to have a clear understanding of the hydrometeor structure and moist thermodynamic processes of these events. Short and Nakamura (2000) and Fu and Liu (2001) provided the first analyses of the vertical structure of rainfall rates in the tropics using satellite data, preceding the case study of the three 1999 depressions by Stano et al. (2002). Since then, there have been numerous further studies using the Tropical Rainfall Measuring Mission (TRMM), but none exploiting the depth of such satellite data on the nearly forty MDs that have occurred since the launch of TRMM. Recently, Bowman and Fowler (2015) used TRMM to examine the diurnal structure of tropical cyclones showing that precipitation within 500 km of the centre had a diurnal cycle with a maximum in the early morning.

We remain, therefore, without even a basic understanding of the moist processes that occur in MDs. Whilst it has been known for some time that the maximum surface

precipitation is to be found several hundred kilometres southwest of the depression centre (Roy and Roy, 1930; Ramanathan and Ramakrishnan, 1933; Mull and Rao, 1949; Desai, 1950; Petterssen, 1956; Mooley, 1973; Godbole, 1977; Daggupaty and Sikka, 1977; Stano et al., 2002; Yoon and Chen, 2005), there is no certainty on the generating mechanism and several prevailing synoptic theories result: the westward axial tilt of the core with height, colocation with a lower-troposphere convergence maximum, cyclonic mixing of cool monsoon circulation with warm, moist southwesterlies from the Bay of Bengal, or even some combination of these. Douglas (1992b) noted that this area was strongly colocated with warm air advection in the lower troposphere. Most recently, Yoon and Chen (2005) suggested that this asymmetry was a consequence of MD water vapour flux convergence coupling with longer period modes of monsoon variability, but showed only that these (10-20 d and 30-60 d) modes could enhance or suppress the MD rainfall, not that they were necessarily the reason for the location of its maximum. Quasigeostrophic uplift has been presented by several authors (Rajamani and Rao, 1981; Boos et al., 2015) as a theoretical link.

Sørland and Sorteberg (2015) tracked 39 monsoon low pressure systems (LPSs) associated with daily extreme rainfall events as given by the gridded gauge precipitation dataset of the India Meteorological Department (Rajeevan et al., 2005, 2006); they attempted to correlate precipitation rates in these LPSs with prognostic parameters, finding the most significant correlation was with 750 hPa vertical velocity. They also posited that a strong negative correlation between surface rain rate and 950 hPa temperature indicated that evaporative cooling from precipitation was responsible for the lower tropospheric cold-core (e.g. Godbole, 1977; Hurley and Boos, 2015) of MDs.

This study comprises three main parts: after discussing the data and methodology in Section 4.2, we will look at TRMM and CloudSat derived composites in Section 4.3, then compare these to a specific case study in Section 4.4, and then explore the diurnal pattern in Section 4.5 before concluding in Section 4.6.

4.2 Methodology

4.2.1 Data

Tropical Rainfall Measuring Mission

This study makes substantial use of data from the TRMM satellite mission, which was operational between December 1997 and October 2014 (Simpson et al., 1988, 1996; Kummerow et al., 1998, 2000). It accommodated five instruments: the TRMM Microwave Imager (TMI); the Precipitation Radar (PR); the Visible Infrared Radiometer (VIRS); the Cloud and Earth Radiant Energy Sensor (CERES); and the Lightning Imaging Sensor (LIS). Throughout, we will be concerned with data output products that inherit from the first three. The PR was a Ku band radar working at 13.8 GHz (Kawanishi et al., 1993, 2000) that provided high spatiotemporal resolution three-dimensional precipitation measurements over both land and ocean and is the primary source of these datasets; for a summary of which TRMM data are used in this study, see Tab. 4.1. The level-2 algorithms (those prefixed with '2') retain the resolution and footprint of the original satellite swath, a 220 km wide track at 4 km $\times$ 4 km $\times$ 250 m (80 vertical levels)[1]; in contrast, the level-3 algorithm used here has global coverage between the 50th parallels, and is a multi-satellite product, also comprising inputs from GMS, GOES-E, GOES-W, Meteosat-7, Meteosat-5, and NOAA-12. This surface precipitation product has a resolution of $0.25^\circ \times 0.25^\circ$.

For calculating latent heat profiles, the hydrometeor heating algorithm (Tao et al., 1993, 2006) is used. Vertical profiles of hydrometeor density are combined with local temperature, wind speed and humidity data in a 1D model that estimates flux, phase change rate, and hence latent heating. The major origins of uncertainty are: uncertainty in vertical wind speed, noise in the hydrometeor profile, particularly near the surface, and difficulties in constraining hydrometeor terminal velocity.

[1]The TRMM orbit was boosted in August 2001, increasing the swath width to 250 km with a footprint of 5 km $\times$ 5 km.

Code	Name	Dependencies	Outputs Used	Citation
2A23	PR Qualitative	PR	rain type bright band storm height	Awaka et al. (1997)
2A25	PR Profile	PR 2A23	rain rate estimated surface rain rate	Iguchi et al. (2000)
2B31	PR Combined	PR TMI 2A23	snow density graupel density drop size distribution latent heating	Haddad et al. (1997a,b)
3B42	TRMM & Other Sensors - 3 Hourly	PR TMI 2A23 other satellites	gridded global precipitation	Huffman et al. (1995, 1997, 2007, 2010); Huffman (1997)

Table 4.1: An overview of the TRMM algorithms and datasets used in this study.

CloudSat

CloudSat is a NASA polar-orbiting A-Train satellite primarily equipped with a 94 GHz cloud profiling active reflectivity radar (Stephens et al., 2002, 2008) which measures the backscattered energy from clouds and precipitation. It has been in almost continuous operation since June 2006, and via the CloudSat Data Processing Centre at Colorado State University, the mission releases numerous cloud quantification and thermodynamic datasets. A summary of those datasets used in this study is given in Tab. 4.2. The radar measures nadir only, and therefore the output swaths have zero-width; the along-track resolution is 1.7 km, and there are 125 vertical levels at a resolution of 250 m.

ERA-Interim

We will make occasional use of the ECMWF-authored ERA-Interim (ERA-I) reanalysis product. This has six-hourly global coverage at N256 ($\sim$ 77 km at equator) resolution (Dee et al., 2011). Quite a number of products are available on a global Gaussian

Code	Outputs Used	Citation
2B-GEOPROF	cloud mask, cloud flag, radar reflectivity	Marchand et al. (2008)
2B-CLDCLASS	cloud scenario	Sassen and Wang (2008)
2B-FLXHR	longwave and shortwave radiative heating effects	L'Ecuyer et al. (2008)
2C-RAIN-PROFILE	liquid and ice precipitation densities	L'Ecuyer and Stephens (2002)
2C-PRECIP-COLUMN	surface precipitation flag and rate	Haynes et al. (2009)

Table 4.2: An overview of the CloudSat datasets used in this study.

grid, either at the surface, on pressure levels (37 in total, from 1000 hPa to 1 hPa), or at sigma or potential vorticity levels. There are also some precipitation related datasets within ERA-I, but as a prognostic variable, it has poor skill when compared with satellite observations (Liu et al., 2014).

4.2.2 Compositing

In §2.1, we outlined an objective-based feature tracking algorithm that was then applied to ERA-Interim reanalysis data over the Indian subcontinent for the period 1979-2014, wherein we identified and corroborated 106 MDs with genesis over either the Bay of Bengal or the subcontinent itself; we shall now use the relevant subset of that data for the TRMM (CloudSat) operation period: 34 (12) depressions during 1998-2014 (2007-present). Furthermore, in some instances (usage of the 3B42 data) we replicate the rotation-composition method from Chapter 3 (also used in, e.g., Catto et al., 2010): for each MD timestep, the depression heading is calculated; the data are then reoriented, centralised, and composited onto a new grid such that the composite heading is due north and the 850 hPa relative vorticity maximum lies above the latitude-longitude origin.

Where data is sparser, compositing the data in this manner is not statistically robust. Instead we can artificially boost the sample size by collapsing the azimuthal

dimension and treating the composite data as a function only of radius and height. This introduces a degeneracy that we can exploit to examine an asymmetry of our choice. The largest mode of spatial asymmetry in MDs is caused by the presence of the Himalayas (discussed in §3.4 and §5.2), and so we shall henceforth define the pseudoradial coordinate, with magnitude equal to the radius and the sign of the normalised latitude; for example, a point 440 km westsouthwest (or any bearing between 90° and 270°) of the centre would have a pseudoradius of -440 km (or -4° using the 111 km/° employed in this study). This method was developed with CloudSat data in mind, but for consistency has been extended to discussions of vertical structure derived from TRMM products.

4.3 Composite structure

Firstly, we shall build a three-dimensional composite in the manner outlined in Section 4.2.2. It is important to gauge the mean structure of precipitation and cloud attributes for two reasons: so that we have a fundamental base for further analysis; and that as the leading-order moment, this is what any model should primarily be tested against.

4.3.1 Hydrometeor distributions

Arguably the outright most important feature of an MD is surface precipitation, so we shall open our discussion of mean structure with this field. Fig. 4.1 presents this in two ways: on the left, unrotated; and on the right, rotated - i.e. the data from each timestep are rotated such that the depression propagates along zero bearing. Note that Fig. 4.1(a) comprises the same data as Fig. 3.2 and is included here to allow easier comparison. The most striking difference between the two, noting the different colour scales, is the magnitude of the central maximum; there are two factors causing it to be reduced in the rotated composite: implicit smoothing during interpolation onto the

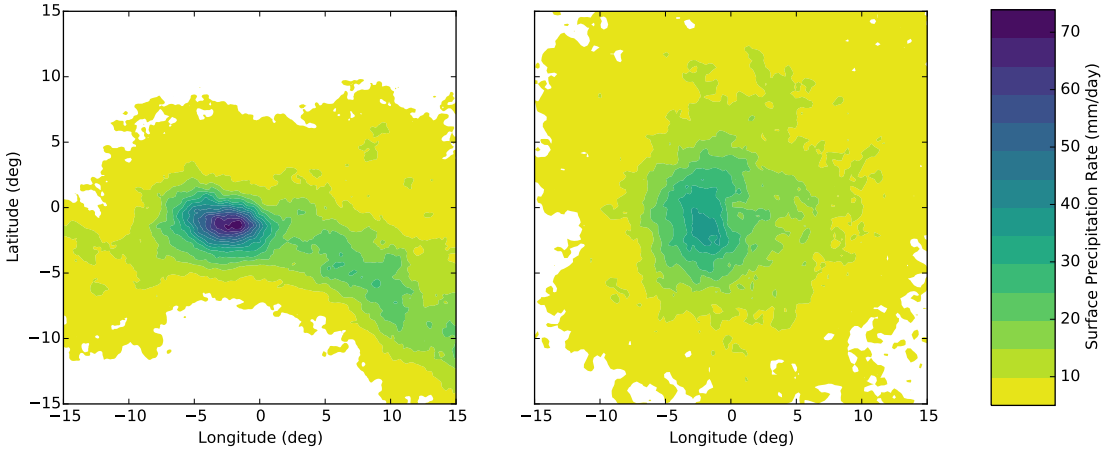

Figure 4.1: Composite mean surface precipitation (mm day^{-1}) from TRMM 3B42 for depressions 1997-2014. Right: the rotated composite, where each timestep is rotated such that the depression is heading due north (i.e. up the page). Left: as right, but with no rotation during compositing.

rotated grid, and the temporal variability of the location of the maximum precipitation in the rotated coordinates (providing extra variance associated with the spread of headings). We should note that both of these factors are unique to precipitation fields, which have categorically the highest variance of any common meteorological variable, and which uniquely do not have composite extrema colocated with the depression centre. As discussed previously, we see the maximum surface precipitation located several hundred kilometres southwest; it has a maximum magnitude of over 70 mm day^{-1} at 1.4°S, 1.7°W, and falls away quickly except for a band in the east representing orographic rainfall along the coast of the Bay of Bengal.

We are now in a position to explore the composite vertical structure of precipitation. The simplest manifestation of this is rain rate, shown in Fig. 4.2; ground clutter returns and any missing data are not included in the composite, therefore any part of the composite with no useful data is shown as the background grey colour. The seemingly very high rainfall rates shown near the surface are an artefact of this process: there, only very high radar reflectivities can surpass ground clutter. The general structure is what we might expect on consideration of the surface precipitation shown in Fig. 4.1, indeed the data from (b) of that figure is collapsed onto the pseudoradius coordinate

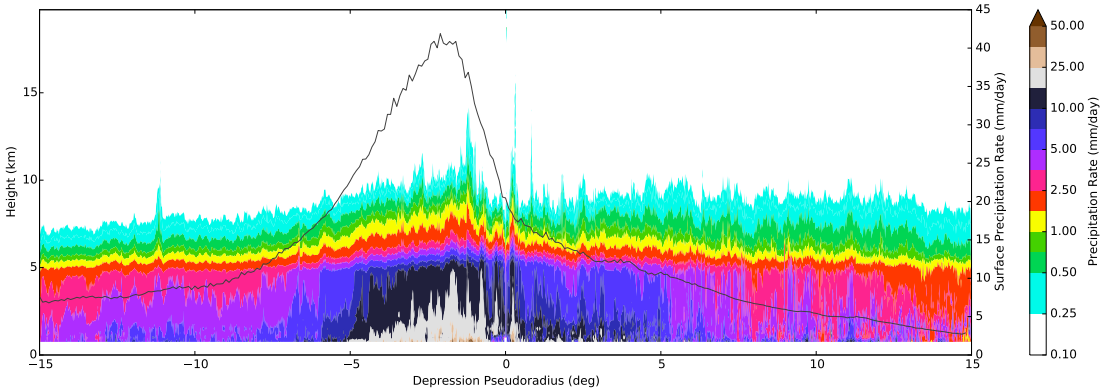

Figure 4.2: Composite vertical profile of rain rate (mm day^{-1}, coloured contours) from TRMM 2A25 as a function of pseudoradius. Overlaid as a dark grey line for illustration is the (unrotated) composite surface rain rate (mm day^{-1}, right axis) from TRMM 3B42 (see Fig. 4.1(a)), also as a function of pseudoradius. Note that the lowest contour is coloured white, and the background, grey.

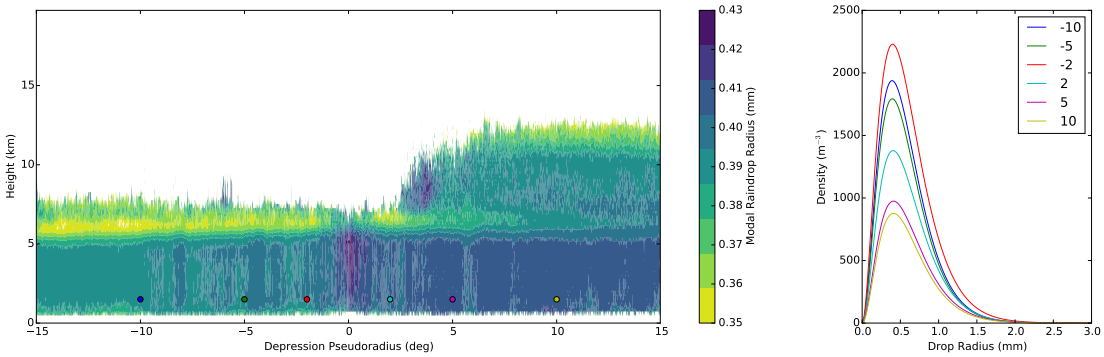

Figure 4.3: Modal raindrop size (mm, radius) throughout the composite, calculated from the drop size distribution parameters in TRMM 2B31. Right: full distributions for selected pseudoradii at a height of 1.5 km, the locations of which are indicated by dots on the left hand figure.

for illustration. Here, the asymmetry is stark: the strongest rains both at the surface and aloft are found several hundred kilometres away from the centre, in the southern half. We note also that the rainfall rates in the upper mid-troposphere ($\sim$ 7 km) are proportional to those much nearer the surface, implying that most surface rainfall is the result of deep convective processes. The effect of the Himalayas in the northern half can also be seen: the ratio of rainfall aloft to that near the surface is higher in the south (e.g. 10-15°) than the north, implying orographic forcing there.

Now we have an idea of the rainfall rates throughout the composite MD, we can

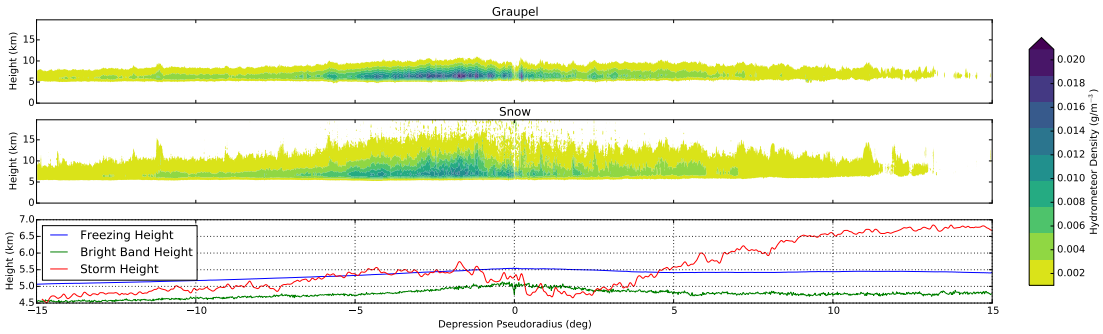

Figure 4.4: Composite vertical profile of graupel (g m^{-3}, top) and snow (g m^{-3}, middle) densities as a function of pseudoradius, from TRMM 2B31. Underneath are the structures of the bright band, storm, and freezing heights, from TRMM 2A23. Note the height scales differ between the top two and bottom panels. The colour scale is the same for both relevant panels.

use data from TRMM 2B31 to estimate raindrop size distributions (DSDs); doing so will further assist our investigation into the physics driving hydrometeors in MDs. We obviously cannot show the varying DSDs throughout the composite, so instead a figure showing the modal raindrop size throughout the MD with some selected DSDs is given (Fig. 4.3). Calculating these distributions is non-trivial and it is beyond the scope of this study to describe the full calculation here; for a full derivation the reader is encouraged to visit Haddad et al. (1997a). What the figure shows us is that there is a well-defined area where the TRMM 2B31 algorithm believes that there is rain, and within it the modal drop size has fairly low variance. It is particularly interesting to note that whilst the highest rainfall rates (see Fig. 4.2) and highest raindrop number densities are found to the south of the centre, the largest drops tend to be found at the centre itself. Raindrop size appears, at least south of the centre, to be fairly uniform with height until within a kilometre or so of the apparent cloud top. This uniformity indicates that these southern areas are well mixed in depth, in contrast with the centre itself, where the drop size generally increases with height implying strong ascent there.

Finally, we can complete our discussion on the composite hydrometeor structure by considering the distribution of frozen water in MDs. Fig. 4.4 shows the expected densities of snow and graupel in the composite MD, as well as the average freezing, bright band, and storm heights. The maxima for snow and graupel densities are to

be found directly above the highest rain rates, indicating an area of deep convection is responsible for both. This is supported by the graupel having a comparable (or even greater) density to snow, indicating the presence of some mixing process allowing the aggregation and refreezing of the latter into the former. One might be surprised to see that there is a very low frozen hydrometeor density in the north around the Himalayas, but this is simply explained: the climatological freezing height in the Himalayan foothills is over 5 km, but almost all rainfall there is orographic and happens below this altitude, resulting in very little ice formation. The height of the bright band gives us an indication of where extant falling snow is melting most rapidly – we do not expect this to be necessarily at the freezing height because there is a fairly shallow temperature gradient and ice has a finite heat capacity. The difference between the bright band and freezing heights can be interpreted as a weak metric for vertical wind speed.

4.3.2 Cloud scenario

The importance of classifying clouds in a hydrometeor-based compositing study such as this is clear: the presence of different types of cloud represent the dominance of crucially different precipitating and non-precipitating mechanisms in the atmosphere. If we can constrain the types most likely to be present throughout the MD, we can better evaluate the physics behind their representation in GCMs and NWP models.

The CloudSat 2B-CLDCLASS product classifies cloud types by using constraints such as spatial cloud properties, cloud temperature, the existence of precipitation, and radiance measurements from other A-Train satellites (Wang and Sassen, 2007). The category bins are: clear, cirrus, altostratus, altocumulus, stratus, stratocumulus, cumulus, nimbostratus, and deep convection, all of which can be found in the tropics (Sassen and Wang, 2008), and indeed over India. Regridding discrete, qualitative data must be done carefully: we cannot simply compute an interpolating function, or calculate distribution moments; instead we must consider the mode. Heeding this, the

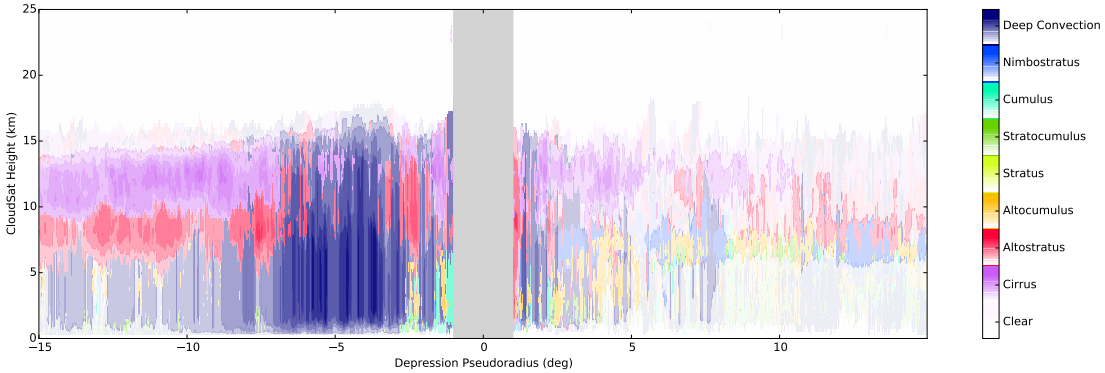

Figure 4.5: Modal cloud scenario in the composite, determined by CloudSat 2B-CLDCLASS. Differing hues represent varying cloud types, with the transparency in each case proportional to the ratio of the modal value and the number of overpasses up to a value of 0.5. Parts of the composite not comprising at least ten satellite overpasses are not shown here. We remind the reader that CloudSat height is referenced above the geoid rather than necessarily the Earth's surface.

modal cloud type composite is given in Fig. 4.5. Here, the hue is a function of the most common type (excluding clear sky); the transparency is zero (i.e. fully opaque) if the ratio of the modal frequency (including clear sky) is greater than or equal to 0.5, below this value they are directly proportional. For example, if the modal cloud type in a particular instance was altostratus, and it was present in 30% of the composite, it would be represented in the figure as a red hue with 60% opacity (40% transparency).

The figure shows that despite all clouds types being present, there are three distinct domains of cloud structure. In the far south, there is the stratification one might expect in a typical tropical environment (Stein et al., 2011): convective clouds in the lower troposphere, becoming altostratus in the mid troposphere, and cirrus tending towards the tropopause; as we move closer to the centre, the initially low-level convective clouds suddenly dominate throughout the height of the troposphere, even rising higher than the cirrus further afield (in agreement with Warner and Grumm, 1984 and Warner, 1984); in the north, however, whilst there is some deep convection much closer to the centre, it tends to be much more mixed: however, there is some mid-level stratus present indicating that Himalayas are forcing orographic cloud there. We might suppose that if the height coordinate were measured from the actual surface, rather than the geoid,

that in the north we would recover dominant stratus at/near the surface; this is indeed the case, although it is not shown here.

We can use these data to explore a little further: by considering the fraction of overpasses that detect cloud (as opposed to clear sky) to generate a cloud cover variable, the result is shown in Fig. 4.6. Here, both the composite from CloudSat overpasses, and an equivalently-constructed composite from ERA-I are shown. Both have clearly captured some structure, but there are stark differences: the ERA-I composite has substantially less cloud in the mid-troposphere, where it suggests almost no cover at all; and in the lower troposphere, where the deep convection is poorly resolved. The ERA-I derived composite does however capture the asymmetry and the high-level cloud structure well when compared to CloudSat. Unfortunately since the comparison of the global all-year climatologies of satellite and reanalysis cloud cover by Jakob (1999), there has been no further research on comparison of these cloud products in the tropics.

Now, we wish to explore the convective and non-convective spatial regimes of the composite MD. Such analysis has been done before using *contoured frequency by altitude diagrams* (CFADs), for single events (e.g. Yuter and Houze, 1995), for domain composites (e.g. Liu et al., 2010), and for system composites (e.g. Hence and Houze, 2011). CFADs display normalised histograms of radar reflectivities as a function of height, and have specifically been used for cloud type analysis with both the 13.8 GHz TRMM PR (Houze et al., 2007), and with the 94 GHz CloudSat radar (Young, 2015). We hypothesize three distinct regimes from Fig. 4.5: generally tropical (e.g. -10°), strongly convective (e.g. -4°), and generally orographic (e.g. 10°). CFADs for these pseudoradii (with an inclusive envelope of 0.4° on each side) are shown in Fig. 4.7 and Fig. 4.8 for TRMM and CloudSat radar reflectivities respectively.

Houze et al. (2007) generated 13.8 GHz reflectivity CFADs for composite stratiform and convective systems within the Indian monsoon. Comparing Fig. 4.7 to Fig. 27 of Houze et al. (2007), we see that the CFAD at a pseudoradius of -4° has a very strong resemblance to their composite of convective cloud structure. Conversely the CFAD at

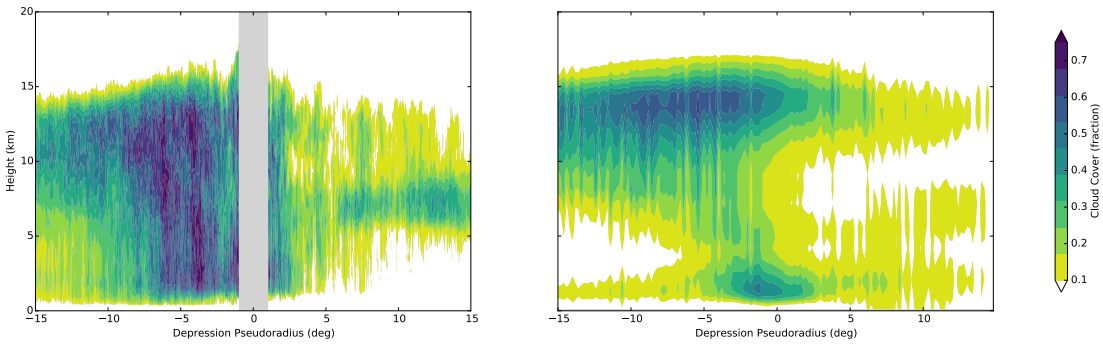

Figure 4.6: Left: cloud cover (fraction of unity) as a function of pseudoradius, as calculated from composite 2B-CLDCLASS data. Right: as left, using ERA-I data. For consistency, both are composited using the same technique.

10° pseudoradius has a clearly stratiform structure, as we might expect from our earlier analysis. Finally, at a pseudoradius of -10°, we note more of a mixed regime, with a slight preference for convective structure, albeit with a less common occurrence than that observed nearer the centre. Repeating this analysis for Fig. 4.8 by comparison with the 94 GHz reflectivity CFAD composites over Africa from Young (2015), we build a very similar picture: mixed with occasional convection at -10°; common convection at -4°, and common stratiform at 10°. Here we also note the strong attenuation in the higher frequency CloudSat radar reflectivity; particularly below 4 km, as also noted by Sindhu and Bhat (2013).

We can attempt to delineate these regimes further by considering the "rain type" product from TRMM 2A23 alongside the simultaneous estimated surface rainfall rate to explore any spatial coherence in precipitation attributable to convective and stratiform processes respectively. The TRMM 2A23 rain type algorithm uses a combination of two methods (Awaka et al., 2007) to determine what type of process rain, if existent, is likely to be have been generated by. The first, the *V-method*, determines precipitation is stratiform if a bright band exists and convective if there is no bright band but the radar reflectivity is above a threshold of 39 dBZ; else it determines it to be "other". The second, the *H-method* (based on Steiner et al., 1995), requires several criteria (39 dBZ reflectivity threshold, high signal-to-noise ratio) to make the determi-

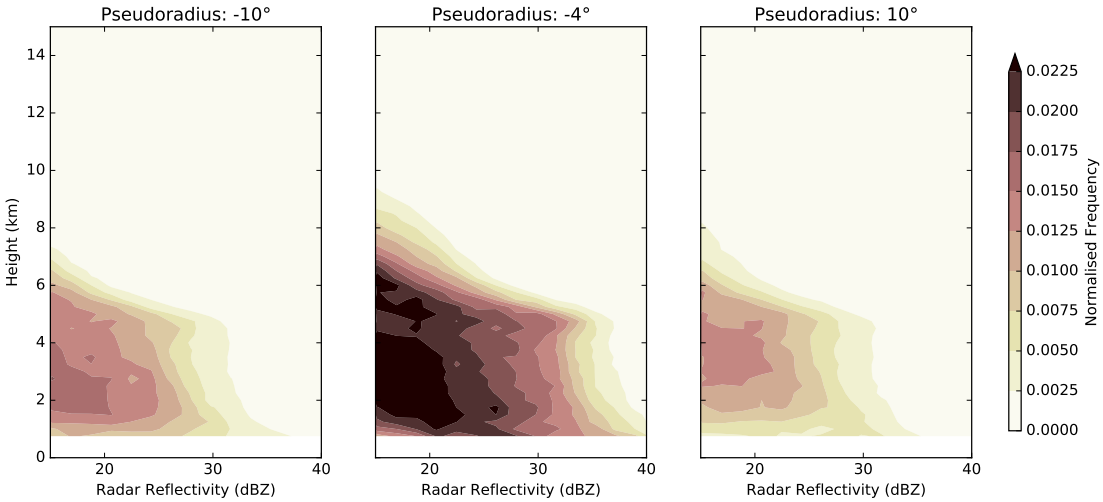

Figure 4.7: Contoured frequency by altitude diagram (CFAD; Yuter and Houze, 1995) for effective radar reflectivity at 13.8 GHz (dBZ) from TRMM 2A25, at pseudoradii of -10° (left), -4° (centre), and 10° (right). The abscissa starts at 15 dBZ, the approximate value of the TRMM PR sensitivity threshold.

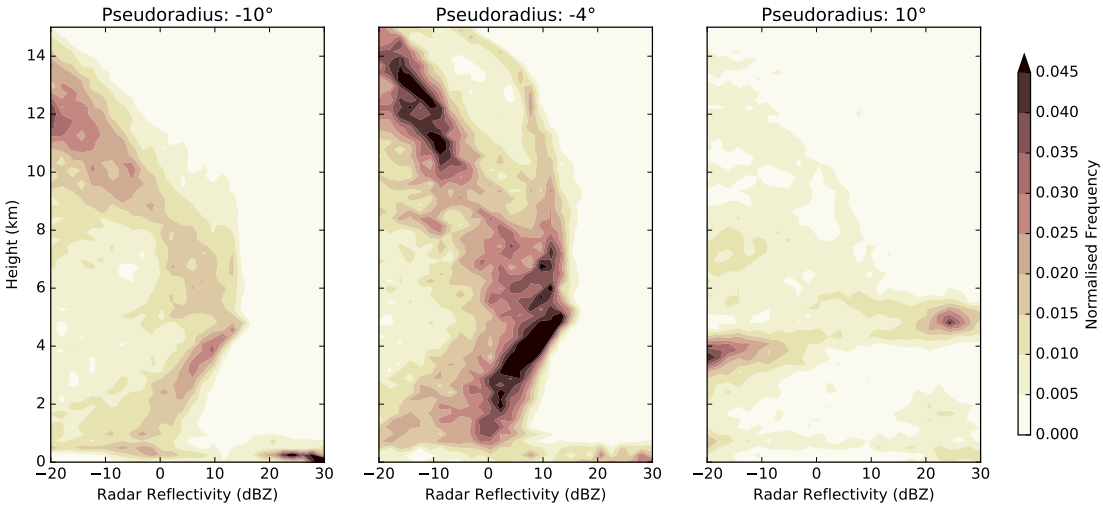

Figure 4.8: As Fig. 4.7 but for radar reflectivities at 94 GHz from CloudSat 2B-GEOPROF. Again, at pseudoradii of -10° (left), -4° (centre), and 10° (right).

nation of convective precipitation; if these criteria are not met but rain is still certain, it is determined to be stratiform; if the signal-to-noise ratio is too weak but rain is possible, it is assigned "other". Subsequently the 2A23 rain type algorithm determines precipitation is definitely stratiform if it is V-stratiform, H-stratiform/other; and correspondingly convective if it is V-convective/other, H-convective. If the H-method and

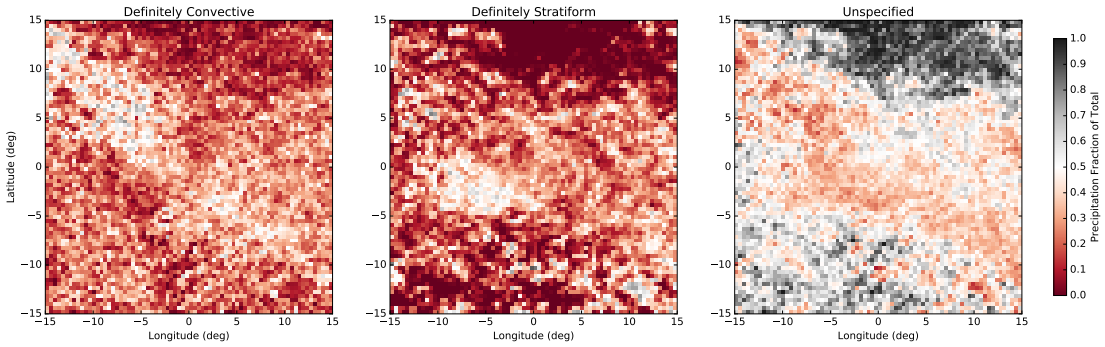

Figure 4.9: Composite rain fraction computed using objective rain type from TRMM 2A23 and estimated surface rain rate from TRMM 2A25. Left: convective; centre: stratiform; right: events not attributable to the previous two categories. See text for a definition of "definitely".

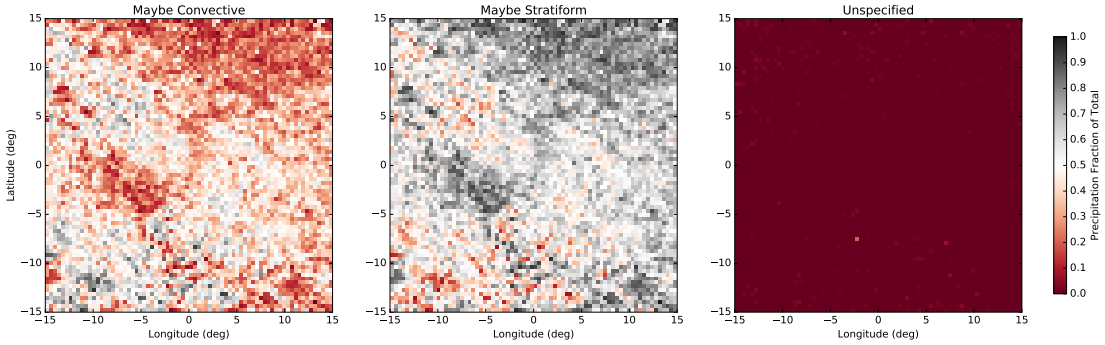

Figure 4.10: As Fig. 4.9 but using a "maybe" threshold (i.e. up to and including "definitely"). Left: convective; centre: stratiform; right: events not attributable to the previous two categories.

V-method explicitly disagree, preference is given to the V-method; this, with other sensible combinations comprise the maybe and probable levels of each type. If neither method can make a determination, but rain is certain, it is given the "other" category.

Fig. 4.9 shows the composite proportion of TRMM 2A25 estimated surface precipitation rate definitely attributable to convective and stratiform systems according to the TRMM 2A23 rain type algorithm, as well as the remainder. Overall, approximately half of the rainfall is attributed, but the algorithm considerably struggled around the Himalayas and south of the peninsula. There is an arguably greater propensity for convective precipitation in the northwest, as the MD starts to push into the drier desert environment of Pakistan; and there is significant area of more likely stratiform precipitation southwest of the centre, a little further out than the location of the precipitation

maximum.

Fig. 4.10 shows the composite proportion of surface precipitation that is at least maybe attributable to convective and stratiform systems, again with the remainder on the right. This time, almost all rainfall events have been assigned a type, bar a handful of outliers. This looks much like an amplification of the signals in Fig. 4.9, except that the rainfall over/around the Himalayas has mostly been designated as stratiform (as we would expect). It is not obvious why we see the high ($\sim 50\%$ definite, $\sim 80\%$ maybe) stratiform allocation covering a significant area approximately 500 km southwest of the centre, as we might expect this to be quite convective. Given the stratiform allocation strongly relies on bright band detection, and we know one can exist there, even in the clearly convective regime closer to the centre (cf. Fig. 4.4 and Fig. 4.5), this could be tricking the algorithm into the wrong diagnosis. Houze (1997) discussed this apparent problem in some detail, but it is clear we should interpret the results displayed in Figs. 4.9 and 4.10 with due caution.

4.3.3 Diabatic heating: latent and radiative

MDs have dense cloud cover at all levels (Godbole, 1977; and see also Fig 3.10(c)) resulting in complicated radiative heating/cooling profiles, which, in this study, we will attempt to demonstrate. Further, the constant flux and phase changing of atmospheric moisture in MDs results in widespread latent heating/cooling. By far the most important phase transition in MDs is lower-tropospheric condensation of warm, water-vapour laden air rising from near the surface (with a secondary contribution from freezing in the mid-troposphere). It has long been proposed that this latent heat release is intrinsic to conditional instability of the second kind and is a potential source of energy for MDs moving over the ocean (e.g. Shukla, 1978). The CloudSat-derived radiative heating profile is shown in Fig. 4.11, and looks as we might naïvely expect from inspection of the cloud cover in Fig. 4.6 – substantial shortwave heating at and slightly beneath the cloud tops (particularly the thicker convective clouds), and long-

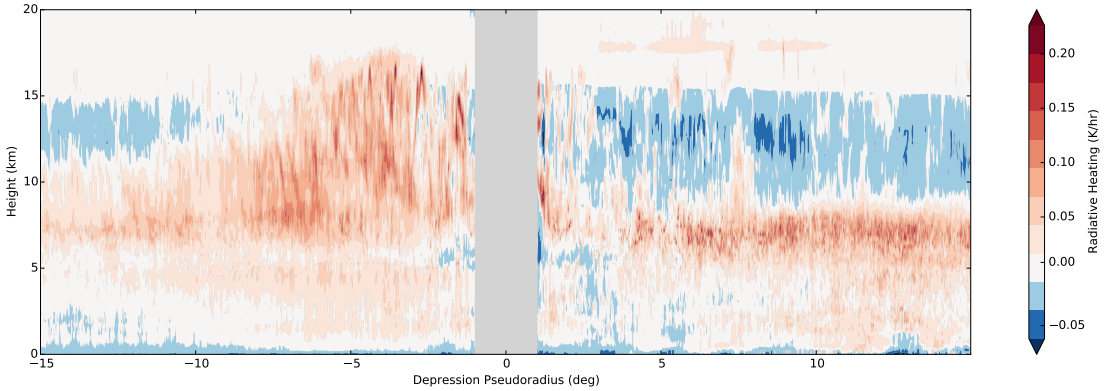

Figure 4.11: Composite vertical radiative heating profile (K hr^{-1}) within the MD from both longwave and shortwave radiation, derived from CloudSat 2B-FLXHR. Data removed as per Fig. 4.5.

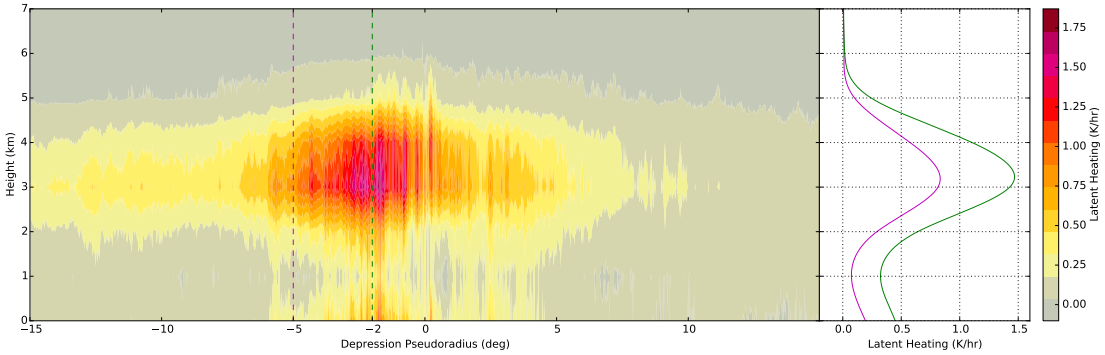

Figure 4.12: Left: composite vertical latent heating profile (K hr^{-1}) from hydrometeor fluxes within the MD as a function of pseudoradius, derived from TRMM 2B31. Right: two selected vertical profiles from the composite, -5° (magenta) and -2° (green). Note the short vertical axis due to negligible mean latent heating rate above the freezing level.

wave cooling elsewhere. The composite heating rates in the upper troposphere south of the centre can reach over 0.2 K hr^{-1}; this value is more than an order of magnitude less than what one might expect at the top of a tropical anvil (Ackerman et al., 1988), but still considerably more than the summer monsoon climatology (not shown). The small magnitude arises because, while the MD is dominated by instances of deep convection whose cloud tops are strongly heated, these vary in height and precise location, and are thus smoothed out in the composite. We will later evaluate this discussion in the context of a case study, in particular diagnosing the features of a large anvil structure.

We can use data from TRMM to inspect the composite latent heating profile, which

is given in Fig. 4.12. This figure also shows two 1D profiles through selected pseudoradii. We can instantly deduce that latent heating is the larger of the two diabatic heat sources in MDs, as it is in the tropics in general (Roca et al., 2010): the intense convective rain south of centre leads to a composite mean latent heating rate of as much as 1.8 K hr^{-1} in the mid-troposphere, supporting the warm-core found there in other studies (e.g. Godbole, 1977, and many others). Note the low-altitude maximum of 3 km ($\sim$ 720 hPa) is compatible with our earlier cloud profile retrievals, but surprising in the context of the vertical temperature structure of a depression, where the anomaly maximum is at around 400 hPa. We note that the case study of Douglas (1992b) suggested diabatic heating was dominant in MDs above 850 hPa with a maximum at around 550 hPa.

4.3.4 Reanalysis composite

We can use ERA-Interim reanalysis data to construct a few more useful composites and complete our discussion. Fig. 4.13 shows the structures of temperature anomaly, vertical velocity, and divergence from left to right respectively, and we can use these to develop the ideas introduced in this section so far. These reanalysis composites are constructed in the same way as those derived from satellite data previously in this study. The similarity of all three panels to those computed from the full three-dimensional composite technique used for MDs in Chapter 3 is a useful indicator that the pseudoradial method used here is robust. Summarising briefly, we have found that the region of maximum rainfall in MDs is colocated with a significant area of deep convection and intense low-tropospheric latent heating rates. There is no clear significant cloud structure to the north of the depression other than the presence of orographically-induced stratus, which are also associated with increased rainfall.

The leftmost panel in Fig. 4.13 shows the composite vertical temperature structure, taken as an anomaly to the June-September summer climatology. It bears some horizontal resemblance to the two diabatic heating fields discussed in the previous section, but this semblance is lost in the vertical. Monsoon depressions are roughly in thermal

wind balance, so we should not expect to be able to explain the gross thermal structure in terms of local heating rates (especially radiative), however it is not implausible that the strong latent heating in the lower middle troposphere warms air that is subsequently lifted by the deep convection in which it generally sits.

The next panel in Fig. 4.13 shows vertical velocity; this is provided by ERA-Interim as ω ($= \partial P/\partial t$), and has been converted to w ($= \partial h/\partial t$) here for convenience. There is a fairly strong similarity between this field and the observed cloud cover structure shown in Fig. 4.6 indicating (as expected) that much of this cloud is convective; we can further support this assertion by noting the maximum upward speed in the lower troposphere is colocated with the maximum rainfall rates (see Fig. 4.2) at each height. Finally, on the right, is a composite of divergence. Given the results so far, and in particular bearing in mind the theory suggested by Yoon and Chen (2005) that the rainfall asymmetry in a depression is controlled by low-level moisture convergence modulated by larger-scale monsoon variability, the fact that the rainfall and convergence maxima are not colocated is perhaps surprising. Given that the gradient of specific humidity across the depression is not steep enough to shift the moisture flux convergence maximum far from the air convergence maximum, moisture convergence is not the mechanism responsible for the asymmetry, in accord with the moisture trajectory analysis in Fig. 3.14 where we saw that the dominant moisture flux convergence terms in MDs were slightly asymmetrical, but not off-centre enough to correctly explain the precipitation maximum. Recalling, then, the three suggested theories for the precipitation southwest maximum in Mooley (1973), we can now rule out the hypothesis that the asymmetry is caused by an off-centre moisture flux convergence maximum. Further, inspection of Fig. 4.6 very strongly suggests that this phenomenon is not due to the westward axial tilt observed in some fields of the MD with height. Ruling these out leaves us with the hypothesis that this activity peaks southwest of the centre due to the cyclonic mixing (and subsequent forced ascent) of warm, humid air from the Arabian Sea with the cooler, drier, continental air mass. If this is correct, and assuming the cause is one

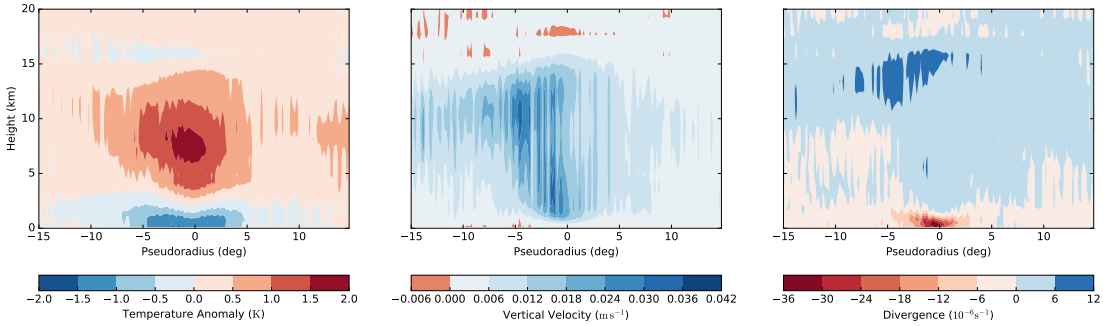

Figure 4.13: Several composite variables as functions of pseudoradii and height. Left: temperature (K) as an anomaly to the boreal summer mean, centre: vertical velocity (m s^{-1}, positive upwards), right: divergence ($10^{-6}s^{-1}$). Data are from ERA-Interim reanalysis for the composite.

of these synoptic mechanisms listed by Mooley (1973), this feature would be unique to the monsoon depressions of India; unfortunately a detailed study of rainfall in global monsoon depressions has not yet been carried out, but some case-study analysis of Australian monsoon depressions by Zhao and Mills (1991), and a more recent study by Berry et al. (2012) of objectively tracked Australian monsoon disturbances, suggests that this is indeed the case.

4.4 Case study

The nature of this research prompts a validation of the satellite products, both with each other and with independent data. For this purpose, we carry out a case study, which further benefits us with some validation of the composite discussed previously. We select an event where TRMM and CloudSat overpasses intersect near an MD centre within a short timeframe. The best such example was the MD of early July 2007, see Fig. 4.14: the overpass intersection was separated by 62 minutes at a distance of just 96 km from the depression centre. This figure also shows the locations of the sixteen gauge sites used for TRMM validation later in this section, as well as the total accumulated rainfall (if $>$ 20 mm) for the UTC day 07 July 2007, for which the depression started on the yellow marker and progressed westward by four markers.

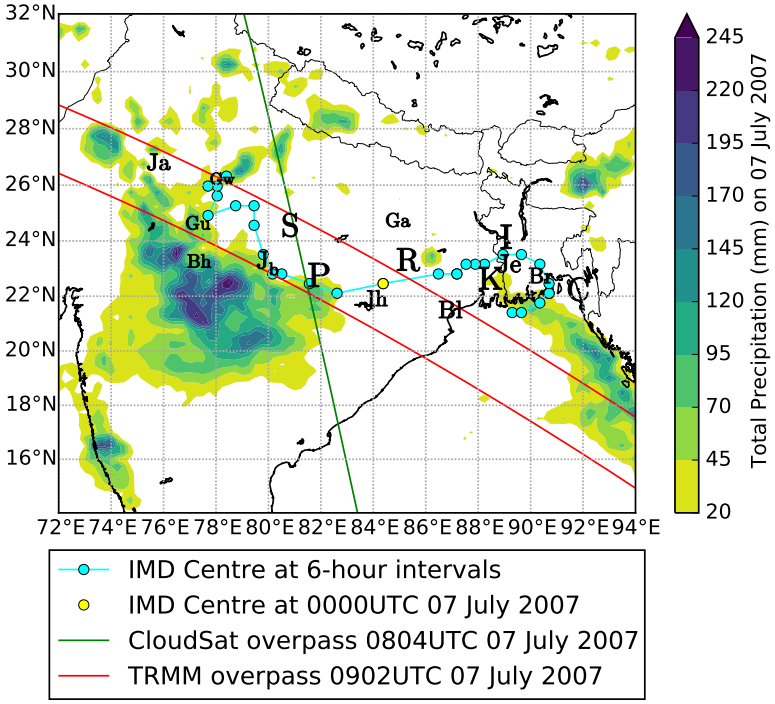

Figure 4.14: Path of the early July 2007 MD: 6 hourly intervals plotted in cyan markers, with the location at 0000UTC 07 July in yellow. The areas covered by the TRMM and CloudSat overpasses are bounded by red and green lines respectively. The locations of the 16 rain gauges used in the rainfall comparison are also shown, west to east they are: Jaipur (Ja), Guna (Gu), Bhopal (Bh), Gwalior (Gw), Jabalpur (Jb), Satna (S), Pendra Road (P), Jharsuguda (Jh), Gaya (Ga), Ranchi (R), Balasore (Bl), Kolkata (K), Ishwardi (I), Jessore (Je), Barisal (Br), and Chittagong (C). Overlaid (coloured contours, mm) is the total precipitation for the UTC day 07 July.

This shows well the propensity for an MD rainfall maximum to be southwest of the centre, which is in fact where almost all the heavy rainfall is; recall that the central India average daily rainfall in July is approximately 10 mm day^{-1}, and so even the *lowest* contour here is twice that value. Note also the presence of an unrelated storm over northeast India and the coastal rainfall associated with southeast Asia, as well as significantly enhanced rainfall over the Western Ghats as a result of the MD enhancing westerlies there. This pattern agrees with Fig. 3.3(b) where it is seen that depressions result in enhanced rainfall along the Western Ghats and along the coast of southeast Asia (among other areas).

The July 2007 event was a fairly typical MD in terms of duration, trajectory, genesis,

and dissipation (see Hurley and Boos, 2015; or the MD statistics that will be discussed in §5.2 and §6.2.1): spending some spin-up time at the head of the Bay of Bengal before making landfall in Bangladesh/northeast India, propagating parallel to the Himalayas before dissipating over northwest India. This makes it a good candidate for this case study, in that there is nothing unusual we should be aware of. We now have an idea of the basic footprint of this particular MD, and are in a position to look at the respective TRMM and CloudSat overpasses. Selected data from each are shown in Fig. 4.15, with TRMM in the top three panels, CloudSat in the next three, and ERA-Interim (following the CloudSat trajectory, but approximately three hours earlier). Each panel is directly analogous to a figure discussed in the previous section with the exception of the third-from-bottom subfigure, which shows the reflectivity (dBZ) measured by CloudSat. For each satellite the data are represented as projections onto the longest global coordinate axis for the overpass in question: latitude for the polar-orbiting CloudSat, and longitude for the 35° inclination TRMM. Since TRMM data are from finite-width swaths, these are meridionally averaged before projection. The location of the centre of the depression at the time of the overpasses was 22.5°N, 81.6°E, and these values on their respective axes in Fig. 4.15 should be taken as such - they are marked with a 'C'. Both overpasses indicate there is some activity directly over the centre, but that there is more intense activity several hundred kilometres away (distinct for each overpass). The data from CloudSat indicate that the centre sits under the edge of a very large anvil cloud whose shape is well captured; large radiative heating across the top and a strong (subsequently attenuated) reflectivity indicate the presence of dense, tall, cloud here. There is also evidence of some activity in the north too, with stratiform and orographic cloud present around the Himalayas. The TRMM overpass was slightly less fortunate with positioning, but still captured some interesting features: a convective bloom approximately 500 km to the west of the depression, some activity associated with the centre and an area to its north, and the coastal rainfall of southeast Asia. All three areas demonstrate convective activity, but the area north of the MD

centre has the weakest: we might expect this given the previous analysis, but even so, there are rainfall rates here of up to 10 mm hr^{-1} driving latent heating of the order of 10 K hr^{-1}. We cannot say with certainty that the deepest convection (in the northwest) is necessarily associated with the depression, but inspection of Fig. 4.14 suggests that it is probable.

The inclusion of some almost contemporaneous ERA-Interim data, nearest-neighbour-interpolated to the CloudSat ground track, permits us to make some general comments on the thermodynamical interpretation of these fields. Firstly, we must note that ERA-Interim has a fairly coarse spatial and temporal resolution: the latter constraint requires us to choose the 1200Z fields, nearly three hours after the relevant CloudSat overpass; this discrepancy will cause some apparent displacement when comparing fields from both. Secondly, we also note that the temperature field is taken as anomaly to the June-September climatology, computed on a gridpoint-by-gridpoint basis. In both reanalysis fields presented in Fig. 4.15 the forms quite closely resemble the gross composite structures computed in §3.4, however, there are also some distinctive features to remark upon.

With some confidence, we can associate the strong vertical lifting at approximately 22°N with the deepest convection, but we also note that much of that same anvil is collocated with lifting confined to the lower troposphere and is flanked by large areas of upper/mid-tropospheric subsidence that appear to be suppressing convection; there is also a deep anomalously warm core aloft with large spatial extent, overlapping both the deep convection and the surrounding area of descent. The large spatial extent of the depression - examination of the anomalous zonal wind (not shown) indicates that 10 m s^{-1} isosurfaces reaching beyond the 15th and 30th parallels - makes it highly plausible that the anomalous ascent at the Himalayan foothills and resulting cloud structure there is also directly related to the circulation of the MD.

The individuality of this MD shows that the results of Section 4.2.2 should be treated as a composite, not a 'mean-state' depression, as can be done for less spatially

variable fields. We can, however, create a composite representation showing the mean when the field is non-zero alongside the probability that that is the case (e.g. the mean rain rate when there is rain, and the overall probability of rain for that location). If we do this, we find two things: firstly, that the shape is very similar with the small exception of a more prominent local extremum at the centre; and secondly, the magnitude of all hydrometeor and diabatic heating fields roughly doubled. The first point supports usage of the composite in the form given throughout this study, as the main source of structure in it is the magnitude of the fields, not the probability of activity at that location.

Now that we have an instantaneous snapshot of this depression, we can further our understanding by examining how its passage affects the atmosphere around it using observational data. Such analysis is fairly rife in literature on a case-study by case-study or small composite basis (e.g. Koteswaram and George, 1960; Krishnamurti et al., 1975, 1976; Daggupaty and Sikka, 1977; Godbole, 1977) and aids understanding of the dynamics involved. The MD in question passed almost directly over a sounding station at Ranchi (see Fig. 4.14), whose daily soundings are observed at 0000UTC. Tephigrams presenting these data are displayed in Fig. 4.16. As expected, they show a typically warm, moist, tropical atmospheric profile with strong vertical wind shear. As the MD passes overhead, the winds strengthen and moisture is carried a lot higher in the troposphere - the entire profile is almost saturated - and significant instabilities have developed, evidenced by the numerous inversions throughout[2]. Note that the superadiabatic layer between 850 and 800 hPa in Fig. 4.16(b) is likely specious and an instrument error. The sounding from the morning after the MD passed overhead (Jul 8) possesses the strongest winds (agreeing with the composites in Figs. 3.4 and 3.12(b)), but is also several degrees warmer since the moisture packed into the column

[2]The humidity (and to a lesser extent, temperature) sensors used in standard soundings generally used by the IMD have a fairly slow response, so it is important to note that the shape of the profile could be an artefact of the sensor becoming wet as it passes through multiple cloud layers. However, if this were a common issue, we would expect many soundings from the area to appear structurally similar and in general this is not the case.

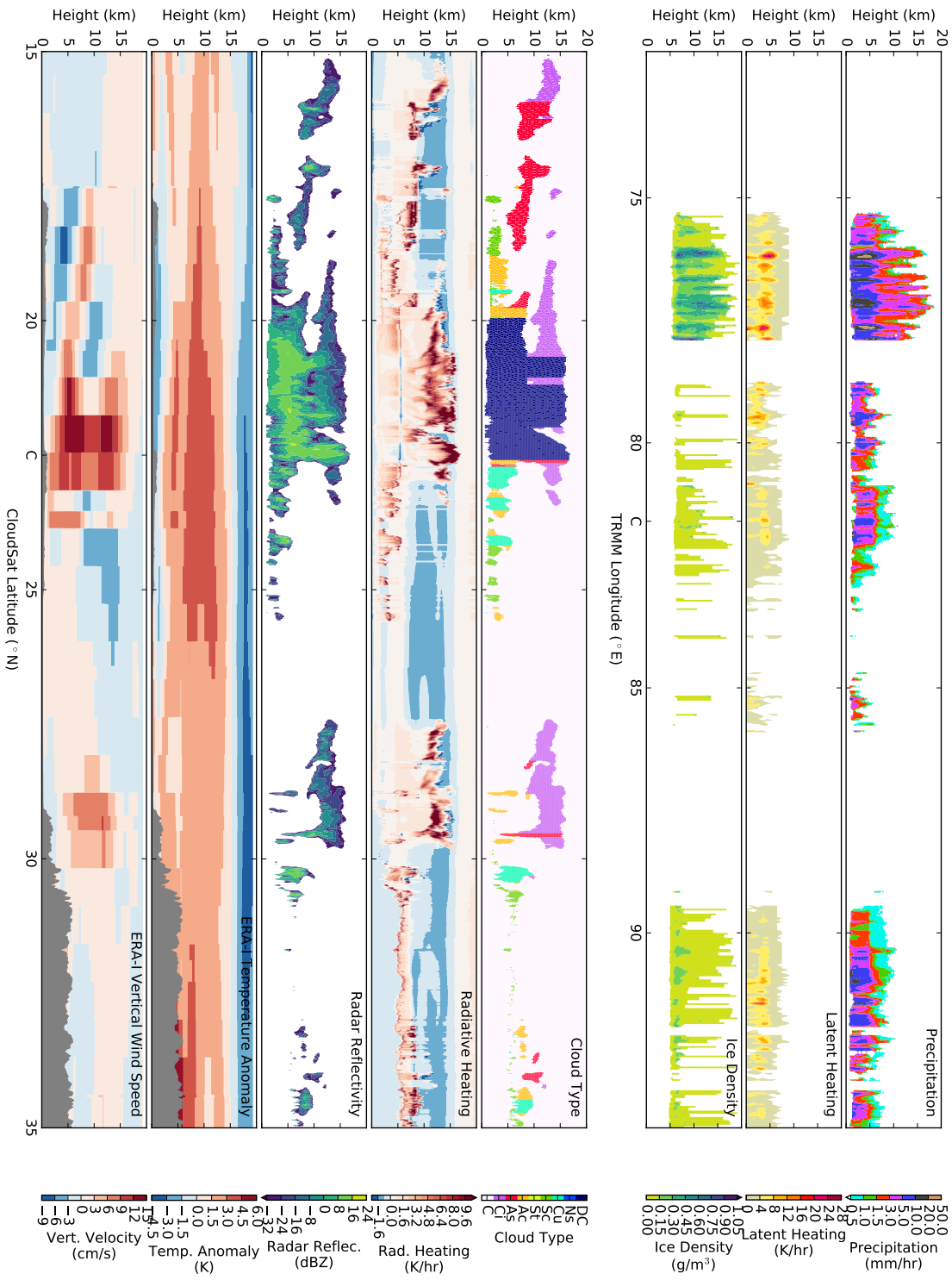

Figure 4.15: Selected data from the TRMM and CloudSat overpasses designated in Fig. 4.14; the bottom two panels are 12Z ERA-Interim data taken as close as possible to the CloudSat overpass path. 'C' on each abscissa marks the location of the centre of the depression at the time of the overpass. Where ERA-I data would be subterranean, they are greyed out.

during the previous day rains out, and the thick cloud clears.

We conclude this section with a a brief validation of the TRMM 3B42 surface rainfall product against some station gauge data. This will, in general, help validate the composite image developed by providing some assurance that the presence of the depression does not cause TRMM to wildly misestimate the rainfall. Such evaluation has been covered in much greater detail for tropical cyclones by Chen et al. (2013) and over orography by Dinku et al. (2007, 2008, 2010); the former found that TRMM underestimated rainfall in tropical cyclones, particularly over land or near orography, the latter found that TRMM performed well over most orography, but with decreasing skill as the topography became more complex. For our evaluation, we will consider the mean and variance of both TRMM 3B42 and gauge-measured rainfall at the sixteen stations presented in Fig. 4.14 over the first half of July 2007. To use TRMM to estimate the daily rainfall accumulated at each station (reproducing the daily gauge data), we took the appropriate pixel ($0.25^\circ \times 0.25^\circ$) from TRMM 3B42 and averaged over the eight relevant three-hourly values. This and the gauge rainfall are shown in Fig. 4.17. Further, as not all stations reported rainfall (zero or otherwise) on all days, the equivalent data were also masked in TRMM. Assuming the gauge data is true, the pattern and variance is captured well by TRMM, however the magnitude is underestimated by as much as 30% on average during the most intense rainfall. This value is in close agreement with that found by Pokhrel and Sikka (2013) for gridded TRMM PR values over the whole peninsula and surrounding ocean. The data from a selection of individual stations along the MD path are presented in Fig. 4.18, they show both the clear westward propagation of the system and the consistency of rainfall underestimation by TRMM.

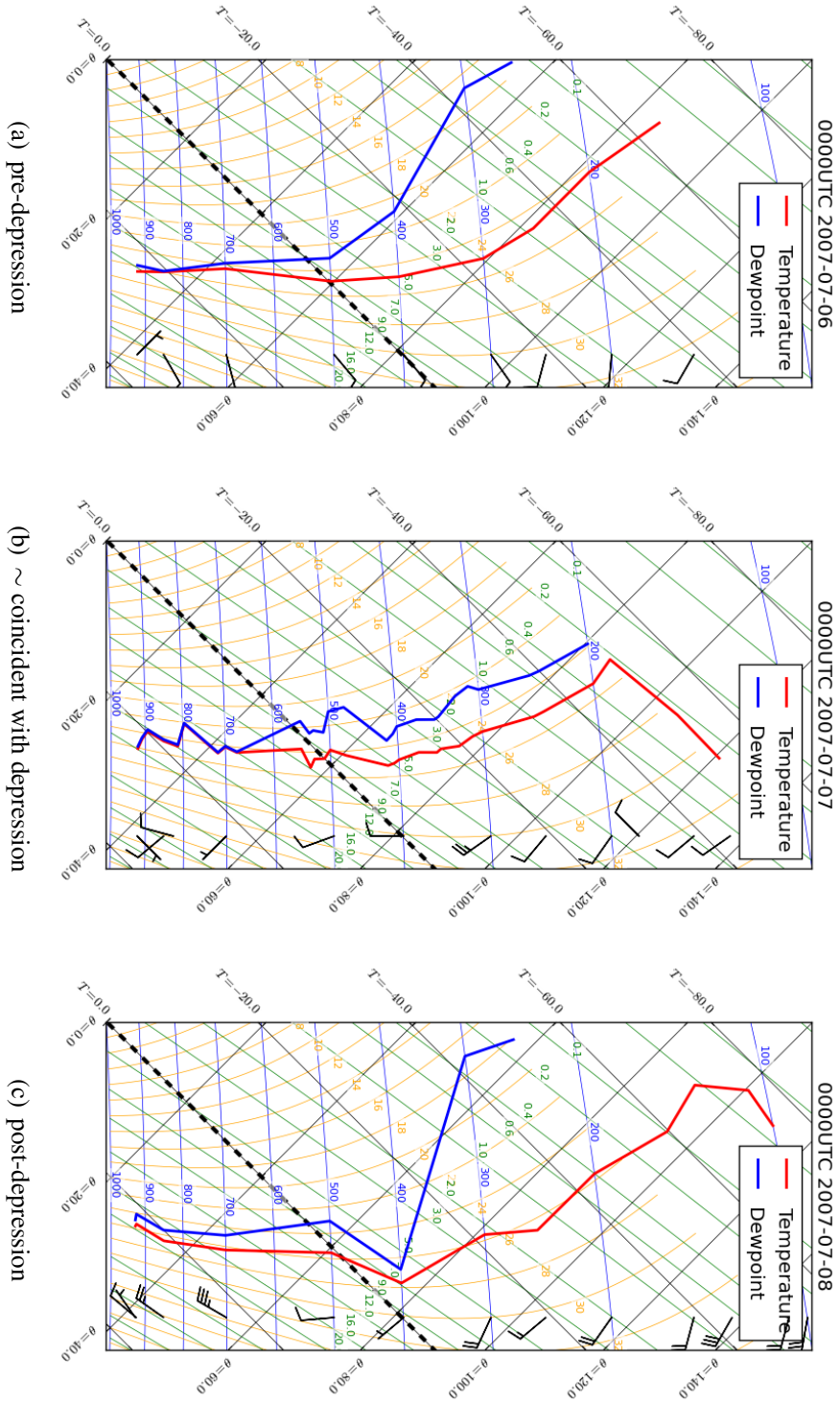

Figure 4.16: Tephigrams for soundings from three consecutive days at Ranchi station (see Fig. 4.14). Red and blue lines show temperature (K) and dewpoint (K) profiles respectively, and on the right of each tephigram, the wind barbs (m s^{-1}) are shown in black. Where ERA-Interim data would be below the surface, they are greyed out.

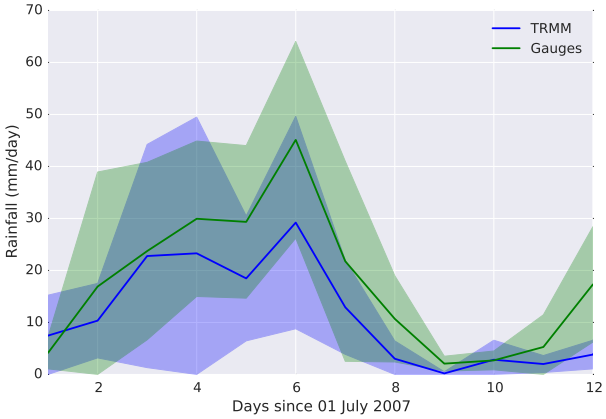

Figure 4.17: Comparison of the average daily precipitation (mm day^{-1}) recorded at the sixteen stations shown in Fig. 4.14 during the depression of early July 2007. Gauge values are given in green, TRMM 3B42 estimates are given in blue. Each shown with a 1σ band. Where gauge measurements were missing, TRMM data were also omitted from the average.

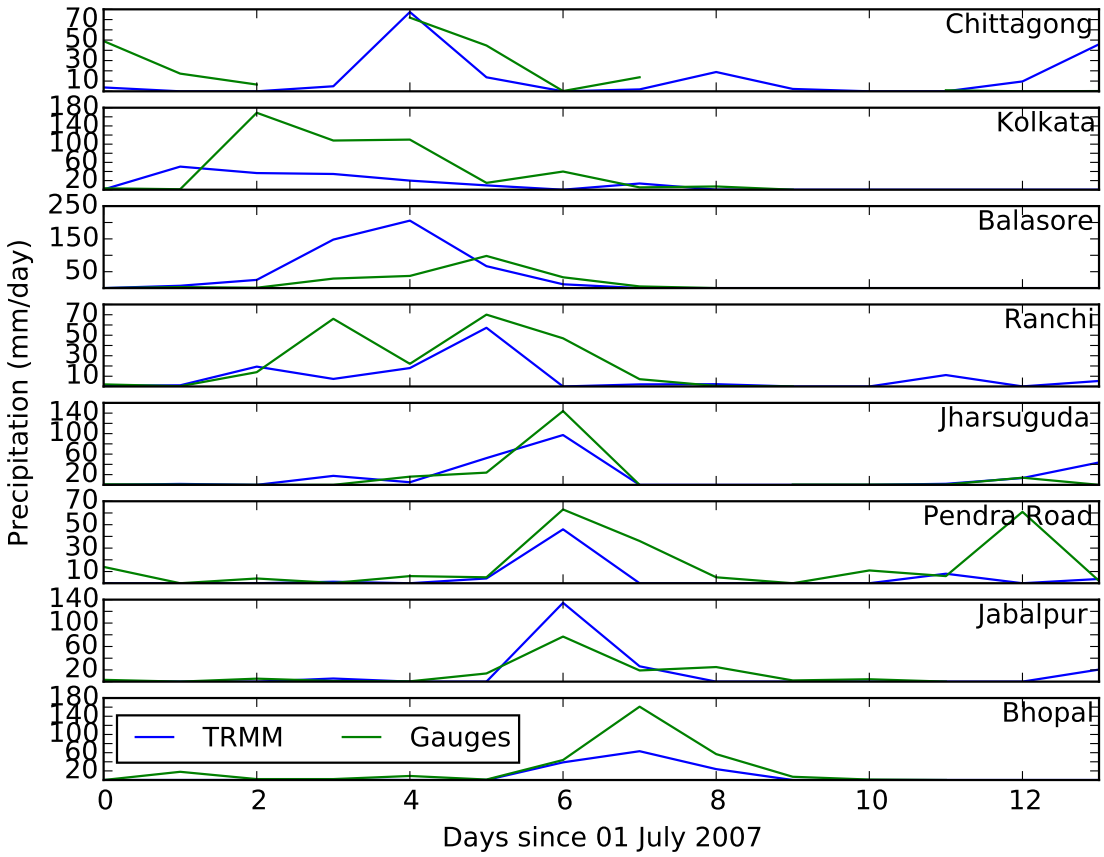

Figure 4.18: Daily precipitation (mm day^{-1}) for eight selected stations along the path of the depression in early July 2007, approximately from east to west. Gauge values are given in green, TRMM 3B42 estimates are given in blue.

4.5 Diurnal variability

It is well known that the day-night cycle drives marked changes in the atmosphere, and it is reasonable therefore to surmise that there will be some diurnal cycle in the thermodynamics of MDs. The better we can quantify this finer-scale variability, the more we can design our NWP models to provide higher quality forecasts. Yet surprisingly, discussion on the diurnal variability of MDs is almost non-existent in the literature. In §3.5.3, we showed that there is a significant contrast between depressions during the day and at night: during the day, MDs are warmer and drier throughout, with a sizeable reduction in low-level cloud cover at the centre.

Recently Bowman and Fowler (2015) used surface rainfall data from TRMM 3B42 to perform a detailed investigation the diurnal cycle of precipitation in a global catalogue of tropical cyclones (IBTrACS, Knapp et al., 2010). They found the amplitude to vary unimodally over the diurnal cycle with a maximum 7% greater than the mean centred at approximately 0600 local time. We are now in a position to repeat this analysis for the composite MD, as shown in Fig. 4.19. This is performed on the rotated composite because this filters out the diurnally-varying land/sea-breeze related coastal rainfall contribution from southeast Asia. The most immediate feature in Fig. 4.19 is the diurnal cycle of the central maximum, which has a peak at 0000UTC (0530IST[3]). The surrounding rainfall also varies diurnally, but out of phase with the central maximum, similar to the land-ocean contrast in the cycles displayed by the rain resulting from tropical convection (Nesbitt and Zipser, 2003; Kikuchi and Wang, 2008).

The thermodynamics behind both types of diurnal cycle are already well understood. Tropical convective precipitation over land peaks in the late afternoon as the result of a number of coupled processes, but can be thought of most simply as cumulative surface heating from insolation generating maxima in sensible and latent surface heat fluxes, promoting static destabilisation (e.g. Byers and Braham, 1948; Ogura and Takahashi, 1971; Bechtold et al., 2004; Hirose and Nakamura, 2005). In contrast, the

[3]Indian Standard Time

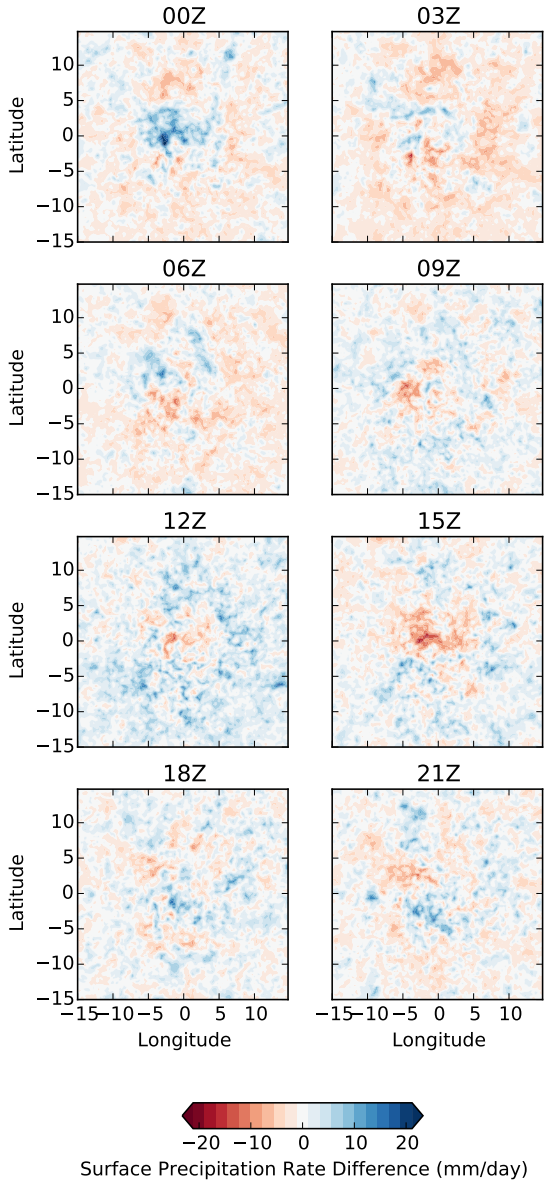

Figure 4.19: Composite rotated structure of surface precipitation rate ($\mathrm{mm\,day^{-1}}$) in MDs at three hour intervals across the UTC day as anomaly to the mean, derived from TRMM 3B42.

diurnal cycle of tropical cyclone precipitation is a result of the enhanced nocturnal radiative cooling of anvil cloud tops destabilising the upper troposphere (e.g. Kraus, 1963; Tripoli, 1992), an effect whose magnitude peaks around local dawn.

We propose that these fields can be simply modelled by fitting a sum of two arbitrarily-phased two-dimensional Gaussian functions with some climatological offset

(or residual), of the form:

$$P(x,y) = P_{\text{residual}}(x,y) + \sum_{n=0}^{1} A_n \exp(-\begin{bmatrix} x - x_{o,n} & y - y_{o,n} \end{bmatrix} \begin{bmatrix} \frac{\cos^2\theta_n}{2\sigma_{x,n}^2} + \frac{\sin^2\theta_n}{2\sigma_{y,n}^2} & \frac{\sin 2\theta_n}{4\sigma_{x,n}^2} - \frac{\sin 2\theta_n}{4\sigma_{y,n}^2} \\ \frac{\sin 2\theta_n}{4\sigma_{x,n}^2} - \frac{\sin 2\theta_n}{4\sigma_{y,n}^2} & \frac{\sin^2\theta_n}{2\sigma_{x,n}^2} + \frac{\cos^2\theta_n}{2\sigma_{y,n}^2} \end{bmatrix} \begin{bmatrix} x - x_{o,n} \\ y - y_{o,n} \end{bmatrix}), \tag{4.1}$$

where P is the observed spatial distribution of the precipitation, P_{residual} is the difference between the observed rainfall and the fitted function, n is an index for the two Gaussian functions, σ_x and σ_y refer to the standard deviation of the Gaussian along the x and y axes respectively, (x_o, y_o) are the coordinates of the centre of the Gaussian, and θ is its rotational phase. We can fit these parameters to our rotated (e.g. Catto et al., 2010) data using the Levenberg-Marquadt algorithm (Levenberg, 1944; Marquadt, 1963), which interpolates between the gradient-descent and Gauss-Newton methods, and is a common algorithm for least squares curve fitting. Although rotation smooths the precipitation pattern (reducing derived intensities, see Fig. 4.1), there is no significant dependence of MD propagation direction on the time of day, so calculations of the relative diurnal cycle will not be affected. Performing this analysis on the rotated composite yields a stable convergence for the fitting algorithm and a robust final fit; indeed, we recover both modes of the diurnal cycle, (Fig. 4.20). The distribution given by this fitted function passes a Pearson's chi-squared goodness-of-fit test at a 95% confidence interval when compared with the observations.

It is evident that the two modes are very much in antiphase, and that the central mode is always responsible for the more intense rainfall: it has a mean value of 25.0 mm day^{-1} compared to 12.1 mm day^{-1} for the outer mode. However, both modes have a similar variability: 70% and 64% peak-to-trough for the central and outer modes respectively. These values are markedly larger than that quoted by Bowman and Fowler (2015) for tropical cyclones because we are considering two distinct modes varying in

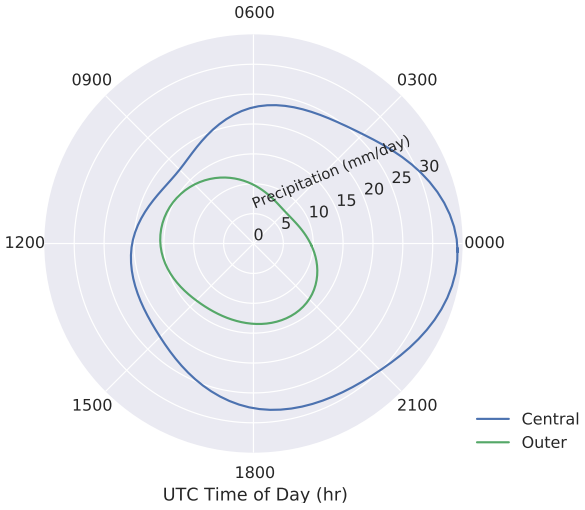

Figure 4.20: Amplitudes of the two diurnal modes of surface precipitation (mm day^{-1}) in the rotated composite, derived from TRMM 3B42.

antiphase, but even if we only fit one Gaussian across the cycle we still recover a diurnal cycle with peak-to-trough variability of 36% and a maximum at 0000UTC. We have shown, therefore, that MDs exhibit substantially greater diurnal variability in surface rainfall than tropical cyclones, and that there are two main processes responsible for this precipitation. Further work is needed to determine to what extent these modes are coupled.

Analysis of the unrotated composite by EOF (empirical orthogonal function) decomposition shows that the diurnal cycle discussed here is the principal mode of variability; the second most dominant mode manifests as an east-west translation of the location of maximum rainfall which also varies on a diurnal cycle: eastmost at 0000UTC, westmost at 1200UTC. This could be due to the zonal gradient of heat flux from the ground as maximum insolation moves westward throughout the day, or some more complicated Rossby wave dynamics via land-sea thermal contrast.

4.6 Conclusions

Indian monsoon depressions are relatively long-lived tropical lows that usually cross central India several times each summer. They are exceptionally moist synoptic-scale systems that often drastically increase precipitation in north and central India during

their passage across the subcontinent. So, a description of the precipitating processes and moist thermodynamics of MDs is important for scientific understanding and the evaluation of climate and NWP models, so that their potential impact on the urban and agrarian cultures in flood-susceptible areas can be better constrained. The method presented here provides a basis whereby MDs in NWP models and GCMs can also be composited and subsequently evaluated.

This is the first such detailed study to use satellite data to bring forward a composite image of these processes, and therefore provides a number of novel results to this field. We have confirmed the long-known presence of a surface rainfall maximum several hundred kilometres southwest of the centre, and attributed it to colocated deep convection. We have shown that this area of convection is substantial, both in the composite, and in a case study, extending for upwards of 500 km from near the centre towards the southwest. We have also shown that the hydrometeor structure is far less symmetric than previously assumed, rain to the north of the centre is up to an order of magnitude less than that found at the same radius south of the centre, and deep convection is entirely absent as a significant process in the north: almost all precipitation is stratiform, driven by interaction with the orography of the Himalayan foothills.

We have shown that MDs have consistently deep convection colocated with the area of maximum precipitation, covering a significant region. Within this, the highest raindrop density is found, directly beneath the highest densities of snow and graupel. The largest raindrops, however, are found at the centre, where, in the comparatively uncommon event of convection occurring, the highest rainfall rates can also be found. Outside of the centre, the raindrop size distributions tend to be uniform with height up to about 5 km, implying that these areas are well mixed. To the south of this deep convection, we have shown the cloud structure to be typically tropical, whereas to the north of the centre it is far more orographically driven.

Our case study shows that the presence of an MD can set up multiple instabilities in the atmosphere and saturates the troposphere up to 600 hPa. Using this example, we

also compared TRMM-based surface rainfall estimates to station gauge-based estimates along the MD track, finding that TRMM 3B42 can significantly underestimate the higher rainfall rates associated with MDs: the highest rainfall rates were underpredicted by 30%.

We discovered and quantified a bimodal diurnal rainfall cycle in MDs: an uncoupled, antiphase cycle with a central mode (associated with the maximum precipitation in the southwest, peak-to peak variation 70%) and an outer mode (associated with the general convective precipitation across the MD, peak-to-peak variation 64%). A full understanding of these dynamical features will require detailed regional simulations with high resolution models.

Further work is now needed to look at the mechanisms responsible for the decay and ultimate dissipation of depressions; what is responsible for the zonal shift of the precipitation maximum across the diurnal cycle; and how convection parameters in numerical models affect their propagation and duration.

In this chapter and the previous one, we have presented a detailed analysis of the structure of MDs and how it varies subject to a variety of factors. As mentioned in Chapter 1, part of the ultimate motivation behind this work is to assess and improve the representation of MDs in NWP models and GCMs; the discussion on structure and variability is a crucial part of this, but we must now strive to understand the mechanism by which these systems propagate to move towards a more complete understanding. In the next chapter, we will propose a simple mechanism and compare it with some similar existing theories.

CHAPTER 5

THE MOVEMENT OF INDIAN MONSOON DEPRESSIONS BY INTERACTION WITH IMAGE VORTICES NEAR THE HIMALAYAN WALL

5.1 Introduction

We showed in Chapter 3 that MDs have their genesis over the northern Bay of Bengal, before propagating towards the west, parallel to the Himalayan massif, and against the direction of the climatological mean flow (see Fig. 5.1). Although the forecasting of these systems is of profound importance, due to the enhanced rainfall which they bring during the monsoon season, their dynamics remain relatively poorly understood. In particular, their basic mode of propagation, against the mean flow, has not until recently been adequately explained. Boos et al. (2015) presented the movement of MDs in terms of the advection of the potential vorticity maximum at 500-450 hPa, above the MD core. At these levels the mean flow is more clearly easterly and the PV structure of the MD can be seen to be advected by the local flow, which includes an additional north-westward component from adiabatic potential vorticity beta drift, rather than the previously established theory of quasi-geostrophic lifting and downshear

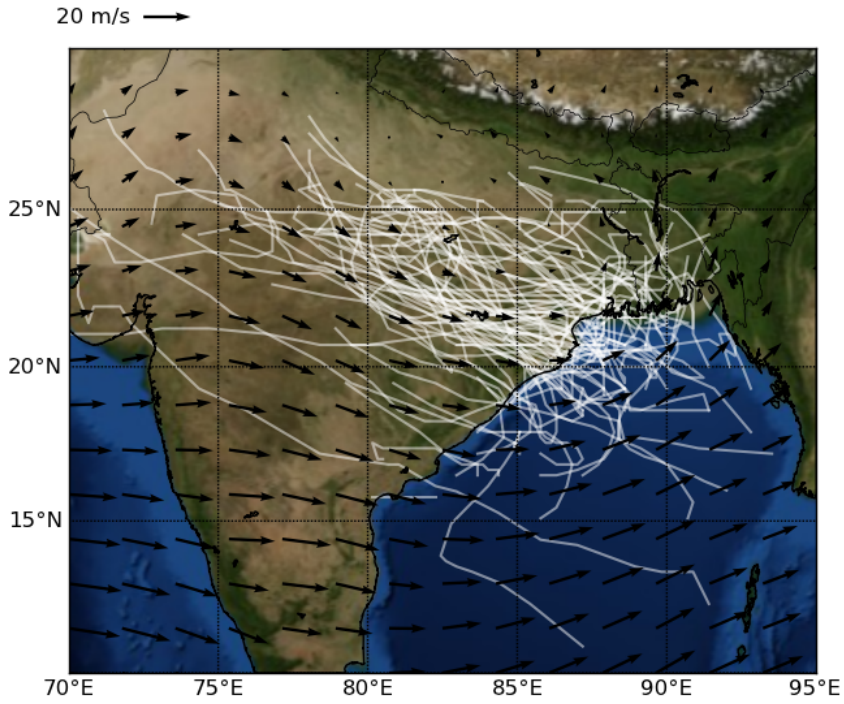

Figure 5.1: Mean boreal summer (JJAS) 850 hPa wind vectors with MD tracks 1979-2013 overlaid in white.

vortex stretching (Sanders, 1984; Chen et al., 2005). Previously, Goswami (1987) had presented this movement as frictional convergence and cumulus heating of a Rossby wave gyre causing vortex stretching to the northwest of the MD, however he did not consider contributions from dynamical uplift and incorrectly predicted a precipitation maximum in the northwest.

Here we propose another, probably complementary first-order explanation for the direction and speed of propagation of MDs, in terms of the interaction of their vorticity structure at low levels with the neighbouring "wall", represented by the Himalayas. We approximate the Indian Monsoon Depression (MD) as a point vortex in two-dimensional flow. Whilst baroclinic processes play a significant rôle in monsoon depressions (Krishnamurti, 1985), a barotropic model remains a good approximation, if we assume the depression winds do not vary much with height in the lower troposphere and that tem-

perature is not advected. This is justifiable because most of the relative vorticity of an MD is confined to a small region at its centre (see (Godbole, 1977) and Fig. 3.12(c)). Poor representation of orography in climate models has previously been blamed for biases relating to MDs (Stowasser et al., 2009). Two-dimensional flow is only strictly accurate for systems in which horizontal divergence is small and vorticity generation by stretching is weak relative to advection. Monsoon depressions are typically tall and narrow, with high Burger number (Bu=NH/fL, where H and L are vertical and horizontal length scales, and f is the Brunt-Väisälä frequency), meaning that the influence of their potential vorticity structure on the ambient flow should be dominated by horizontal circulation rather than vertical stratification (e.g. Hoskins and James, 2014, p.339). However, vorticity tendencies due to stretching remain significant (Boos et al., 2015). Previous authors (see Krishnamurti, 1985) have shown that baroclinic effects in monsoon depressions are in fact strong, and undoubtedly the effects of deep convection in the monsoon system introduce significant vorticity tendencies in the environment of a monsoon depression. Therefore we must see the 2D model as a highly idealised system, which neglects some important tendencies related to vorticity generation by stretching, but from which we can nevertheless hope to build dynamical insight into certain physical processes.

Invoking this approximation, we define the point-vortex vorticity field:

$$\omega = \kappa \cdot \delta(x - x_{\mathrm{v}})\delta(y - y_{\mathrm{v}})\,, \tag{5.1}$$

where κ is the circulation, δ is the Dirac delta-function, and (x_{v}, y_{v}) is the location of the vortex. The circulation, κ, around a point vortex, vorticity ω, is given by:

$$\kappa = \oint_{\partial S} \mathbf{v} \cdot d\mathbf{l} = \iint_{S} \omega \cdot d\mathbf{S}\,, \tag{5.2}$$

where $\mathbf{v}$ is the flow velocity vector field, $d\mathbf{l}$ is an element of the closed line boundary ∂S to the surface S through which the vorticity vectors pass and $d\mathbf{S} = \mathbf{n}dS$, where $\mathbf{n}$ is

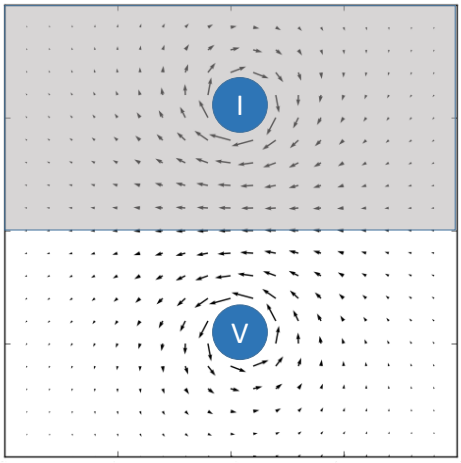

Figure 5.2: Flow around a pair of counter-rotating ideal point vortices, identical to an ideal point vortex, V, and its corresponding image vortex, I, in the image plane (grey).

the unit vector normal to S. In the case of a point vortex in two-dimensional flow (the approximation to which we will consider), $\mathbf{S}$ is chosen to be coplanar with the fluid.

To represent interaction with the orography, we make an approximation of the Himalayas as a vertical plane (normal to the surface) and impose the resulting boundary condition of no normal flux. We can make use of the standard result (e.g. Batchelor, 2000) that such a boundary condition is satisfied by replacing the plane with an equal and opposite image vortex (of strength $-\kappa$), whose location is the point of reflection of the original vortex in that plane. If the projection of the vertical plane onto the surface is given by $ax + by + c = 0$, then the location of the required image vortex is $-((by_{\mathrm{v}} + c)/a, (ax_{\mathrm{v}} + c)/b)$. The resulting flow around each vortex causes the other vortex to be advected parallel to the wall, as indicated in Fig. 5.2. We also note the intensification of winds on the "Himalayan" side of the vortex. This appears to be at variance with the findings of Godbole (1977), who found that winds to the south of the depression centre were stronger than to the north; however, this discrepancy is reconciled immediately when we subtract the background monsoonal flow, as shown in Fig. 5.3. This flow exhibits a strong meridional shear which significantly amplifies westerlies south of the MD centre.

The velocity field due to each point vortex is

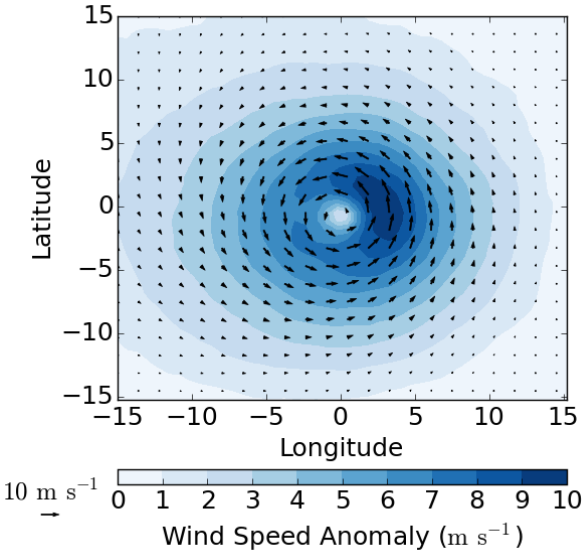

Figure 5.3: Composite 850 hPa MD winds with the boreal summer climatology subtracted (as Fig. 3.4(b)). In this composite, the data for individual time steps are rotated such that the direction of propagation is due north (up the page) and translated such that the centre is at 0°N, 0°W on a regular lat/lon grid. Here, therefore, the Himalayas lie to the right.

$$\begin{bmatrix} u \\ v \end{bmatrix} = \frac{\kappa}{2\pi r^2} \begin{bmatrix} -(y - y_\mathrm{j}) \\ (x - x_\mathrm{j}) \end{bmatrix} , \tag{5.3}$$

where $r = \sqrt{(x - x_\mathrm{j})^2 + (y - y_\mathrm{j})^2}$ is the distance from vortex j. Thus, in the absence of background flow, our point-vortex representation of an MD will propagate westwards, parallel to the Himalayas, at a speed

$$v_\mathrm{l} = \kappa / 4\pi R, \tag{5.4}$$

where R is the distance between the vortex and boundary representing the mountains. Incorporating the existence of a background flow (see Fig. 5.1), $\mathbf{v_{flow}}$, gives the following expression:

$$\frac{|\mathbf{v} - \mathbf{v_{flow}}|}{v_\mathrm{l}} = 1 , \tag{5.5}$$

where we have introduced the notation $\mathbf{v}$ for the propagation vector of the vortex. Therefore, if an MD behaves like a point vortex adjacent to the Himalayan "wall", the

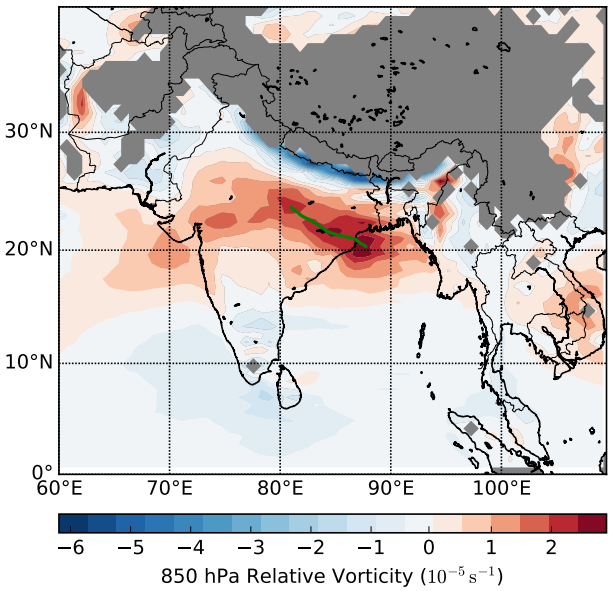

Figure 5.4: Modified from Fig. 3.28, 850 hPa relative vorticity (10^{-5} s^{-1}) on June-September depression days as an anomaly to the boreal summer mean; greyed out where the orography is higher than the 850 hPa level. The green line represents the average path of tracked depressions.

expression on the left of (eq. 5.5) should evaluate to 1.

By examining the rôle played by the Himalayas in the general presence of depressions (see Fig. 5.4), it could be argued that the shape of the Himalayan wall shows significant curvature and may be better approximated by a cylinder, than by a simple plane intersecting the horizontal level. The motion of a point vortex adjacent to a cylindrical barrier can also be computed using image vortices, using the method of Milne-Thomson (1940) (described in Batchelor (2000)), and in this case two image vortices are needed; one of strength κ at the centre of the cylinder, and one of strength $-\kappa$ at an image point of the real vortex, inside the cylinder. From these we obtain the following relationship for the motion of the point vortex:

$$\frac{|\mathbf{v} - \mathbf{v}_{\text{flow}}|}{v_{\text{cyl}}} = 1\,, \tag{5.6}$$

where a is the radius of curvature of the cylinder and

$$v_{\text{cyl}} = v_{\text{l}} \cdot \left[\left(1 + \frac{r}{a}\right)\left(1 + \frac{r}{2a}\right)\right]^{-1} \tag{5.7}$$

For a full derivation, see Appendix B. Therefore, this correction factor for curvature of

the Himalayan wall acts to reduce the resulting speed of the point vortex.

5.2 Data and methods

For the purposes of calculating circulation, relative vorticity data were collected from the 850 hPa level, as that is where the vorticity and wind speed maxima tend to occur (see Fig. 3.12). We have used 1-arcminute resolution data from ETOPO1 (`https://www.ngdc.noaa.gov/mgg/global/global.html`) to find the regions within the southern Himalayan foothills where the orography rises above 850 hPa (1.5 km). For the sake of the linear model, a least-squares linear regression of these points suggests that the linear Himalayan wall has a direction parallel with 282° ; for the cylindrical model, a least-squares circle fit gives the wall a radius of curvature of 2570 km centred at 89.1°N, 44.7°E. Note that here, and throughout this study, we measure direction as a bearing clockwise from due north (i.e. due west is 270°).

For each six-hourly timestep of reanalysis data that contained an MD, we define the propagation vector as the mean velocity vector connecting the present MD location with its location in the previous timestep (i.e. if the depression has travelled 3.6 km due west during the previous six hours, its propagation vector[1] will have magnitude 1 m s^{-1} and direction 270°). We also define the climatological 850 hPa wind vector co-located with the depression centre by taking the value of 21-day running mean wind fields (analogous to the method of Hurley and Boos, 2015) at the location of the MD centre. Resolving the climatological wind vector onto the direction of the propagation vector (i.e., computing $|\mathbf{v_{flow}}| \cdot \cos(\alpha)$, where $\mathbf{v_{flow}}$ is the climatological wind vector and α is the difference in angle between $\mathbf{v_{flow}}$ and $\mathbf{v}$, the propagation vector) for each timestep gives a mean value of -3.15 m s^{-1}; indicating that MDs generally travel in a direction opposing the ambient flow. This indicates the importance of including $|\mathbf{v} - \mathbf{v_{flow}}|$ in our calculations.

[1]The propagation speed for each MD timestep is actually calculated by dividing the great circle distance between its start and end points by its duration (6 hours).

For comparison with our model, we present three simple alternative models: a climatological model and a pair of beta-drift models. For the climatological model, which is intended as a basic benchmark for variability, we simply make the assumption that all MDs at all times travel at the average MD velocity (that is to say, we take the mean propagation vector, 1.66 m s^{-1} on 332°, and assert that all MDs should have this velocity at all timesteps).

For the beta-drift models, we assume that MDs propagate as cyclones advecting higher-latitude planetary vorticity from the north to west of the centre. We therefore expect that if MDs propagated using this mechanism they should also travel northwestward. There are then two options, both of which are carried out here, when considering the background wind: we either include it directly in the calculation (referred to hereafter as 'beta drift + flow') or we subtract it from the result (referred to hereafter as 'beta drift')[2]. For these, we shall use a modified Rankine vortex of the form:

$$v_\theta(r) = \begin{cases} C_1 r & \text{if } r < r_m \\ C_2 r^{-\sigma} & \text{if } r \geq r_m \end{cases} \tag{5.8}$$

$$v_r(r) = -\lambda v_\theta \,, \tag{5.9}$$

where C_1 and C_2 are arbitrary constants related to intensity, r is the distance from the centre, σ is a structure parameter, λ is a horizontal convergence parameter, r_m is the radius of maximum wind speed, and v_θ and v_r are the azimuthal (clockwise positive) and radial (outward positive) components of wind speed respectively. For the MDs in our dataset (1526 six-hourly timesteps over 106 depressions), the value of the convergence parameter is typically positive (as expected) but close to zero: averaging 0.06 with a standard deviation of 0.18; the structure parameter has an average of 0.83 and a standard deviation of 1.59, compared with 0.5-0.6 for tropical cyclones (Leslie and

[2]To clarify, this is different from the mechanism proposed by Boos et al. (2015), which is horizontal nonlinear advection of the mid-level (500 hPa) potential vorticity maximum.

Holland, 1995), and exactly 1 for the point vortex. Both parameters were calculated for each timestep by using logarithmic and linear regressions respectively for the reanalysis gridpoints in the region $r_m < r < 2r_m$. Then, following Holland (1983), the direction of propagation due to beta drift in the absence of background flow, θ_m (as measured clockwise from due north), is given by:

$$\theta_m = \arctan\left(\frac{1}{\lambda(2-\sigma)}\right), \tag{5.10}$$

and the subsequent drift velocity, v_m, by:

$$v_m = \frac{\beta r_m^2}{1-\sigma^2}(\sin\theta_m + \lambda(2-\sigma)\cos\theta_m), \tag{5.11}$$

where $\beta = \partial f/\partial y$ is the standard notation for rate of change of the Coriolis parameter with increasing meridional distance. Again, following Holland (1983), this can be adapted to include the effect of a local background flow with velocity v_b and direction (defined, like θ_m, as the angle measured counterclockwise from due north) θ_b:

$$\theta_d = \arctan\left[\frac{\frac{1-\sigma^2}{r^2}v_b\sin\theta_b + \beta}{\frac{1-\sigma^2}{r^2}v_b\cos\theta_b + \lambda(2-\sigma)\beta}\right], \tag{5.12}$$

and:

$$v_d = v_b\cos(\theta_d - \theta_b) + \frac{\beta r^2}{1-\sigma^2}(\sin\theta_d + \lambda(2-\sigma)\cos\theta_d). \tag{5.13}$$

An important caveat here is that if MDs really were exact point vortices, they would not propagate using this mechanism because $v_d \to \infty$ as $\sigma \to 1$.

5.3 Results

We start by considering the distribution of velocities for MDs in the period considered. The average MD speed is 4.24 m s^{-1} with standard deviation 3.1 m s^{-1}, and the average

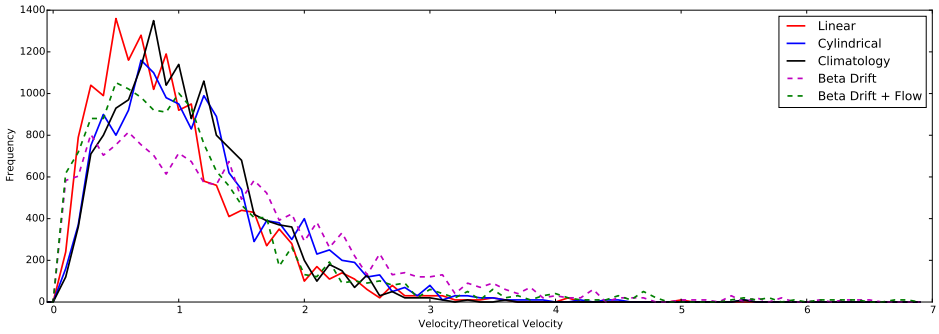

Figure 5.5: Histogram showing the ratio of observed to predicted IMD propagation velocities for each of the five models discussed in the text calculated for all timesteps present in the dataset. Red and blue represent our linear and cylindrical models respectively; black represents a simple model based on the climatology; dashed green (magenta) represents a simple beta drift model (not) including background monsoonal flow.

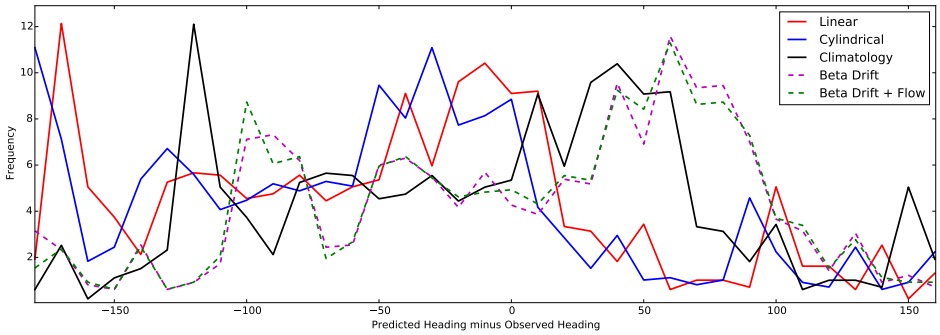

Figure 5.6: As with Fig. 5.5 but showing the difference between the predicted heading and the observed heading.

heading is 332°. When the velocities are normalised (see Fig 5.5), both point-vortex models perform well. The cylindrical model, with a mean normalised speed of 1.08 and standard deviation of 0.68, slightly outperforms the linear model, with a mean of 0.90 and standard deviation of 0.61, in that it predicts the propagation speed with marginally better accuracy, but higher variance.

Figs. 5.5 and 5.6 show, respectively, distributions of the speed and angle predictions from each model compared to reality. Table 5.1 tabulates the means and standard deviations of each. We see that in predicting velocity, our linear and cylindrical models perform well – both have markedly lower variance than either of the beta drift models and predict the propagation velocity very accurately. Both beta drift models and the linear model struggle to predict the lowest observed velocities (not shown), but the

cylindrical model and climatology predict these somewhat more accurately. Further, both beta drift models suffer badly with underprediction (i.e. high values of $(|\mathbf{v} - \mathbf{v}_{\text{flow}})|/v_{\text{model}}$, beyond the right edge of the frequency distribution in Fig. 5.5) of MD speed in quite a number of cases. As a comparison metric, we propose computing the fraction of the 1526 pairs of data from the two distributions in Figs. 5.5 and 5.6 that, when used to predict the location of an MD (by extrapolating the diagnosed velocity), travelling at 3 m s^{-1}, 24 hours in advance, are correct to within 100 km – the approximate radius of the area of heavy surface rainfall (as confirmed in Fig. 4.1). The calculated success rates were, in descending order: cylindrical - 0.296, climatological - 0.280, linear - 0.274, beta drift - 0.215, beta drift + flow - 0.195. If we expand this to bootstrapping 10,000 random unmatched pairs, the performance of the linear and cylindrical models drop (the other three do not), resulting in the climatological model scoring most highly. This strongly implies that these two models at least partially describe the propagation mechanism, and that the cylindrical model performs best overall.

A two-tailed Student's t-test confirmed that the means for the linear and cylindrical model results were significantly different at the 99% confidence level. Both of our models however, have some small systematic error in predicting the propagation direction, giving it a northward bias. To reiterate, the values given for standard deviation are dimensionless, as are those for the mean.

It is known that monsoon depressions exist in other areas, notably Australia and Central Africa (Hurley and Boos, 2015). In these locations, the depressions also exist over land, but do not have significant orography with which to interact; therefore we might assume that they would propagate poleward and westward less frequently if the mechanism proposed in this study were correct. Using the global database of depressions outlined in Hurley and Boos (2015), we found that Indian monsoon depressions propagate westward and poleward significantly more frequently than those in either the Australian or African basins, and more rapidly than those in the Australian basin.

Model	$\overline{\left(\frac{\lvert\mathbf{v}-\mathbf{v}_{\text{flow}}\rvert}{v_{\text{model}}}\right)}$	St. Dev.	$\overline{\theta_{\text{actual}}-\theta_{\text{model}}}$	St. Dev.
Lin.	0.90	0.61	-37.8°	84.8°
Cyl.	1.08	0.68	-23.3°	88.3°
Clim.	1.00	0.56	0.0°	80.7°
B.D.	1.35	1.28	10.6°	82.2°
B.D.F.	1.14	1.25	14.1°	81.6°

Table 5.1: Means and standard deviations of the normalised predicted velocity, $|\mathbf{v} - \mathbf{v}_{\text{flow}}|/v_{\text{model}}$, and the error in predicted heading, $\theta_{\text{actual}} - \theta_{\text{model}}$, for each of the five models. (Lin. = Linear, Cyl. = Cylindrical, Clim. = Climatology, B.D. = Beta Drift, B.D.F. = Beta Drift + Flow)

African monsoon depressions propagated westward most rapidly of all, likely owing to the strong environmental easterlies at around 650 hPa in the African Easterly Jet. This dominates the organisation of African Easterly Waves in that region, and closed depressions are not particularly common there – systems exist mostly as open waves with a maximum amplitude at the jet level.

5.4 Conclusions

From these results it seems that a simple, first order explanation for the propagation of MD vortices is that of the model of a point vortex interacting with the "cylindrical wall" of the Himalayas. Figure 5.5 shows that the mean speed of vortices is very close to the value predicted by this model, with standard deviation $\sim 1.0\ \mathrm{m\,s^{-1}}$ (cf. $\sim 1.1\ \mathrm{m\,s^{-1}}$ for actual MDs).

Departures from this model ($|\mathbf{v}-\mathbf{v}_{\text{flow}}|/v_{\text{cyl}}$) have standard deviation 0.68 (Fig 5.5). Partly this could be due to errors in our calculations (finite size of vortex, vortex maximised at another level, etc.), but also we can assume that other physical and dynamical processes will influence the movement of real MDs from case to case. Such processes include upper-level interactions and diabatic effects. There may be more boundary-layer friction for vortices close to the mountains. The image vortex causes an irrotational deformation flow acting on the real vortex. In reality, this deformation

flow exists to satisfy the correct boundary condition imposed by the mountains. We should expect forecast models to capture this very well.

Boos et al. (2015) showed how MD movement can be inferred through the advection of the 450 hPa PV maximum in the MD by the local flow at that level, which is enhanced by beta drift, in which the PV anomalies induced by the meridional flow around the vortex generate a meridional northwestward advection of the vortex. Our arguments relating to the advection of the 850 hPa vortex maximum are probably complementary to the results of Boos et al. (2015), in that we invoke the advection of the MD structure, rather than wave-propagation mechanisms presented by earlier authors. Boos et al. (2015) also show how the alignment of the 500 hPa PV structure with that at 700 hPa can explain the upwind advection of the MD PV at the lower level. On average, the 500 hPa PV lies to the southwest of the 700 hPa potential vortex, and is consistent with shifting the 700 hPa circulation field to the southwest of the PV at that level. In consequence, the circulation induced at 700 hPa by the 500 hPa PV acts to advect the 700 hPa PV toward the northwest, as observed. Boos et al. (2015) note that a Rossby scale height for these systems is typically 2.3 km, meaning that this vertical influence of the 500 hPa PV will be significantly weaker at 850 hPa, but it remains likely that some influence will be felt. Quite likely, the topographic effects of the Himalayas described in this paper, which will be strongest in the lower levels, combine constructively in the vertical to produce systematic advection to the northwest throughout the lower troposphere, and to maintain the vertical alignment of the monsoon depressions as described by Boos et al. (2015) and in Chapter 3. It would be reasonable now to state that the PV maximum of an MD is advected westwards by the local wind in the mid-troposphere (modified by beta drift) while its low level structure also moves northwestward, against the mean wind at this level, due to interaction with image vortices behind the Himalayan barrier. For these reasons, the dynamics of MDs are probably unique worldwide.

The intensification of the flow on the Himalayan side of the vortex, as observed

in real MDs, is generated by the sum of flows from the MD and its image, and will act to enhance the southeasterly recurvature of the monsoonal winds from the Bay of Bengal. The presence of the mountains, or equivalently the image vortex, increases the moisture advection in the Indo-Gangetic Plain and is an important factor in the amplification of rainfall by MDs within the monsoon season.

In Chapter 1, we partially motivated this thesis by stressing the importance of using the anticipated results to validate models. Now, equipped with a relatively complete picture of the structure and processes governing MDs, we are in a position to assess how good numerical weather prediction models are at forecasting MDs. Both in this and the wider context, an important leading question is: is the resolution, N768, used operationally (and in this chapter) good enough?

CHAPTER 6

THE EFFECT OF HORIZONTAL RESOLUTION ON INDIAN MONSOON DEPRESSIONS IN THE MET OFFICE NWP MODEL

6.1 Introduction

Numerical model resolution has consistently been shown to play a critical role in both deterministic (Mass et al., 2002) and ensemble (Buizza et al., 1998) forecasts; at all spatial scales: e.g. mesoscale (Bryan and Morrison, 2012), synoptic (Hill and Lackmann, 2009; Murakami and Sugi, 2010) and global (Roeckner et al., 2006); all timescales: e.g. climate (Roeckner et al., 2006; Johnson et al., 2016) and weather (Mass et al., 2002); all locations: e.g. the Asian monsoon (Sperber et al., 1994; Johnson et al., 2016) and polar regions (Boville, 1991); and across a number of processes (Pope and Stratton, 2002), particularly for those involving precipitation (Giorgi and Marinucci, 1996). While there has been much work undertaken to determine the sensitivity of tropical cyclone structure and intensity to model resolution (e.g. Gentry and Lackmann, 2010; Strachan et al., 2013), no such study has been carried out for monsoon depressions. These studies leave little doubt that increasing horizontal resolution in a deterministic

model gives improved forecasts, that is to say that for a given lead time, the structure of meteorological fields becomes closer to those observed during analysis. However these increases in resolution come at at a significant computational cost, and it is important to determine whether similar improvements could be gained more cheaply by focussing on improvement of model parameterisations.

In this chapter, we propose to disentangle this problem using the numerical weather prediction (NWP) framework of the Met Office Unified Model (MetUM). This can be run globally at a large range of horizontal resolutions, allowing us to probe how well MDs are represented overall and at what resolutions important processes are well illustrated.

We start with a discussion on the experimental setup of the MetUM, along with the tracking algorithm and other data sources used in §6.2. We then examine how the MD propagation and duration is affected by resolution in §6.3, before extending this intercomparison to the monsoon trough itself in §6.4. We then examine the composite MD structure in a selection of fields in §6.5, discussing vertical structure (§6.5.1) and horizontal (§6.5.2), before focussing on the representation of clouds (§6.5.3) and presenting a detailed analysis of the diurnal cycle of precipitation (§6.5.4).

6.2 The Met Office Unified Model and experimental setup

Here, we outline the experimental setup and the data used. We open with a discussion of the case study selection before looking at the MetUM and how we have set it up to work at a range of horizontal resolutions. We then discuss the method used to track MDs in our data, and an algorithm developed to allow fair comparison of fields at different resolutions. We conclude this section with a discussion on external data sources.

6.2.1 Case study selection

Seven MDs were selected from the IMD eAtlas (`http://www.rmcchennaieatlas.tn.nic.in`) subject to the following criteria: firstly, the genesis point should be in or near the Bay of Bengal so that the governing circulation and orography is inter-comparable; secondly, they should be recent, to ensure the analysis from which the forecast is initiated has high resolution and is of good quality; and thirdly, that the MD featured notable spatial propagation - some spin up near the coast and simply do not have coherent propagation, despite lasting for several days or longer, and these were not selected. A summary of these seven MDs is given in Table 6.1; they represent a good spread of mean headings (despite the typically low variance in this field, see §5.2), durations, propagation speeds, and timing with the monsoon season. This is a reasonable sample size, larger than that of Godbole (1977) or Stano et al. (2002), comparable with Sarker and Choudhary (1988), but smaller than the climatological studies of Hurley and Boos (2015) and that considered in Chapter 3. The IMD uses a subjective method with synoptic surface charts to track and classify incident monsoon disturbances (hereafter referred to as IMD tracks) which contrasts with our objective method; as such, we have independently tracked these disturbances (hereafter referred to as ERA-I tracks) subject to the criteria discussed earlier in this section using ERA-Interim data (Dee et al., 2011). Fig. 6.1 shows a comparison of these track pairs. Note that the MDs we tracked objectively from reanalysis data tend to have longer duration than the official MDs declared by the IMD due to our weaker wind criterion (< 8.5 m s^{-1} at 850 hPa rather than at the surface).

6.2.2 Overview of the Unified Model

The version of the Met Office Unified Model (MetUM) used for this study runs the Global Atmosphere (GA) and JULES Global Land (GL) configuration (Walters et al., 2015). The current dynamical core of the MetUM (ENDGame; Wood et al., 2014) solves the non-hydrostatic, fully compressible, deep-atmosphere equations of motion

Start date	Duration (UTC)	Mean speed (m s^{-1})	Heading (°)
30/07/2013 00Z	40	6.1	281
20/08/2013 00Z	54	4.9	278
21/07/2014 00Z	48	5.8	273
03/08/2014 12Z	71	4.8	294
20/06/2015 00Z	40	2.9	334
10/07/2015 00Z	51	6.8	309
16/09/2015 00Z	60	6.4	280

Table 6.1: A summary of the seven MDs used in this study. Data are computed directly from the high resolution IMD eAtlas tracks. Duration is defined as the total (contiguous) time for which the IMD classified the disturbance as a depression.

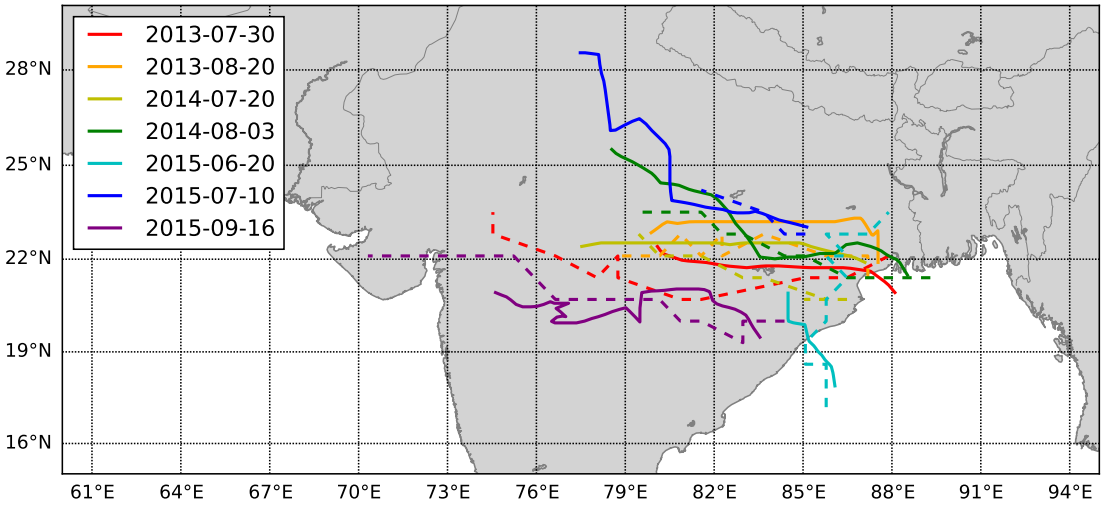

Figure 6.1: Comparison of official IMD tracks (solid) with those tracked objectively from ERA-Interim (dashed). The average length of the latter is longer due to the relaxed MD wind criterion used in this study. Depression start dates are as given in Table 6.1.

using a semi-implicit semi-Lagrangian scheme on a regular latitude/longitude grid, with an explicit diffusion scheme. Regardless of horizontal resolution, it was run with 85 vertical levels, this corresponds to a resolution of about 100 m in the lower troposphere, decreasing to more than 5 km in the thermosphere with a lid at 85 km (0.004 hPa). A number of parameterisations are also implemented, including:

Convection The scheme proposed by Gregory and Rowntree (1990) forms the basis of the convective parameterisation used in the MetUM. This is extended to include phenomena including downdraughts (Gregory and Allen, 1991) and depth-specific convective momentum transport (shallow: Grant and Brown, 1999; Grant, 2001, mid-level: Gregory et al., 1997, deep: Stratton et al., 2009). CAPE closure is used for mid-level and deep convection, and with some exceptions for stability, is fixed at one hour (Fritsch and Chappell, 1980). Recently this has been updated to better model detrainment and plume buoyancy and humidity (Derbyshire et al., 2011).

Sub-grid orography Effects from sub-gridscale orography can accumulate to become important on the larger scale; in our study, the most relevant example of this is the potential for mechanical convection to be forced by the unresolved features of the Western Ghats and Himalayan foothills. In the MetUM, effects on this intermediate scale (which also include orographic drag) are handled by a scheme based on Lott and Miller (1997), whereas finer-scale interactions involving stress and torque from roughness friction are estimated by a scheme based on Wood and Mason (1993). In very high resolution models, subgrid turbulence is effected by a 3D Smagorinsky scheme where stress is proportional to eddy viscosity, which in turn is proportional to the square of the grid spacing. For comparison, at our coarser resolutions, turbulent eddy viscosity is set at a fractional value of the boundary layer depth. Towards the grey zone, a blended scheme is used (Honnert et al., 2011).

Turbulent mixing A scheme based on Lock et al. (2000) with extensions from Lock (2001) and Brown et al. (2008) is used to parameterise turbulence in the MetUM. This scheme also largely governs motion in the atmospheric boundary layer (for which it was originally intended), upholding adiabatic conservation laws with a first-order turbulence closure.

Precipitation and cloud Local convective precipitation is handled directly by the convection scheme (see above). However, much of the rainfall associated with monsoon depressions is stratiform in nature due to the large scale moisture convergence they induce in the lower troposphere (see Fig. 3.14). This is handled by a scheme based on Wilson and Ballard (1999), with specific precipitation extensions based on discussions in Tripoli and Cotton (1980); Abel and Shipway (2007); Abel et al. (2010); and Abel and Boutle (2012). Cloud fraction and condensate are computed using a prognostic scheme (Wilson et al., 2008).

In this experiment, we keep fairly close to the operational use of the model by the Met Office. That is to say it is run globally and with forced, persisted SSTs in atmosphere-only mode, although we perform no data assimilation. The model physics and parameterisations do not change as a function of resolution; the model timestep of 15 minutes is stable at all resolutions.

6.2.3 The spectrum of resolutions

For this study, the NWP model was run over eight resolutions, ranging from that currently used for the Met Office Hadley Centre low-resolution climate model, increasing to the current NWP forecasting model resolution of N768, through to two higher resolutions expected to be operational in the near future (N1024 and N1280). A summary of these resolutions including the number of gridpoints they use and the approximate zonal gridpoint spacing at the equator is given in Table 6.2. For each of the seven case studies, the NWP model was run at all eight resolutions, with a fixed 85 vertical levels; the initiation date for each forecast was selected as 00UTC on the day before the IMD officially declared the depression.

6.2.4 Description of the tracking algorithm

We use the fixed-domain objective feature-based tracking algorithm described in §2.1. Since ancillary surface roughness lengths vary significantly with model resolution and

Name	Gridpoints ($n_x \times n_y$)	Resolution (km)
N96	192×144	208
N216	432×324	93
N320	640×480	63
N512	1024×768	39
N640	1280×960	31
N768	1526×1152	26
N1024	2048×1536	20
N1280	2560×1920	16

Table 6.2: A summary of the eight horizontal resolutions used in this study, with dimensions of the global grid, and zonal resolution at the equator. n_x and n_y refer to the number of longitudes and latitudes respectively used to construct the grid.

have a strong effect on surface winds, we adopt a slight scale-invariant adaptation: we use 850 hPa wind as the primary tracking criterion. If resolution were not variable, we would use the standard IMD criteria of closed surface isobars over land and surface wind speed over the ocean. This has the clear caveat of being more sensitive to weaker disturbances as MD winds tend to reach a maximum just above the boundary layer (see Fig. 3.12(b)), and we shall subsequently accept that some parts of the resulting MD tracks would technically be classified as monsoon lows.

6.2.5 Adaptive downsampling

During the course of this study, we will be exploring data represented at resolutions spanning more than an order of magnitude. This presents a problem with comparative analysis, particularly for fields with a high spatial frequency, such as vorticity. Conventionally, increasing or slightly decreasing resolution is achieved by some optimal-order bivariate interpolation; however this can – and will, beyond a certain point – cause significant aliasing problems, even at high interpolation orders. This means that the data become misrepresented, particularly when looking for extreme values (e.g. in determining the maximum intensity a system achieves). To circumvent this, we must consider

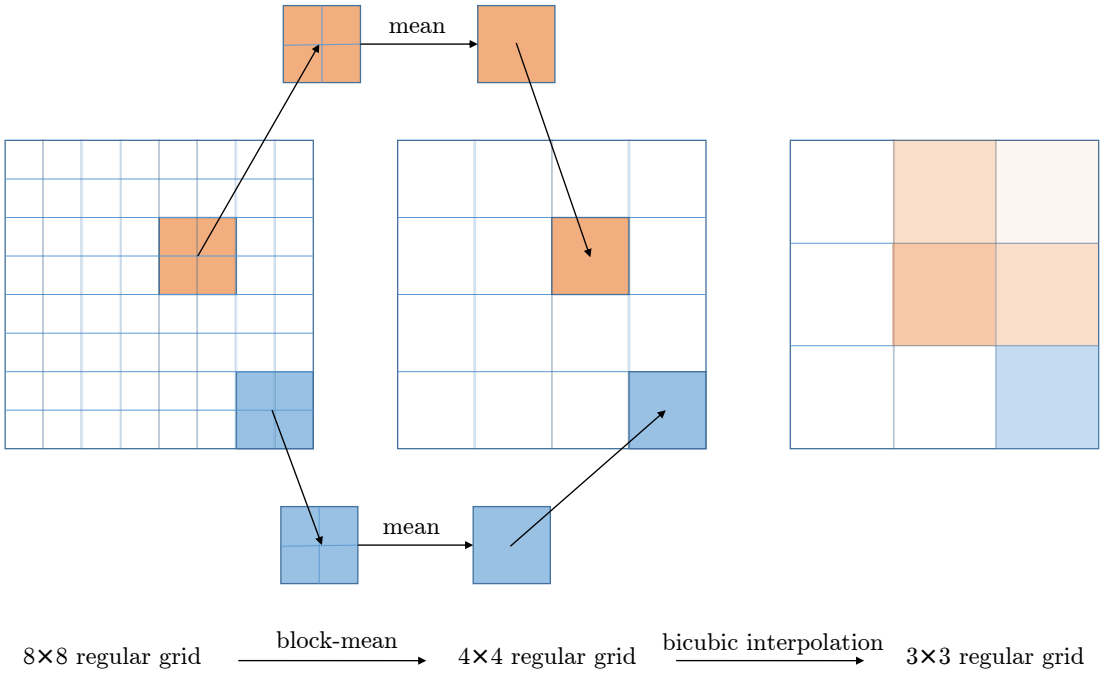

Figure 6.2: Pictorial example of adaptive downscaling from an 8×8 grid to a 3×3 grid. The leftmost grid (8×8) contains some sparse data, represented by the orange and blue blocks; firstly the resolution is reduced to the closest divisor of the original that is higher than the target (here 4×4, as $4|8$ and $4 \geq 3$). We then use a two-dimensional interpolation method to downsample from this intermediate resolution to the final 3×3 grid.

what it means to represent data at lower resolutions – it is, essentially, *zooming out*; thus we should expect to be able to traverse from to a low resolution grid, L (size: $L_l \times L_w$), from a higher resolution grid, H ($aL_l \times bL_w : a, b \in \mathbb{Z}$), via a block-mean reduction of the form:

$$L_{ij} = \frac{1}{ab} \sum_{k=ai}^{a(i+1)} \sum_{l=bj}^{b(j+1)} H_{km} \,. \tag{6.1}$$

It is reasonable to assume that in a real-world application, a and b will not necessarily be integers; in this case it is safe to perform the above using their floors and then trivial to apply a suitable (in our case, biquintic) interpolater to the lower resolution data to adjust it to the required resolution. An example of this procedure is shown pictorially in Fig. 6.2 for an 8×8 to 3×3 conversion.

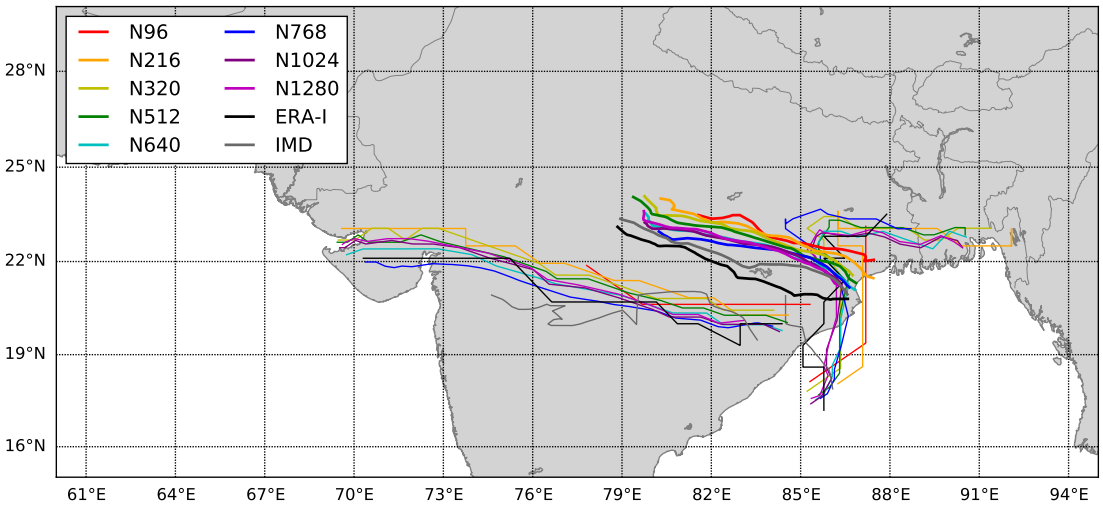

Figure 6.3: A selection of tracks from the case study experiments. In bold are the mean tracks for each resolution, normalised by duration; the westward propagating tracks that traverse the peninsula are from the 16/09/2015 MD, and those propagating northwards toward the Ganges Delta are from the 20/06/2015 MD. In black are the tracks computed from ERA-Interim, and in grey are the official IMD tracks.

6.3 Propagation and duration

The NWP models at each resolution for each case study were run for seven days, which is substantially longer than any of the MD durations given in Table 6.1. The previously described tracking algorithm was applied to the output data to determine whether an MD was present in the forecast, and if so, what its track was. In all 56 forecasts (seven case studies at eight resolutions each), an MD of sufficient length to not be dismissed as a transient feature was detected. Examples of tracks from two case studies, along with the overall averages are shown in Fig. 6.3, the average tracks (in bold) are computed from normalised durations (that is to say, if one had two MDs of duration 48 and 60 hours, the halfway point of the average track would be taken from the coordinates at 24 and 30 hours respectively). Also given in the figure are the official tracks from the IMD (grey) and as computed from ERA-Interim reanalysis (black). The two case studies given are a longer westward system that terminates on the west coast and another propagating northward that terminates over Bangladesh, from the 16/09/2015 and 20/06/2015 experiments respectively. It is evident from the two examples and

the 7-member multi-depression mean shown in Fig. 6.3 that increasing the resolution improves the track forecasts: the genesis/termination points, durations, and along-track coordinates all tend towards greater accuracy. We can look at the forecast track accuracy more quantitatively by normalising the track lengths and computing the mean distance error compared to the IMD or ERA-I tracks; i.e. we consider a given lifetime percentage and for each resolution calculate the mean distance between its tracks and the 'truthful' ones. This is done for each resolution, tested against both IMD and ERA-I tracks, and the results are given in Fig. 6.4(a) and Fig. 6.4(b) respectively. We see that the errors generally grow with time, with N96 performing particularly poorly. Regardless of whether the comparison is made with ERA-I or IMD tracks – although it strictly ought to be the former – it is evident that above N216 resolution, error reductions become more marginal in terms of track position.

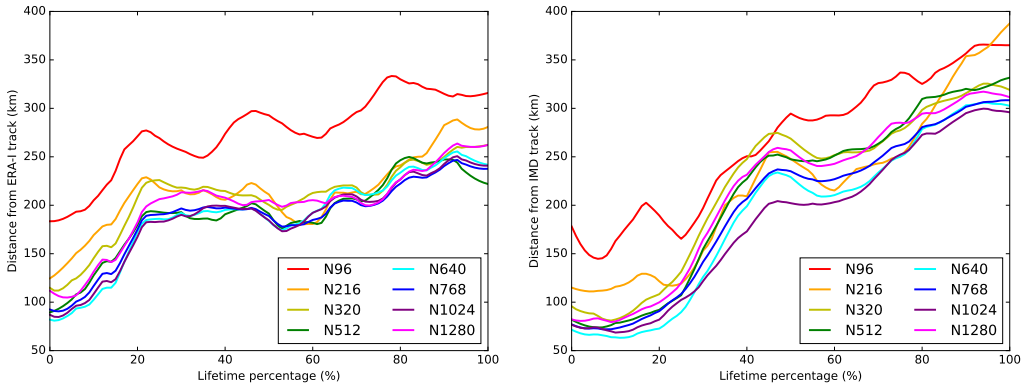

(a) ERA-Interim (b) IMD

Figure 6.4: Mean distance from (a) ERA-Interim track and (b) IMD track as a function MD lifetime percentage. Duration normalisation is carried out before averaging, as in Fig. 6.3.

6.4 Representation of the monsoon trough during depressions

To understand the relationship between model, resolution, and depression, we must first consider the environment in which depressions are embedded: the Indian monsoon

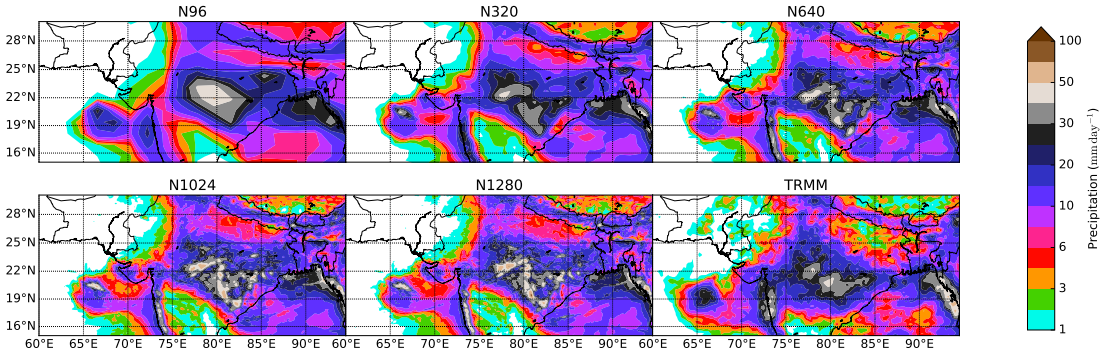

Figure 6.5: Mean precipitation (mm day^{-1}) in the monsoon depression-trough and surrounding area for a selection of resolutions, compared against the same period(s) for TRMM-TMPA 3B42. Each is averaged over the same set of dates and times: those in which a MD was considered present in ERA-Interim by our tracking algorithm.

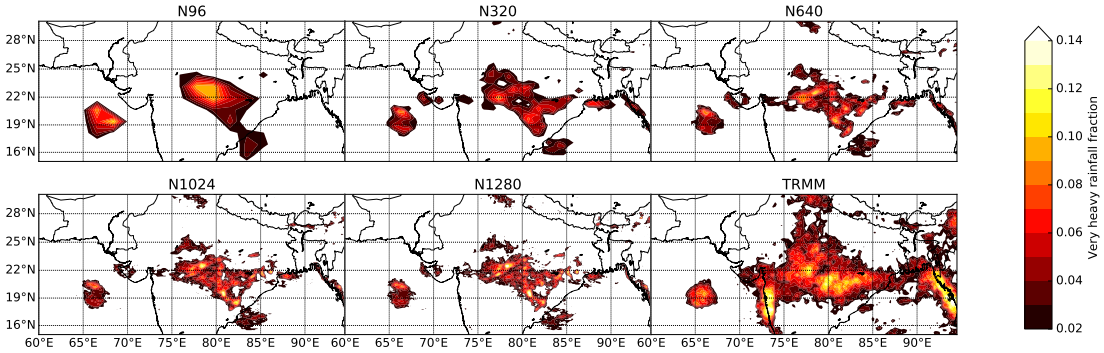

Figure 6.6: Fraction of total time for which "very heavy" rainfall events were present in the depression-trough for a selection of resolutions, compared against the same period(s) for TRMM-TMPA 3B42. "Very heavy" is defined by the IMD as rates exceeding 125 mm day^{-1}. Computation as in Fig. 6.5.

trough. It is a favourable environment for MDs, a low pressure area with large moisture fluxes, wrapped in lower-tropospheric cyclonic winds, which tend to strengthen during the passage of a depression (see Fig. 3.20(a)). Thus, the discussion of the nature of a depression-trough[1] in models and its sensitivity to resolution is an important part of a clear analysis of MDs in NWP models.

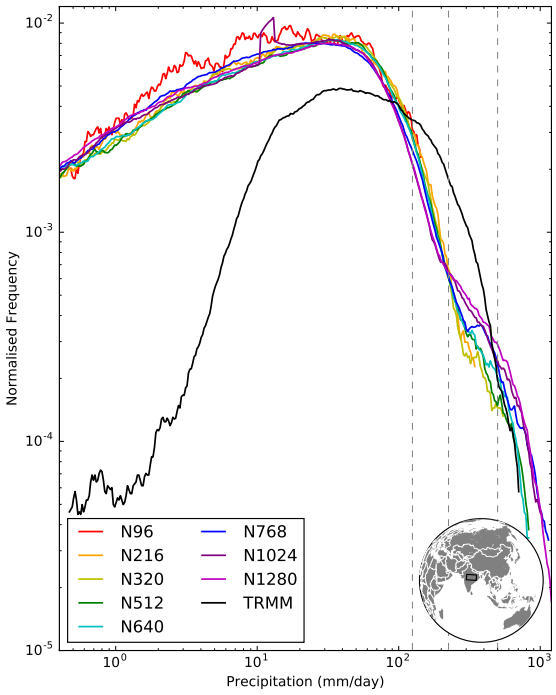

Figure 6.7: Normalised log-histogram of precipitation (mm day^{-1}) in the depression-trough during the case-study MDs. Here, the trough is defined simply as a box bound by the coordinates: 20-25°N, 75-85°E. Breaks in lines indicate zero counts.

6.4.1 Rainfall

Fig. 6.5 shows a comparison of mean rainfall across the case studies for a range of resolutions with each other and the TRMM 3B42 surface precipitation product for the same period. We see that increasing the resolution consistently does two things to the mean picture: reveals a more complex structure, and results in generally higher maximum rainfall rates. Naïvely, we might say that these can be explained directly by considering how the fields are represented - finer detail simply cannot be depicted at the lower resolutions, there are not enough pixels; and the highest rainfall rates have very small spatial scale and thus tend to get smoothed as resolution is reduced. However, this is not the complete story: the structure becomes more filamental[2] with increasing resolution, providing evidence that finer mesoscale processes are being represented in the model (whether or not they exist in reality); further, both the mean rainfall in the trough and the frequency of "very heavy" rainfall events, officially defined by

[1]We shall hereafter use the term *depression-trough* to refer to the trough when it is co-existent with a monsoon depression

[2]That is to say it is anisotropic, which we would not expect if this detail came about solely as a result of having a "sharper" image.

the IMD as rates of 125 mm day^{-1} or greater, also increase with resolution. Fig. 6.6 gives a depiction of the latter: the fraction of timesteps where a MD was considered present in ERA-Interim (for the relevant range of dates) in which the model/TRMM 3B42 determined that very heavy surface precipitation was present. We see that the frequency of such events in the trough increases with resolution, tending towards the values suggested by TRMM, however the orographic representation over the Western Ghats and across western Indochina remains poor throughout: for example, precipitation predicted by the model over the Ghats is too frequent, too weak, and in the wrong location; and this is important to quantify because the rainfall over the mountainous west coast is heavily modulated by the presence of MDs (see Fig. 3.3). The lower-tropospheric cyclonic circulation associated with a typical MD strengthens the monsoon westerlies over the Western Ghats, increasing the associated orographic rainfall. It is also evident that while the forecast frequency of heavy rain improves with resolution, the total amount of rain associated with the MD becomes a clear overestimate when compared to TRMM; and across all resolutions, the model tends to constrict the spatial scale of heavy rainfall events to be closer to the MD centre. Note also the footprint of a disturbance in the Arabian Sea - this was contemporaneous with the June 2015 disturbance - it is included in these maps of the composite depression-trough, but will be excluded from depression composites in subsequent sections.

We can interrogate the bulk rainfall statistics a little more by looking at a histogram of precipitation rates in the depression trough; unfortunately it is difficult to compare individual events due to the individual storms being typically smaller than the forecast track errors. This is done across all case studies (using dates from ERA-I tracks), giving over 160 timesteps. For a simple definition of the trough (20-25°N, 75-85°E), the histograms are shown in Fig. 6.7. The distributions from TRMM 3B42[3] and the model at all resolutions are significantly different, although from resolutions of about N512 upwards (even after downscaling), the model is capable of representing the higher rainfall

[3]Recall the resolution of TRMM 3B42 roughly equates to N720

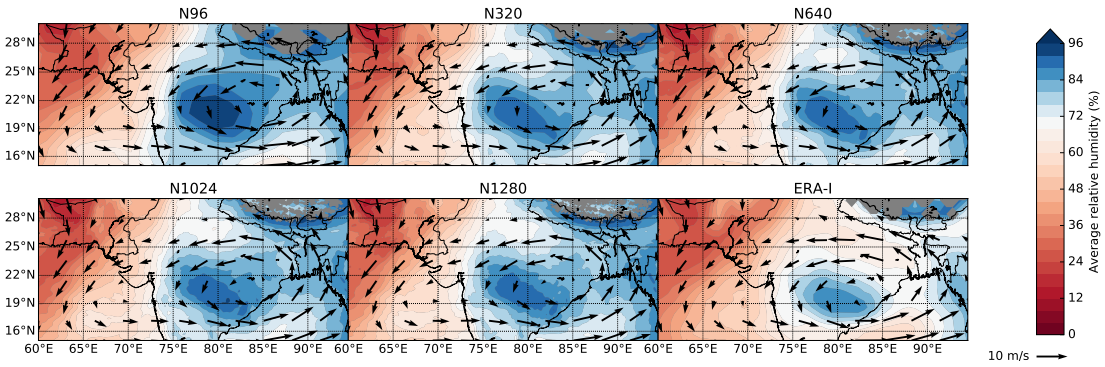

Figure 6.8: Mean 500 hPa relative humidity and 500 hPa winds in the monsoon depression-trough and surrounding area for a selection of resolutions, compared against the same period(s) for ERA-Interim. Computation as in Fig. 6.5.

rates that TRMM suggests exist there. There are three distinct regimes with boundaries at approximately 125 mm day^{-1} (coincidentally) and 500 mm day^{-1}. In the low-rate regime, we see that regardless of resolution, the model overestimates the frequency (by as much as an order of magnitude as the 0.1 mm hr^{-1} resolution of TRMM 3B42 is approached). This exaggerated drizzle is a well-known issue in global models (e.g. Dai, 2006; Stephens et al., 2010). This is compensated for by an under-representation of higher rainfall rates in the model, although above about 225 mm day^{-1} this sharply improves with increasing resolution. In the very-high rate regime, resolutions below N512 produce nothing, whereas N512 and above tend to overestimate the frequency and amount; though this should be taken with the caveat that these events are rare (of the order of two or three over the total dataset of each resolution).

6.4.2 Synoptic circulation

Now, it has been shown that mid-tropospheric relative humidity is an important factor in the modulation of MD genesis (Ditchek et al., 2016), that MDs are capable of organising mid-tropospheric circulation that is absent in the climatology (e.g. Fig. 3.12(b)), and further, that fields at these altitudes are thermodynamically coupled to precipitating events at the surface (see Chapter 4, in particular Fig. 4.5). Bearing this in mind, Fig. 6.8 shows the mean 500 hPa depression-trough relative humidity and winds for

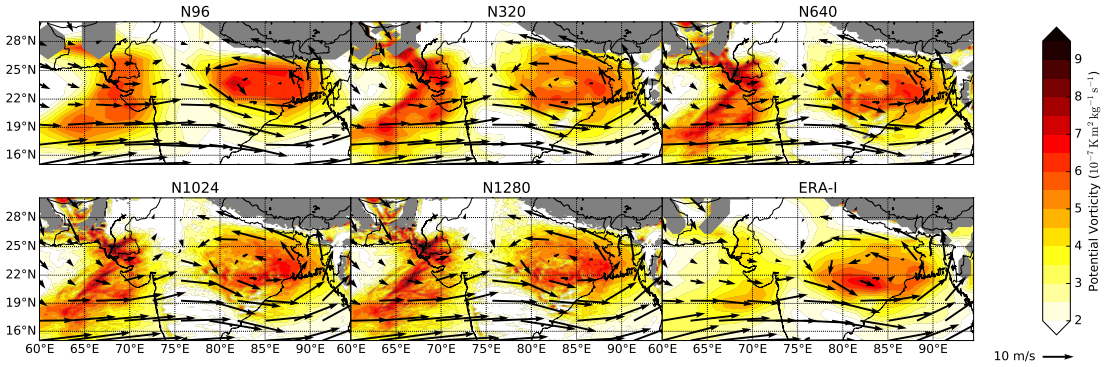

Figure 6.9: Mean 700 hPa potential vorticity ($10^{-7}\,\mathrm{K\,m^2\,kg^{-1}\,s^{-1}}$) and 850 hPa winds in the monsoon depression-trough and surrounding area for a selection of resolutions, compared against the same period(s) for ERA-Interim. Computation as in Fig. 6.5. Where orography is above 700 hPa, the coloured contours are greyed out.

a selection of resolutions, with that from ERA-Interim (for the same dates) for comparison. The relative humidity at this altitude is consistently over-estimated by the model (typically 5-10% in the trough), but this improves with increasing resolution. We also note that the maximum relative humidity moves south (towards that observed in ERA-I) with increasing resolution; this is likely to be at least related to the tracks having lower latitude (cf. Fig. 6.3). The circulation is well represented at all shown resolutions, although in the model it is more convergent over the trough than in the reanalysis, and this is exacerbated by a resolution increase; it is perhaps important to note that this is correlated with an increase in the average precipitation for the region.

The circulation at 700 hPa, shown along with potential vorticity in Fig. 6.9 looks similar to that at 500 hPa, with the exception of the strong monsoon westerlies south of the disturbance. At low resolutions, the trough PV is displaced - too far to the northeast, but this improves with resolution, perhaps indicating a better representation of the known axial tilt in MDs. We also note that the PV over the Arabian Sea and near the high orography in Pakistan is severely overestimated at all resolutions, when compared to the reanalysis.

Summarising, we have seen that an increase in model resolution is correlated with an intensification of activity in the depression-trough: an increase in moisture, stronger

circulation, and associated higher rainfall rates. As such, we should expect that increasing resolution should also be correlated with stronger MDs. However, the impact of increasing resolution is small once we get beyond N320.

6.5 Evaluation of composite depression structure

Now that we have explored in some detail the sensitivity of a depression-trough to changes in horizontal model resolution, we shall look at the performance of the models from an MD-centred point of view. This is simply done via the construction of a composite, which has been done before for, e.g. tropical cyclones (Catto et al., 2010) and monsoon depressions in observations (Godbole, 1977; Keshavamurty et al., 1978; Sarker and Choudhary, 1988; Prasad et al., 1990) and reanalysis (Hurley and Boos, 2015; and Chapter 3). Simply put, the composite is composed by taking all depression-timesteps, centering the data for the field of interest on the depression centre, and then taking the average. For a formal description, the reader is encouraged to visit Appendix A.

One simple method, commonly used in the context of tropical cyclones, to overview the system-relative composite is to examine the extreme values of intensity-related variables as a function of resolution, averaged over the case studies. Fig. 6.10 shows the appropriate extreme (or mean) values for surface pressure, 350 hPa temperature anomaly, total precipitable water (TPW), and free convective depth; the values are computed from a 1000 km-sided box surrounding the centre, with blue dots marking the values from individual case studies and the blue line their average. The green line in each subplot marks the mean value from the ERA-I tracks and all fields are interpolated to N216 for comparison using the algorithm outlined in §6.2.5, which is an important step to undertake when performing intercomparison of extreme values across differing resolutions. The first field under consideration (Fig. 6.10(a)) is the lowest central surface pressure associated with the MD during its lifetime: parallel to

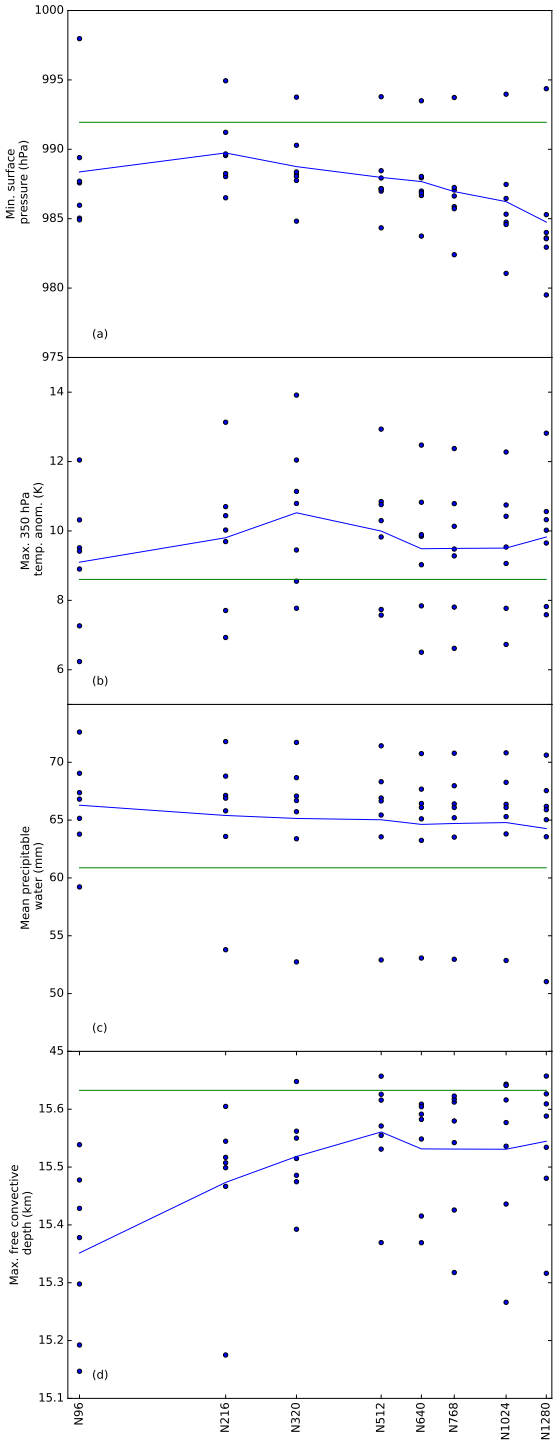

Figure 6.10: A selection of intensity diagnostics as functions of resolution. From top to bottom: minimum surface pressure obtained (hPa), maximum temperature anomaly at 350 hPa relative to climatology (K), mean precipitable water (mm), and maximum free convective depth (km). Each is computed from a 1000 km-sided box surrounding the centre, with the value for each MD case study; these individual values are plotted as blue circles at each resolution with the mean given by the blue line. The green line represents the value obtained by performing the same computation on the ERA-I track. Here, free convective depth is defined as the difference in altitude between the levels of free convection and neutral buoyancy.

similar studies for tropical cyclones (e.g. Strachan et al., 2013) we see that increasing the resolution strengthens the minimum surface pressure associated with the system irrespective of appropriate downsampling, though unfortunately even at some of the lowest model resolutions (N216: 989.7 hPa), it is still lower than the values suggested by ERA-I reanalysis, and deepens substantially beyond this (N1280: 984.8 hPa). During our discussion of representation of the depression-trough in the MetUM (e.g. Fig. 6.9), we initially suspected that MDs may be more intense in the model than in reality, and this corroborates that analysis.

We know that MDs are largely in thermal wind balance with the latent heat induced warm core aloft, and that the highest temperature anomalies are found at around 350 hPa, so this is an important metric to consider when discussing intensity; Fig. 6.10(b) shows the maximum values of the 350 hPa temperature anomaly (see Fig. 6.13 and associated discussion for an explanation of how the climatology is generated for the MetUM). This is handled far better than surface pressure by the MetUM, where the predicted values of approximately 9.5 K in the models at higher resolution is insignificantly separated from the ERA-I value of 8.7 K; and this accuracy generally improves with increasing resolution, especially beyond N320. It is still clear, however, that these extremes are too high at all resolutions.

Latent heat release in the troposphere is strongly coupled with the moisture presence, and so we turn our attention to a good proxy of this: total precipitable water. Fig. 6.10(c) shows the mean values of column TPW in the aforementioned box across the resolutions; this again is improved (compared to reanalysis) by increasing resolution from 66.3 mm at N96 to 64.3 mm at N1280, however the degree of improvement is marginal when compared to the overall error against the reanalysis value of 60.9 mm. So, the model asymptotically tends to roughly a 5% overapproximation of the total mass of water in the atmosphere surrounding the MD. This is not due to a temperature discrepancy (as we have briefly seen earlier in this section and will confirm later on examination of the vertical profile of temperature), there is simply more moisture being

put into the troposphere. This corroborates the behaviour of the trough that we saw in Fig. 6.8, and is not a problem generally found in the tropics (Martin et al., 2006), so we can fairly safely assume there is something special about the representation of monsoon depressions that is causing this. We extend this discussion a little further by considering the changes in tropospheric stability associated with the depression. For this, a good proxy is CAPE, although as we will come to see, it is rather too noisy to use when looking for extreme values. Instead, we consider free convective depth, the difference in altitude between the level of free convection and the level of neutral buoyancy; the larger this value, the more latent heat can theoretically be deposited throughout the troposphere. The maximum values for this are shown as a function of resolution in Fig. 6.10(d), and we can immediately see a rapid improvement with increasing resolution, tailing off at about N512 where the mean maximum free convective depth of 15.56 km compares favourably to the reanalysis value of 15.63 km. Clearly, then, the issue of too much moisture and over-intensification of the vortex does not appear to be related to atmospheric stability. This is one of a great many features affected by the convective parameterisation scheme, which in part explains its overall improvement with resolution.

6.5.1 Vertical structure

Monsoon depressions involve a number of complex, moist thermodynamic processes occurring over irregular orography and land surface type that result in characteristic vertical structure that has been qualified in some detail by previous authors (Godbole, 1977; Hurley and Boos, 2015) and in Chapter 3. One consistent, common feature in the vertical structure is a bimodal PV core: a maximum at ∼500 hPa primarily caused by the upper-tropospheric warm core, and one at ∼700 hPa primarily caused by the lower-tropospheric relative vorticity maximum. South-north cross-sections across the composite PV for MDs at each resolution, as well as those derived from the ERA-I and IMD tracks using ERA-I reanalysis, are shown in Fig. 6.11. The bimodal structure

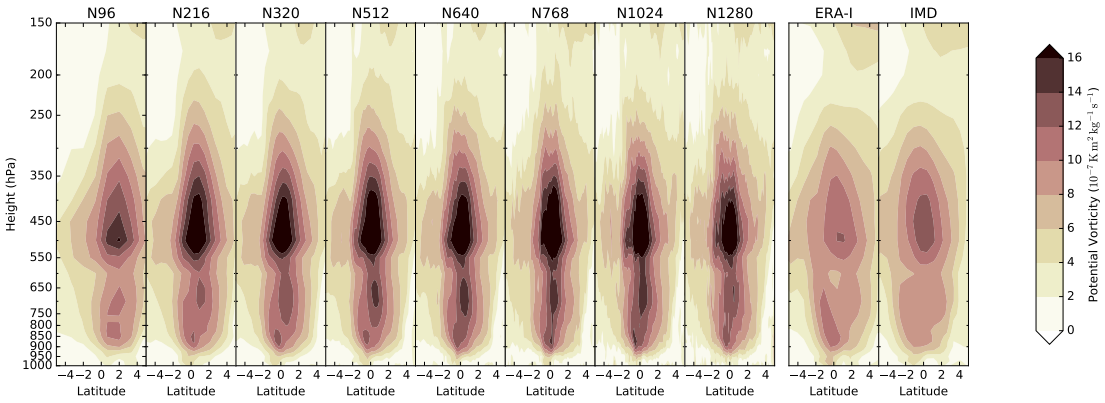

Figure 6.11: Mean composite potential vorticity ($10^{-7}\,\mathrm{K\,m^2\,kg^{-1}\,s^{-1}}$) for the case study MDs. Tracked MDs in the forecasts and reanalysis are centralised such that their centres lie at the origin of the composite. Here, south-north cross-sections through the composite origin are presented for all resolutions, and the composites derived from both our ERA-I tracks and the IMD tracks (i.e. the tracks determined from ERA-I and those given by the IMD, both applied to ERA-I data – see text for more details). The reader is reminded that the ERA-I equatorial resolution of ~ 78 km is approximately N256 (in reality, it is exactly T255).

itself is clearly well captured across the range of horizontal resolutions, although the magnitude of the maxima is too great by as much as 50%. This error is essentially consistent across the resolutions (with the exception of N96) which is apparently contradictory to recent work (Roberts et al., 2015) that suggests tropical cyclone intensity and horizontal model resolution are strongly correlated, although their study is a climate run with several hundred events (i.e. the cyclones spin up from the model rather than initial analyses). We note here that the MetUM model output was made to match the vertical levels available as ERA-I output data, 24 levels between 1000 and 150 hPa (approximately 200 m resolution in the PBL, decreasing to 2 km at the tropopause).

Since both maxima in PV are significantly overestimated by the model, we should expect this to be reflected in the primary contributors to each. We shall start by looking at the distributions of lower-tropospheric relative vorticity as a function of resolution. Now, we cannot be certain, although it is likely, that the vorticity maxima (climatologically found at the centre at 850 hPa) will necessarily be at the tracked MD centres - MDs are not strictly line vortices (as discussed in §5.1), and they tilt westward with height (Godbole, 1977); so, to capture the values associated with the vortical core,

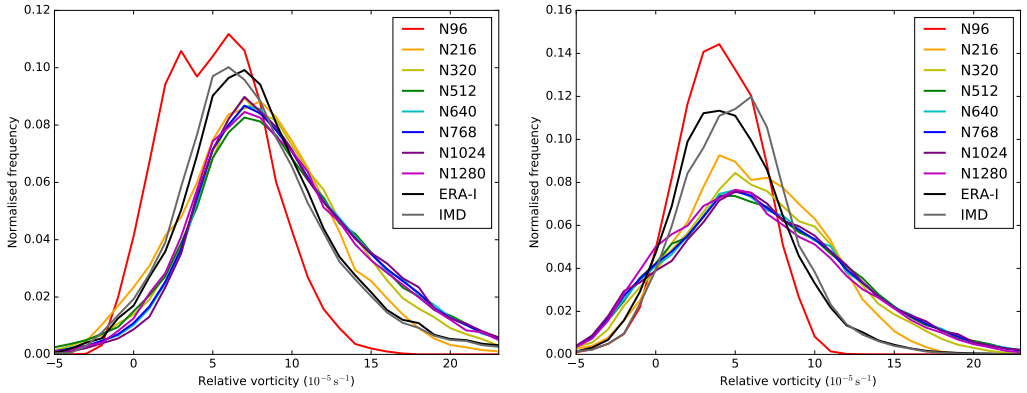

(a) 925-750 hPa (b) 650-300 hPa

Figure 6.12: Normalised histograms of relative vorticity (10^{-5} s^{-1}) for each resolution and the ERA-I and IMD tracks. These are taken at all times where an MD is present, from a cuboid of horizontal length 400 km centred on the origin, and vertical extent (a) 925-750 hPa and (b) 650-300 hPa.

we take all relative vorticity values in a prescribed cuboids of length 400 km centred on the MD centre with vertical extent 925-750 hPa and 650-300 hPa. All values within these cuboids are taken for all times where an MD is present in any of the case-study data and collected into histograms, which are given in Fig. 6.12. Although these data were coarsened to T255 resolution (lower than this was undesirable because it leaves data sparse in the domain used), the lower resolutions were found (using a broader domain) to be insensitive to downsampling. We note that all histograms closely resemble the gamma function, and that increasing resolution causes increased positive skewness with diminishing return; this indicates an increasing variance which is not reflective of the distributions found for reanalysis MDs (grey and black in Fig. 6.12). There is also a gain in intensity with increasing resolution until N512; this is more apparent in the mid-tropospheric sample of Fig. 6.12(b) where we also see the model performs substantially more poorly by overpredicting the MD intensity. Had we not opted to downsample the data from higher resolutions before producing the histograms, we would have recovered (not shown) a figure much like Fig. 8 of Strachan et al. (2013). We note that on statistical tests of these distributions at both levels, the three lowest resolutions were each significantly different from each other at the 99% confidence

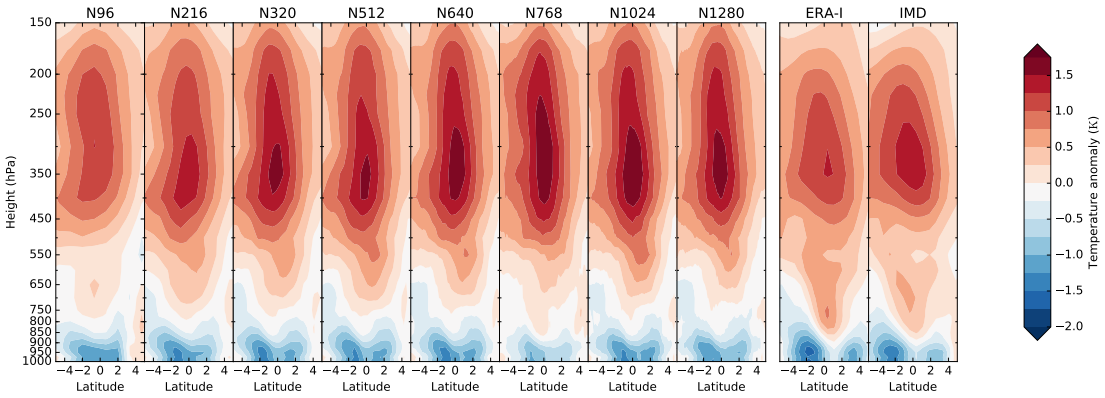

Figure 6.13: Mean composite temperature anomaly (K) for the case study MDs. Compositing method as in Fig. 6.11. Here the anomaly is against the climatology computed for the thirty-seven total forecast days (with these dates also used to compute climatology for the reanalysis structures).

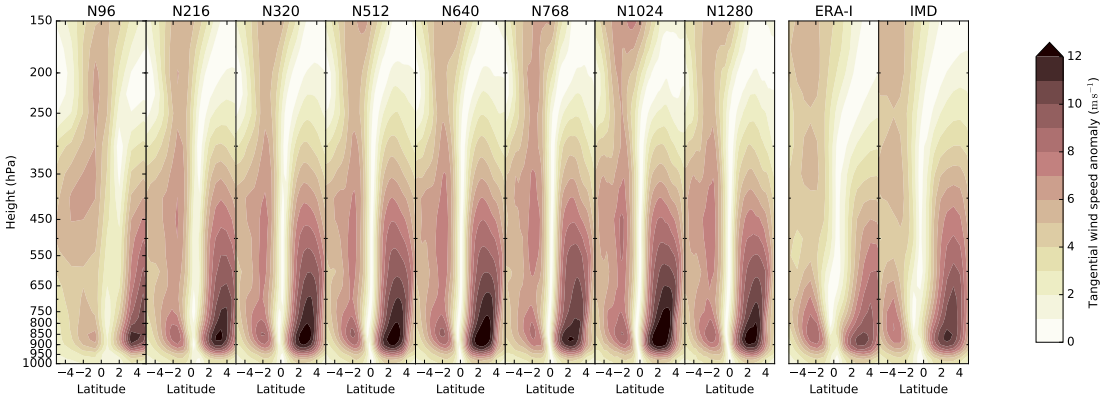

Figure 6.14: Mean composite wind speed anomaly (m s^{-1}) for the case study MDs. Construction of the composite is as Fig. 6.11 and the anomaly is taken against the climatology, whose computation is as in Fig. 6.13.

level, as well as from the five highest and the IMD/ERA-I tracks (the two latter sets were also significantly different from each other at this level, although the members of each set were not individually significantly different from each other). The differences in intensity prediction between the two altitude segments shown in Figs. 6.12(a) and 6.12(b) are important: this is a first indicator that a primary cause of the model's failings is rooted in the upper/mid-troposphere.

MD structure in the upper/mid-troposphere is strongly influenced by latent heat release there, so the next logical step is to examine the vertical thermal structure of

depressions. This, in the form of temperature, is given for each resolution, with the ERA-I and IMD track composites for comparison, in Fig. 6.13. Since perturbations to the temperature caused by MDs are roughly two orders of magnitude smaller than the vertical gradient through the troposphere, we look at the temperature anomaly, rather than the raw temperature field. For composites computed from both model output and reanalysis data, the anomaly was computed by subtracting the short climatology from the total forecast period (37 days over the seven MDs); this is realistically too short a period to conduct a sound analysis (climatologically, one would expect one or two MDs in a period of this length), although comparison of the ERA-I/IMD composites with other vertical thermal composites (e.g. Godbole, 1977; and Fig. 3.15) indicates that they are fairly representative. In the model, the magnitude of the warm anomaly in the mid-troposphere increases with resolution until N320; at resolutions thereafter the warm anomaly remains approximately constant. In contrast, there is little difference between the boundary layer cold anomalies in any resolution, other than perhaps a more defined structure with increasing resolution. Comparing the composite structure from the models to those from the reanalysis, it is evident again that the MD intensity is overestimated. Not only are the warm anomalies aloft roughly a quarter of a kelvin too strong, but they are significantly elongated in the vertical, extending up to a kilometre higher than in the reanalysis. Conversely the cold anomaly near the surface is well-represented in both magnitude and shape at all resolutions, arguably being slightly too confined to the centre.

We shall conclude this particular discussion with an exploration of the vertical wind structure given in Fig. 6.14 which is also presented as an anomaly so as to remove the effects of the monsoon jets. As expected, the structure is asymmetrical with wind speed being substantially higher north of the centre than south. The MetUM captures this asymmetry at all resolutions, and matches the intensity of the weaker lobe in the reanalysis composites whilst overestimating the intensity in the stronger lobe. We also note a deeper circulation: the model has a well-established mid-tropospheric cyclone

that is all but absent in the reanalysis, likely coupled with the stronger and deeper latent heat release seen in Fig. 6.13. Again, once the resolution is increased beyond N320, no significant changes in structure or intensity are noted in the composite.

Summarising the composite form, we have seen that in an NWP setup the MetUM generally captures the spatial structure of monsoon depressions well[4], improving with resolution until about N512; however, the intensity is typically overestimated, increasing with resolution early on until saturation at N320. We remark at this stage the caveat of having a relatively low-resolution reanalysis (i.e. one that falls between N216 and N320); the only thing we can say with certainty is that the composites at N216 and N320 are too intense and that this bias appears to worsen with resolution, but this cannot be properly verified without higher resolution observational/reanalysis data. In the mid-troposphere, this is explained by an increase in the frequency of events of greater intensity (saturating at N320); in the lower troposphere this is exacerbated by a shift in the mode too.

6.5.2 Horizontal structure

Quantifying horizontal structure of MDs is also important: at the surface, interaction of the synoptic flow with local orography and sharp gradients in land type supports complicated, asymmetrical structure both there and aloft. One of the most strongly affected, and important, variables in this context is surface precipitation, so we shall start the discussion there. Fig. 6.15 shows composite surface rainfall for the case studies at each of the eight resolutions considered in this study, with equivalent computations based on the ERA-I/IMD tracks, taking precipitation data from TRMM 3B42. One of the most apparent features follows directly from inspection of the behaviour of rainfall in the monsoon trough in general (see Fig. 6.5), that is that the model at all resolutions tends to produce smoother, more coherent patterns. Increasing resolution

[4]We must note, however, that this is in the specific case where we have initialised the model quite close to the start date, as one would do in forecasting. We make no assertions about how a climate model would perform, particularly once biases develop in the atmosphere.

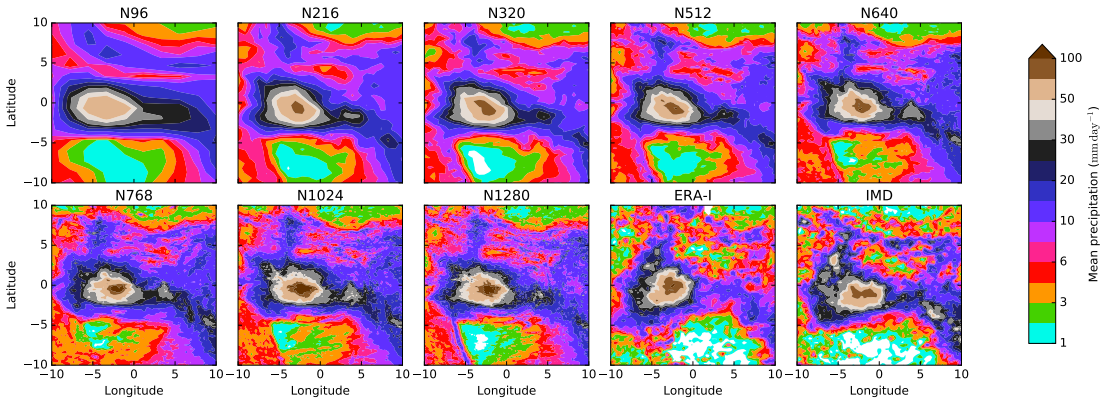

Figure 6.15: Composite total surface precipitation (mm day^{-1}, method as in Fig. 6.11) for all resolutions, as well as for the ERA-I and IMD case study tracks as computed from TRMM 3B42.

produces finer spatial features that slowly tend towards the observational structure, and causes an increase in the values associated with the near-central maximum. In combination, these result in finer resolutions seemingly producing ever higher fidelity results when it comes to rainfall. There are a few systematic problems across the spectrum of model resolutions however, some of which we have already noted while discussing representation of the trough: orographic rainfall in the southwest (Western Ghats) and northeast (Himalayan foothills) is consistently overestimated, although this does improve slightly in the northeast with increasing resolution. Inspection of the data (not shown) suggests that the model has a tendency to produce constant low rain rates at these locations which is not reflective of reality; further the rain shadow to the south, which is not so immediately obvious in Fig. 6.5 generally has too much precipitation, something that gets worse with resolution until N1280. Of course, these specific failings are not directly linked to the presence of an MD, the orography is there regardless of the state of the trough, but it is known, for example, that MDs increase (decrease) rainfall along the Western Ghats (Himalayan foothills) by as much as 15 mm day^{-1} (see Fig. 3.3(b)), and based on what we have seen so far, it seems unlikely that this would be well represented given the poor spatial structure and intensity seen (particularly over the Ghats) in Figs. 6.5 and 6.6.

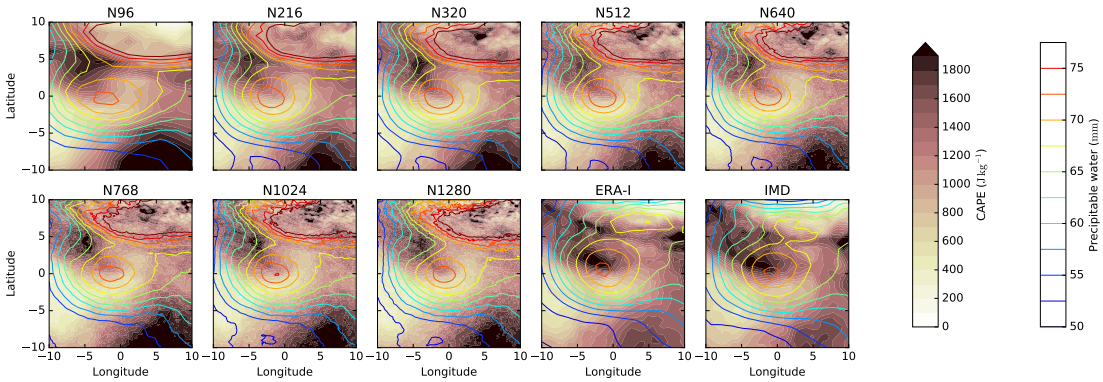

Figure 6.16: Composite CAPE (J kg^{-1}, filled contours) and total column precipitable water (mm, line contours) for each resolution, as well as for the ERA-I and IMD case study tracks as computed from ERA-Interim.

We can use other diagnostics to pick apart the precipitation structure, and it would be appropriate to select these based on the salient pretense that they ought to represent contrasting factors: for example the amount of water available in the column and the ability of the column to rain out said water, for which total precipitable water and CAPE respectively are suitable proxies. Fig. 6.16 gives the composite (horizontal) structure of TPW (mm) and CAPE (J kg^{-1}) across all resolutions and for ERA-I/IMD tracks in ERA-Interim data. These are presented such that darker block contours represent higher CAPE values and redder line contours represent higher values of precipitable water. At first glance, we see that the model has a tendency to overestimate TPW and underestimate CAPE in the vicinity of the MD centre. In terms of quantity, these errors appear to mostly cancel each other out when it comes to the precipitation composite, and although CAPE is only a proxy (if it is indeed even that) for convective rainfall, we shall see later that the majority of rain associated with the MD in the model can be attributed to convective events. In terms of spatial structure, the TPW is fairly well represented: the central maximum is arguably pushed slightly too far from the centre, particularly in the lower resolutions, but this is certainly recovered at resolutions upwards of N768; the MetUM appears to do a fairly poor job over the Tibetan plateau, and it is worth noting here that these 'parcel ascent' variables were computed from the conditions at the local surface, starting from the orographic height.

This failure does not have a significant spatial reach, however, as TPW values become rapidly comparable to those given by the reanalysis beyond the foothills. Conversely, the spatial distribution of CAPE in the model composites is quite different to that suggested by the analysis. For the sake of clarity, we note that this is computed at each timestep and then composited, i.e. it is the composite of the CAPE, as opposed to the CAPE of the composite. Across resolutions, the MetUM has a tendency to place the maximum CAPE (associated with the MD) several hundred kilometres too far to the northwest, such that it no longer really has an overlap with the MD centre. We also note that values over the ocean (far southeast) are overestimated, and values over the Himalayan foothills (near northeast) are generally underestimated.

6.5.3 Cloud structure

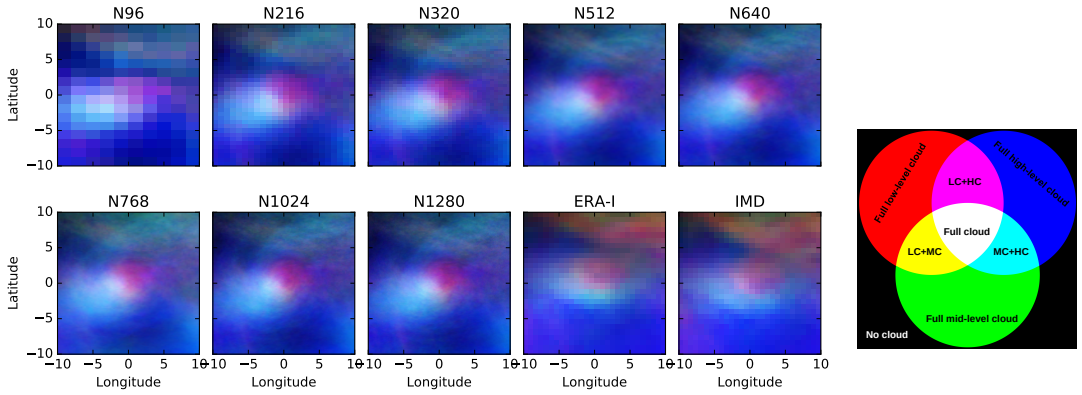

Figure 6.17: Composite cloud cover fraction for all resolutions, and ERA-I and IMD tracks determined from ERA-I. The bounding heights for the model cloud levels are defined on sigma levels that from the surface equate to 0.0 km≤low<1.8 km≤mid<5.5 km≤high<13.7 km, and for ERA-I reanalysis are defined on sigma levels that from the surface equate to 0.0 km≤low<1.9 km≤mid<6.3 km≤high. The colour scheme is explained in the right-hand subfigure.

Now, having looked at precipitation and related fields in some detail in the horizontal, we turn our attention to cloud. Cloud cover is important in the context of a depression for a number of reasons: firstly, it plays an important part in governing the thermal and diurnal structure – radiative cooling at the top caps the warm thermal

core aloft and sets up the static instability at night that is responsible for enhanced precipitation at the surface, and it serves to block insolation near the centre causing the cold thermal core at the surface; secondly it has long been thought that convective instability of the second kind (CISK; Charney and Eliassen, 1964) is at least in part responsible for the intensification of MDs (Krishnamurti et al., 1975; Sikka, 1977; Shukla, 1978; Keshavamurty et al., 1978; Chen et al., 2005). That having been said, any cross-section of a composite field that is fundamentally binary is limited in what it can tell us; however, we can use combinations of colour to represent three variables simultaneously. We can use this in conjunction with the model/reanalysis output fields of low-/mid-/high-level cloud cover which assess the fractional cloud amount between two pre-defined heights. For both the MetUM output and ERA-Interim, these heights are defined on sigma levels that correspond to (from the surface):

$$\text{low} < 1.8\,\text{km} \leq \text{mid} < 5.5\,\text{km} \leq \text{high} < 13.7\,\text{km} \tag{6.2}$$

for the MetUM and

$$\text{low} < 1.9\,\text{km} \leq \text{mid} < 6.3\,\text{km} \leq \text{high} \tag{6.3}$$

for ERA-Interim. Fig. 6.17 shows the composites for these variables across model resolutions (and for ERA-I/IMD tracks) displayed in colour space: that is to say, if each of low-/mid-/high-level cloud cover have a range of 0 to 1, and we define coordinates in RGB colour space, (R, G, B) such that (0, 0, 0) is black and (1, 1, 1) is white, then we can represent cloud cover by the unique colour coordinate (C_L, C_M, C_H) where C_L, C_M, and C_H are low-/mid-/high-level cloud cover fractions respectively; thus, for example, full low-level cloud cover with nothing above it would be represented as pure red. Looking at Fig. 6.17(a) with this in mind, we see a common structure emerging across the resolutions and in the reanalysis composites: full cloud cover in the region immediately southwest of the centre, extending for several hundred kilometres,

conversely in the northeast quadrant, low-level cloud dominates; there is also ubiquitous high-level cloud, along with a mix of all types over the Himalayas in the far northeast. This overview agrees with the CloudSat-derived composite in Fig. 4.5, which suggested deep cloud persisted south of the centre, transitioning to lighter, lower-level cloud in the north with stratus and altostratus over the Himalayas. There are, unusually, few differences across the resolutions when it comes to spatial distributions or even magnitudes: the axis separating deep cloud and low-level cloud rotates from north-south at lower resolutions, and finer structure becomes apparent, including traces of individual squall lines and rain bands. These compare fairly well to the reanalysis composites (even given the different classification boundaries between the two sets of products) although there are some subtle differences: the deep cloud cover to the southwest of the centre is weaker than suggested by the MetUM composites, and tends to be elongated and wrapped around the centre as opposed to being roughly isotropic with a well defined maximum; and the Himalayas are handled differently, but since these are purely modelled products (even in the reanalysis), it is likely inconsequential.

6.5.4 Diurnal cycle

The diurnal cycle of Indian monsoon depressions was first characterised and detailed in §4.5 using observations from TRMM 3B42. We showed that two strongly-varying modes of differing spatial scales existed almost in antiphase, and that these could, together, be simply modelled as the sum of two arbitrarily phased Gaussians (form given in §4.5). This function was then fit to diurnally separated data (by which we mean composites of 00Z, 03Z, 06Z, ..., 18Z) to recover the two distinct modes: an outer mode peaking at dusk with small magnitude and large scale, related to the tropical convection cycle over land, and a central mode peaking at dawn with large magnitude and small scale, related to the radiation-induced instability in the column. We now repeat the analysis of §4.5 across our range of resolutions to determine to what extent the MetUM is capable of capturing the diurnal cycle, and how resolution affects it.

Resolution	min(time) c-mode max(time)	min(time) o-mode max(time)
TRMM	17.48(09)	7.52(03)
3B42	34.09(00)	15.58(12)
	16.87(12)	2.35(12)
N1280	39.25(00)	6.80(06)
	17.66(09)	2.48(12)
N1024	40.91(00)	6.58(06)
	16.28(09)	2.42(12)
N768	36.03(00)	6.56(06)
	15.81(09)	2.28(12)
N640	31.23(00)	6.54(06)
	13.87(12)	2.66(15)
N512	32.63(00)	6.29(06)
	12.43(09)	2.65(15)
N320	27.51(00)	6.18(06)
	13.38(12)	2.53(12)
N216	25.18(00)	6.39(00)
	5.32(15)	2.18(18)
N96	13.08(00)	5.36(00)

Table 6.3: Values (mm hr^{-1}) and times (UTC) of the maxima and minima for the outer (o-) and central (c-) modes of MD precipitation diurnal variability (i.e. A_{outer} and A_{central} respectively), computed from fitting eq. 4.5 to the respective composites for each resolution. Also provided are the climatological values for MDs between 1998 and 2014 using TRMM 3B42 data, from the analysis discussed in §4.5.

The maximum and minimum values of the amplitude coefficients, A_n, (mm hr^{-1}) for each mode and each resolution are given in Tab. 6.3, along with their respective times (to the nearest 3 hours, representative of the model output temporal resolution): we see that the central mode is very well captured from N512 upwards (though a little too intense), but the outer mode is rather poorly represented – both in being far too weak, and in getting the timings entirely incorrect. The failure of the model to accurately represent the outer mode is in line with the peak of tropical convective activity in parametrized models coinciding with the solar zenith (e.g. Rio et al., 2009), and there is no reason that we should necessarily expect this common issue with global models

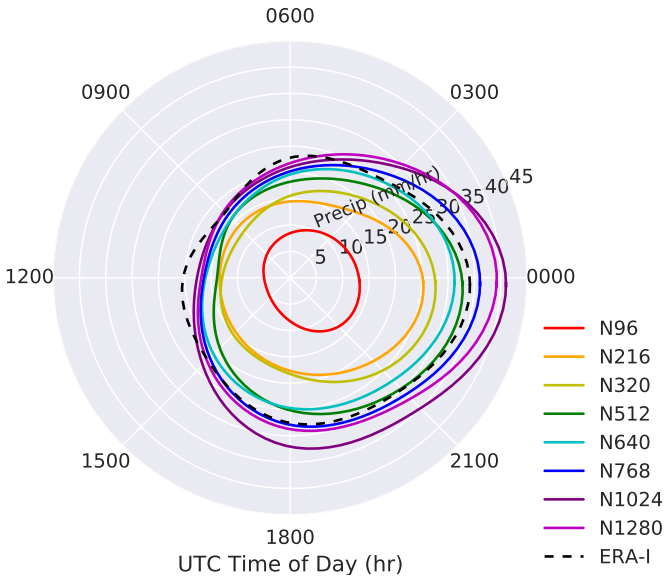

Figure 6.18: Amplitude, as a function of time (UTC) of the central (c-) mode for precipitation (mm hr^{-1}) for MDs across all resolutions (solid, coloured), and the climatology for ERA-I-tracked MDs in TRMM 3B42 (dashed, black).

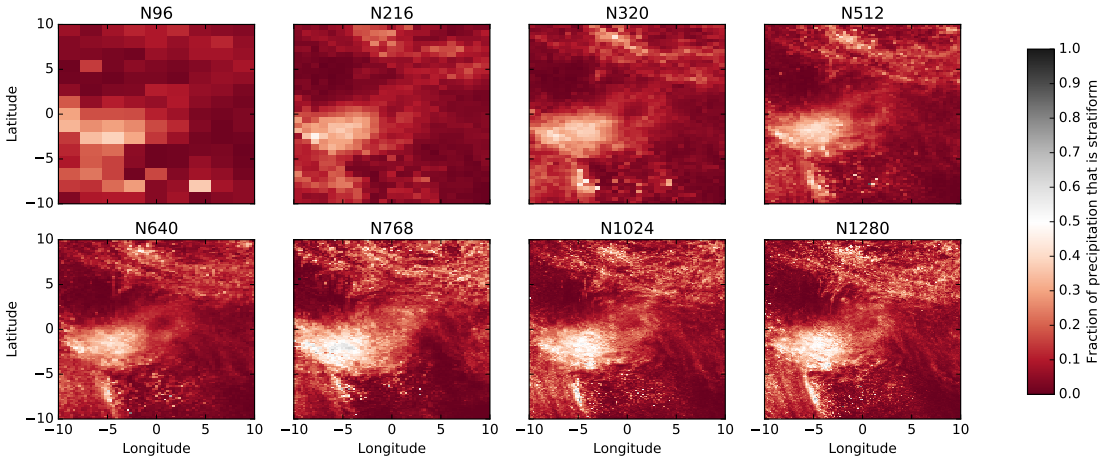

Figure 6.19: Composite fraction of surface precipitation caused by stratiform processes (as opposed to convective) in the model, across all resolutions. This is intended to allow direct comparison with the values from TRMM climatologies in Figs. 4.9 and 4.10

to be magically fixed by the presence of a nearby MD.

We next turn our focus to the representation of the central mode. This is responsible for 67% of the MD precipitation in observations (up to around 85% in the higher resolution models), and MDs are in turn responsible for a majority of monsoon precipitation in northern India (Mooley, 1973), so it is clearly important that this is well represented in forecast models. Fig. 6.18 shows the values of A_{central} (mm hr^{-1}) as a function of time across all resolutions and for the climatology; as we might have

expected from Tab. 6.3, resolutions greater than N512 capture the cycle very well with slight overestimation of the magnitude that is recovered slightly at N1280, although there is also a faint semidiurnal signal in the observations that does not appear to be replicated by the model. This high fidelity at the finer resolutions is a strong indicator that the bulk of MD precipitation is not being generated by the convective parameterisation scheme. We test this by interrogating the model output to determine whether this is the case, since the convective and microphysical (large-scale) schemes in the MetUM keep their precipitation output separate, so we can compute the composite ratio of stratiform/convective precipitation. Fig. 6.19 shows the ratio of stratiform precipitation to total precipitation for the composite MD across all resolutions. The reader is encouraged to compare this with the climatology as determined by TRMM, given in Figs. 4.9 and 4.10. As noted there, satellite observations regarding the attempted separation of precipitation into purely stratiform or convective mechanisms is nontrivial and is riddled with caveats; however, they produced climatologies at two different confidence levels: one where TRMM was essentially certain of the diagnosis either way (this left approximately half of the precipitation unaccounted for), and one where all precipitation was prescribed to either convective or stratiform regimes regardless of the certainty. It was speculated there based on the work of Houze (1997) that for the latter case the stratiform fraction could be substantially overestimated and so we might expect Fig. 6.19 to more closely resemble the 'definitely stratiform' regime presented in §4.3.2. This is indeed the case, and therefore indicates one of two things: either the MetUM is underestimating stratiform precipitation in the monsoon trough region or TRMM precipitation radar is overestimating it; based on our earlier analysis of the outer diurnal mode of precipitation and recent discussion, it seems most likely that the latter is true. Intercomparison of the ratios reveals that the increase in composite precipitation rate near the MD centre with finer model resolution is strongly correlated with increased stratiform precipitation; and representation over orography (Western Ghats, Himalayan foothills) is also improved.

6.6 Conclusions

We have examined the relationship between Indian monsoon depressions and horizontal resolution in the Met Office Unified Model. Seven case studies were used in the global model at eight resolutions ranging from N96 (208 km) to N1280 (16 km). We then compared the resulting tracks, vertical and horizontal structure of the MDs, and the representation of the monsoon trough.

On the whole, we have seen that the MetUM represents the spatial structure of monsoon depressions fairly well. This improves with increasing resolution but typically saturates at (i.e. there are diminishing returns beyond) N320 or N512 (well below the operational resolution of the Met Office, N768). Unfortunately, even at the lowest resolutions, the intensity across many fields is overestimated, a problem that increases with resolution but typically saturates at N320. That having been said, we have compared these fields to those in ERA-Interim, whose resolution falls between N216 and N320; without observations or reanalysis at a higher resolution, it is not possible to say with certainty that errors worsen in those fields compared to ERA-I. Even so, the mean rainfall structure and rate is generally well captured, including some finer detail, at N640 and above; and the same holds even for CAPE at N768 and above, although the structure is not as centralised as reanalysis suggests.

It is not clear why N320 is the resolution beyond which little improvement in representation is gained. One might suppose that among the phenomena important for the growth and sustainment of MDs, there are none with length scale 15-60 km. This is plausible if we consider common mesoscale events in the subcontinent: mesoscale convective systems (MCSs) have a scale of the order of 10^5 m and are known to interact constructively with tropical depressions (e.g. Houze, 1989) whereas individual thunderstorms and convective cells have a length scale of the order 10^3 m and are thus parameterised at all resolutions presented here. A detailed analysis, which has not been done here, would be needed to verify this.

We also looked at the diurnal cycle, finding that the mode governing the heavy (and typically mostly stratiform) rainfall associated with the central-southwest maximum was well represented and had amplitude increasing with resolution with the optimal resolution being between N640 and N768. Conversely the mode associated with the weaker, larger-scale (mostly convective) precipitation is represented very poorly, a fact that does not change with resolution. This is likely due to the requirement of convective parameterisation, a constraint that cannot be lifted until resolution reaches the order of 4 km (∼N5000). It remains an open question how models at convection-permitting resolution represent MDs and will be the subject of future work.

Overall, and taking into account the inflated cost of running higher resolution models, it seems that a resolution of N512 (or at a push, N320) is sufficient to describe the composite MD structure in an initialised NWP model framework, although if one weights the track forecast highly, increasing this to N768 is recommended.

It is not clear what process in the model drives its tendency to overpredict MD intensity (although we again recall the caveat of low ERA-I resolution). We have seen that the mid-tropospheric warm anomaly is too strong, indicating too much latent heat release there, although this is not backed up by the presence of more mid-level cloud as one would expect. It is possible that the known difficulty of writing an effectual convective parameterisation and the high dependence of tropical depressions on said convection is the prominent source of this bias, but correctly determining this would require a subsequent study to explore the sensitivity of MDs to model physics.

We have covered a range of resolutions also used in climate models (usually N512 and below). Although this problem differs slightly in that the MDs are not initialised, we can assume some similarity in structure is likely given the spin-up time in our case studies. Based on the behaviour of the depression-trough, it seems likely that increasing resolution would cause a higher MD genesis rate, particularly in the north of the Bay of Bengal, where the trough deepens the most. This agrees in principle with the sensitivity tests of Johnson et al. (2016). Given the discussion above, we suspect

that gains in structural representation would be marginal beyond N320.

In the previous chapter, we showed that predictors our propagation model retained some variance, which would not be the case if the model were entirely correct with no other factors influencing the MD tracks. This is evidently, and reasonably, not the case, consider Fig. 3.17 where we showed that CAPE has a well defined maximum ahead of the MD centre. It is not a big jump to suggest that land surface conditions in the advance of an MD play some role in its behaviour. Now, having shown that the Met Office NWP model represents MDs with fairly high fidelity, we can use it to further probe this problem in the next chapter, where we will explore the role of arguably the most important land surface variable (in the context of MDs), soil moisture, and use this NWP model to determine its relationship with depressions.

CHAPTER 7

THE EFFECT OF SOIL MOISTURE PERTURBATIONS ON INDIAN MONSOON DEPRESSIONS IN A NUMERICAL WEATHER PREDICTION MODEL

7.1 Introduction

Whilst the spin-up mechanism of MDs remains uncertain (Cohen and Boos, 2016), it appears likely that convective instability of the second kind (CISK; Charney and Eliassen, 1964) plays at least some role (Shukla, 1978); however, their primary propagation mechanism has been well described, albeit fairly recently (Boos et al., 2015), as a coupling of horizontal nonlinear advection of the mid-tropospheric potential vorticity maximum and, as we proposed in Chapter 5, an image vortex interaction of the lower-tropospheric PV maximum with the no-normal flow condition imposed by the Himalayas.

It also remains unclear what synoptic variables, if any, control the duration and ultimate dissipation of MDs; there is some evidence that a contemporaneous monsoon flood year or active spell tends to extend the duration of depressions in the north of the peninsula (Krishnamurthy and Shukla, 2007; Krishnamurthy and Ajayamohan,

2010), although this has not yet been disentangled into a primarily synoptic (primed troposphere) or mesoscale (primed land surface) theoretical framework. Nevertheless, recent work has shown that favourable conditions (e.g. higher vorticity, more moisture) at both scales is correlated with increased MD activity, duration, or intensity: e.g. for soil moisture by Chang et al. (2009); Kishtawal et al. (2013), and for the active phase of the monsoon in §3.6.

Eltahir (1998) was the first to provide a solid theoretical pathway to accompany the long-held assertion that an increase in large-scale soil moisture induces enhanced precipitation. He proposed that the drops in surface albedo and Bowen ratio caused by wetting soil work to increase the near-surface specific moist static energy and boundary layer moist static energy gradient, which results in more favourable conditions for precipitation. If, however, this is to be an important process in MDs, it is likely to be indirect[1]: the area of maximum precipitation is found to the southwest of the centre (e.g. Ramanathan and Ramakrishnan, 1933) where the (adiabatic) quasigeostrophic omega equation (e.g. Holton and Hakim, 2012),

$$\left(\nabla^2 + \frac{f_0^2 \partial^2}{\sigma \partial p^2}\right) \omega \approx \frac{f_0 \partial \mathbf{v_g}}{\sigma \partial p} \cdot \nabla \left(\frac{\nabla^2 \Phi}{f_0} + f\right) , \tag{7.1}$$

predicts where the greatest ascent associated with the balanced MD vortex will be (Boos et al., 2015); in contrast the Bowen ratio tends to reach a minimum just ahead (northwest) of the centre (see Fig. 3.9). To elucidate this, following §3.3, Fig. 7.1 shows the mean Bowen ratio (ERA-Interim; Dee et al., 2011) and precipitation (TRMM; Kummerow et al., 1998; Huffman et al., 2010) for a 106-depression composite (34-depression composite for precipitation, given the shorter extent of TRMM data) in which location and orientation are normalised such that the centre lies at the origin and the heading is up the page; land-only data were used. As asserted, there is little spatial similarity between the extrema of precipitation and Bowen ratio - indicating that if we

[1]It must also overcome a negative feedback at the MD centre – the associated lower-tropospheric cold core (see Godbole, 1977; and Fig. 3.15(a)) acts to cool the surface and increase stability there.

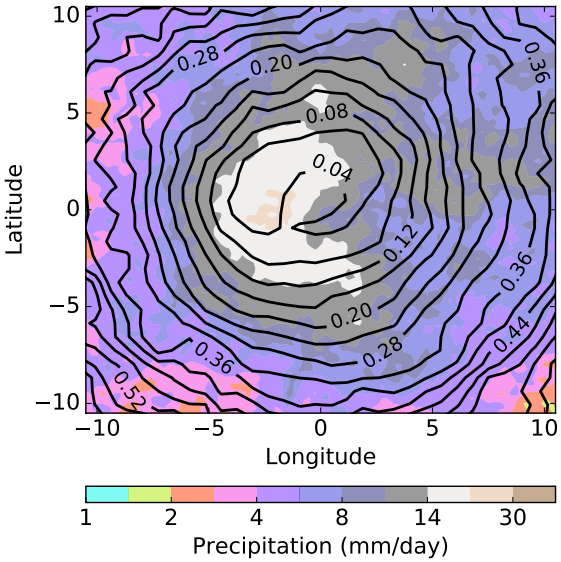

Figure 7.1: Bowen ratio (lines) and precipitation (colours) for a 34-depression composite (1998-2014), as described in §3.3.1; the composite is normalised such that the centre of each depression is placed at the origin, and each is rotated so that the heading is up the page. For both fields, only points over land were composited.

are to believe previous work suggesting a link between MD behaviour and underlying soil moisture, it may be a more subtle feedback, or work on a finer spatial scale, than that suggested by Eltahir (1998). The caveat here is that surface fluxes are an entirely modelled product in ERA-I, and so have substantial uncertainty; however this is at least partially addressed by the similarity of composite MD precipitation between ERA-I and TRMM, and the fact that most rainfall near the centre of a depression is stratiform in nature (Hunt et al., 2016b). To date, a number of studies have shown that assimilation of soil moisture, or better initial representation of it, improves the forecast of monsoon depressions in mesoscale models (Chandrasekar et al., 2007; Vinod Kumar et al., 2007; Chandrasekar et al., 2008; Rajesh and Pattnaik, 2016).

Soil moisture is one of the meteorological variables subject to greatest change with respect to the progression of the Indian monsoon, largely due to its correlation with accumulated precipitation. The NOAA CPC reanalysis soil moisture climatology (Van den Dool et al., 2003) and the ESA CCI satellite-derived soil moisture climatology (Liu et al., 2011, 2012a; Wagner et al., 2012) for India for each summer month are given in Fig. 7.2(a) and Fig. 7.2(b) respectively and show a clear northwestward advance through most of the season: some areas in the monsoon trough have Septem-

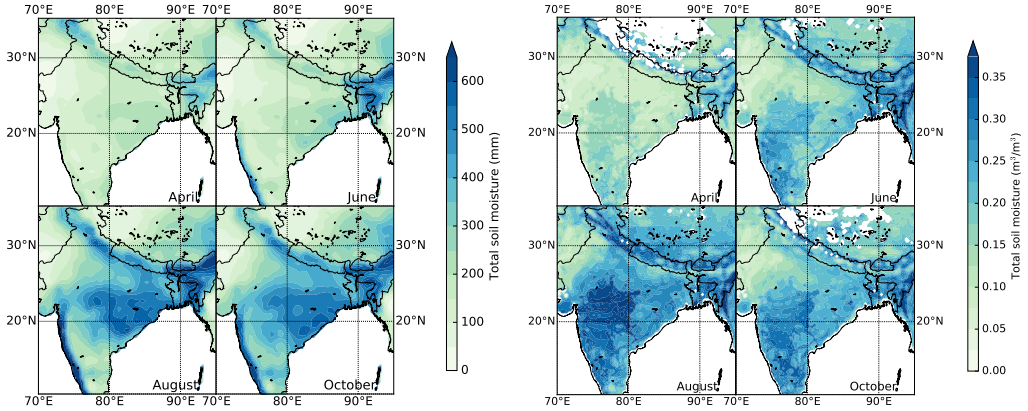

(a) NOAA Climate Prediction Center (1948-2016) (b) ESA Climate Change Initiative (1991-2014)

Figure 7.2: Monthly soil moisture climatologies for the Indian peninsula from two products: (a) NOAA CPC reanalysis total soil moisture (data provided by the NOAA/OAR/ESRL PSD, Boulder, Colorado, USA, from their website at `http://www.esrl.noaa.gov/psd/`) and (b) ESA CCI satellite-derived volumetric soil moisture.

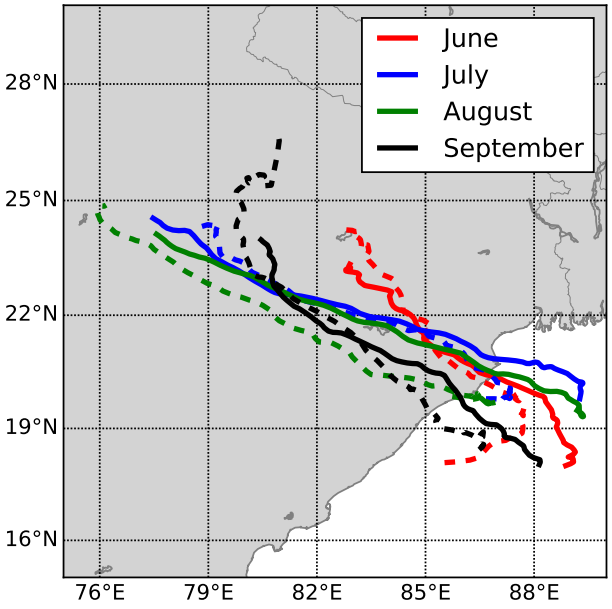

Figure 7.3: Average MD tracks for each month (June through September represented by red, blue, green, and black respectively) during the Indian monsoon. Solid lines represent mean tracks from the database outlined in §3, dashed lines from the Hurley and Boos (2015) database. These tracks also include days where the disturbance is classified as a monsoon low, as well as a monsoon depression.

ber soil moisture more than double that of June. Naïvely, then, we might expect MD tracks to penetrate deeper inland later into the monsoon season, given the expected influence of antecedent soil moisture on the development of MDs. Fig. 7.3 shows the mean MD track for each month (1979-2015) from the track datasets from Chapter 3 and Hurley and Boos (2015) respectively; note that the MD tracks have been extended

to include parts where the depression is strictly in a monsoon low regime (that is to say, the surface winds are below 8.5 m s^{-1}). There is some weak evidence here to suggest that not only do MDs tend to progress further inland later in the season, they also seem more likely to have over-land genesis. This should be taken with the caveat that large-scale conditions over the subcontinent also clearly play some part, given that there is evidence that the September tracks start to recede, despite high levels of soil moisture remaining.

So, if soil moisture has some effect on the duration of MDs, which seems at least plausible, we are then faced with with the secondary question of whether antecedent soil moisture patterns could affect the heading of existing MDs. Chen et al. (2005) showed that, in theory, the off-centre latent heat released by the asymmetric rainfall distribution would interact with the local circulation to create a negative velocity potential southwest of the MD centre, and therefore that there would be some tendency for the MD to move in that direction. Depressions typically move northwestward, rather than southwestward (they even tend to veer north/northeastward during lysis), however; but while this can be ruled out as a primary effect, it remains plausible as a secondary one. Two simple experiments are therefore proposed: firstly a uniform change in soil moisture across the monsoon trough region to determine the sensitivity of MD duration to antecedent land surface conditions; secondly a uniform change in soil moisture in the highly farmed region across the Himalayan foothills (typically several hundred kilometres north of MD tracks; Roy et al., 2015) to determine to what extent MDs can be steered by soil moisture.

We will discuss the experimental setup and outline the methodology in §7.2, then outline and interrogate the results, looking at contrasts in track and structure in §7.3 before concluding in §7.4.

7.2 The Met Office Unified Model and experimental setup

7.2.1 Overview and case study selection

The version of the Met Office Unified Model (hereafter, the UM) used for this study runs the Global Atmosphere 6.0 scheme (GA6.0; Walters et al., 2015) at N768 resolution ($\sim$ 26 km) with 85 vertical levels over a global domain; the numerical scheme is semi-implicit and semi-Lagrangian (Davies et al., 2005), and due to the resolution a number of subgrid processes are parameterised, including convection (e.g. Gregory and Rowntree, 1990, with additions).

In choosing an appropriate case study to use in this experiment, we were subject to two criteria: firstly, and more importantly, that the MD happened within the last few years - this means that higher resolution, better quality analyses are available for initialisation; secondly, that the MD had a track resembling the average for MDs (see Fig. 7.3) that it could be seen as a fair representative of the spectrum of MDs incident on the east coast of the peninsula. The most suitable such event was the MD of early August 2014, which featured depression-status wind speeds from 200 km south of Kolkata until it was downgraded to a monsoon low 400 km due south of Delhi. All experiments were initialised at 00Z on August 3rd, the day this event was declared a monsoon depression.

7.2.2 The land surface scheme

The operational land surface model in the Met Office UM is the Joint UK Land Environment Simulator (JULES; Best et al., 2011). This employs the Met Office Surface Exchanges Scheme (MOSES; Cox et al., 1999; Essery et al., 2003) to handle hydrological processes both subterranean and in the boundary layer. A brief description of the governing equations in the soil hydrology subroutine, which is taken from the relevant part of the MOSES documentation, is given in Appendix C. The interaction between clouds and shortwave/longwave radiation is also handled explicitly by the prognos-

tic cloud scheme in the UM (PC2; Wilson et al., 2008) following Edwards and Slingo (1996).

7.2.3 Ensemble generation

There are two types of stochastic perturbation that can be employed to generate a spread of forecasts in a numerical weather prediction model: uncertainties in the analysis can be represented by perturbing the initial conditions, whereas uncertainties in the model can be represented by using any number of physics perturbations (e.g. time-varying parameterisations). Operationally, the Met Office use The Met Office Global and Regional Ensemble Prediction System (MOGREPS; Bowler et al., 2008), to generate ensemble NWP runs; given that this was designed specifically for the UM, we aim to make our ensemble generation as similar as possible. MOGREPS uses two distinct stochastic physics schemes: random parameters (RP) and stochastic kinetic energy backscatter (SKEB). The former uses the premise that many parameters in the various parameterisations in the UM are tuned to empirical values that appear to give the best representation of the relevant process, these can be periodically varied at differing frequencies between physically reasonable values to produce a spread of forecasts; the latter reintroduces kinetic energy lost through poor representation of the mechanisms by which small-scale processes cascade energy to larger scales (Shutts, 2005). Initial tests suggested that using SKEB perturbations tended to artificially weaken MDs and cause them to have much shorter tracks. Thus in our study we used a stochastic perturbed tendencies (SPT) scheme which simply randomly perturbs the summation of tendencies from all parameterisations in the model (Buizza et al., 1999).

In our ensemble, we must also attempt to represent uncertainties in the analyses that are used to initialise the model. In MOGREPS this is typically done by applying an ensemble transform Kalman filter (ETKF; Bishop et al., 2001) to a previous ensemble run, assimilating observations to assess where perturbations will have the largest impact. As operational ensemble analyses were not readily available for our

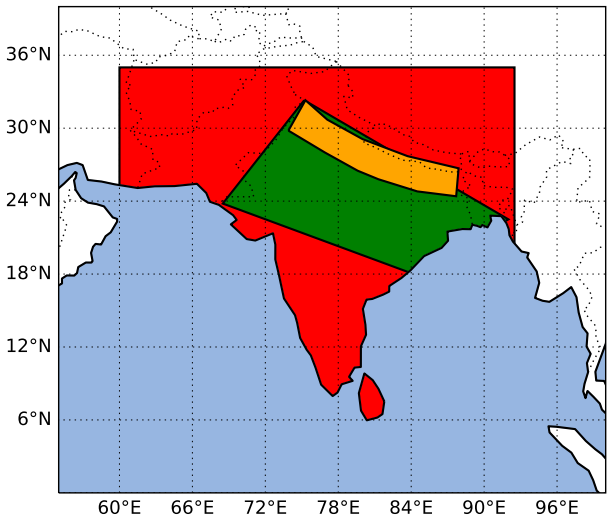

Figure 7.4: Map showing the three masks used in the experiments in this study. The red box covers the entire peninsula and some of the rest of South Asia, the green box approximates the region where the monsoon trough is most active, and the orange box covers the intensely irrigated and farmed area in the Himalayan foothills.

case study, we opted to simulate the uncertainty by adding white noise of amplitude 0.5 K to boundary layer potential temperature. Sensitivity tests determined that this gave a realistic spread of MD tracks from a short initialisation without suppressing the development and progression of the depression. For each sub-experiment, which are differentiated by varying soil moisture in the same region, a ten-member ensemble was used; for each ensemble member, a random seed was used such that across each experiment each ensemble was generated via the same set of pseudorandom parameters to allow intercomparability.

7.2.4 Soil moisture ancillaries

As discussed in §7.1, two case study experiments are proposed to explore the sensitivity of duration and heading respectively to underlying soil moisture. Fig. 7.4 shows the masks used to set up the soil moisture ancillary files: the red polygon covers much of South Asia, the green polygon covers the typical monsoon trough region, and the orange covers the sub-Himalayan arable land that is becoming increasingly intensively irrigated and farmed. In each instance, the soil moisture control (perturbations to which will be used in the experiments) is the August climatology as computed from a fully coupled high-resolution climate simulation in the UM. This was chosen to reduce

spin-up/resolution issues that could be introduced by using a climatology from, e.g., either of the datasets in Fig. 7.2.

For the first experiment (hereafter: *trough zone*), soil moisture in the monsoon trough region (the green polygon in Fig. 7.4) - in which MD tracks are typically entirely embedded - was altered to 1%, 80%, 100% (control), 120%, and 500%[2] of its August climatological value. The values of 1% and 500% were chosen to represent two extremes: the barrenness of soil after an extended break period or pre-monsoon, and saturated soil during an active period respectively. In actuality, whilst the latter is not uncommon, soil moisture values typically do not fall below 20% of the climatological value; however this is a sensitivity test, not a forecast, and we are interested on the limits of the impact of soil moisture on an MD. Conversely, for the second experiment (hereafter: *arable zone*), soil moisture over South Asia (the red polygon in Fig. 7.4) is set to 1% of its August climatological value, except for inside the arable sub-Himalayan area (orange polygon) where the values were set to 1%, 50%, 100%, and 500% of the climatology. This region was traced to resemble, as much as possible, the belt of sub-Himalayan arable grassland where irrigation is becoming rapidly and increasingly prevalent (Roy et al., 2015) - the area where anthropogenic changes to the surface are likely to have the biggest impact. Values of soil moisture approaching 1% of the August climatology could be found in an *extremely* dry pre-monsoon period, but we remind the reader that the purpose of this experiment is to test the effect of soil moisture contrast in the region, not necessarily to replicate a physical event.

7.2.5 Tracking

The tracking algorithm used to determine the trajectories of MDs in output data is that described in §2.1. Data at individual timesteps in the output are filtered subject to the IMD criteria for MDs (minimum 8.5 m s^{-1} surface wind speed and two closed

[2]This value unsurprisingly gives significant oversaturation across much of the region. Where this was the case, soil moisture values at these locations were set to their saturation values. In reality, this scaling is achievable only over the dry northwest, and the average saturation value over the trough region is approximately 167%.

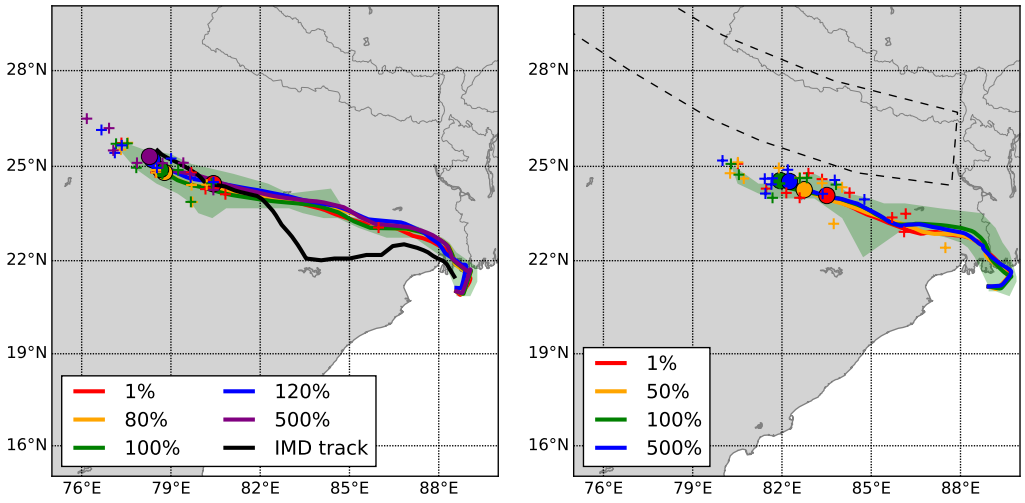

(a) Trough zone (b) Arable zone

Figure 7.5: Track results from varying soil moisture in (a) the monsoon trough and (b) the sub-Himalayan *arable zone*. For each sub-experiment, the average track is given by the thick line with its termination given by the filled circles, and the individual ensemble 10-member track terminations are given by crosses of the same colour. Also shown, in pale green, is a concave hull of the "100%" (for (a), this is simply the control) ensemble plume for each experiment. In (a), the official MD track from the Indian Meteorology Department is given by the solid black line; in (b), the border of the *arable zone* is denoted by the dashed black line.

surface isobars at even hPa values) as well as some transient-filtering criteria (lower-tropospheric vorticity above 1×10^{-5} s^{-1}, smoothed vorticity must be local maximum), and single-timepoint candidates are linked together using a simple nearest-neighbour algorithm.

7.3 Results

7.3.1 Tracks

Tracking results from the *trough zone* experiment are shown in Fig. 7.5(a). The average tracks for each sub-experiment (thick, coloured lines) were computed using normalised track durations for each of the 10 ensemble members; that is to say points were grouped and averaged by total MD lifetime fraction rather than absolute time since genesis, with termination points for all ensemble members across the experiment given by crosses of

the relevant colour. The pale green area underneath is a concave hull of all points of all ensemble tracks from the control sub-experiment (i.e. underlying soil moisture set at 100% of the August climatology).

A first inspection of the average tracks seems to suggest that an increase in underlying antecedent soil moisture results in deeper penetration of MDs through the monsoon trough region - this is visible both in the average termination points and the individual ones. Further inspection indicates that both the 500% and 120%, and 100% and 80% average tracks are closely matched pairs, both along track and at termination. The former couple is a result of the August soil climatology already being fairly close to saturation in this region, so the difference between 20% extra moisture and saturation is fairly small. Performing Hotelling's t^2-test[3] (Hotelling, 1992) to assess whether the sub-experiment ensemble terminations are distinct from each other, we find that all pairs apart from the aforementioned two are significantly different from each other at the 95% confidence level. This leads us to conclude there is a likely causal relationship between large-scale antecedent soil moisture in the monsoon trough region, and the duration/distance travelled by incident monsoon depressions.

The *arable zone* experiment was set up to determine to what extent moisture changes in relatively distant soil could affect the steering of a contemporaneous MD. Recall that for this experiment, the soil moisture over South Asia was set to 1% of the climatology, and to the value specified (1%, 50%, 100%, or 500%) of the climatology in the sub-Himalayan belt. The results from this experiment are presented in Fig. 7.5(b) in an identical fashion to those from the *trough zone* experiment. In the absence of a control run, the concave hull given is for the "100%" ensemble plume. While it may seem contrived to have such extremely dry soil over almost the entire peninsula for the sake of establishing a strong contrast for our experiment, these desiccated conditions are not particularly uncommon in the pre-onset conditions of late May (Fan and

[3]This is the multidimensional generalisation of the standard student's t-test for determining whether data are significantly different from each other. We have also applied Welch's generalisation to allow for unequal variance in the two comparison populations (Welch, 1947).

van den Dool, 2004) where extreme surface temperatures and scarce precipitation are usual, and depressions can still form in the Bay of Bengal (Rao and Jayamaran, 1958; Mooley, 1980).

An initial overview of Fig. 7.5(b) suggests two broad characteristics: firstly, that the spread of ensemble mean terminations is smaller than in the *trough zone* experiment - this is almost certainly attributable to the altered soil area both having a smaller area and being further away, and thus being less influential; secondly, that all the average tracks are shorter than in the previous experiment - plausibly due to a larger area of desiccation than in the 1% *trough zone* sub-experiment resulting in even less water being available over the peninsula, bearing in mind that MDs draw moisture in from distances of up to 1000 km (see, e.g. Fig. 3.4). We also note that whilst the latitudes of the lyses are perfectly correlated with the fractional soil moisture changes (e.g. 500% track finishes northmost, 1% finishes southmost), the mean track for the 100% sub-experiment is longer than that for the 500% ensemble. Repeating the termination point significance analysis carried out for the *trough zone* experiment, we find that the three wettest sub-experiments have mean track termination points significantly different from the driest (1%), but not from each other, at a 95% confidence level.

7.3.2 Structure and evolution

Having established that soil moisture changes, both local and distant, are capable of significantly altering the track of a passing MD, we will now examine the differing synoptic structure that these changes cause and attempt to bring the discussion to its conclusion. The largest contrast was seen in the *trough zone* experiment, so we shall start the discussion there. Fig. 7.6 shows longitude-height cross-sections through 500%-minus-1% composite variables from the *trough zone* experiment. We will briefly note here that structural changes of similar shape are found by comparing composites arising from smaller changes in soil moisture, but with varying losses in magnitude, and hence, significance. The centre of the MD (assuming one existed) at each timepoint

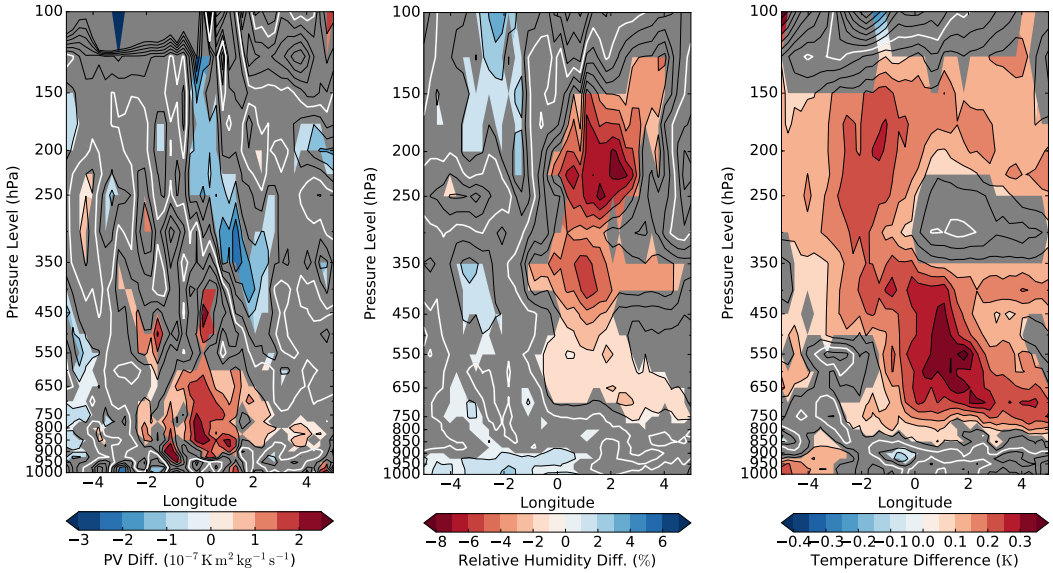

(a) Potential vorticity (b) Relative humidity (c) Temperature

Figure 7.6: Differences in selected fields of the composite mean ensembles for the 500% and 1% (the former minus the latter) *trough zone* experiment. The composite is normalised such that its centre lies at the origin, but no rotation is carried out; these are then presented as a height-longitude cross section (at zero latitude). Greyed areas indicate the difference between the sub-experiment composites was not met at the 95% significance level according to a 10,000 member bootstrap test. The selected fields are: (a) potential vorticity (10^{-7} K m^2 kg^{-1} s^{-1}), (b) relative humidity (%), and (c) temperature (K). White lines on each subfigure indicate the zero contour.

across all ensemble members for the relevant sub-experiment is centered at the origin; but unlike Fig. 7.1, we do not rotate these composites since the soil moisture changes introduced were anisotropic. We note that these differences are consistent across the other, non-extreme, experiments (not shown) albeit with reduced areas of significance (typically more confined to the upper troposphere) and smaller magnitudes.

We see that the composite MD for the wettest soil moisture case (in contrast to the driest) is more intense, as the mid-tropospheric thermal high (Godbole, 1977; Hurley and Boos, 2015; Fig. 3.15(a)) is markedly stronger, with accompanied strengthening of both the 700 hPa and 500 hPa PV maxima; secondarily there is evidence of an anomalous west-east circulation with enhanced ascent ahead of the MD centre (i.e. to the west) with enhanced relative humidity there, and decreased humidity and PV in

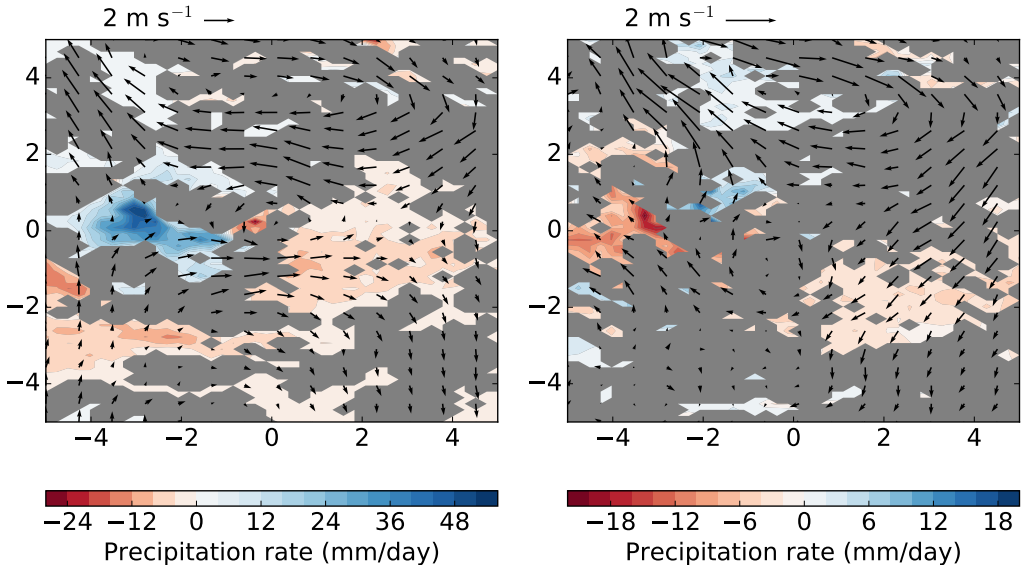

(a) Trough zone (b) Arable zone

Figure 7.7: Longitude-latitude cross-sections of composite precipitation (mm day^{-1}) and 850 hPa winds, taken as the difference of the ensemble means for the 500% and 1% sub-experiments (i.e. 500% mean minus 1% mean) of (a) the *trough zone* experiment and (b) the *arable zone* experiment. Construction and representation of significance are identical to that of Fig. 7.6. Note that while these composites are centred on the MD, they are not rotated.

the upper troposphere behind the centre; and, further, there is evidence of increased westward axial tilt with height. We would expect these effects to be associated with increased precipitation west of the centre, and we see in Fig. 7.7(a) that this is indeed the case. Fig. 7.7 gives the 500%-minus-1% horizontal composite surface precipitation and 850 hPa wind for both experiments. In the case of the *trough zone* experiment, we see, as expected from the previous discussion, a substantial increase (beyond 40 mm day^{-1}) in precipitation downshear (i.e. to the west) of the MD, with some slight reduction towards the east of the centre; however it is not clear whether the increase in soil moisture enhances precipitation via the Eltahir mechanism, or simply whether it allows more moisture to be inserted into the MD that then grows by other means. The 850 hPa composite difference winds are also given in this figure; they indicate the increased soil moisture sets up a large-scale, weak anomalous anti-cyclone that is split roughly in half, noticeably intensifying the zonal components of the MD circulation near the

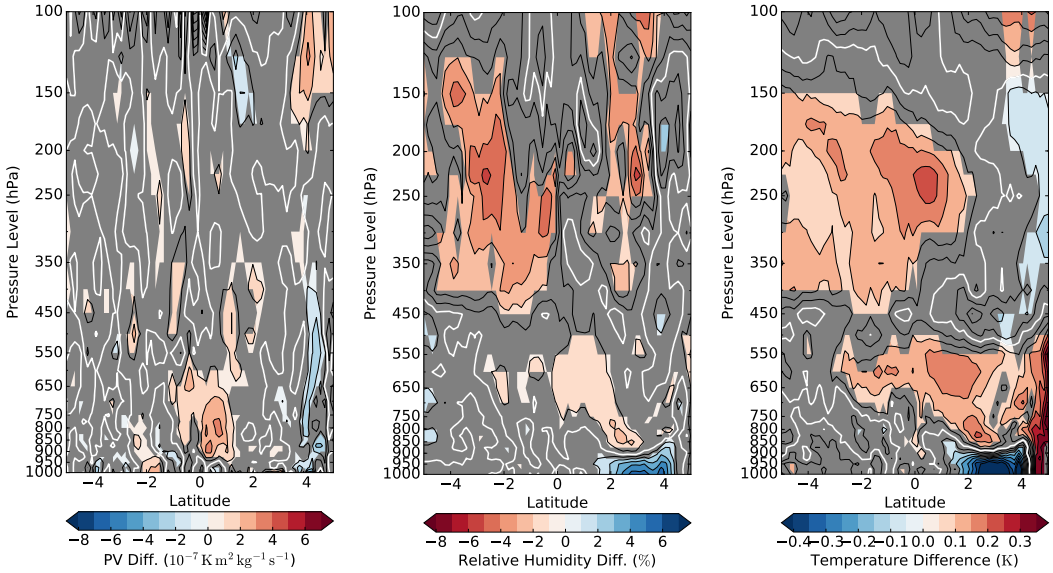

(a) Potential vorticity (b) Relative humidity (c) Temperature

Figure 7.8: Differences in selected fields of the composite mean ensembles for the 500% and 1% *arable zone* experiment. Construction identical to Fig. 7.6, except that these are latitude-height cross-sections. The selected fields are: (a) potential vorticity (10^{-7} K m^2 kg^{-1} s^{-1}), (b) relative humidity (%), and (c) temperature (K). White lines on each subfigure indicate the zero contour.

centre, thus making the core more cyclonic. This localised feature enhancement of the MD is very similar to the behaviour over ocean (see §3.5.2) where features (particularly wind) tend to have greater magnitude but smaller radial extent.

For comparison, the equivalent figure to Fig. 7.7(a) for the *arable zone* experiment is Fig. 7.7(b). Here, the consequence of increased soil moisture is largely confined to the north of the MD as expected, where a very weak anticyclone is established over the cold high associated with the wetter ground; although the effect is weaker than in the *trough zone* experiment, there is still an appreciable increase in the strength of the zonal circulation in the north quadrant of the MD. There is little change to the precipitation, except for a slight increase in the north over the increased soil moisture and a reduction in the west. On reflection, we should expect little difference to the large-scale structure of the MD, but the strongest contrast is likely to be meridional given the nature of our perturbation; therefore, we now consider some latitude-height cross-sections for the

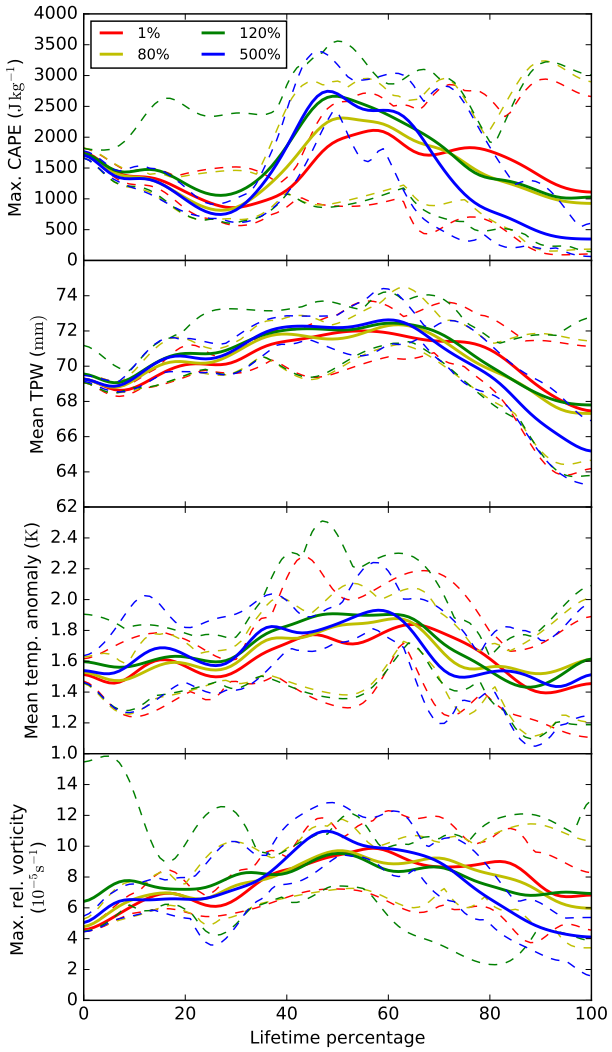

Figure 7.9: Selected fields as a function of normalised depression lifetime for the trough experiment, with the soil moisture changes coloured thus: 1% - red, 80% - yellow, 120% - green, 500% - blue.

From top to bottom, they are: the maximum CAPE (J kg^{-1}) found in the advance quadrant[4]of the MD; mean total precipitable water (mm); mean temperature anomaly (K) between 850 and 400 hPa; and maximum relative vorticity (10^{-5}s^{-1}). Each is computed over a box of side length 250 km centred on the MD centre.

The thick, solid lines represent the ensemble average, with the thinner, dashed lines representing the ensemble minimum and maximum values.

500%-minus-1% difference composites. These are given for potential vorticity, relative humidity, and temperature in Fig. 7.8. It is clear (and unsurprising) that the effect of changing *arable zone* soil moisture is felt substantially less by the MD than changing *trough zone* soil moisture, since the *arable zone* soil moisture perturbation is some distance from the MD core. The most prominent effect of wetting the soil there is to set up a wet, cool boundary layer; this, in turn, acts to vertically extend the warm core of the MD while slightly reducing moisture in the upper troposphere. Computation of mean CAPE (not shown) for each sub-experiment suggests a slight increase around the centre with increasing soil moisture. There is no real evidence of this apparent

strengthening, however, in the precipitation or lower-tropospheric wind fields – the only appreciable increase in magnitude is of the 700 hPa PV maximum.

It is also important to consider how varying soil moisture affects MDs as a function of their lifetime. For example, one would suppose the impact to be quite minimal while most of the MD is over the ocean. To test this, we can explore how selected fields from the trough experiment ensemble sets vary as a function of depression lifetime[5] - this is given for four fields in Fig. 7.9, in which the colours red, yellow, green, and blue represent fractional changes to trough soil moisture of 1%, 80%, 120%, and 500% respectively. Each field is computed over a box of side length 250 km centred on the MD centre. The topmost field in the figure is maximum CAPE found in the quadrant of the aforementioned box that contains the next track point of the MD. There is a marked region (roughly 40-70% through the MD lifetime) where the average maximum CAPE in all sub-experiments is significantly higher than during the rest of the lifetime, and it is in this region that a change in soil moisture has the strongest effect, with the extreme sub-experiments' ensemble members almost having zero overlap. We also note that here, as well as in the other fields, predictability is rapidly lost (i.e. the ensemble spread significantly widens) once the MD starts to dissipate, and further that in this regime the effect of varying soil moisture becomes negligible. In this particular instance, it is also true that during the spin-up phase of the MD, there is no obvious correlation between increased soil moisture and enhanced CAPE. Second from top in Fig. 7.9 is the mean total precipitable water in the area surrounding the MD centre. This field is less variable than CAPE but still displays a clear maximum across all sub-experiments at approximately 60% of the MD lifetime before rapidly falling away. As with maximum CAPE, there is significant correlation between trough soil moisture and mean total precipitable water as well as a significant difference between the values of the extreme sub-experiments during the middle period where the MD is at its strongest, followed by

[4]Delineated into NW, NE, SE, and SW; that is, if the MD is propagating WNW, CAPE is computed in the NW quadrant.

[5]This is simply a normalised time axis: 0% is the time of MD genesis, 100% is the time of MD lysis.

a complete loss of correlation, significance, and predictability after this point; although unlike CAPE, the correlation and significance are retained during spin-up. Second from bottom is the mean lower/mid-tropospheric temperature anomaly (averaged 850-400 hPa), here the picture is much the same as for total precipitable water, although the correlation is no longer significant at the 95% confidence level, and the ensemble spread does not widen as much during lysis. Finally, at the bottom is maximum relative vorticity in the lower troposphere (900-800 hPa); whilst this is an inherently variable field, and consequently although there is arguably some correlation between it and soil moisture during the period of maximum intensity, it is not significant, nor is the difference between the two extreme sub-experiments significant more than occasionally. That having been said, any semblance of correlation vanishes, as with the other fields, during the dissipation phase.

7.4 Discussion and conclusion

Monsoon depressions are responsible for the majority of the precipitation incident throughout the summer across northern peninsular India and the monsoon trough region. Previous work has established the possibility of at least a correlative connection between antecedent soil moisture and the behaviour of incident MDs, but this is the first study to investigate the nature of that relationship. Soil moisture, in two key areas where it has previously been identified as variable and of meteorological importance, was varied through multiples of the climatology in a selected NWP case study run in the Met Office Global Unified Model.

We have presented the results of a set of idealised sensitivity tests, each with multiple ensemble members, initialised from the analysis of a typical depression chosen in August 2014. Whilst we have framed these tests in the context of a single MD, significant differences have emerged between the ensembles due to the imposition of soil moisture anomalies; we hope that this will motivate further study of other events to

explore the climatological relationship between MDs and soil moisture.

We found that both the structure and propagation of the MD was significantly sensitive to changes in soil moisture in the monsoon trough region: wetter conditions there caused a strengthening of the MD with increased central PV and a warmer thermal core, as well as a more pronounced westward axial tilt. Such cases were also found to travel further inland before dissipating. Further, we found that these changes were greatest (among variables associated with MD strength: CAPE, TPW, mid-tropospheric temperature, and lower-tropospheric vorticity) during the period when the MD is most intense, and that varying soil moisture has no noticeable effect on the MD during its spin-down.

In the other experiment, soil across South Asia was kept desiccated while moisture in the sub-Himalayan *arable zone* was varied. This had a lesser effect on both the structure and track of the case study, although some significant differences persisted: tracks in the wetter cases terminated later, and there was some weak strengthening of the MD in the middle and upper troposphere.

We also noted that in the wetter *trough zone* experiments, the ensemble composite MD became more axially confined (as well as more intense), mimicking MD behaviour over the ocean as seen in §3.5.2. This suggests that added soil moisture in this region provides more moisture to the lower troposphere and subsequently enhances convective activity related to the MD. This is further enhanced by increased lower-level convergence to the west of the centre.

This leaves us with several questions for further study. Firstly, how exactly does a monsoon depression interact with the boundary layer? It has been indicated both here and in previous work that MDs are very efficient at moving water from the surface through the PBL and into the troposphere, despite not having particularly high wind speeds (by definition MDs lie at between 5 and 7 on the Beaufort Scale). This could be appropriately investigated by examination of a case study in a mesoscale-resolution NWP model. Secondly, how would an incident MD respond to horizontal gradients in

soil moisture, rather than the block changes performed in this study; for example with increasing (and decreasing) values both along track and across track? Thirdly, even though we have spoken of CISK as the energy source for MDs, this is not certainly true. Uncovering the true MD spin-up mechanism would provide invaluable direction for future research on the topic, and could be investigated using mechanism-denial experiments in a suitable NWP framework (cf. Craig and Gray, 1996).

CHAPTER 8

CONCLUSIONS AND FUTURE WORK

8.1 Discussion

We developed the first large-sample, multi-variable monsoon depression composite (concurrently and independently with Hurley and Boos, 2015). This 106-system composite was built by applying a newly-developed tracking algorithm that used the monsoon depression criteria specified by the India Meteorological Department to the ERA-Interim reanalysis dataset. After ensuring it was statistically robust, we confirmed features that are known to be present in MDs, such as a precipitation maximum in the southwest quadrant, and westward tilt with height. We then described the mean structure, quantifying, for example, the warm-core-over-cold-core thermal structure and discovering a bimodal structure in potential vorticity. The size of our composite meant it was the first such dataset that could be used to probe the effects of external forcing: using a bootstrap method to check for statistical significance, we found compelling evidence that the presence of a La Niña or active monsoon spell significantly strengthens contemporaneous MDs, but we found no such relationship with changing values of the Indian Ocean Dipole Index. By separating the composite into land-centred and ocean-centred subsets, we discovered significant differences between the two, noting in particular the

larger spatial scale, lower intensity, and lower asymmetry found over the ocean. We also found significant differences in most fields across the diurnal cycle; focusing in particular on precipitation, we identified separable modes with distinct diurnal cycles, one resembling tropical convection over land that described the large-scale precipitation, and one resembling tropical cyclone precipitation that described the more intense precipitation found southwest of the centre.

On finding the substantial intensification of winds on the Himalayan side of the MD, we noted, after some approximation, the similarity to a rectilinear vortex in the presence of an infinite wall. This motivated us to explore whether the Himalayas played a role in the northwestward propagation of MDs as such a model would predict. We derived appropriate forms for predicted propagation velocity and direction of MDs (assuming both planar and cylindrical forms for the Himalayas) and tested it against several other models, finding it to perform best of all, and suggesting that this could complement the mid-tropospheric beta drift model proposed by Boos et al. (2015).

We also ran numerous case studies of MDs at a range of resolutions (N96, N216, N320, N512, N640, N768, N1024, N1280) in the MetUM NWP framework, to validate the composite structure and explore the sensitivity of MDs to changing resolution. We found that the MetUM typically overestimated the intensity of the systems, but did a generally good job of capturing the structure, which improved with resolution until approximately N512 ($\sim$ 40 km resolution). Further, we showed that the quality of the forecast tracks improved substantially with resolution until N512, where the gain became saturated. The reason behind the overestimated intensity of the MDs was not clear, although we noted lower level relative humidity in the trough was overestimated by 5-10%, and the magnitude of the mid-tropospheric warm anomaly associated with MDs was overestimated by as much as 30%, so clearly there is a link to latent heat release there. We also looked at the diurnal cycle – arguably the largest progenitor of variability – of precipitation, finding of the two modes that the one associated with broad-scale tropical convection was represented extremely poorly in both phase and

magnitude, but that the one associated with the heavy precipitation near the centre of the MD was very well replicated, having correct phase and improving magnitude with increased resolution.

We asked in §1.2 whether the propagation might be further modulated by secondary effects such as land surface state. To explore this we set up a NWP model with varying soil moisture ancillaries, finding that increased soil moisture in the monsoon trough resulted in MDs with higher intensity and deeper penetration into the subcontinent (and vice versa for decreased soil moisture). We also tested whether an increase in soil moisture in the Himalayan foothills could steer MDs onto a more northward trajectory; this was found to be the case, also some increase in duration was found with increasing moisture there.

8.2 Limitations

We spent much of the early part of this work in discussion of the monsoon depression composite, in particular exploring its structure and variability subject to various forcings. It is crucial that this is not misinterpreted as the expectation of a depression snapshot, and thus that individual MDs should be compared against it only with great caution. This is highlighted in particular in the variables with substantial variance, such as the shortwave radiative heating rates at the top of the anvil whose high magnitudes and moderate spatial uncertainty combine to make a mean composite picture that looks quite different from the individual events that comprise it. Fortunately, this is not all too common, and a typical depression bears a strong resemblance to composite fields with low spatial variance. Further to this, in Chapter 3 in particular, we limited discussion to the *rotated* composite, i.e. normalised according to heading as well as location. Now, while most MDs propagate northwestward with only minor variation, some propagate in entirely different directions, most notably those that track along the eastern Indian coast. This, along with the subtle along-track variations in heading

that exist for any synoptic system result in a smoothing out of absolute effects – some related to the environment (in particular orography), and some related to the system itself, such as the westward axial tilt. Therefore, in adopting an approach designed to evaluate features with regard to *ahead of* or *behind* the depression, we do lose some other structural information.

Another problem with the composite in general (again, particularly in Chapter 3) is that we have only used one dataset. ERA-Interim provided the data for both our tracking and structural exploration (until we looked at sparse satellite data in Chapter 4) without considering whether these results were robust under a change of dataset. A number of other reanalyses are available at similar resolution for the same period, such as the Japanese 55-year Reanalysis (JRA-55, Kobayashi et al., 2015) or the NASA Modern Era Retrospective-Analysis for Research and Applications (MERRA, Rienecker et al., 2011). These would, at the very least, provide us assurances about the stability of purely modelled fields, such as cloud cover and surface fluxes, in the composite. On a similar theme, the discussion in Chapter 4 could have benefitted from comparison among a greater number of satellite products, although this presents the caveat of differing radar frequencies (see, for example, the strong differences in MD CFADs at 13.8 GHz and 94 GHz in Figs. 4.7 and 4.8). Also lacking from our study at any point (excepting a few radiosondes) were ground-based (as opposed to satellite-based) observations. The IMD do not make sub-daily data for their automatic rain gauges or weather stations freely available to the public, and their Doppler weather radar (DWR) data, for which they have some sixteen stations operational, is entirely unavailable except for contemporaneous images. The latter would certainly have been invaluable to further investigation of mesoscale processes in the vicinity of a monsoon depression. Even with the ability to assimilate these observations, forecasts could be further improved by using high resolution observations to constrain the model physics. For example: carefully positioned lidars would reveal a great deal of information about processes in the boundary layer during interaction with MDs, of which we know very

little; flux towers would allow a much deeper exploration of the relationship between soil moisture (among other things) and a passing disturbance; and radiometers would give us information on how mesoscale cloud processes in MDs develop over time, including interaction with squall lines and convective systems.

We have not performed a detailed verification of the tracking algorithm described in §2.1, and used throughout, here, only corroborating its output with the publicly available data provided by the IMD. Due to the subjective nature of the latter, it is entirely possible that some events have been eliminated from the dataset because IMD suggested that they were not of sufficient strength to be promoted in category from low to depression (either through human error or instrument error). This would not have had a significant effect on the composite, but forewarns us of the issue of sensitivity: we noted in Fig. 6.1 the difference in tracks obtained simply by removing the surface pressure criterion and changing the height at which the wind criterion was applied; and in Fig. 3.1 we saw that differences between track datasets could be induced simply by approximating the isobar criterion (Hurley and Boos (2015) used surface pressure anomaly relative to a 21-day running mean as a proxy for closed isobars). A short study on the sensitivity of tracking algorithms would thus have been an important addition to this work.

8.3 Future work

A number of important questions were raised during the completion of the work underlying this thesis; here, we synthesise the most important of those not tackled in the work chapters.

There is no doubt that the Indian monsoon is famous for the rainfall it brings to the subcontinent, and we have seen that monsoon depressions are consistently capable of organising large areas of substantial precipitation, yet previous studies have wildly varying estimates of what fraction of monsoon rainfall they compute that monsoon

depressions are responsible for, as discussed in §1.1 the values range from around 10% (Dhar and Bhattacharya, 1973) to more than 50% (Yoon and Chen, 2005). Clearly, this is an area that requires further exploration, and it is important to quantify this number in the context of recent research that argues the case of diminishing frequency of monsoon depressions (e.g. Dash et al., 2004; Prajeesh et al., 2013). One particular problem to overcome is how to attribute particular rainfall events to an MD (should one exist); as we saw in Fig. 4.14, just because an MD is present does not mean all contemporaneous precipitation on the peninsula is related to it. This could feasibly be split into three categories: direct, indirect (e.g. heavier rainfall over the Western Ghats caused by enhanced westerlies, Fig. 3.3(b)), and unrelated (such as a distinct mesoscale convective system in a different part of the subcontinent).

This leads on to another important problem: classification. For a great many years, the IMD has followed the Beaufort scale for classifying a depression over the ocean (between 5 and 7 on the scale, or 8.5-16.5 m s^{-1}, at the surface) with some empirically derived equivalent in closed isobars once the MD transitions across the coast to land to mitigate the effect of surface friction, and there are essentially two key problems with this. Firstly, the choice of division is fundamentally arbitrary: the original Beaufort scale was based on how the wind affected the sails of ships in the Victorian-era Royal Navy, and there is clearly no significant difference between two monsoon disturbances whose maximum surface winds are, for example, 8.4 and 8.6 m s^{-1} respectively. Secondly, and arguably more importantly, such disturbances are predominantly rain-bringing systems embedded in a rainy season. If one believes the relationship between quasigeostrophic ascent and rainfall (first suggested by Rajamani and Rao, 1981; and later rediscovered by Boos et al., 2015), which makes a compelling argument for the southwest precipitation maximum, then rainfall does not even have a direct relationship with surface wind speed, but rather its vertical derivative (along with the spatial derivative of relative vorticity). It seems sensible, then, that monsoon disturbances should in fact be categorised by precipitation, rather than surface wind or

pressure; so long as appropriate filters are applied (some minimal vorticity to remove convective cells, some minimum spatial scale to remove mesoscale convective storms, and perhaps a further check for bimodal PV and mid-tropospheric warm core), the result ought be robust. If such a route were to be followed, one must also pay careful attention to the problem of attribution raised in the previous paragraph.

Underlying all of this, however, is the consistently unanswered question: what is the mechanism by which monsoon disturbances intensify in the Bay of Bengal? Some authors have argued that baroclinic instability alone is sufficient (Rao and Rajamani, 1968; Lindzen et al., 1983; Saha and Chang, 1983; Krishnakumar et al., 1992), while recent work has shown that this is unlikely, even when moisture is considered (Cohen and Boos, 2016). Others have found that purely barotropic models can represent the intensification (Keshavamurty et al., 1978; Singh et al., 1980; Saha, 1983)[1]; but it is most common to find studies that suggest a barotropic-baroclinic instability is the cause, either alone (Krishnamurti et al., 1976; Goswami et al., 1980), or with support from CISK (Shukla, 1978; Mishra and Salvekar, 1980; Moorthi and Arakawa, 1985). Older studies typically suggested less theoretical mechanisms that rely on forcing from orographic or frontal sources (e.g. Roy and Roy, 1930; Ramanathan and Ramakrishnan, 1933; Desai, 1950). It seems likely that some combination of CISK, barotropic instability, and baroclinic instability is the cause of intensification, but this is yet to be verified with real-world data, a problem we are now in a position to tackle. A simple thought experiment suggests that baroclinic effects ought not be entirely ruled out, consider the (inviscid) vorticity equation:

$$\frac{D\boldsymbol{\zeta}}{Dt} = (\boldsymbol{\zeta} \cdot \nabla)\mathbf{u} - \boldsymbol{\zeta}(\nabla \cdot \mathbf{u}) + \frac{1}{\rho^2}\nabla\rho \times \nabla p + \nabla \times \left(\frac{\mathbf{B}}{\rho}\right) , \tag{8.1}$$

where the symbols have their usual meanings, and $\mathbf{B}$ is the summary effect of external body forces. The baroclinic term can be re-expressed using the ideal gas law and some manipulation:

[1]Note that this is a different Saha to the one that suggested a purely baroclinic process.

$$\frac{1}{\rho^2}\nabla\rho\times\nabla p=-\frac{R}{p}\nabla T\times\nabla p\,. \tag{8.2}$$

At the head of the Bay of Bengal, where much of the MD genesis occurs, lower-tropospheric/PBL value of $(\nabla T\times\nabla p)\cdot\hat{\mathbf{k}}$ is negative[2] implying positive vorticity generation there, in contrast to the Arabian Sea, where it is negative and very few MDs form during the monsoon season.

As discussed in §7.4, an appropriate first step in the spin-up problem might be to follow the mechanism denial experiment of Craig and Gray (1996) which ought rule out competing theories such as Wind-induced surface heat exchange (WISHE; Emanuel, 1986). The antithesis of this problem is also important: what is the mechanism by which depressions, and then lows, spin down towards the northwest of India? Obviously, moisture becomes less readily available further along the typical MD track, but the variability in their lysis points is substantial (see, for example, Fig. 3.1, and recall from Chapter 7 that antecedent soil moisture is at least partly responsible). Recently, Parker et al. (2016) have shown that intrusions of dry air from Pakistan can inhibit the monsoon onset, and as outbreaks of these northerlies occur throughout the monsoon season, it is plausible they may interact with MDs and accelerate their dissipation.

We have shown that the Himalayan orography likely plays some role in guiding monsoon depressions along their typical northwestward track, and we have also shown that increased model resolution improves track forecasts in a direction perpendicular to the orientation of the Himalayas (whose representation improves with resolution) and average MD tracks. It is reasonable, therefore, to pose the following question: how important is representation of orography in MD track forecasting? This is a subtle problem to tackle and one must bear in mind that the monsoon system itself is very sensitive to orographic forcing (Chakraborty et al., 2006; Boos and Kuang, 2010). This leads us onto another important discussion of sensitivity in the MetUM: our work in

[2]The reason for this is that ∇T points northward due to the inverted equator-pole temperature gradient that also drives the monsoon, whereas ∇p points southeastward, i.e. away from the trough.

Chapter 6 was restricted only to resolutions where convection had to be parameterised. We paid no attention there to the choice of parameterisation or schemes that comprised it, simply using the form typically adopted by the Met Office for their own NWP runs. Given the known difficulties in parameterising convection, and the dominance of deep convection in MDs we found in §4.3, we might reasonably suspect a significant relationship between the two. Previous authors have considered this sensitivity in the context of the monsoon as a whole (Ratnam and Kumar, 2005; Mukhopadhyay et al., 2010), although for monsoon depressions only changes in the convective scheme as a whole have been examined (Das et al., 2002; Ratnam and Cox, 2006) which leaves the important question of how simulated depressions respond to changes in, for example, entrainment rates or CAPE closure schemes, unanswered. As operational model resolutions improve with time, many parameterisations, including the convective scheme, are likely to become obsolete (although this could still be very distant for climate models); whilst some studies have looked at simulated depressions in convection-permitting models (e.g. Potty et al., 2000) these lack a comparison to the results of using coarser resolutions that require parameterisation. We must, then, ask: should we expect a jump in forecast features of MD when switching to a convection-permitting model? Related, we saw in §3.5.2 that there was a significant structural change when the MD moved from the ocean to land; some of this (the increase in asymmetry) can be explained by the increased proximity to the Himalayas, but some will be left to be explained by interactions in the boundary layer. Given this is also parameterised, what improvement could we expect in representing the sea-land transition by using a large eddy resolving model?

8.4 Applications and implications

General comments: One of the most important side-effects of creating composites from tracking and reanalysis data is the compilation of a statistical database against

which we can now compare past, current, and future MDs. Placing them, for example, on probability density functions relating to vorticity or precipitation could be a useful metric of intensity. The reanalysis/satellite composites can be further used to allow comparison with composite GCM/NWP outputs, as we did in Chapter 6. There is further use in this catalog in the context of longer climate runs, because we can use it to test the fidelity of interannual variability imposed on MDs by, for example, ENSO, which would provide an important test of tropical circulation.

For forecasters: The effect of an MD is felt across a very large area, in particular, precipitation is modified over much of the peninsula (see Fig. 3.3(b)). This knowledge will be of use for forecasters, and is further improved by the new characterisation of the diurnal cycle and direct rainfall footprint, allowing for more accurate flood warnings to be issued. As we saw in §6.5.4, an NWP that parameterises convection does a miserable job of capturing the large-scale rainfall (unlike the smaller-scale more intense rainfall caused by low-level moisture flux convergence) associated with MDs, so forecasters must be wary of using such products.

For model developers: It appears as though N512 (40 km) is sufficient resolution to represent all important aspects of a monsoon depression in an initialised global model forecast, despite the apparent over-intensification to which the MetUM seems prone. Therefore, until we can perform such forecasts in a convection-permitting model, it seems as though the the focus should be on improving analyses and parameterisations. For example, in the case of the former, we have shown that soil moisture plays a critical role in the variability of MD duration; in the case of the latter, we have shown that the Himalayas play an important part in their propagation. We cannot comment, however, on the application of these results to a non-initialised model.

APPENDIX A

FORMAL DESCRIPTION OF SYSTEM COMPOSITE

The four-dimensional (three spatial axes, one temporal axis) composites for a given field are created by using the tracking data to find the centre of the MD at each timestep in the output data (should one exist), and then extracting the surrounding data; that is to say if all output data is precisely described by some function $f(x, y, z, t)$ and the disjoint[1] sets of track loci are: $\{x_n, y_n, t_n\}_m$, and we specify some domain of interest, of side length L, invoking the notation $\Delta_i^x = (x_i - L, x_i + L)$ for the interval describing the domain centred on x_i, then the composite is simply the discontinuous function $f(\Delta_{n,m}^x, \Delta_{n,m}^y, z, t_{n,m})$. This function is just a finite-domain translation of the original, and the new horizontal axes are selected at each m, n such that $x_{m,n} = y_{m,n} = 0$, i.e. $f(\Delta_{n,m}^x, \Delta_{n,m}^y, z, t_{n,m}) \equiv g(x', y', z, t')$, where $x' = x - x_{n,m}$, $y' = x - y_{n,m}$, $t' = t_{n,m}$ and $f : \Delta^{x'}, \Delta^{y'}$. Thus to examine a mean vertical cross-section taken north to south, we compute $\overline{g(0, y', z, t')}$ where the bar denotes a time mean; for a mean horizontal composite at height $z = Z$, we would compute $\overline{g(x', y', Z, t')}$.

To extend this to a *rotated* composite, after translation we apply the additional affine transformation:

[1] Of course, there's no mathematical reason that the sets of loci must be disjoint, but as of yet, no two MDs have been observed to merge.

$$x'' = x' \cos\theta - y' \sin\theta \tag{A.1}$$

$$y'' = x' \sin\theta + y' \cos\theta\,, \tag{A.2}$$

where θ is the metric of rotation (in our case, the current heading of the MD). We then have $g(x', y', z, t', \theta) \equiv h(x'', y'', z, t')$ and proceed as above, replacing g with h.

APPENDIX B

DERIVATION OF CYLINDRICAL MODEL PROPAGATION VELOCITY

This derivation loosely follows the method outlined in Milne-Thomson (1960). We start by invoking the definition of a meromorphic complex velocity potential function, w:

$$w \equiv w(z) = \phi(z) + i\psi(z)\,, \tag{B.1}$$

where ϕ is the velocity potential that describes irrotational flow in the fluid, ψ is the stream function that describes its solenoidal flow, and $z = x + iy = re^{i\theta}$ is the complex coordinate. A rectilinear vortex filament centred at z_ω then has the complex potential

$$w = i\omega \ln(z - z_\omega) = \frac{i\kappa}{2\pi} \ln(z - z_\omega)\,, \tag{B.2}$$

where ω and κ are, respectively, the vorticity and circulation of the vortex.

Now, consider a two-dimensional inviscid fluid on an infinite plane. This fluid satisifies the generic form

$$w = f(z)\,. \tag{B.3}$$

If we impinge upon this flow a cylinder whose cross-section is described by the boundary $|z| = a$, the resulting complex potential becomes

$$w = f(z) + \bar{f}\left(\frac{a^2}{z}\right), \tag{B.4}$$

as long as there are no singularities in $f(z < a)$; for a proof, the reader is encouraged to visit Milne-Thomson (1940).

Thus, combining equations (B.2) and (B.4), we deduce that the complex potential for a fluid containing a point vortex at z_ω and a cylinder, radius $|a|$, centred at the origin is:

$$w = i\omega \ln(z - z_\omega) - i\omega \ln\left(\frac{a^2}{z} - \bar{z}_\omega\right), \tag{B.5}$$

or, to within a constant:

$$w = i\omega \ln(z - z_\omega) - i\omega \ln\left(z - \frac{a^2}{\bar{z}_\omega}\right) + i\omega \ln(z), \tag{B.6}$$

and in polar coordinates:

$$w = i\omega \left[\ln(re^{i\theta} - r_\omega e^{i\theta_\omega}) - \ln(re^{i\theta} - \frac{a^2}{r_\omega}e^{i\theta_\omega}) + \ln(re^{i\theta})\right]. \tag{B.7}$$

From this, it is clear that the combination of the vortex and the cylinder induces two image vortices of equal magnitude to the original: one at the origin, and one with opposing sign at the point $z = a^2/\bar{z}_\omega$. Now, we are interested in how this flow advects the original vortex, i.e., the form of $\mathbf{v}_{\text{flow}} = [v_r, v_\theta] = [v_r^S, v_\theta^R] + [v_r^R, v_\theta^S]$ at $z = z_\omega$, where superscripts R and S represent the irrotational and soleniodal contributions respectively. These can be calculated directly from the complex potential since:

$$v_r^R = \frac{\partial \phi}{\partial r};\ v_r^S = -\frac{1}{r}\frac{\partial \psi}{\partial \theta};\ v_\theta^R = \frac{1}{r}\frac{\partial \phi}{\partial \theta};\ v_\theta^S = \frac{\partial \psi}{\partial r}. \tag{B.8}$$

Since we want to know how this flow advects the vortex, we are interested in the

values of these derivatives at $r = r_\omega$ and $\theta = \theta_\omega$, and we ignore the singularity at $(r_\omega, \theta_\omega)$ because the vortex cannot self-advect. We find that the only non-zero velocity component is:

$$v_\theta^S = \mathrm{Im}\left\{\frac{\partial w}{\partial r}\right\}_\omega = \omega\left(\frac{1}{r_\omega} - \frac{1}{r_\omega - a^2/r_\omega}\right) = \frac{\omega a^2}{r_\omega(r_\omega^2 - a^2)}\,, \tag{B.9}$$

and using distance from the boundary, $R = r_\omega - a$, and circulation for a point vortex, $\kappa = 2\pi\omega$, we obtain the desired relationship:

$$v_{\mathrm{cyl}} = \frac{\kappa}{4\pi R}\left[\left(1 + \frac{r}{a}\right)\left(1 + \frac{r}{2a}\right)\right]^{-1}\,. \tag{B.10}$$

APPENDIX C

OVERVIEW OF THE LAND SURFACE SCHEME USED IN THE MODEL

Four soil layers are used, for both the thermodynamic and hydrological subroutines, at depths from the surface of 10, 25, 65, and 200 cm respectively; the prognostic total soil water in each layer is given by:

$$M = \rho_w \Delta z \Theta_u \tag{C.1}$$

where ρ_w is the density of water, Δz is the thickness of the layer, and Θ_u is the liquid water concentration (for the sake of this discussion, we neglect frozen water, although it is catered for in the scheme). This is subject to the transport equation:

$$\frac{dM_n}{dt} = W_{n-1} - W_n - E_n \,, \tag{C.2}$$

where subscript n denotes the layer, W_n and W_{n-1} the diffusion terms in the layer and that immediately below it, and E_n is the evapotranspiration (including interaction with roots). The evapotranspiration function is controlled by land usage and vegetation data

embedded in JULES, whereas the diffusion terms are prescribed by the Darcy equation:

$$W = K\left(\frac{\partial \Psi}{\partial z} + 1\right), \tag{C.3}$$

where K is the hydraulic conductivity and Ψ is the soil water suction function. Within MOSES these are respectively described by the Clapp-Hornberger relationships (Clapp and Hornberger, 1978):

$$\Psi = \Psi_s S_u^{-b} \tag{C.4}$$

$$K = K_s S_u^{2b+3}, \tag{C.5}$$

where Ψ_s, K_s and b are empirical constants that can be set on model initialisation. For this study, the default values used operationally by the Met Office were used.

There are then two boundary conditions: at the surface, the flux (aside from evaporation) is computed as the summation of canopy throughfall, snowmelt, and surface runoff; underneath the bottom (Nth) layer, the drainage (W_N) is set to equal the hydraulic conductivity.

Finally, the evaporation to the atmosphere from soil at the surface is given by:

$$E = \rho C_H U_1 [q_{\text{sat}}(T_\star, p_\star) - q_1] \left[f_a + (1 - f_a)\frac{g_s}{g_s + C_H U_1}\right] \tag{C.6}$$

where f_a is the tile saturation fraction (e.g. 1 for ice, lake, ocean, 0 for dry rock), ρ is the density of air, g_s is the surface soil conductivity, U is the wind speed, C_H is the surface flux heat exchange coefficient, q is specific humidity; and the subscripts $\star$, 1, and sat refer to the surface, lowest atmospheric model level, and saturation respectively.

BIBLIOGRAPHY

Abel, S. J., and I. A. Boutle, 2012: An improved representation of the raindrop size distribution for single-moment microphysics schemes. *Quart. J. Roy. Meteor. Soc.*, **138 (669)**, 2151–2162, doi:10.1002/qj.1949, URL http://dx.doi.org/10.1002/qj.1949.

Abel, S. J., and B. J. Shipway, 2007: A comparison of cloud-resolving model simulations of trade wind cumulus with aircraft observations taken during RICO. *Quart. J. Roy. Meteor. Soc.*, **133 (624)**, 781–794, doi:10.1002/qj.55, URL http://dx.doi.org/10.1002/qj.55.

Abel, S. J., D. N. Walters, and G. Allen, 2010: Evaluation of stratocumulus cloud prediction in the Met Office forecast model during VOCALS-REx. *Atmos. Chem. Phys.*, **10 (21)**, 10 541–10 559, doi:10.5194/acp-10-10541-2010, URL http://www.atmos-chem-phys.net/10/10541/2010/.

Ackerman, T. P., K.-N. Liou, F. P. J. Valero, and L. Pfister, 1988: Heating rates in tropical anvils. *J. Atmos. Sci.*, **45 (10)**, 1606–1623, doi:10.1175/1520-0469(1988)045⟨1606:HRITA⟩2.0.CO;2, URL http://dx.doi.org/10.1175/1520-0469(1988)045⟨1606:HRITA⟩2.0.CO;2.

Adler, R. F., and Coauthors, 2003: The version-2 global precipitation climatology project (GPCP) monthly precipitation analysis (1979-present). *J. Hydrometeor.*, **4 (6)**, 1147–1167, doi:10.1175/1525-7541(2003)004⟨1147:TVGPCP⟩2.0.CO;2, URL http://dx.doi.org/10.1175/1525-7541(2003)004⟨1147:TVGPCP⟩2.0.CO;2.

Ananthakrishnan, R., and K. L. Bhatia, 1958: Tracks of monsoon depressions and their recurvature towards Kashmir. *Proc. Symp. Monsoons of the World, New Delhi, Hind Union Press*, 157–172.

Annamalai, H., J. M. Slingo, K. R. Sperber, and K. Hodges, 1999: The mean evolution and variability of the Asian summer monsoon: Comparison of ECMWF and NCEP–NCAR reanalyses. *Monthly Weather Review*, **127 (6)**, 1157–1186, doi:10.1175/1520-0493(1999)127⟨1157:TMEAVO⟩2.0.CO;2, URL http://dx.doi.org/10.1175/1520-0493(1999)127⟨1157:TMEAVO⟩2.0.CO;2.

Awaka, J., T. Iguchi, H. Kumagai, and K. Okamoto, 1997: Rain type classification algorithm for TRMM precipitation radar. *Geoscience and Remote Sensing, 1997. IGARSS'97. Remote Sensing-A Scientific Vision for Sustainable Development., 1997 IEEE International*, IEEE, Vol. 4, 1633–1635, doi:10.1109/IGARSS.1997.608993, URL http://dx.doi.org/10.1109/IGARSS.1997.608993.

Awaka, J., T. Iguchi, and K. Okamoto, 2007: *Rain Type Classification Algorithm*, 213–224. Springer Netherlands, Dordrecht, doi:10.1007/978-1-4020-5835-6_17, URL http://dx.doi.org/10.1007/978-1-4020-5835-6_17.

Batchelor, G. K., 2000: *An Introduction to Fluid Dynamics*. 3rd ed., Cambridge University Press.

Bechtold, P., J.-P. Chaboureau, A. Beljaars, A. Betts, M. Köhler, M. Miller, and J.-L. Redelsperger, 2004: The simulation of the diurnal cycle of convective precipitation over land in a global model. *Quart. J. Roy. Meteor. Soc.*, **130 (604)**, 3119–3137, doi:10.1256/qj.03.103, URL http://dx.doi.org/10.1256/qj.03.103.

Bell, R., K. I. Hodges, P. L. Vidale, J. Strachan, and M. Roberts, 2014: Simulation of the global ENSO-tropical cyclone teleconnection by a high-resolution coupled general circulation model. *J. Climate*, **27**, 6404–6422, doi:10.1175/JCLI-D-13-00559.1, URL http://dx.doi.org/10.1175/JCLI-D-13-00559.1.

Bengtsson, L., S. Hagemann, and K. I. Hodges, 2004: Can climate trends be calculated from reanalysis data? *J. Geophys. Res. Atmos.*, **109 (D11)**, doi:10.1029/2004JD004536, URL http://dx.doi.org/10.1029/2004JD004536.

Berrisford, P., and Coauthors, 2011: The ERA-Interim archive Version 2.0. Shinfield Park, Reading, 23 pp., URL http://www.ecmwf.int/sites/default/files/elibrary/2011/8174-era-interim-archive-version-20.pdf.

Berry, G. J., M. J. Reeder, and C. Jakob, 2012: Coherent synoptic disturbances in the Australian monsoon. *J. Climate*, **25 (24)**, 8409–8421, doi:10.1175/JCLI-D-12-00143.1, URL http://dx.doi.org/10.1175/JCLI-D-12-00143.1.

Best, M. J., and Coauthors, 2011: The Joint UK Land Environment Simulator (JULES), model description–Part 1: energy and water fluxes. *Geosci. Model Dev.*, **4 (3)**, 677–699, doi:10.5194/gmd-4-677-2011, URL http://www.geosci-model-dev.net/4/677/2011/.

Bishop, C. H., B. J. Etherton, and S. J. Majumdar, 2001: Adaptive sampling with the ensemble transform Kalman filter. Part I: Theoretical aspects. *Mon. Wea. Rev.*, **129 (3)**, 420–436, doi:10.1175/1520-0493(2001)129⟨0420:ASWTET⟩2.0.CO;2, URL http://dx.doi.org/10.1175/1520-0493(2001)129⟨0420:ASWTET⟩2.0.CO;2.

Boettcher, M., and H. Wernli, 2011: Life cycle study of a diabatic Rossby wave as a precursor to rapid cyclogenesis in the North Atlantic-dynamics and forecast performance. *Mon. Wea. Rev.*, **139 (6)**, 1861–1878, doi:10.1175/2011MWR3504.1, URL http://dx.doi.org/10.1175/2011MWR3504.1.

Boos, W. R., J. V. Hurley, and V. S. Murthy, 2015: Adiabatic westward drift of Indian monsoon depressions. *Quart. J. Roy. Meteor. Soc.*, **141**, 1035–1048, doi:10.1002/qj.2454, URL http://dx.doi.org/10.1002/qj.2454.

Boos, W. R., and Z. Kuang, 2010: Dominant control of the South Asian monsoon by orographic insulation versus plateau heating. *Nature*, **463 (7278)**, 218–222, doi:10.1038/nature08707, URL http://dx.doi.org/10.1038/nature08707.

Bosilovich, M. G., J. Chen, F. R. Robertson, and R. F. Adler, 2008: Evaluation of global precipitation in reanalyses. *J. Appl. Meteor. Climatol.*, **47 (9)**, 2279–2299, doi:10.1175/2008JAMC1921.1, URL http://dx.doi.org/10.1175/2008JAMC1921.1.

Boville, B. A., 1991: Sensitivity of simulated climate to model resolution. *J. Climate*, **4 (5)**, 469–485, doi:10.1175/1520-0442(1991)004⟨0469:SOSCTM⟩2.0.CO;2, URL http://dx.doi.org/10.1175/1520-0442(1991)004⟨0469:SOSCTM⟩2.0.CO;2.

Bowler, N. E., A. Arribas, K. R. Mylne, K. B. Robertson, and S. E. Beare, 2008: The MOGREPS short-range ensemble prediction system. *Quart. J. Roy. Meteor. Soc.*, **134 (632)**, 703–722, doi:10.1002/qj.234, URL http://dx.doi.org/10.1002/qj.234.

Bowman, K. P., and M. D. Fowler, 2015: The diurnal cycle of precipitation in tropical cyclones. *J. Climate*, **28**, 5325–5334, doi:10.1175/JCLI-D-14-00804.1, URL http://dx.doi.org/10.1175/JCLI-D-14-00804.1.

Bromwich, D. H., K. M. Hines, and L.-S. Bai, 2009: Development and testing of polar weather research and forecasting model: 2. Arctic Ocean. *J. Geophys. Res. Atmos.*, **114 (D8)**, doi:10.1029/2008JD010300, URL http://dx.doi.org/10.1029/2008JD010300.

Brown, A. R., R. J. Beare, J. M. Edwards, A. P. Lock, S. J. Keogh, S. F. Milton, and D. N. Walters, 2008: Upgrades to the boundary-layer scheme in the Met Office numerical weather prediction model. *Bound.-Lay. Meteor.*, **128 (1)**, 117–132, doi:10.1007/s10546-008-9275-0, URL http://dx.doi.org/10.1007/s10546-008-9275-0.

Bryan, G. H., and H. Morrison, 2012: Sensitivity of a simulated squall line to horizontal resolution and parameterization of microphysics. *Mon. Wea. Rev.*, **140 (1)**, 202–225, doi:10.1175/MWR-D-11-00046.1, URL http://dx.doi.org/10.1175/MWR-D-11-00046.1.

Buizza, R., M. Milleer, and T. N. Palmer, 1999: Stochastic representation of model uncertainties in the ECMWF ensemble prediction system. *Quart. J. Roy. Meteor. Soc.*, **125 (560)**, 2887–2908, doi:10.1002/qj.49712556006, URL http://dx.doi.org/10.1002/qj.49712556006.

Buizza, R., T. Petroliagis, T. N. Palmer, J. Barkmeijer, M. Hamrud, A. Hollingsworth, A. Simmons, and N. Wedi, 1998: Impact of model resolution and ensemble size on the performance of an ensemble prediction system. *Quart. J. Roy. Meteor. Soc.*, **124 (550)**, 1935–1960, doi:10.1002/qj.49712455008, URL http://dx.doi.org/10.1002/qj.49712455008.

Byers, H. R., and R. R. Braham, 1948: Thunderstorm structure and circulation. *J. Meteor.*, **5 (3)**, 71–86, doi:10.1175/1520-0469(1948)005⟨0071:TSAC⟩2.0.CO;2, URL http://dx.doi.org/10.1175/1520-0469(1948)005⟨0071:TSAC⟩2.0.CO;2.

Catto, J. L., L. C. Shaffrey, and K. I. Hodges, 2010: Can climate models capture the structure of extratropical cyclones? *J. Climate*, **23**, 1621–1635, doi:10.1175/2009JCLI3318.1, URL http://dx.doi.org/10.1175/2009JCLI3318.1.

Cetrone, J., and R. A. Houze, 2006: Characteristics of tropical convection over the ocean near Kwajalein. *Mon. Wea. Rev.*, **134**, 834–853.

Chakraborty, A. N. R. S., R. S. Nanjundiah, and J. Srinivasan, 2006: Theoretical aspects of the onset of Indian summer monsoon from perturbed orography simulations in a GCM. *Annales Geophysicae*, **24 (8)**, 2075–2089, URL https://hal.archives-ouvertes.fr/hal-00318140.

Chandrasekar, A., K. Alapaty, and D. S. Niyogi, 2007: The effect of a surface data assimilation technique and the traditional four-dimensional data assimilation on the simulation of a monsoon depression over India using a mesoscale model. *Nat. Hazards*, **42 (2)**, 439–453, doi:10.1007/s11069-006-9080-3, URL http://dx.doi.org/10.1007/s11069-006-9080-3.

Chandrasekar, A., K. Alapaty, and D. S. Niyogi, 2008: The impacts of indirect soil moisture assimilation and direct surface temperature and humidity assimilation on a mesoscale model simulation of an Indian monsoon depression. *J. Appl. Meteor. Climatol.*, **47 (5)**, 1393–1412, doi:10.1175/2007JAMC1599.1, URL http://dx.doi.org/10.1175/2007JAMC1599.1.

Chang, H. I., D. Niyogi, A. Kumar, C. M. Kishtawal, J. Dudhia, F. Chen, U. C. Mohanty, and M. Shepherd, 2009: Possible relation between land surface feedback and the post-landfall structure of monsoon depressions. *Geophys. Res. Lett.*, **36**, doi:10.1029/2009GL037781, URL http://dx.doi.org/10.1029/2009GL037781.

Charney, J. G., and A. Eliassen, 1964: On the growth of the hurricane depression. *J. Atmos. Sci.*, **21 (1)**, 68–75, doi:10.1175/1520-0469(1964)021⟨0068:OTGOTH⟩2.0.CO;2, URL http://dx.doi.org/10.1175/1520-0469(1964)021⟨0068:OTGOTH⟩2.0.CO;2.

Chen, T.-C., J.-H. Yoon, and S.-Y. Wang, 2005: Westward propagation of the Indian monsoon depression. *Tellus*, **57A**, 758–769, doi:10.1111/j.1600-0870.2005.00140.x, URL http://dx.doi.org/10.1111/j.1600-0870.2005.00140.x.

Chen, Y.-J., E. E. Ebert, K. J. E. Walsh, and N. E. Davidson, 2013: Evaluation of TRMM 3B42 precipitation estimates of tropical cyclone rainfall using PACRAIN data. *J. Geophys. Res. Atmos.*, **118 (5)**, 2184–2196, doi:10.1002/jgrd.50250, URL http://dx.doi.org/10.1002/jgrd.50250.

Clapp, R. B., and G. M. Hornberger, 1978: Empirical equations for some soil hydraulic properties. *Water Resour. Res.*, **14 (4)**, 601–604, doi:10.1029/WR014i004p00601, URL http://dx.doi.org/10.1029/WR014i004p00601.

Cohen, N. Y., and W. R. Boos, 2014: Has the number of Indian summer monsoon depressions decreased over the last 30 years? *Geophys. Res. Lett.*, **41**, 7846–7853, doi:10.1002/2014GL061895, URL http://dx.doi.org/10.1002/2014GL061895.

Cohen, N. Y., and W. R. Boos, 2016: Perspectives on moist baroclinic instability: implications for the growth of monsoon depressions. *J. Atmos. Sci.*, **73 (4)**, 1767–1788, doi:10.1175/JAS-D-15-0254.1, URL http://dx.doi.org/10.1175/JAS-D-15-0254.1.

Cox, P. M., R. A. Betts, C. B. Bunton, R. L. H. Essery, P. R. Rowntree, and J. Smith, 1999: The impact of new land surface physics on the gcm simulation of climate and climate sensitivity. *Climate Dyn.*, **15 (3)**, 183–203, doi:10.1007/s003820050276, URL http://dx.doi.org/10.1007/s003820050276.

Craig, G. C., and S. L. Gray, 1996: CISK or WISHE as the mechanism for tropical cyclone intensification. *J. Atmos. Sci.*, **53 (23)**, 3528–3540, doi:10.1175/1520-0469(1996)053⟨3528:COWATM⟩2.0.CO;2, URL http://dx.doi.org/10.1175/1520-0469(1996)053⟨3528:COWATM⟩2.0.CO;2.

Dacre, H. F., M. K. Hawcroft, M. A. Stringer, and K. I. Hodges, 2012: An extratropical cyclone atlas: A tool for illustrating cyclone structure and evolution characteristics. *Bull. Amer. Meteor. Soc.*, **93**, 1497–1502, doi:10.1175/BAMS-D-11-00164.1, URL http://dx.doi.org/10.1175/BAMS-D-11-00164.1.

Daggupatty, S. J., and D. R. Sikka, 1977: On the vorticity budget and vertical velocity distribution associated with the life cycle of a monsoon depression. *J. Atmos. Sci.*, **34**, 773–792.

Daggupaty, S. M., and D. R. Sikka, 1977: On the vorticity budget and vertical velocity distribution associated with the life cycle of a monsoon depression. *J. Atmos. Sci.*, **34 (5)**, 773–

792, doi:10.1175/1520-0469(1977)034⟨0773:OTVBAV⟩2.0.CO;2, URL http://dx.doi.org/10.1175/1520-0469(1977)034⟨0773:OTVBAV⟩2.0.CO;2.

Dai, A., 2006: Precipitation characteristics in eighteen coupled climate models. *J. Climate*, **19 (18)**, 4605–4630, doi:10.1175/JCLI3884.1, URL http://dx.doi.org/10.1175/JCLI3884.1.

Das, P. K., 1952: Monsoon depressions in the Bay of Bengal. *Indian J. Meteor. Geophys.*, **3**, 225–229.

Das, S., A. K. Mitra, G. R. Iyengar, and J. Singh, 2002: Skill of medium-range forecasts over the Indian monsoon region using different parameterizations of deep convection. *Wea. Forecasting*, **17 (6)**, 1194–1210, doi:10.1175/1520-0434(2002)017⟨1194:SOMRFO⟩2.0.CO;2, URL http://dx.doi.org/10.1175/1520-0434(2002)017⟨1194:SOMRFO⟩2.0.CO;2.

Dash, S. K., J. R. Kumar, and M. S. Shekhar, 2004: On the decreasing frequency of monsoon depressions over the Indian region. *Current Science - Bangalore*, **86 (10)**, 1404–1410.

Davies, T., M. J. P. Cullen, A. J. Malcolm, M. H. Mawson, A. Staniforth, A. A. White, and N. Wood, 2005: A new dynamical core for the Met Office's global and regional modelling of the atmosphere. *Quart. J. Roy. Meteor. Soc.*, **131 (608)**, 1759–1782, doi:10.1256/qj.04.101, URL http://dx.doi.org/10.1256/qj.04.101.

Dee, D. P., and Coauthors, 2011: The ERA-Interim reanalysis: configuration and performance of the data assimilation system. *Quart. J. Roy. Meteor. Soc.*, **137 (656)**, 553–597, doi:10.1002/qj.828, URL http://dx.doi.org/10.1002/qj.828.

DeMaria, M., 1996: The effect of vertical shear on tropical cyclone intensity change. *J. Atmos. Sci.*, **53**, 2076–2088, doi:10.1175/1520-0469(1996)053⟨2076:TEOVSO⟩2.0.CO;2, URL http://dx.doi.org/10.1175/1520-0469(1996)053⟨2076:TEOVSO⟩2.0.CO;2.

Derbyshire, S. H., A. V. Maidens, S. F. Milton, R. A. Stratton, and M. R. Willett, 2011: Adaptive detrainment in a convective parametrization. *Quart. J. Roy. Meteor. Soc.*, **137 (660)**, 1856–1871, doi:10.1002/qj.875, URL http://dx.doi.org/10.1002/qj.875.

Desai, B. N., 1950: On the development and structure of monsoon depressions in India. *Indian J. Meteor. Geophys.*, **22**, 330–336.

Dhar, O. N., and B. K. Bhattacharya, 1973: Contribution of tropical disturbances to the water resources of Ganga basin. *Vayu Mandal*, **3**, 76–79.

Dhar, O. N., and P. R. Rakhecha, 1976: Does the absence of cyclonic disturbances cause deficient rainfall in north Indian subdivisions during monsoon months? *Proc. Indian Natl. Sci. Acad.*, **42**, 81–89.

Ding, Y.-H., 1981: A case study of formation and structure of a depression over the Arabian Sea. *Chin. J. Atmos. Sci.*, **5**, 267–280.

Ding, Y.-H., X.-Q. Fu, and B.-Y. Zhang, 1984: A study of the structure of a monsoon depression over the Bay of Bengal during the summer MONEX. *Adv. Atmos. Sci.*, **1**, 62–75, doi:10.1007/BF03187617, URL http://dx.doi.org/10.1007/BF03187617.

Dinku, T., P. Ceccato, E. Grover-Kopec, M. Lemma, S. J. Connor, and C. F. Ropelewski, 2007: Validation of satellite rainfall products over East Africa's complex topography. *Int. J. Remote Sens.*, **28 (7)**, 1503–1526, doi:10.1080/01431160600954688, URL http://dx.doi.org/10.1080/01431160600954688.

Dinku, T., S. Chidzambwa, P. Ceccato, S. Connor, and C. Ropelewski, 2008: Validation of high-resolution satellite rainfall products over complex terrain. *Int. J. Remote Sens.*, **29 (14)**, 4097–4110, doi:10.1080/01431160701772526, URL http://dx.doi.org/10.1080/01431160701772526.

Dinku, T., S. J. Connor, and P. Ceccato, 2010: *Comparison of CMORPH and TRMM-3B42 over Mountainous Regions of Africa and South America*, 193–204. Springer Netherlands, Dordrecht, doi:10.1007/978-90-481-2915-7_11, URL http://dx.doi.org/10.1007/978-90-481-2915-7_11.

Ditchek, S. D., W. R. Boos, S. J. Camargo, and M. K. Tippett, 2016: A genesis index for monsoon disturbances. *J. Climate*, doi:10.1175/JCLI-D-15-0704.1, URL http://dx.doi.org/10.1175/JCLI-D-15-0704.1.

Douglas, M. W., 1992a: Structure and dynamics of two monsoon depressions. Part I: Observed structure. *Mon. Wea. Rev.*, **120 (8)**, 1524–1547, doi:10.1175/1520-0493(1992)120⟨1524:SADOTM⟩2.0.CO;2, URL http://dx.doi.org/10.1175/1520-0493(1992)120⟨1524:SADOTM⟩2.0.CO;2.

Douglas, M. W., 1992b: Structure and dynamics of two monsoon depressions. Part II: Vorticity and heat budgets. *Mon. Wea. Rev.*, **120 (8)**, 1548–1564, doi:10.1175/1520-0493(1992)120⟨1548:SADOTM⟩2.0.CO;2, URL http://dx.doi.org/10.1175/1520-0493(1992)120⟨1548:SADOTM⟩2.0.CO;2.

Edwards, J. M., and A. Slingo, 1996: Studies with a flexible new radiation code. I: Choosing a configuration for a large-scale model. *Quart. J. Roy. Meteor. Soc.*, **122**, 689–719.

Efron, B., 1979: Bootstrap methods: Another look at the jackknife. *Ann. Stat.*, **7**, 1–26, doi:10.1214/aos/1176344552, URL http://dx.doi.org/10.1214/aos/1176344552.

Eltahir, E. A. B., 1998: A soil moisture–rainfall feedback mechanism: 1. Theory and observations. *Water Resour. Res.*, **34 (4)**, 765–776, doi:10.1029/97WR03499, URL http://dx.doi.org/10.1029/97WR03499.

Emanuel, K. A., 1986: An air-sea interaction theory for tropical cyclones. Part I: Steady-state maintenance. *J. Atmos. Sci.*, **43**, 585–604.

Essery, R. L. H., M. J. Best, R. A. Betts, P. M. Cox, and C. M. Taylor, 2003: Explicit representation of subgrid heterogeneity in a GCM land surface scheme. *J. Hydrometeor.*, **4 (3)**, 530–543, doi:10.1029/97WR03499, URL http://dx.doi.org/10.1029/97WR03499.

Fan, Y., and H. van den Dool, 2004: Climate Prediction Center global monthly soil moisture data set at 0.5 degree resolution for 1948 to present. *J. Geophys. Res. Atmos.*, **109 (D10)**, doi:10.1029/2003JD004345, URL http://dx.doi.org/10.1029/2003JD004345.

Felton, C. S., B. Subrahmanyam, and M. V. S. N., 2013: ENSO-modulated cyclogenesis over the Bay of Bengal. *J. Climate*, **26**, 9806–9818, doi:10.1175/JCLI-D-13-00134.1, URL http://dx.doi.org/10.1175/JCLI-D-13-00134.1.

Frank, W. M., 1977: The structure and energetics of the tropical cyclone I. Storm structure. *Mon. Wea. Rev.*, **105 (9)**, 1119–1135, doi:10.1175/1520-0493(1977)105⟨1119:TSAEOT⟩2.0.CO;2, URL http://dx.doi.org/10.1175/1520-0493(1977)105⟨1119:TSAEOT⟩2.0.CO;2.

Fritsch, J. M., and C. F. Chappell, 1980: Numerical prediction of convectively driven mesoscale pressure systems. Part II: Mesoscale model. *J. Atmos. Sci.*, **37 (8)**, 1734–1762, doi:10.1175/1520-0469(1980)037⟨1734:NPOCDM⟩2.0.CO;2, URL http://dx.doi.org/10.1175/1520-0469(1980)037⟨1734:NPOCDM⟩2.0.CO;2.

Fu, Y., and G. Liu, 2001: The variability of tropical precipitation profiles and its impact on microwave brightness temperatures as inferred from TRMM data. *J. Appl. Meteor.*, **40**, 2130–2143, doi:10.1175/1520-0450(2001)040⟨2130:TVOTPP⟩2.0.CO;2, URL http://dx.doi.org/10.1175/1520-0450(2001)040⟨2130:TVOTPP⟩2.0.CO;2.

Gentry, M. S., and G. M. Lackmann, 2010: Sensitivity of simulated tropical cyclone structure and intensity to horizontal resolution. *Mon. Wea. Rev.*, **138 (3)**, 688–704, doi:10.1175/2009MWR2976.1, URL http://dx.doi.org/10.1175/2009MWR2976.1.

George, C. J., and R. K. Datta, 1965: A synoptic study of monsoon depression in the month of September 1963. *Indian J. Meteor. Geophys.*, **16**, 213–220.

Giorgi, F., and M. R. Marinucci, 1996: A investigation of the sensitivity of simulated precipitation to model resolution and its implications for climate studies. *Mon. Wea. Rev.*, **124 (1)**, 148–166, doi:10.1175/1520-0493(1996)124⟨0148:AIOTSO⟩2.0.CO;2, URL http://dx.doi.org/10.1175/1520-0493(1996)124⟨0148:AIOTSO⟩2.0.CO;2.

Godbole, R. V., 1977: The composite structure of the monsoon depression. *Tellus*, **29**, 25–40, doi:10.1111/j.2153-3490.1977.tb00706.x, URL http://dx.doi.org/10.1111/j.2153-3490.1977.tb00706.x.

Goswami, B. N., 1987: A mechanism for the west-north-west movement of monsoon depressions. *Nature*, **326 (6111)**, 376–378, doi:10.1038/326376a0, URL http://dx.doi.org/10.1038/326376a0.

Goswami, B. N., R. N. Keshavamurty, and V. Satyan, 1980: Role of barotropic, baroclinic and combined barotropic-baroclinic instability for the growth of monsoon depressions and mid-tropospheric cyclones. *Proceedings of the Indian Academy of Sciences-Earth and Planetary Sciences*, **89 (1)**, 79–97.

Grant, A. L. M., 2001: Cloud-base fluxes in the cumulus-capped boundary layer. *Quart. J. Roy. Meteor. Soc.*, **127 (572)**, 407–421, doi:10.1002/qj.49712757209, URL http://dx.doi.org/10.1002/qj.49712757209.

Grant, A. L. M., and A. R. Brown, 1999: A similarity hypothesis for shallow-cumulus transports. *Quart. J. Roy. Meteor. Soc.*, **125 (558)**, 1913–1936, doi:10.1002/qj.49712555802, URL http://dx.doi.org/10.1002/qj.49712555802.

Gregory, D., and S. Allen, 1991: The effect of convective scale downdrafts upon NWP and climate simulations. *Preprints, 9th conference on numerical weather prediction, Denver. Amer Meteor Soc*, 122–123.

Gregory, D., R. Kershaw, and P. M. Inness, 1997: Parametrization of momentum transport by convection. II: Tests in single-column and general circulation models. *Quart. J. Roy. Meteor. Soc.*, **123 (541)**, 1153–1183, doi:10.1002/qj.49712354103, URL http:/dx.doi.org/10.1002/qj.49712354103.

Gregory, D., and P. R. Rowntree, 1990: A mass flux convection scheme with representation of cloud ensemble characteristics and stability-dependent closure. *Mon. Wea. Rev.*, **118 (7)**, 1483–1506, doi:10.1175/1520-0493(1990)118⟨1483:AMFCSW⟩2.0.CO;2, URL http://dx.doi.org/10.1175/1520-0493(1990)118⟨1483:AMFCSW⟩2.0.CO;2.

Haddad, Z. S., D. Short, S. L. Durden, E. Im, S. Hensley, M. B. Grable, R. Black, and Coauthors, 1997a: A new parametrization of the rain drop size distribution. *Geoscience and Remote Sensing, IEEE Transactions on*, **35 (3)**, 532–539, doi:10.1109/36.581961, URL http://dx.doi.org/10.1109/36.581961.

Haddad, Z. S., E. A. Smith, C. D. Kummerow, T. Iguchi, M. R. Farrar, S. L. Durden, M. Alves, and W. S. Olson, 1997b: The TRMM day-1 radar/radiometer combined rain-profiling algorithm. *J. Meteor. Soc. Japan*, **75**, 799–809.

Hawkins, H. F., and S. M. Imbembo, 1976: The structure of a small, intense hurricane – Inez 1966. *Mon. Wea. Rev.*, **104**, 418–442, doi:10.1175/1520-0493(1976)104⟨0418:TSOASI⟩2.0.CO;2, URL http://dx.doi.org/10.1175/1520-0493(1976)104⟨0418:TSOASI⟩2.0.CO;2.

Hawkins, H. F., and D. T. Rubsam, 1968: Hurricane Hilda, 1964. II: Structure and budgets of the hurricane on October 1, 1964. *Mon. Wea. Rev.*, **96**, 617–636, doi:10.1175/1520-0493(1968)096⟨0617:HH⟩2.0.CO;2, URL http://dx.doi.org/10.1175/1520-0493(1968)096⟨0617:HH⟩2.0.CO;2.

Haynes, J. M., T. S. L'Ecuyer, G. L. Stephens, S. D. Miller, C. Mitrescu, N. B. Wood, and S. Tanelli, 2009: Rainfall retrieval over the ocean with spaceborne W-band radar. *J. Geophys. Res. Atmos.*, **114 (D8)**, doi:10.1029/2008JD009973, URL http://dx.doi.org/10.1029/2008JD009973.

Hence, D. A., and R. A. Houze, 2011: Vertical structure of hurricane eyewalls as seen by the TRMM precipitation radar. *J. Atmos. Sci.*, **68 (8)**, 1637–1652, doi:10.1175/2011JAS3578.1, URL http://dx.doi.org/10.1175/2011JAS3578.1.

Hess, M., P. Koepke, and I. Schult, 1998: Optical properties of aerosols and clouds. *Bull. Amer. Meteor. Soc.*, **79**, 831–44, doi:10.1175/1520-0477(1998)079⟨0831:OPOAAC⟩2.0.CO;2, URL http://dx.doi.org/10.1175/1520-0477(1998)079⟨0831:OPOAAC⟩2.0.CO;2.

Hill, K. A., and G. M. Lackmann, 2009: Analysis of idealized tropical cyclone simulations using the Weather Research and Forecasting model: Sensitivity to turbulence parameterization and grid spacing. *Mon. Wea. Rev.*, **137 (2)**, 745–765, doi:10.1175/2008MWR2220.1, URL http://dx.doi.org/10.1175/2008MWR2220.1.

Hines, K. M., and D. H. Bromwich, 2008: Development and testing of polar weather research and forecasting (WRF) model. Part I: Greenland ice sheet meteorology*. *Mon. Wea. Rev.*, **136 (6)**, 1971–1989, doi:10.1175/2007MWR2112.1, URL http://dx.doi.org/10.1175/2007MWR2112.1.

Hirose, M., and K. Nakamura, 2005: Spatial and diurnal variation of precipitation systems over Asia observed by the TRMM Precipitation Radar. *J. Geophys. Res. Atmos.*, **110 (D5)**, doi:10.1029/2004JD004815, URL http://dx.doi.org/10.1029/2004JD004815.

Hodges, K. I., 1994: A general method for tracking analysis and its application to meteorological data. *Mon. Wea. Rev.*, **122 (11)**, 2573–2586, doi:10.1175/1520-0493(1994)122⟨2573:AGMFTA⟩2.0.CO;2, URL http://dx.doi.org/10.1175/1520-0493(1994)122⟨2573:AGMFTA⟩2.0.CO;2.

Holland, G. J., 1983: Tropical cyclone motion: Environmental interaction plus a beta effect. *J. Atmos. Sci.*, **40 (2)**, 328–342, doi:10.1175/1520-0469(1983)040⟨0328:TCMEIP⟩2.0.CO;2, URL http://dx.doi.org/10.1175/1520-0469(1983)040⟨0328:TCMEIP⟩2.0.CO;2.

Holton, J. R., and G. J. Hakim, 2012: *An introduction to dynamic meteorology*, Vol. 88. Academic press.

Honnert, R., V. Masson, and F. Couvreux, 2011: A diagnostic for evaluating the representation of turbulence in atmospheric models at the kilometric scale. *J. Atmos. Sci.*, **68 (12)**, 3112–3131, doi:10.1175/JAS-D-11-061.1, URL http://dx.doi.org/10.1175/JAS-D-11-061.1.

Hoskins, B. J., and K. I. Hodges, 2002: New perspectives on the Northern hemisphere winter storm tracks. *J. Atmos. Sci.*, **59 (6)**, 1041–1061, doi:10.1175/1520-0469(2002)059⟨1041:NPOTNH⟩2.0.CO;2, URL http://dx.doi.org/10.1175/1520-0469(2002)059⟨1041:NPOTNH⟩2.0.CO;2.

Hoskins, B. J., and I. N. James, 2014: *Fluid Dynamics of the Midlatitude Atmosphere*. John Wiley and sons, ISBN 978-0-470-79519-4. 408pp.

Hotelling, H., 1992: The generalization of Student's ratio. *Breakthroughs in Statistics*, Springer, 54–65, doi:10.1007/978-1-4612-0919-5_4, URL http://dx.doi.org/10.1007/978-1-4612-0919-5_4.

Houze, R. A., 1989: Observed structure of mesoscale convective systems and implications for large-scale heating. *Quart. J. Roy. Meteor. Soc.*, **115 (487)**, 425–461, doi:10.1002/qj.49711548702, URL http:/dx.doi.org/10.1002/qj.49711548702.

Houze, R. A., 1997: Stratiform precipitation in regions of convection: A meteorological paradox? *Bull. Amer. Meteor. Soc.*, **78 (10)**, 2179–2196, doi:10.1175/1520-0477(1997)078⟨2179:SPIROC⟩2.0.CO;2, URL http://dx.doi.org/10.1175/1520-0477(1997)078⟨2179:SPIROC⟩2.0.CO;2.

Houze, R. A., 2010: Review: Clouds in tropical cyclones. *Mon. Wea. Rev.*, **138**, 293–344, doi:10.1175/2009MWR2989.1, URL http://dx.doi.org/10.1175/2009MWR2989.1.

Houze, R. A., D. C. Wilton, and B. F. Smull, 2007: Monsoon convection in the Himalayan region as seen by the TRMM Precipitation Radar. *Quart. J. Roy. Meteor. Soc.*, **133 (627)**, 1389–1411, doi:10.1002/qj.106, URL http://dx.doi.org/10.1002/qj.106.

Huffman, G. J., 1997: Estimates of root-mean-square random error for finite samples of estimated precipitation. *J. Appl. Meteor.*, **36 (9)**, 1191–1201, doi:10.1175/1520-0450(1997)036⟨1191:EORMSR⟩2.0.CO;2, URL http://dx.doi.org/10.1175/1520-0450(1997)036⟨1191:EORMSR⟩2.0.CO;2.

Huffman, G. J., R. F. Adler, D. T. Bolvin, and E. J. Nelkin, 2010: The TRMM multi-satellite precipitation analysis (TMPA). *Satellite rainfall applications for surface hydrology*, Springer, 3–22, doi:10.1007/978-90-481-2915-7_1, URL http://dx.doi.org/10.1007/978-90-481-2915-7_1.

Huffman, G. J., R. F. Adler, B. Rudolf, U. Schneider, and P. R. Keehn, 1995: Global precipitation estimates based on a technique for combining satellite-based estimates, rain gauge analysis, and NWP model precipitation information. *J. Climate*, **8 (5)**, 1284–1295, doi:10.1175/1520-0442(1995)008⟨1284:GPEBOA⟩2.0.CO;2, URL http://dx.doi.org/10.1175/1520-0442(1995)008⟨1284:GPEBOA⟩2.0.CO;2.

Huffman, G. J., and Coauthors, 1997: The global precipitation climatology project (GPCP) combined precipitation dataset. *Bull. Amer. Meteor. Soc.*, **78 (1)**, 5–20, doi:10.1175/1520-0477(1997)078⟨0005:TGPCPG⟩2.0.CO;2, URL http://dx.doi.org/10.1175/1520-0477(1997)078⟨0005:TGPCPG⟩2.0.CO;2.

Huffman, G. J., and Coauthors, 2007: The TRMM multisatellite precipitation analysis (TMPA): quasi-global, multiyear, combined-sensor precipitation estimates at fine scales. *J. Hydrometeor.*, **8**, 38–55, doi:10.1175/JHM560.1, URL http://dx.doi.org/10.1175/JHM560.1.

Hunt, K. M. R., and D. J. Parker, 2016: The movement of Indian monsoon depressions by interaction with image vortices near the Himalayan wall. *Quart. J. Roy. Meteor. Soc.*, **142 (698A)**, 2224–2229, doi:10.1002/qj.2812, URL http://dx.doi.org/10.1002/qj.2812.

Hunt, K. M. R., and A. G. Turner, 2016: The effect of soil moisture perturbations on Indian monsoon depressions in a numerical weather prediction model. *J. Climate*, submitted.

Hunt, K. M. R., and A. G. Turner, 2017: The representation of Indian monsoon depressions at different horizontal resolutions in the met office unied model. *J. Climate*, doi:10.1002/qj.3030, URL http://dx.doi.org/10.1002/qj.3030, accepted.

Hunt, K. M. R., A. G. Turner, P. M. Inness, D. E. Parker, and R. C. Levine, 2016a: On the structure and dynamics of Indian monsoon depressions. *Mon. Wea. Rev.*, **144 (9)**, 3391–3416, doi:10.1175/MWR-D-15-0138.1, URL http://dx.doi.org/10.1175/MWR-D-15-0138.1.

Hunt, K. M. R., A. G. Turner, and D. E. Parker, 2016b: The spatiotemporal structure of precipitation in Indian monsoon depressions. *Quart. J. Roy. Meteor. Soc.*, doi:10.1002/qj.2901, URL http://dx.doi.org/10.1002/qj.2901, in press.

Hunt, K. M. R., A. G. Turner, and L. C. Shaffrey, 2017: A climatology of western disturbances. *Quart. J. Roy. Meteor. Soc.*, in preparation.

Hurley, J. V., and W. R. Boos, 2015: A global climatology of monsoon low pressure systems. *Quart. J. Roy. Meteor. Soc.*, **141**, 1049–1064, doi:10.1002/qj.2447, URL http://dx.doi.org/10.1002/qj.2447.

Iguchi, T., T. Kozu, R. Meneghini, J. Awaka, and K. Okamoto, 2000: Rain-profiling algorithm for the TRMM precipitation radar. *J. Appl. Meteor.*, **39 (12)**, 2038–2052, doi:10.1175/1520-0450(2001)040⟨2038:RPAFTT⟩2.0.CO;2, URL http://dx.doi.org/10.1175/1520-0450(2001)040⟨2038:RPAFTT⟩2.0.CO;2.

IMD, 2015: Frequently asked questions (FAQs) on monsoon. India Meteorological Department, accessed: 2016-10-13, http://www.imd.gov.in/section/nhac/monsoonfaq.pdf.

IMD, 2016: Terminologies and glossary. India Meterological Department, accessed: 2016-10-27, http://imd.gov.in/section/nhac/termglossary.pdf.

Jakob, C., 1999: Cloud cover in the ECMWF reanalysis. *J. Climate*, **12 (4)**, 947–959, doi:10.1175/1520-0442(1999)012⟨0947:CCITER⟩2.0.CO;2, URL http://dx.doi.org/10.1175/1520-0442(1999)012⟨0947:CCITER⟩2.0.CO;2.

Jastrow, R., and M. Halem, 1972: Simulation studies and the design of the First GARP Global Experiment. Technical Report NASA-TM-X-69613, NASA. URL https://ntrs.nasa.gov/archive/nasa/casi.ntrs.nasa.gov/19730022850.pdf.

Jha, U., 2003: *Land, Labour, and Power: Agrarian Crisis and the State in Bihar (1937-52)*. Aakar Books.

Johnson, S. J., and Coauthors, 2016: The resolution sensitivity of the South Asian monsoon and Indo-Pacific in a global 0.35 degree AGCM. *Climate Dyn.*, **46 (3-4)**, 807–831, doi:10.1007/s00382-015-2614-1, URL http://dx.doi.org/10.1007/s00382-015-2614-1.

Kawanishi, T., H. Takamatsu, T. Kozu, K. Okamoto, and H. Kumagai, 1993: TRMM precipitation radar. *Geoscience and Remote Sensing Symposium, 1993. IGARSS'93. Better Understanding of Earth Environment., International*, IEEE, 423–425, doi:10.1109/IGARSS.1993.322315, URL http://dx.doi.org/10.1109/IGARSS.1993.322315.

Kawanishi, T., and Coauthors, 2000: TRMM precipitation radar. *Adv. Space Res.*, **25 (5)**, 969–972.

Keshavamurty, R. N., G. C. Asnani, P. V. Pillai, and S. K. Das, 1978: Some studies of the growth of monsoon disturbances. *Proceedings of the Indian Academy of Sciences-Section A, Earth and Planetary Sciences*, **87 (3)**, 61–75.

Kikuchi, K., and B. Wang, 2008: Diurnal precipitation regimes in the global tropics. *J. Climate*, **21**, 2680–2696, doi:10.1175/2007JCLI2051.1.

Kikuchi, K., and B. Wang, 2010: Formation of tropical cyclones in the Northern Indian Ocean associated with two types of tropical intraseasonal oscillation modes. *J. Meteor. Soc. Japan*, **88**, 475–496, doi:10.2151/jmsj.2010-313, URL http://dx.doi.org/10.2151/jmsj.2010-313.

Kishtawal, C., D. Niyogi, B. Rajagopalan, M. Rajeevan, N. Jaiswal, and U. Mohanty, 2013: Enhancement of inland penetration of monsoon depressions in the Bay of Bengal due to prestorm ground wetness. *Water Resour. Res.*, **49 (6)**, 3589–3600, doi:10.1002/wrcr.20301, URL http://dx.doi.org/10.1002/wrcr.20301.

Knapp, K. R., M. C. Kruk, D. H. Levinson, H. J. Diamond, and C. J. Neumann, 2010: The international best track archive for climate stewardship (IBTrACS) unifying tropical cyclone data. *Bull. Amer. Meteor. Soc.*, **91 (3)**, 363–376, doi:10.1175/2009BAMS2755.1, URL http://dx.doi.org/10.1175/2009BAMS2755.1.

Kobayashi, S., and Coauthors, 2015: The JRA-55 reanalysis: General specifications and basic characteristics. *J. Meteor. Soc. Japan*, **93 (1)**, 5–48, doi:10.2151/jmsj.2015-001, URL http://dx.doi.org/10.2151/jmsj.2015-001.

Koteswaram, P., and C. A. George, 1958: On the formation of monsoon depressions in the Bay of Bengal. *Indian J. Meteor. Geophys.*, **9**, 9–22.

Koteswaram, P., and C. A. George, 1960: A case study of a monsoon depression in the Bay of Bengal. *Monsoons of the World*, 145–56.

Kozu, T., and Coauthors, 2001: Development of precipitation radar onboard the Tropical Rainfall Measuring Mission (TRMM) satellite. *IEEE Trans. Geosci. Rem. Sens.*, **39**, 102–116, doi:10.1109/36.898669, URL http://dx.doi.org/10.1109/36.898669.

Kraus, E. B., 1963: The diurnal precipitation change over the sea. *J. Atmos. Sci.*, **20 (6)**, 551–556, doi:10.1175/1520-0469(1963)020⟨0551:TDPCOT⟩2.0.CO;2, URL http://dx.doi.org/10.1175/1520-0469(1963)020⟨0551:TDPCOT⟩2.0.CO;2.

Kripalani, R., and S. V. Singh, 1986: Rainfall probabilities and amount associated with monsoon depression over India. *Mausam*, **37**, 111–116.

Krishnakumar, V., R. N. Keshavamurty, and S. V. Kasture, 1992: Moist baroclinic instability and the growth of monsoon depressionslinear and nonlinear studies. *Proc. Indian Natl. Sci. Acad.*, **101 (2)**, 123–152.

Krishnamurthy, V., and R. S. Ajayamohan, 2010: Composite structure of monsoon low pressure systems and its relation to Indian rainfall. *J. Climate*, **23**, 4285–4305, doi:10.1175/2010JCLI2953.1, URL http://dx.doi.org/10.1175/2010JCLI2953.1.

Krishnamurthy, V., and J. Shukla, 2007: Intraseasonal and seasonally persisting patterns of Indian monsoon rainfall. *J. Climate*, **20**, 3–20, doi:10.1175/JCLI3981.1, URL http://dx.doi.org/10.1175/JCLI3981.1.

Krishnamurti, T. N., 1985: Summer monsoon experiment-a review. *Mon. Wea. Rev.*, **113 (9)**, 1590–1626, doi:10.1175/1520-0493(1985)113⟨1590:SMER⟩2.0.CO;2, URL http://dx.doi.org/10.1175/1520-0493(1985)113⟨1590:SMER⟩2.0.CO;2.

Krishnamurti, T. N., P. Ardanuy, Y. Ramanathan, and R. Pasch, 1981: On the onset vortex of the summer monsoon. *Mon. Wea. Rev.*, **109 (2)**, 344–363, doi:10.1175/1520-0493(1981)109⟨0344:OTOVOT⟩2.0.CO;2, URL http://dx.doi.org/10.1175/1520-0493(1981)109⟨0344:OTOVOT⟩2.0.CO;2.

Krishnamurti, T. N., M. Kanamitsu, R. V. Godbole, C.-B. Chang, F. Carr, and J. H. Chow, 1975: Study of a monsoon depression (I). *J. Meteor. Soc. Japan*, **53 (4)**, 227–240, URL https://www.jstage.jst.go.jp/article/jmsj1965/53/4/53_4_227/_article/-char/en/.

Krishnamurti, T. N., M. Kanamitsu, R. V. Godbole, C.-B. Chang, F. Carr, and J. H. Chow, 1976: Study of a monsoon depression (II), dynamical structure. *J. Meteor. Soc. Japan*, **54 (4)**, 208–225.

Krishnan, R., D. C. Ayantika, V. Kumar, and S. Pokhrel, 2011: The long-lived monsoon depressions of 2006 and their linkage with the Indian Ocean Dipole. *Int. J. Climatol.*, **31 (9)**, 1334–1352, doi:10.1002/joc.2156, URL http://dx.doi.org/10.1002/joc.2156.

Kulshrestha, S. M., and M. G. Gupta, 1964: Satellite study of an inland monsoon depression. *Indian J. Meteor. Geophys.*, **15**, 175–183.

Kummerow, C., W. Barnes, T. Kozu, J. Shiue, and J. Simpson, 1998: The Tropical Rainfall Measuring Mission (TRMM) sensor package. *J. Atmos. Oceanic Technol.*, **15**, 809–817, doi:10.1175/1520-0426(1998)015⟨0809:TTRMMT⟩2.0.CO;2, URL http://dx.doi.org/10.1175/1520-0426(1998)015⟨0809:TTRMMT⟩2.0.CO;2.

Kummerow, C., and Coauthors, 2000: The status of the Tropical Rainfall Measuring Mission (TRMM) after two years in orbit. *J. Appl. Meteor.*, **39 (12)**, 1965–1982, doi:10.1175/1520-0450(2001)040⟨1965:TSOTTR⟩2.0.CO;2, URL http://dx.doi.org/10.1175/1520-0450(2001)040⟨1965:TSOTTR⟩2.0.CO;2.

La Seur, N. E., and H. F. Hawkins, 1963: An analysis of Hurricane Cleo (1958) based on data from research reconnaissance aircraft. *Mon. Wea. Rev.*, **91**, 694–709, doi:10.1175/1520-0493(1963)091⟨0694:AAOHCB⟩2.3.CO;2, URL http://dx.doi.org/10.1175/1520-0493(1963)091⟨0694:AAOHCB⟩2.3.CO;2.

L'Ecuyer, T. S., and G. L. Stephens, 2002: An estimation-based precipitation retrieval algorithm for attenuating radars. *J. Appl. Meteor.*, **41 (3)**, 272–285, doi:10.1175/1520-0450(2002)041⟨0272:AEBPRA⟩2.0.CO;2, URL http://dx.doi.org/10.1175/1520-0450(2002)041⟨0272:AEBPRA⟩2.0.CO;2.

L'Ecuyer, T. S., N. B. Wood, T. Haladay, G. L. Stephens, and P. W. Stackhouse, 2008: Impact of clouds on atmospheric heating based on the R04 CloudSat fluxes and heating rates data set. *J. Geophys. Res. Atmos.*, **113 (D8)**, doi:10.1029/2008JD009951, URL http://dx.doi.org/10.1029/2008JD009951.

LeMone, M. A., E. J. Zipser, and S. B. Trier, 1998: The role of environmental shear and thermodynamic conditions in determining the structure and evolution of mesoscale convective systems during TOGA-COARE. *J. Atmos. Sci.*, **55**, 3493–3518, doi:10.1175/1520-0469(1998)055⟨3493:TROESA⟩2.0.CO;2, URL http://dx.doi.org/10.1175/1520-0469(1998)055⟨3493:TROESA⟩2.0.CO;2.

Leslie, L. M., and G. J. Holland, 1995: On the bogussing of tropical cyclones in numerical models: A comparison of vortex profiles. *Meteor. Atmos. Phys.*, **56**, 101–110, doi:10.1007/BF01022523, URL http://dx.doi.org/10.1007/BF01022523.

Levenberg, D., 1944: A method for the solution of certain non-linear problems in least squares. *Quart. Appl. Math.*, **2**, 164–168, URL http://www.jstor.org/stable/43633451.

Levine, R. C., and G. M. Martin, 2016: On the climate model simulation of indian monsoon low pressure systems and the effect of remote disturbances and systematic biases. *Climate Dyn.*, submitted.

Lindzen, R. S., B. Farrell, and A. J. Rosenthal, 1983: Absolute barotropic instability and monsoon depressions. *J. Atmos. Sci.*, **40 (5)**, 1178–1184, doi:10.1175/1520-0469(1983)040⟨1178:ABIAMD⟩2.0.CO;2, URL http://dx.doi.org/10.1175/1520-0469(1983)040⟨1178:ABIAMD⟩2.0.CO;2.

Liu, C., R. P. Allan, M. Brooks, and S. Milton, 2014: Comparing tropical precipitation simulated by the Met Office NWP and climate models with satellite observations. *J. Appl. Meteor. Climatol.*, **53**, 200–214, doi:10.1175/JAMC-D-13-082.1, URL http://dx.doi.org/10.1175/JAMC-D-13-082.1.

Liu, Y.-Y., W. A. Dorigo, R. M. Parinussa, R. A. M. de Jeu, W. Wagner, M. F. McCabe, J. P. Evans, and A. I. J. M. Van Dijk, 2012a: Trend-preserving blending of passive and active microwave soil moisture retrievals. *Remote Sens. Env.*, **123**, 280–297, doi:10.1016/j.rse.2012.03.014, URL http://dx.doi.org/10.1016/j.rse.2012.03.014.

Liu, Y.-Y., R. Parinussa, W. A. Dorigo, R. A. M. De Jeu, W. Wagner, A. I. J. M. Van Dijk, M. F. McCabe, and J. P. Evans, 2011: Developing an improved soil moisture dataset by blending passive and active microwave satellite-based retrievals. *Hydrol. Earth Syst. Sci.*, **15 (2)**, 425–436, doi:doi:10.5194/hess-15-425-2011, URL http://www.hydrol-earth-syst-sci.net/15/425/2011.

Liu, Z., R. Marchand, and T. Ackerman, 2010: A comparison of observations in the tropical western pacific from ground-based and satellite millimeter-wavelength cloud radars. *J. Geophys. Res. Atmos.*, **115 (D24)**, doi:10.1029/2009JD013575, URL http://dx.doi.org/10.1029/2009JD013575.

Liu, Z., D. Ostrenga, W. Teng, and S. Kempler, 2012b: Tropical Rainfall Measuring Mission (TRMM) precipitation data and services for research and applications. *Bull. Amer. Meteor. Soc.*, **93**, 1317–1325, doi:10.1175/BAMS-D-11-00152.1, URL http://dx.doi.org/10.1175/BAMS-D-11-00152.1.

Lock, A. P., 2001: The numerical representation of entrainment in parameterizations of boundary layer turbulent mixing. *Mon. Wea. Rev.*, **129 (5)**, 1148–1163, doi:10.1175/1520-0493(2001)129⟨1148:TNROEI⟩2.0.CO;2, URL http://dx.doi.org/10.1175/1520-0493(2001)129⟨1148:TNROEI⟩2.0.CO;2.

Lock, A. P., A. R. Brown, M. R. Bush, G. M. Martin, and R. N. B. Smith, 2000: A new boundary layer mixing scheme. Part I: Scheme description and single-column model tests. *Mon. Wea. Rev.*, **128 (9)**, 3187–3199, doi:10.1175/1520-0493(2000)128⟨3187:ANBLMS⟩2.0.CO;2, URL http://dx.doi.org/10.1175/1520-0493(2000)128⟨3187:ANBLMS⟩2.0.CO;2.

Lott, F., and M. J. Miller, 1997: A new subgrid-scale orographic drag parametrization: Its formulation and testing. *Quart. J. Roy. Meteor. Soc.*, **123 (537)**, 101–127, doi:10.1002/qj.49712353704, URL http://dx.doi.org/10.1002/qj.49712353704.

Marchand, R., G. G. Mace, T. Ackerman, and G. Stephens, 2008: Hydrometeor detection using CloudSat - an earth-orbiting 94-ghz cloud radar. *Journal of Atmospheric and Oceanic Technology*, **25 (4)**, 519–533, doi:10.1175/2007JTECHA1006.1, URL http://dx.doi.org/10.1175/2007JTECHA1006.1.

Marquadt, D., 1963: An algorithm for least-squares estimation of nonlinear parameters. *SIAM J. Appl. Math.*, **11**, 431–441, doi:10.1137/0111030, URL http://dx.doi.org/10.1137/0111030.

Martin, G. M., M. A. Ringer, V. D. Pope, A. Jones, C. Dearden, and T. J. Hinton, 2006: The physical properties of the atmosphere in the new Hadley Centre Global Environmental Model (HadGEM1). Part I: Model description and global climatology. *J. Climate*, **19 (7)**, 1274–1301, doi:10.1175/JCLI3636.1, URL http://dx.doi.org/10.1175/JCLI3636.1.

Mass, C. F., D. Ovens, K. Westrick, and B. A. Colle, 2002: Does increasing horizontal resolution produce more skillful forecasts? *Bull. Amer. Meteor. Soc.*, **83 (3)**, 407, doi:10.1175/1520-0477(2002)083⟨0407:DIHRPM⟩2.3.CO;2, URL http://dx.doi.org/10.1175/1520-0477(2002)083⟨0407:DIHRPM⟩2.3.CO;2.

Milne-Thomson, L. M., 1940: Hydrodynamical images. *Math. Proc. Cambridge Philos. Soc.*, **36**, 246–247, doi:10.1017/S0305004100017242, URL http://dx.doi.org/10.1017/S0305004100017242.

Milne-Thomson, L. M., 1960: *Theoretical Hydrodynamics*. 4th ed., Macmillan and Company Limited, St. Martin's Street, London WC2.

Mishra, S. K., and P. S. Salvekar, 1980: Role of baroclinic instability in the development of monsoon disturbances. *J. Atmos. Sci.*, **37 (2)**, 383–394, doi:10.1175/1520-0469(1980)037⟨0383:ROBIIT⟩2.0.CO;2, URL http://dx.doi.org/10.1175/1520-0469(1980)037⟨0383:ROBIIT⟩2.0.CO;2.

Moalafhi, D. B., J. P. Evans, and A. Sharma, 2016: Evaluating global reanalysis datasets for provision of boundary conditions in regional climate modelling. *Climate Dyn.*, 1–19, doi:10.1007/s00382-016-2994-x, URL http://dx.doi.org/0.1007/s00382-016-2994-x.

Mooley, D. A., 1973: Some aspects of Indian monsoon depressions and the associated rainfall. *Mon. Wea. Rev.*, **101**, 271–280, doi:10.1175/1520-0493(1973)101⟨0271:SAOIMD⟩2.3.CO;2, URL http://dx.doi.org/10.1175/1520-0493(1973)101⟨0271:SAOIMD⟩2.3.CO;2.

Mooley, D. A., 1980: Severe cyclonic storms in the Bay of Bengal, 1877-1977. *Mon. Wea. Rev.*, **108 (10)**, 1647–1655, doi:10.1175/1520-0493(1980)108⟨1647:SCSITB⟩2.0.CO;2, URL http://dx.doi.org/10.1175/1520-0493(1980)108⟨1647:SCSITB⟩2.0.CO;2.

Mooley, D. A., and J. Shukla, 1989: Main features of the westward-moving low pressure systems which

form over the Indian region during the summer monsoon season and their relation to the monsoon rainfall. *Mausam*, **40 (2)**, 137–152.

Moorthi, S., and A. Arakawa, 1985: Baroclinic instability with cumulus heating. *Journal of the atmospheric sciences*, **42 (19)**, 2007–2031, doi:10.1175/1520-0469(1985)042⟨2007:BIWCH⟩2.0.CO;2, URL http://dx.doi.org/10.1175/1520-0469(1985)042⟨2007:BIWCH⟩2.0.CO;2.

Mukhopadhyay, P., S. Taraphdar, B. N. Goswami, and K. Krishnakumar, 2010: Indian summer monsoon precipitation climatology in a high-resolution regional climate model: Impacts of convective parameterization on systematic biases. *Wea. Forecasting*, **25 (2)**, 369–387, doi:10.1175/2009WAF2222320.1, URL http://dx.doi.org/10.1175/2009WAF2222320.1.

Mulky, G. R., and A. K. Banerji, 1960: The mean upper-wind circulation around monsoon depressions in India. *J. Meteor.*, **17**, 8–14, doi:10.1175/1520-0469(1960)017⟨0008:TMUWCA⟩2.0.CO;2, URL http://dx.doi.org/10.1175/1520-0469(1960)017⟨0008:TMUWCA⟩2.0.CO;2.

Mull, S., and Y. P. Rao, 1949: Indian tropical storms and zones of heavy rainfall. *Indian J. Phys.*, **23**, 371–377.

Murakami, H., and M. Sugi, 2010: Effect of model resolution on tropical cyclone climate projections. *Sola*, **6**, 73–76, doi:10.2151/sola.2010-019, URL http://dx.doi.org/10.2151/sola.2010-019.

Nair, S., G. Srinivasan, and R. Nemani, 2009: Evaluation of multi-satellite TRMM derived rainfall estimates over a western state of India. *J. Meteor. Soc. Japan*, **87**, 927–939, doi:10.2151/jmsj.87.927, URL http://dx.doi.org/10.2151/jmsj.87.927.

Nesbitt, S. W., and E. J. Zipser, 2003: The diurnal cycle of rainfall and convective intensity according to three years of trmm measurements. *J. Climate*, **16 (10)**, 1456–1475, doi:10.1175/1520-0442(2003)016⟨1456:TDCORA⟩2.0.CO;2, URL http://journals.ametsoc.org/doi/abs/10.1175/1520-0442%282003%29016%3C1456%3ATDCORA%3E2.0.CO%3B2.

Ogura, Y., and T. Takahashi, 1971: Numerical simulation of the life cycle of a thunderstorm cell. *Mon. Wea. Rev.*, **99 (12)**, 895–911, doi:10.1175/1520-0493(1971)099⟨0895:NSOTLC⟩2.3.CO;2, URL http://dx.doi.org/10.1175/1520-0493(1971)099⟨0895:NSOTLC⟩2.3.CO;2.

Pai, D. S., L. Sridhar, M. Rajeevan, O. P. Sreejith, N. S. Satbhai, and B. Mukhopadhyay, 2013: Development and analysis of a new high spatial resolution (0.25deg x 0.25 deg) long period (1901-2010) daily gridded rainfall data set over India. Tech. Rep. 1, National Climate Centre, India Meteorological Department.

Parker, D. J., P. Willetts, C. Birch, A. G. Turner, J. H. Marsham, C. M. Taylor, S. Kolusu, and G. M. Martin, 2016: The interaction of moist convection and mid-level dry air in the advance of the onset of the Indian monsoon. *Quart. J. Roy. Meteor. Soc.*, doi:10.1002/qj.2815, URL http://dx.doi.org/10.1002/qj.2815.

Petterssen, S., 1956: *Weather Analysis and Forecasting*, Vol. 1. 2nd ed., McGraw Hill, URL http://krishikosh.egranth.ac.in/handle/1/21100.

Pisharoty, P. R., and G. C. Asnani, 1957: Rainfall around monsoon depressions over india. *Indian J. Meteor. Geophys.*, **8**, 15–20.

Pokhrel, S., and D. Sikka, 2013: Variability of the TRMM-PR total and convective and stratiform rain fractions over the Indian region during the summer monsoon. *Climate Dyn.*, **41 (1)**, 21–44, doi:10.1007/s00382-012-1502-1, URL http://dx.doi.org/10.1007/s00382-012-1502-1.

Pope, V., and R. Stratton, 2002: The processes governing horizontal resolution sensitivity in a climate model. *Climate Dyn.*, **19 (3-4)**, 211–236, doi:10.1007/s00382-001-0222-8, URL http://dx.doi.org/10.1007/s00382-001-0222-8.

Potty, K. V. J., U. C. Mohanty, and S. Raman, 2000: Numerical simulation of monsoon depressions over India with a high-resolution nested regional model. *Meteor. Appl.*, **7 (1)**, 45–60, doi:10.1017/S1350482700001432, URL http://dx.doi.org/10.1017/S1350482700001432.

Potty, K. V. J., U. C. Mohanty, and S. Raman, 2001: Simulation of boundary layer structure over the Indian summer monsoon trough during the passage of a depression. *J. Appl. Meteor.*, **40 (7)**, 1241–1254, doi:10.1175/1520-0450(2001)040⟨1241:SOBLSO⟩2.0.CO;2, URL http://dx.doi.org/10.1175/1520-0450(2001)040⟨1241:SOBLSO⟩2.0.CO;2.

Prajeesh, A. G., K. Ashok, and D. V. Bhaskar Rao, 2013: Falling monsoon depression frequency: a Gray-Sikka conditions perspective. *Sci. Rep.*, **3**, 1–8, doi:10.1038/srep02989, URL http://dx.doi.org/10.1038/srep02989.

Prakash, S., and R. M. Gairola, 2014: Validation of trmm-3b42 precipitation product over the tropical indian ocean using rain gauge data from the rama buoy array. *Theor. Appl. Clim.*, **115 (3-4)**, 451–460, doi:10.1007/s00704-013-0903-3, URL http://dx.doi.org/10.1007/s00704-013-0903-3.

Prasad, K., S. R. Kalsi, and R. K. Datta, 1990: On some aspects of wind and cloud structure of monsoon depressions. *Mausam*, **41**, 365–370.

Praveen, V., S. Sandeep, and R. S. Ajayamohan, 2015: On the relationship between mean monsoon precipitation and low pressure systems in climate model simulations. *J. Climate*, **28 (13)**, 5305–5324, doi:10.1175/JCLI-D-14-00415.1, URL http://dx.doi.org/10.1175/JCLI-D-14-00415.1.

Preparata, F. P., and M. Shamos, 2012: *Computational geometry: an introduction*. Springer Science & Business Media.

Raghavan, K., 1967: Influence of tropical storms on monsoon rainfall in India. *Weather*, **22**, 250–256, doi:10.1002/j.1477-8696.1967.tb02929.x, URL http://dx.doi.org/10.1002/j.1477-8696.1967.tb02929.x.

Rajamani, S., and K. V. Rao, 1981: On the occurrence of rainfall over southwest sector of monsoon depression. *Mausam*, **32**, 215–220.

Rajeevan, M., J. Bhate, J. D. Kale, and B. Lal, 2005: Development of a high resolution daily gridded rainfall data for the indian region. *Meteor. Monogr.*, **22**, URL ftp://squall.met.fsu.edu/LAU/070108_1446/doc/ref_report.pdf.pdf.

Rajeevan, M., J. Bhate, J. D. Kale, and B. Lal, 2006: High resolution daily gridded rainfall data for the indian region: Analysis of break and active monsoon spells. *Curr. Sci.*, **91 (3)**, 296–306, URL http://repository.ias.ac.in/94353/.

Rajesh, P. V., and S. Pattnaik, 2016: High resolution land surface response of inland moving Indian monsoon depressions over Bay of Bengal. *SPIE Asia-Pacific Remote Sensing*, Remote Sensing and Modeling of the Atmosphere, Oceans, and Interactions VI, 98820K, doi:10.1117/12.2239712, URL http://dx.doi.org/10.1117/12.2239712.

Ramage, C. S., 1959: Hurricane development. *J. Meteor.*, **16**, 227–237, doi:10.1175/1520-0469(1959)016⟨0227:HD⟩2.0.CO;2, URL http://dx.doi.org/10.1175/1520-0469(1959)016⟨0227:HD⟩2.0.CO;2.

Ramage, C. S., 1971: *Monsoon Meteorology*. Academic Press, New York.

Ramanathan, K. R., and K. P. Ramakrishnan, 1933: The Indian southwest monsoon and the structure of depressions associated with it. *Mem. Ind. Meteor. Dept.*, **26**, 13–36.

Rao, K., and S. Rajamani, 1970: Diagnostic study of a monsoon depression by geostrophic baroclinic model. *Indian J. Meteor. Geophys.*, **21**, 187–194.

Rao, K., and S. Rajamani, 1972: Study of heat sources and sinks and the generation of available potential energy in the Indian region during the southwest monsoon season. *Mon. Wea. Rev.*, **100**, 383–388, doi:10.1175/1520-0493(1972)100⟨0383:SOHSAS⟩2.3.CO;2.

Rao, K. N., and S. Jayamaran, 1958: A statistical study of frequency of depressions and cyclones in the Bay of Bengal. *Indian J. Meteor. Geophys.*, **9**, 187–194.

Rao, K. V., and S. Rajamani, 1968: *Diagnostic study of a monsoon depression by geostrophic baroclinic model*. Institute of Tropical Meteorology.

Rao, K. V., G. S. P. Rao, and S. Rajamani, 1978: Diagnostic study of a monsoon depression. *Indian J. Meteor. Geophys.*, **29**, 260–272.

Rasmusson, E. M., and T. H. Carpenter, 1983: The relationship between Eastern Equatorial Pacific sea surface temperatures and rainfall over India and Sri Lanka. *Mon. Wea. Rev.*, **111**, 517–528, doi:10.1175/1520-0493(1983)111⟨0517:TRBEEP⟩2.0.CO;2, URL http://dx.doi.org/10.1175/1520-0493(1983)111⟨0517:TRBEEP⟩2.0.CO;2.

Ratnam, J. V., and E. A. Cox, 2006: Simulation of monsoon depressions using MM5: sensitivity to cumulus parameterization schemes. *Meteor. Atmos. Phys.*, **93 (1-2)**, 53–78, doi:10.1007/s00703-005-0160-9, URL http://dx.doi.org/10.1007/s00703-005-0160-9.

Ratnam, J. V., and K. K. Kumar, 2005: Sensitivity of the simulated monsoons of 1987 and 1988 to convective parameterization schemes in MM5. *J. Climate*, **18 (14)**, 2724–2743, doi:10.1175/JCLI3390.1, URL http://dx.doi.org/10.1175/JCLI3390.1.

Reed, R. J., and E. E. Recker, 1971: Structure and properties of synoptic-scale wave disturbances in the equatorial western pacific. *J. Atmos. Sci.*, **28 (7)**, 1117–1133, doi:10.1175/1520-0469(1971)028⟨1117:SAPOSS⟩2.0.CO;2, URL http://dx.doi.org/10.1175/1520-0469(1971)028⟨1117:SAPOSS⟩2.0.CO;2.

Riehl, H., and R. J. Shafer, 1944: The recurvature of tropical storms. *J. Meteor.*, **1 (1)**, 42–54, doi:10.1175/1520-0469(1944)001⟨0001:TROTS⟩2.0.CO;2, URL http://dx.doi.org/10.1175/1520-0469(1944)001⟨0001:TROTS⟩2.0.CO;2.

Rienecker, M. M., and Coauthors, 2011: MERRA: NASA's modern-era retrospective analysis for research and applications. *J. Climate*, **24 (14)**, 3624–3648, doi:10.1175/JCLI-D-11-00015.1, URL http://dx.doi.org/10.1175/JCLI-D-11-00015.1.

Rio, C., F. Hourdin, J.-Y. Grandpeix, and J.-P. Lafore, 2009: Shifting the diurnal cycle of parameterized deep convection over land. *Geophys. Res. Lett.*, **36 (7)**, doi:10.1029/2008GL036779, URL http://dx.doi.org/10.1029/2008GL036779.

Roberts, M. J., and Coauthors, 2015: Tropical cyclones in the UPSCALE ensemble of high-resolution global climate models. *J. Climate*, **28 (2)**, 574–596, doi:10.1175/JCLI-D-14-00131.1, URL http://dx.doi.org/10.1175/JCLI-D-14-00131.1.

Roca, R., and Coauthors, 2010: On the water and energy cycles in the tropics. *Comptes Rendus Geoscience*, **342 (4)**, 390–402, doi:http://dx.doi.org/10.1016/j.crte.2010.01.003, URL http://www.sciencedirect.com/science/article/pii/S1631071310000143.

Roeckner, E., and Coauthors, 2006: Sensitivity of simulated climate to horizontal and vertical resolution in the ECHAM5 atmosphere model. *J. Climate*, **19 (16)**, 3771–3791, doi:10.1175/JCLI3824.1, URL http://dx.doi.org/10.1175/JCLI3824.1.

Ropeleski, C. F., and M. S. Halpert, 1987: Global and regional scale precipitation patterns associated with the El Niño/Southern Oscillation. *Mon. Wea. Rev.*, **115**, 1606–1626, doi:10.1175/1520-0493(1987)115⟨1606:GARSPP⟩2.0.CO;2, URL http://dx.doi.org/10.1175/1520-0493(1987)115⟨1606:GARSPP⟩2.0.CO;2.

Rosenfeld, D., and I. M. Lensky, 1998: Satellite-based insights into precipitation formation processes in continental and maritime convective clouds. *Bull. Amer. Meteor. Soc.*, **79**, 2457–2476, doi:10.1175/1520-0477(1998)079⟨2457:SBIIPF⟩2.0.CO;2, URL http://dx.doi.org/10.1175/1520-0477(1998)079⟨2457:SBIIPF⟩2.0.CO;2.

Roy, P. S., and Coauthors, 2015: Development of decadal (1985–1995–2005) land use and land cover database for India. *Remote Sens.*, **7 (3)**, 2401–2430, doi:10.3390/rs70302401, URL http://dx.doi.org/10.3390/rs70302401.

Roy, S. C., and A. K. Roy, 1930: Structure and movement of cyclones in the Indian seas. *Beitr. Phys. Atm.*, **26**, 224–234.

Saha, K., and C. P. Chang, 1983: The baroclinic processes of monsoon depressions. *Mon. Wea. Rev.*, **111 (7)**, 1506–1514, doi:10.1175/1520-0493(1983)111⟨1506:TBPOMD⟩2.0.CO;2, URL http://dx.doi.org/10.1175/1520-0493(1983)111⟨1506:TBPOMD⟩2.0.CO;2.

Saha, S., 1983: Behaviour of monsoon depressions in a primitive equation barotropic model. *Mausam*, **34**, 27.

Saji, N. H., B. N. Goswami, P. N. Vinayachandran, and T. Yamagata, 1999: A dipole mode in the tropical Indian ocean. *Nature*, **401**, 360—363, doi:10.1038/43854, URL http://dx.doi.org/10.1038/43854.

Salari, V., and I. K. Sethi, 1990: Feature point correspondence in the presence of occlusion. *IEEE Transactions on Pattern Analysis and Machine Intelligence*, **12 (1)**, 87–91, doi:10.1109/34.41387, URL http://dx.doi.org/10.1109/34.41387.

Sanders, F., 1984: Quasi-geostrophic diagnosis of the monsoon depression of 58 July 1979. *J. Atmos. Sci.*, **41**, 538–552, doi:10.1175/1520-0469(1984)041⟨0538:QGDOTM⟩2.0.CO;2, URL http://dx.doi.org/10.1175/1520-0469(1984)041⟨0538:QGDOTM⟩2.0.CO;2.

Sarker, R. P., and A. Choudhary, 1988: A diagnostic study of monsoon depressions. *Mausam*, **39**, 9–18.

Sassen, K., and Z. Wang, 2008: Classifying clouds around the globe with the CloudSat radar: 1-year of results. *Geophys. Res. Lett.*, **35 (4)**, doi:10.1029/2007GL032591, URL http://dx.doi.org/10.1029/2007GL032591.

Schenkel, B. A., and R. E. Hart, 2012: An examination of tropical cyclone position, intensity, and intensity life cycle within atmospheric reanalysis datasets. *J. Climate*, **25 (10)**, 3453–3475, doi:10.1175/2011JCLI4208.1, URL http://dx.doi.org/10.1175/2011JCLI4208.1.

Seetaramayya, P., S. S. Parasnis, S. G. Nagar, and K. G. Vernekar, 1993: Thermodynamic structure of the boundary layer in relation to a monsoon depression over the Bay of Bengal-A case study.

Bound.-Lay. Meteor., **65 (3)**, 307–314, doi:10.1007/BF00705532, URL http://dx.doi.org/10.1007/BF00705532.

Shimrat, M., 1962: Algorithm 112: Position of point relative to polygon. *Communications of the ACM*, **5 (8)**, 434, doi:10.1145/368637.368653, URL http://dx.doi.org/10.1145/368637.368653.

Short, D. A., and K. Nakamura, 2000: TRMM radar observations of shallow precipitation over the tropical oceans. *J. Climate*, **13**, 4107–4124, doi:10.1175/1520-0442(2000)013⟨4107:TROOSP⟩2.0.CO;2, URL http://dx.doi.org/10.1175/1520-0442(2000)013⟨4107:TROOSP⟩2.0.CO;2.

Shukla, J., 1978: CISK-barotropic-baroclinic instability and the growth of monsoon depressions. *J. Atmos. Sci.*, **35 (3)**, 495–508, doi:10.1175/1520-0469(1978)035⟨0495:CBBIAT⟩2.0.CO;2, URL http://dx.doi.org/10.1175/1520-0469(1978)035⟨0495:CBBIAT⟩2.0.CO;2.

Shutts, G., 2005: A kinetic energy backscatter algorithm for use in ensemble prediction systems. *Quart. J. Roy. Meteor. Soc.*, **131 (612)**, 3079–3102, doi:10.1256/qj.04.106, URL http://dx.doi.org/10.1256/qj.04.106.

Sikka, D. R., 1977: Some aspects of the life history, structure and movement of monsoon depressions. *Pure Appl. Geophys.*, **115**, 1501–1529, doi:10.1007/BF00874421, URL http://dx.doi.org/10.1007/BF00874421.

Sikka, D. R., 2006: *A study on the monsoon low pressure systems over the Indian region and their relationship with drought and excess monsoon seasonal rainfall*. Center for Ocean-Land-Atmosphere Studies, Center for the Application of Research on the Environment.

Sikka, D. R., and D. K. Paul, 1975: A diagnostic study on the structure of monsoon depressions. *Geophys. Fluid Dynamics Workshop, Monsoon Meteorology, II Sc*, Vol. 136182.

Simpson, J., R. F. Adler, and G. R. North, 1988: A proposed Tropical Rainfall Measuring Mission (TRMM) satellite. *Bull. Amer. Meteor. Soc.*, **69 (3)**, 278–295, doi:10.1175/1520-0477(1988)069⟨0278:APTRMM⟩2.0.CO;2, URL http://dx.doi.org/10.1175/1520-0477(1988)069⟨0278:APTRMM⟩2.0.CO;2.

Simpson, J., C. Kummerow, W.-K. Tao, and R. F. Adler, 1996: On the Tropical Rainfall Measuring Mission (TRMM). *Meteor. Atmos. Phys.*, **60 (1-3)**, 19–36, doi:10.1007/BF01029783, URL http://dx.doi.org/10.1007/BF01029783.

Sindhu, K., and G. Bhat, 2013: Comparison of CloudSat and TRMM radar reflectivities. *J. Earth. Syst. Sci.*, **122 (4)**, 947–956, doi:10.1007/s12040-013-0316-9, URL http://dx.doi.org/10.1007/s12040-013-0316-9.

Singh, S. S., A. A. Kulkarni, and D. R. Sikka, 1980: On some aspects of initialization and forecasts in the Indian monsoon region. *Mon. Wea. Rev.*, **108 (9)**, 1315–1325, doi:10.1175/1520-0493(1980)108⟨1315:OSAOIA⟩2.0.CO;2, URL http://dx.doi.org/10.1175/1520-0493(1980)108⟨1315:OSAOIA⟩2.0.CO;2.

Slingo, J. M., 1987: The development and verification of a cloud prediction scheme for the ECMWF. *Quart. J. Roy. Meteor. Soc.*, **113**, 899–927, doi:10.1256/smsqj.47708, URL http://dx.doi.org/10.1256/smsqj.47708.

Sørland, S. L., and A. Sorteberg, 2015: The dynamic and thermodynamic structure of monsoon low-pressure systems during extreme rainfall events. *Tellus A*, **67**, doi:10.3402/tellusa.v67.27039, URL http://dx.doi.org/10.3402/tellusa.v67.27039.

Sperber, K. R., H. Annamalai, I.-S. Kang, A. Kitoh, A. Moise, A. Turner, B. Wang, and T. Zhou, 2013: The Asian summer monsoon: an intercomparison of CMIP5 vs. CMIP3 simulations of the late 20th century. *Climate Dyn.*, **41 (9-10)**, 2711–2744, doi:10.1007/s00382-012-1607-6, URL http://dx.doi.org/10.1007/s00382-012-1607-6.

Sperber, K. R., S. Hameed, G. L. Potter, and J. S. Boyle, 1994: Simulation of the northern summer monsoon in the ECMWF model: sensitivity to horizontal resolution. *Mon. Wea. Rev.*, **122 (11)**, 2461–2481, doi:10.1175/1520-0493(1994)122⟨2461:SOTNSM⟩2.0.CO;2, URL http://dx.doi.org/10.1175/1520-0493(1994)122⟨2461:SOTNSM⟩2.0.CO;2.

Stano, G., T. N. Krishnamurti, T. S. V. Vijaya Kumar, and A. Chakraborty, 2002: Hydrometeor structure of a composite monsoon depression using the TRMM radar. *Tellus A*, **54**, 370–381, doi:10.1034/j.1600-0870.2002.01330.x, URL http://dx.doi.org/10.1034/j.1600-0870.2002.01330.x.

Stein, T. H., D. Parker, J. Delanoë, N. Dixon, R. J. Hogan, P. Knippertz, R. Maidment, and J. Marsham, 2011: The vertical cloud structure of the West African monsoon: A 4 year climatology using

CloudSat and CALIPSO. *J. Geophys. Res. Atmos.*, **116 (D22)**, doi:10.1029/2011JD016029, URL http://dx.doi.org/10.1029/2011JD016029.

Steiner, M., R. A. Houze, and S. E. Yuter, 1995: Climatological characterization of three-dimensional storm structure from operational radar and rain gauge data. *J. Appl. Meteor.*, **34 (9)**, 1978–2007, doi:10.1175/1520-0450(1995)034⟨1978:CCOTDS⟩2.0.CO;2, URL http://dx.doi.org/10.1175/1520-0450(1995)034⟨1978:CCOTDS⟩2.0.CO;2.

Stephens, G. L., and Coauthors, 2002: The CloudSat mission and the A-Train: a new dimension of space-based observations of clouds and precipitation. *Bull. Amer. Meteor. Soc.*, **83 (12)**, 1771–1790, doi:10.1175/BAMS-83-12-1771, URL http://dx.doi.org/10.1175/BAMS-83-12-1771.

Stephens, G. L., and Coauthors, 2008: CloudSat mission: Performance and early science after the first year of operation. *J. Geophys. Res. Atmos.*, **113 (D8)**, doi:10.1029/2008JD009982, URL http://dx.doi.org/10.1029/2008JD009982.

Stephens, G. L., and Coauthors, 2010: Dreary state of precipitation in global models. *J. Geophys. Res. Atmos.*, **115 (D24)**, doi:10.1029/2010JD014532, URL http://dx.doi.org/10.1029/2010JD014532.

Stern, D. P., and D. S. Nolan, 2012: On the height of the warm core in tropical cyclones. *J. Atmos. Sci.*, **69**, 1657–1680, doi:10.1175/JAS-D-11-010.1, URL http://dx.doi.org/10.1175/JAS-D-11-010.1.

Stowasser, M., H. Annamalai, and J. Hafner, 2009: Response of the South Asian summer monsoon to global warming: mean and synoptic systems. *J. Climate*, **22 (4)**, 1014–1036, doi:10.1175/2008JCLI2218.1, URL http://dx.doi.org/10.1175/2008JCLI2218.1.

Strachan, J., P. L. Vidale, K. Hodges, M. Roberts, and M.-E. Demory, 2013: Investigating global tropical cyclone activity with a hierarchy of AGCMs: The role of model resolution. *J. Climate*, **26 (1)**, 133–152, doi:10.1175/JCLI-D-12-00012.1, URL http://dx.doi.org/10.1175/JCLI-D-12-00012.1.

Stratton, R. A., A. Stirling, and S. Derbyshire, 2009: Changes and developments to convective momentum transport (CMT) parameterization based on analysis of CRM and SCM: Technical note 530. Tech. rep., Technical report 530, UK Met Office.

Sunqvist, H., E. Berge, and J. E. Kristjánsson, 1989: Condensation and cloud studies with a mesoscale numerical weather prediction model. *Mon. Wea. Rev.*, **117**, 1641–1657, doi:10.1175/1520-0493(1989)117⟨1641:CACPSW⟩2.0.CO;2, URL http://dx.doi.org/10.1175/1520-0493(1989)117⟨1641:CACPSW⟩2.0.CO;2.

Tao, W.-K., S. Lang, J. Simpson, and R. Adler, 1993: Retrieval algorithms for estimating the vertical profiles of latent heat release. *J. Meteor. Soc. Japan*, **71 (6)**, 685–700.

Tao, W.-K., and Coauthors, 2006: Retrieval of latent heating from TRMM measurements. *Bull. Amer. Meteor. Soc.*, **87 (11)**, 1555–1572, doi:10.1175/BAMS-87-11-1555, URL http://dx.doi.org/10.1175/BAMS-87-11-1555.

Tripoli, G. J., 1992: An explicit three-dimensional nonhydrostatic numerical simulation of a tropical cyclone. *Meteor. Atmos. Phys.*, **49 (1-4)**, 229–254, doi:10.1007/BF01025409, URL http://dx.doi.org/10.1007/BF01025409.

Tripoli, G. J., and W. R. Cotton, 1980: A numerical investigation of several factors contributing to the observed variable intensity of deep convection over south Florida. *J. Appl. Meteor.*, **19 (9)**, 1037–1063, doi:10.1175/1520-0450(1980)019⟨1037:ANIOSF⟩2.0.CO;2, URL http://dx.doi.org/10.1175/1520-0450(1980)019⟨1037:ANIOSF⟩2.0.CO;2.

Turner, A. G., P. M. Inness, and J. M. Slingo, 2005: The role of the basic state in the ENSO-monsoon relationship and implications for predictability. *Quart. J. Roy. Meteor. Soc.*, **131**, 781–804, doi:10.1256/qj.04.70, URL http://dx.doi.org/10.1256/qj.04.70.

Van den Dool, H., J. Huang, and Y. Fan, 2003: Performance and analysis of the constructed analogue method applied to us soil moisture over 1981–2001. *J. Geophys. Res. Atmos.*, **108 (D16)**, doi:10.1029/2002JD003114, URL http://dx.doi.org/10.1029/2002JD003114.

Vinod Kumar, A., A. Chandrasekar, K. Alapaty, and D. Niyogi, 2007: The impact of assimilating soil moisture, surface temperature, and humidity and the traditional four dimensional data assimilation on the simulation of a monsoon depression over India using a mesoscale model. *J. Appl. Meteor. Climatol.*, **47**, 1393–1412, doi:10.1175/2007JAMC1599.1, URL http://dx.doi.org/10.1175/2007JAMC1599.1.

Wagner, W., W. Dorigo, R. de Jeu, D. Fernandez, J. Benveniste, E. Haas, and M. Ertl, 2012: Fusion of active and passive microwave observations to create an essential climate variable data record on soil moisture. *Proceedings of the XXII International Society for Photogrammetry and Remote*

Sensing (ISPRS) Congress, Melbourne, Australia, Vol. 25, doi:10.5194/isprsannals-I-7-315-2012, URL http://dx.doi.org/10.5194/isprsannals-I-7-315-2012.

Walters, D., and Coauthors, 2015: The Met Office Unified Model Global Atmosphere 6.0/6.1 configurations. *Geosci. Model Dev. Disc.*, doi:10.5194/gmd-2016-194, URL http://dx.doi.org/10.5194/gmd-2016-194, accepted.

Wang, Z., and K. Sassen, 2007: Level 2 cloud scenario classification product process description and interface control document. Online, accessed: 2015-11-23, http://www.cloudsat.cira.colostate.edu/sites/default/files/products/files/2B-CLDCLASS_PDICD.P_R04.20070724.pdf.

Warner, C., 1984: Core structure of a Bay of Bengal monsoon depression. *Mon. Wea. Rev.*, **112 (1)**, 137–152, doi:10.1175/1520-0493(1984)112⟨0137:CSOABO⟩2.0.CO;2, URL http://dx.doi.org/10.1175/1520-0493(1984)112⟨0137:CSOABO⟩2.0.CO;2.

Warner, C., and R. H. Grumm, 1984: Cloud distributions in a Bay of Bengal depression. *Mon. Wea. Rev.*, **112**, 153–172, doi:10.1175/1520-0493(1984)112⟨0154:CDIABO⟩2.0.CO;2, URL http://dx.doi.org/10.1175/1520-0493(1984)112⟨0154:CDIABO⟩2.0.CO;2.

Webster, P. J., V. O. Magaa, T. N. Palmer, J. Shukla, R. A. Tomas, M. Yanai, and T. Yasunari, 1998: Monsoons: Processes, predictability, and the prospects for prediction. *J. Geophys. Res. Oceans*, **103 (C7)**, 14 451–14 510, doi:10.1029/97JC02719, URL http://dx.doi.org/10.1029/97JC02719.

Webster, P. J., and S. Yang, 1992: Monsoon and ENSO: Selectively interactive systems. *Quart. J. Roy. Meteor. Soc.*, **118**, 877–926, doi:10.1002/qj.49711850705, URL http://dx.doi.org/10.1002/qj.49711850705.

Welch, B. L., 1947: The generalization of student's' problem when several different population variances are involved. *Biometrika*, **34 (1/2)**, 28–35, doi:10.2307/2332510, URL http://www.jstor.org/stable/2332510.

Willetts, P. D., and Coauthors, 2016: The 2015 Indian summer monsoon onset-Phenomena, forecasting and research flight planning. *Weather*, in press.

Williams, K. T., and W. M. Gray, 1973: Statistical analysis of satellite-observed trade wind cloud clusters in the western North Pacific. *Tellus*, **25 (4)**, 313–336, doi:10.1111/j.2153-3490.1973.tb00617.x, URL http://dx.doi.org/10.1111/j.2153-3490.1973.tb00617.x.

Wilson, D. R., and S. P. Ballard, 1999: A microphysically based precipitation scheme for the UK Meteorological Office Unified Model. *Quart. J. Roy. Meteor. Soc.*, **125 (557)**, 1607–1636, doi:10.1002/qj.49712555707, URL http://dx.doi.org/10.1002/qj.49712555707.

Wilson, D. R., A. C. Bushell, A. M. Kerr-Munslow, J. D. Price, and C. J. Morcrette, 2008: PC2: A prognostic cloud fraction and condensation scehem. I: Scheme description. *Quart. J. Roy. Meteor. Soc.*, **134**, 2093–2107, doi:10.1002/qj.333, URL http://dx.doi.org/10.1002/qj.333.

Wood, N., and P. J. Mason, 1993: The pressure force induced by neutral, turbulent flow over hills. *Quart. J. Roy. Meteor. Soc.*, **119 (514)**, 1233–1267, doi:10.1002/qj.49711951402, URL http://dx.doi.org/10.1002/qj.49711951402.

Wood, N., and Coauthors, 2014: An inherently mass-conserving semi-implicit semi-Lagrangian discretization of the deep-atmosphere global non-hydrostatic equations. *Quart. J. Roy. Meteor. Soc.*, **140 (682)**, 1505–1520, doi:10.1002/qj.2235, URL http://dx.doi.org/10.1002/qj.2235.

Yianilos, P. N., 1993: Data structures and algorithms for nearest neighbor search in general metric spaces. *SODA*, Vol. 93, 311–21.

Yoon, J.-H., and T.-C. Chen, 2005: Water vapor budget of the Indian monsoon depression. *Tellus A*, **57 (5)**, 770–782, doi:10.1111/j.1600-0870.2005.00145.x, URL http://dx.doi.org/10.1111/j.1600-0870.2005.00145.x.

Young, M. P., 2015: Improved rainfall monitoring for Africa. Ph.D. thesis, University of Reading, U.K.

Yuter, S. E., and R. A. Houze, 1995: Three-dimensional kinematic and microphysical evolution of Florida cumulonimbus. Part II: Frequency distributions of vertical velocity, reflectivity, and differential reflectivity. *Mon. Wea. Rev.*, **123 (7)**, 1941–1963, doi:10.1175/1520-0493(1995)123⟨1941:TDKAME⟩2.0.CO;2, URL http://dx.doi.org/10.1175/1520-0493(1995)123⟨1941:TDKAME⟩2.0.CO;2.

Zhao, S., and G. A. Mills, 1991: A study of a monsoon depression bringing record rainfall over Australia. Part II: Synoptic-diagnostic description. *Mon. Wea. Rev.*, **119 (9)**, 2074–2094, doi:10.1175/1520-0493(1991)119⟨2074:ASOAMD⟩2.0.CO;2, URL http://dx.doi.org/10.1175/1520-0493(1991)119⟨2074:ASOAMD⟩2.0.CO;2.